An Experimental and Numerical Study of Two-Phase Flow in Horizontal Tube Bundles

Mohammed Abdulrahman Almeshaal, B.Eng., M.Sc.

A dissertation for the degree of Doctor of Philosophy (Ph.D.)

Heriot-Watt University

School of Engineering and Physical Sciences

January 2013

Abstract

An effective design for a kettle reboiler is dependent on fitness for purpose while reducing costs. Thus, accurate information concerning two-phase flow behaviour within it is important. Experimental and numerical studies have been carried out in this research to gain a more detailed understanding of the phenomena associated with two-phase flow in a thin-slice kettle reboiler. The kettle reboiler contained 241 electrically heated tubes arranged as 17 rows of 17 columns in an in-line layout with an outside diameter of 19 mm and a pitch-to-diameter ratio of 1.34. The working fluids used in this investigation were pentane and the refrigerant R113. They were boiled at atmospheric pressure at uniform heat fluxes in the range of 10 to 40 kW/m^2.

The patterns of flow inside the kettle reboiler were investigated experimentally using ordinary and high speed cameras. Visual observation of the flow patterns showed that the flow in the tube bundle was two-dimensional at heat fluxes of 20 kW/m^2 and above. The quantity of foam and recirculation above the tube bundle were found to depend on both the heat flux and the working fluid used. Observations of the two-phase flow pattern in the shell indicated that the movement of fluid from the centre column of the bundle was affected by the down flow into the top of the tube bundle. Two flow patterns in the tube bundle were identified: bubbly and intermittent. At low heat fluxes, bubbly flow dominated, then, with increasing heat flux, bubble coalescence led to the development of vapour slugs and intermittent flow was observed.

Pressure drop measurements were made in three columns within the tube bundle. The results showed that at heat fluxes below 20 kW/m^2, the pressure drop remained nearly constant and equal to the all-liquid value. At a heat flux of 20 kW/m^2 and above, the pressure drop was found to increasingly fall below the all-liquid value as the bundle row number increased. This effect was especially evident in the centre of the bundle. A change in the flow pattern caused the pressure distribution up the tube bundle to change from roughly constant to decaying with height.

Based on a number of assumptions, the two-fluid model has been applied. The two-fluid model's drag coefficient and tube resistance were deduced from a one-dimensional model. The two-fluid model predictions show good agreement with the experimental results for the pressure distribution and flow distribution. Grid sizes of 10, 8 and 4 mm for the bundle and the pool were considered. It was found that the predicted bundle

results were not affected by changing the grid size. However, in the pool region, a small grid size was needed. A grid size of 10 mm was used in the bundle while 4 mm was used in the pool. The pool velocity predictions compared well with measured values available in the open literature.

The results indicated that the bundle flow is not significantly affected by the pool flow. This allows the two-fluid model to be further refined: simplifying it and reducing the computational time. A bundle-only two fluid model has been developed to accurately predict two-phase flow behaviour in the kettle reboiler tube bundle. Information available from earlier studies has been used to develop this model because of the difficulties associated with measuring the void fraction and velocities within the tube bundle. The model uses two different boundary conditions: (1) static liquid pressure in the pool and (2) variation of pressure in the pool based on the flow pattern transition. The results predicted by the model have been compared with experimental data and with one and two-fluid models at different heat fluxes. Boundary condition (1) was found to be in good agreement with experimental data and the one and two-fluid models at a heat flux of 10 kW/m^2. This was because the transition flow pattern was not achieved and the bundle was surrounded by a static pool. Boundary condition (2) is based on the Kutateladze number (Ku), which sets the transition point from bubbly to intermittent flow at a certain height in the bundle. For $Ku \leq 1.09$, the bundle flow would be surrounded by liquid, and if $Ku > 1.09$, the bundle flow would be surrounded by two-phase flow. At heat fluxes of 20 kW/m^2 and above, boundary condition (2) has been found to be in good agreement with experimental data and the values predicted from the one and two-fluid models for liquid velocities, vertical mass flux and void fraction. The bundle-only model accurately predicts the trend line of constant and decaying pressure drop measured at low and high heat fluxes, respectively, and the observed flow phenomena in the kettle reboiler. The key feature of the model presented is that it allows two-phase flow in the kettle reboiler to be simulated by only modelling the tube bundle. Thus the model is simplified and less computational time is required.

A central column model was developed using the minimum pressure gradient approach. The predicted results from this model were compared with experimental data and the values predicted by the two-fluid model and the bundle-only model. Reasonable agreement was obtained indicating that the flow distribution may be linked to the minimum pressure gradient.

Acknowledgements

First I thank God for making it possible for me to complete this study.

I wish to express my sincere gratitude to my supervisor Dr David A. McNeil for his invaluable advice, support and continual encouragement throughout the study. I am indebted to him for all his guidance, suggestions and extensive discussion, and his careful reading of this thesis.

My deep appreciation is extended to all members of the School of Engineering and Physical Sciences who supported me during the work, particularly Dr P. A. Kew, Mr. Richard Kinsella, Mr. Kenny Carruthers and Mr. Aziz Aftab.

A very big thank you goes to my wonderful parents for their moral support and encouragement. I am forever grateful to my wife for her love, patience and encouragement, and to my lovely daughters for all their patience.

Special thanks go to the "Saudi Ministry of Higher Education" for their financial support and for their care.

Finally, I would like to thank my office mates, friends and everyone who assisted me in some way along the journey of completing this thesis.

ACADEMIC REGISTRY
Research Thesis Submission

Name*:*	Mohammed Abdulrahman Almeshaal		
School/PGI:	Engineering and Physical Sciences(EPS)		
Version: *(i.e. First, Resubmission, Final)*	Final	Degree Sought (Award **and** Subject area)	PhD, Mechanical Engineering

Declaration

In accordance with the appropriate regulations I hereby submit my thesis and I declare that:

1) the thesis embodies the results of my own work and has been composed by myself
2) where appropriate, I have made acknowledgement of the work of others and have made reference to work carried out in collaboration with other persons
3) the thesis is the correct version of the thesis for submission and is the same version as any electronic versions submitted*.
4) my thesis for the award referred to, deposited in the Heriot-Watt University Library, should be made available for loan or photocopying and be available via the Institutional Repository, subject to such conditions as the Librarian may require
5) I understand that as a student of the University I am required to abide by the Regulations of the University and to conform to its discipline.

* *Please note that it is the responsibility of the candidate to ensure that the correct version of the thesis is submitted.*

Signature of Candidate*:*	Mohammed Almeshaal	Date:	

Submission

Submitted By *(name in capitals):*	MOHAMMED ABDULRAHMAN ALMESHAAL
Signature of Individual Submitting:	
Date Submitted:	

For Completion in the Student Service Centre (SSC)

Received in the SSC by *(name in capitals):*			
Method of Submission (Handed in to SSC; posted through internal/external mail):			
*E-thesis Submitted (**mandatory for final theses)***			
Signature:		Date:	

Table of Contents

List of Figures

List of Tables

Nomenclature

a	Distance Between the tubes	m
A_{gl}	The Cross Sectional Area of All Bundles	m^2
C_p	Pressure Coefficient	-
C_0	The Distribution Parameter or Overflow Factor	-
C	Constant	-
T	Time	s
C_D	Drag Coefficient	-
C_{ap}	Capillary Number	-
D	Tube Diameter	m
D_p	Bubble Diameter	m
f_l	The bundle Friction Factor	-
F_{gl}	Force on the Liquid by the Gas per Unit Volume N/m^3	-
F_r	Froude Number	-
F_{sg}	Force on the Gas By the Solid Per unit Volume	N/m^3
F_{sl}	Force On Liquid By The Solid Per Unit Volume	N/m^3
g	Gravitational Acceleration, $9.81 m/s^2$	
G	Mass Flux kg/m^2s	
h_{fg}	Latent Heat	J/kg
j	Superficial Velocity	-
j_{gc}	Gas Superficial Critical Velocity	m/s
L	Length of Tube	m
m	Mass Flow Rate	kg/s
N	Number of Bubbles	-
P_r	Tube Pitch	m
P	Pressure	Pa
q	Heat Flux	W/m^2
Q	Power	W
Q	Volume Liquid Flow Rate	m^3/s
Re	Reynolds Number	-
Ri	Richardson Number	-

S	Slip Ratio	-
u	Velocity in X-direction	m/s
v	Velocity in Y-direction	m/s
v_r	Relative Velocity	m/s
x	Quality	-
X_{tt}	Martinelli Parameter	-
n	Refractive Index	-

Greek Letters

ϕ	Porosity	-
ρ	Density	Kg/m^3
ε	Volume Fraction	-
α	Void Fraction	-
σ	Surface Tension	-
ϕ_l^2	Two-Phase Friction Multiplier	-
μ	Dynamic Viscosity	Ns/m^2
μ_{gj}	The Drift Velocity	m/s

Subscripts

j	Column Number
C	Continuous
g	Gas
h	Homogenous
l	Liquid
l_o	Liquid Only
min	Minimum
max	Maximum
P	Particle
i	Row Number
s	South Face
e	East Face
n	North Face
w	West Face
$2\emptyset$	Two-phase

List of Publications by the Candidate

1. McNeil, D.A., Bamardouf, K., Burnside, B.M. and Almeshaal, M.A., *Investigation of flow phenomena in a kettle reboiler*, International Journal of Heat and Mass Transfer, 2010, 53,pp. 836-848.

2. Almeshaal, M.A. and McNeil, D.A., *Investigation of two phase flow patterns in a kettle reboiler, 4th Saudi International Conference*, SIC-2010, July 30-31, 2010, Manchester, UK.

3. Almeshaal, M.A. and McNeil, D.A., *Modelling a boiling in a kettle reboiler, 5th Saudi International Conference*, SIC-2011, June 23-26, 2011, Coventry, UK.

4. Almeshaal, M.A. and McNeil, D.A., *A simplified model for the simulation of two-phase flow in a kettle reboiler, 6th Saudi International Conference*, SIC-2012, October 11-14, 2012, London, UK.

5. Almeshaal, M.A. and McNeil, D.A., *Assessing the use of an optical probe for measuring void fraction in a heat exchanger, 6th Saudi International Conference* SIC-2012, October 11-14, 2012, London, UK.

CHAPTER 1

Introduction

1.1 Background

The phenomenon of two-phase flow within tube bundles occurs in many types of currently used industrial processing equipment such as air conditioning, refrigeration, water chillers, reboiler and distillation devices [1]. Previous research over the past decades has been focused on two phase flow in simple internal geometries. In the case of complex geometries, such as tube bundle flows in a kettle reboiler, multiple issues need to be investigated [2]. The kettle reboiler can be classified as a shell and tube heat exchanger, where heat exchange occurs as a fluid moves vertically through the horizontal tube bundles. A schematic of the kettle reboiler is shown in Fig. 1.1.

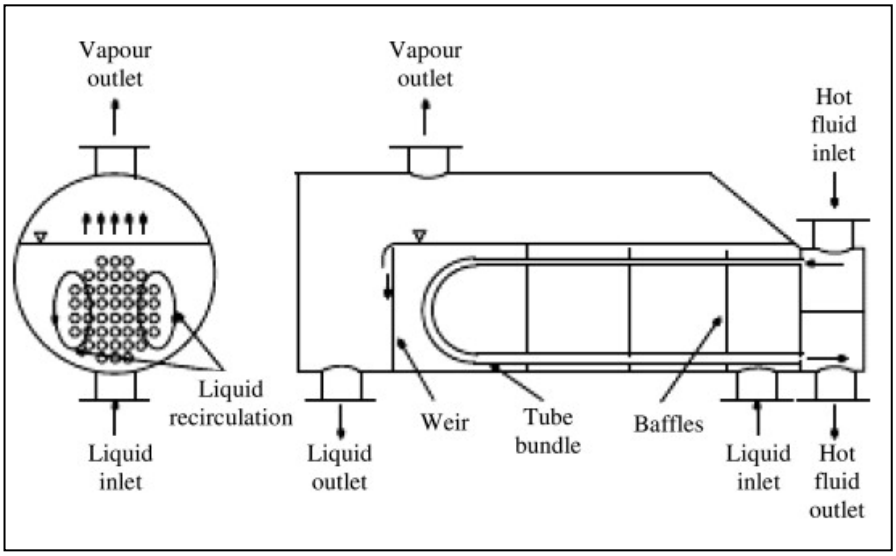

Figure 1.1: Typical schematic of the kettle reboiler

A typical kettle reboiler is composed of a tube bundle, which is located in a pool of liquid, with a space above it that allows efficient liquid and vapour separation. The operation of a kettle reboiler can be described as follows: The level of liquid in the pool is controlled by a weir fixed in the shell, such that the tube bundle is continuously submerged in fluid. The liquid undergoes a boiling process on the shell side, with the flow outside the tubes gaining heat from the in-tube fluid. Within the tube bundle, the generated vapour causes a two-phase flow to move towards the free surface of the pool. Next, vapour is separated from the liquid in the space above the pool. Vapour then exits

from the shell through the vapour outlet and liquid recirculates down to the bottom portion of the tube bundle. The difference in the fluid density between the bundle and pool cause the recirculation phenomenon [3]. Within the kettle reboiler, the occurrence of a recirculation flow can lead to large change in the heat transfer coefficient.

Pool boiling and convective boiling are the two phase change processes of boiling heat transfer in the heat exchanger. If boiling heat transfer occurs without any external force for fluid movement it is called pool boiling. If flow circulation is created by natural circulation or by means of an external force (pump), then the boiling heat transfer process is called flow boiling (pool and convective boiling). In the kettle reboiler flow boiling occurs. Despite the existence of a strong relationship between the heat transfer coefficient and the hydrodynamics, most kettle reboiler research has been dedicated to investigating heat transfer resistance rather than hydrodynamics. For an accurate understanding of this heat transfer resistance, it is necessary to have knowledge of the circulation flow rate as this allows the flow pattern, void fraction and two-phase pressure drop to be characterised.

The most common application for a kettle reboiler is as a boiler that is connected to the bottom of a distillation column. In this case a mixture of two or more components, commonly petroleum based hydrocarbons, enter the kettle reboiler. This liquid supply is provided by a gravitational feed from the distillation column sump. In the reboiler, the feed fluid components are vaporized on the shell side of the bundle. The vapour generated in the tube bundle rises due to buoyancy and, upon reaching the shell's liquid-free surface, separates from the surface and returns to the distillation column. The liquid that remains in the reboiler either flows over the weir as 'product' or recirculates within the reboiler. The vapour produced is dominated by the most volatile component and therefore separation has occurred. In most cases, the recirculating flow rate exceeds the feed flow rate to the bundle [52, 57].

1.2 Justification for the study

Due to a lack of available models of the interior local conditions on the shell side of a kettle reboiler, there is much scope for improving the process of its design. Researchers and manufacturers are interested in building kettle reboilers that can be economically constructed and maintained, generate vapour efficiently and have a long life. An efficient kettle reboiler, with minimum pressure change and minimum thermal stress,

and where approach to the critical heat flux is avoided, can be designed if an understanding of the hydrodynamics of the reboiler is gained [4]. Obviously, many geometric parameters need to be considered in the design of a kettle reboiler, for example: tube, shell, tube bundle offset and weir height. At the same time the high heat transfer coefficient associated with the boiling phenomena must be maintained [13].

Minimizing the diameter and wall thickness of tubes and minimizing the number of tube supports in the kettle reboiler would result in significant cost saving. A disadvantage, however, is that the resultant lighter and more flexible tubes would be more prone to flow induced vibration [41].

Vibration has not previously been considered in the design of kettle reboilers because generous safety factors were used that adequately dealt with this problem. Niels [86] reported that using this approach may lead to an overdesign of more than 300%. However, where it was necessary to make parts tighter, increase the flow velocity and reduce the pressure drop in order to improve performance, a lower safety factor was required [34].

Vibration problems may be avoided if designers have a more complete understanding of the characteristics or mechanisms of two-phase flow, including pressure drop, flow regimes, mass flux and void fraction inside kettle reboiler [17, 41, 42, 45]. This would include understanding the mechanism of the interaction between the tubes and the two-phase flow and developing predictive correlations. This all demands a more detailed investigation of two-phase flow characteristics inside the tube bundle [58].

Flow in the operational kettle reboiler is ultimately three dimensional and the pattern of flow in the evaporation process is complex. An analysis of the recirculation flow rate in three dimensions is desirable. Due to the complexities of the flow, most researchers have assumed that flow within the bundle is essentially vertical, and they have produced one-dimensional models of the recirculation flow. Void fraction and two-phase friction multiplier correlations are necessary parameters for developing such models [5]. This model is applicable only for low heat flux values, typically less than 20 kW/m^2. The one-dimensional model deviates from experimental data at higher heat fluxes. This is because of the existence of a two-dimensional flow pattern. The exact reason for this lateral (two-dimensional) flow is still unclear. A few researchers have suggested that lateral flow is present as a consequence of the shape of the shell [6].

Attempts have been made to produce an extensive analysis that models two-dimensional flow inside the kettle reboiler. Different types of modelling approaches, such as algebraic slip, the one-fluid model and the two-fluid model have been used [7]. Void fraction and tube bundle flow resistance values are needed to construct a one-fluid model. Compared to the one-dimensional model, the two-dimensional model provides more significant information about the flow in the kettle reboiler. It also provides valuable data that cannot be easily obtained through experiments. The two-fluid model uses conservation equations for mass, momentum and energy for each phase. These are solved together with closure equations that give the interaction between the phases and the phase-tube interaction [7].

Recently, the technique of computational fluid dynamics (CFD) has been used to solve many industrial problems. Several researchers have used CFD codes to develop a two-dimensional model for the kettle reboiler [8]. The accuracy of the computational two–dimensional model for solving the two-phase flow depends on the number of nodes and on the empirical correlations that are required to determine the forces acting between gas and the liquid in the governing equations. Several forces, such as the drag force and the force exerted by the tubes, act in the flow domain. These forces are important for estimating the slip velocity, as an estimate of this can be obtained by balancing the buoyancy and drag forces. Some investigations have been conducted to determine the interfacial drag and the wall force correlations. However, the generated force correlations were not effective in predicting experimental data.

1.3 Objectives of study

In the present work, an extensive study has been carried out on the parameters that are necessary to develop a model for a boiling fluid in a kettle reboiler using the two-fluid model. These parameters are the resistive force in the flow and the pool and the bundle drag coefficient. Appropriate boundary conditions have also been developed that allow the flow patterns within the kettle reboiler to be simulated. To validate the two-fluid model, new experiments to visualize the two-phase flow in the kettle reboiler have been undertaken. These focus extensively on the flow movements between tubes within the bundle. In addition, new measurements of the pressure drop of two-phase flow throughout the bundle have been carried out. Several simulations have also been performed to compare the two-fluid model predictions with experimental data and predictions from other models available in the open literature. The comparisons

included two-phase pressure drop, flow patterns, liquid velocities, void fraction and mass flux at various heat fluxes. In the present study, the value of the heat flux was varied from 10 to 40 kW/m^2.

1.4 Structure of this thesis

A brief outline of this thesis is as follows: In Chapter 2, a literature survey of previous experimental and numerical research relevant to this study is presented. This covers flow pattern, circulation velocities, void fraction, two-phase multiplier and pressure drop in the kettle reboiler and heat exchanger arrays. Chapter 3 describes the apparatus, the experimental procedures, and the method of data analysis. Chapter 4 assesses the use of an optical fibre probe for measuring void fraction in a tube bundle. Chapter 5 discusses the experimental flow pattern observations and pressure drop measurements. In Chapter 6, the theoretical concepts of the two-dimensional, two-phase model, related correlations and equations are discussed for the situation in which pentane is used as the working two-phase fluid in this model. This chapter also presents the assumptions made in modelling the complex tube geometry of the kettle reboiler and the boundary conditions. Chapter 7 describes the predicted results of the two-dimensional, two-fluid model for pressure drop, liquid and vapour velocity, and void fraction of the two-phase cross-flow in the tube bundle. This chapter also presents the central column fluid model and compares its results to those predicted from the two dimensional, two-fluid model. Chapter 8 presents the predicted velocities and mass flux from the two-dimensional, two-fluid model and gives comparisons between the predicted and experimental data of Burnside et al. [2] in the shell. In Chapter 9, a bundle only two-dimensional, two-fluid model is developed and the predicted results are compared with the data predicted from the two-dimensional, two-fluid model and the experimental results. The conclusion and recommendations for future studies are given in Chapter 10.

CHAPTER 2

Literature Review

2.1 Introduction

To design an efficient kettle reboiler, a clearer understanding of the local parameters such as flow, pressure drop, liquid and vapour velocities, heat transfer coefficient and void fraction is needed. In past decades the thermal part of the two-phase flow outside of the tubes in the tube bundle has been the main area researched [9]. More recent studies have indicated that convective evaporation is equally as important as nucleate boiling. The overall heat transfer coefficient significantly depends on the flow past the tube, and thus a complex coupling exists between the hydrodynamics and heat transfer [10]. The understanding of two-phase flow in the tube bundles has been limited by a lack of a detailed description of the hydrodynamics of this process.

This chapter presents a review of the papers published on two-phase flow across the tube bundle with emphasis placed on hydrodynamic two-phase flow. The type of the flow pattern in the tube bundle and techniques utilized to determine flow patterns will be discussed. It will also review the pressure drop and void fraction. Finally it will concentrate on previous studies of analytical and numerical work that have been used for tube bundles.

2.2 Flow pattern

It is essential to understand the flow pattern since many other parameters depend on it. It is expected that it will influence the two phase pressure drop, void fraction, heat and mass transfer during the phase change heat transfer process.

Cornwell et al. [11] investigated the flow pattern of R113 in a kettle reboiler of 241 electrically heated tubes (diameter: 19.05mm, length: 25.4mm). The tubes were arranged in 17 rows and 17 columns on an in-line configuration with a square pitch of 25.4mm, Fig. 2.1. A high speed camera was used by the authors to investigate the flow patterns at heat fluxes of 10, 20 and 50 kW/m^2.

From visual observation of the flow pattern it was seen that, at all heat fluxes, the flow was two-dimensional both around and within the tube bundle. At a heat flux of 20

kW/m^2, the liquid flow was observed to enter the bundle from the sides, leading it to move horizontally within the middle region of the bundle. The direction of the flow changes to approximately vertical as it arrives at the upper region, Fig. 2.2. It is emphasised by the authors that a two-dimensional model is needed to analyse the flow in the kettle reboiler as the one-dimensional model does not provide an accurate description.

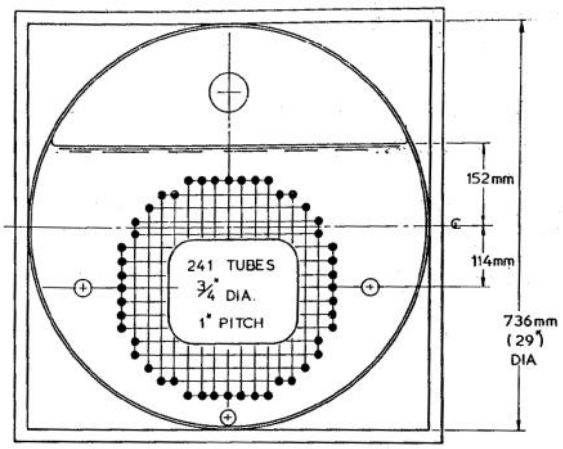

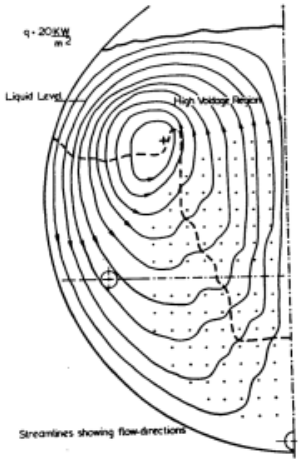

Figure 2.1: Kettle reboiler [11]

Figure 2.2: Flow pattern at 20 kW/m^2 [11]

Figure 2.3 shows the local flow pattern between tubes. The lower tube region is shown in Fig. 2.3 (a). Here, the quantity of boiling is low so few bubbles are produced and consequently the fluid is roughly in single liquid phase. By contrast, in the upper tube region the high velocity, high voidage flow was concentrated in the vertical gaps between tubes with almost pure liquid in the gaps above and below each tube, Fig.2.3 (b).

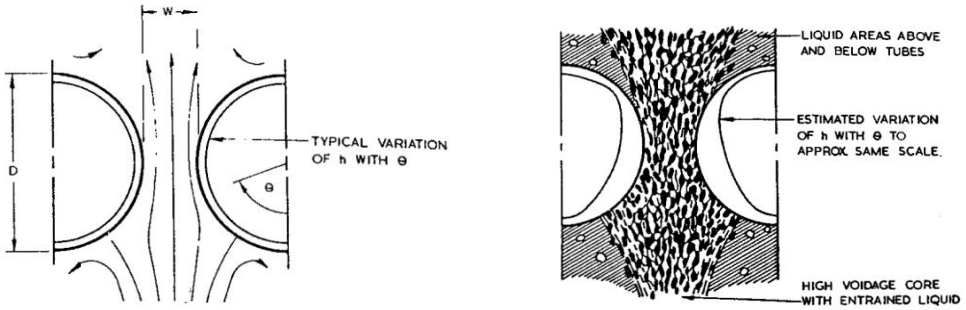

a) (b)

Figure 2.3: Two-phase flow pattern between tubes (a) Lower tubes (b) Upper tubes

Andrews and Cornwell [12] investigated the flow pattern in a thin-slice of a reboiler, as shown in Fig. 2.4. The bundle consisted of 97 copper tubes (diameter: 19.0mm, length: 183mm) arranged on a 25.4 mm square pitch. Electrically heated tubes were used to boil R113 within the tube bundle at heat fluxes of 5, 10 and 15 kW/m^2. By using a visual technique it was observed that between the columns there was a high voidage flow moving upwards, and between the rows there were liquid flow regions.

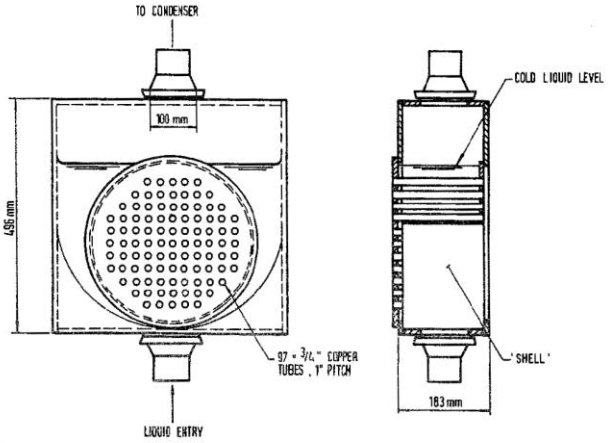

Figure 2.4: The reboiler of Andrews and Cornwell [12]

Another experimental investigation of the flow patterns in a kettle reboiler was made by King and Jensen [13]. In this study only half of the boiler was considered. It consisted of 75 tubes made of a brass alloy C-360 (outside diameter: 15.9mm, length: 168.3mm), and arranged in a square, in-line layout with a 1.5:1 pitch to diameter ratio, as shown in Fig. 2.5. R113 was boiled in the reboiler at heat fluxes of 10, 30, 50 and 70 kW/m^2. In this investigation two types of operating mode were used: kettle reboiler and submerged evaporator. In each case the vapour left the rig through an outlet of 50.8 mm diameter.

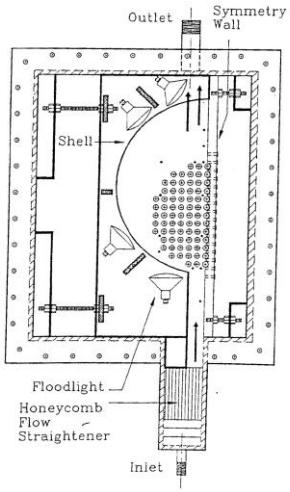

Figure 2.5: The kettle reboiler of King and Jensen [13]

The first mode simulated a kettle reboiler with a two-phase level above the tubes bundle (plume height) of 40 and 80 mm.

The flow pattern was described on the basis of the observation of how small bubbles moved within the flow. The authors found that along the bundle's side natural circulation occurred and they attributed this to the difference in the flow density between the bundle and the shell.

The circulation region in the shell at a heat flux of 10kW/m^2 and plume height of 80mm is shown in Fig. 2.6. This was comprised of bubbly flow, which was seen between the tube columns in the vertical channels, and liquid flow between the tube rows in the horizontal regions. At 10kW/m^2 the major direction of flow movement was vertically across the bundle, with some horizontal flow seen at the bundle side as a result of natural circulation.

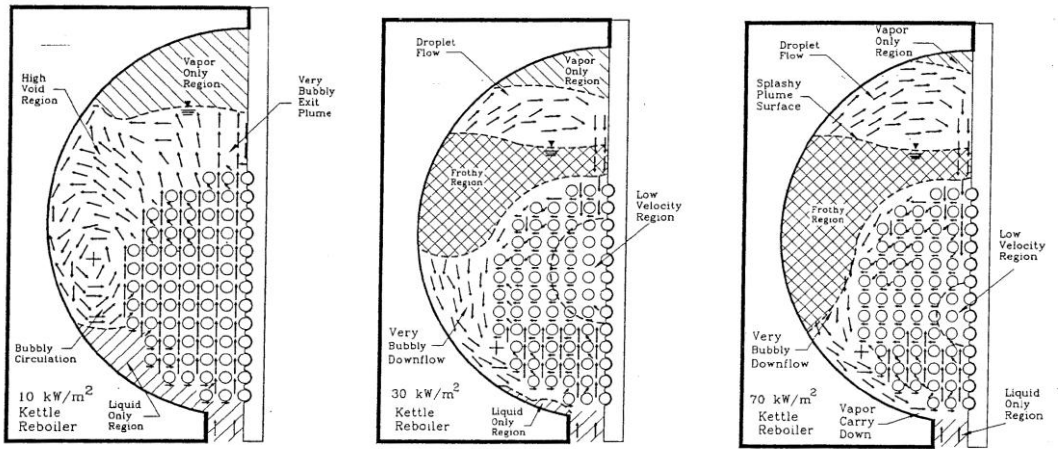

(a) (b) (c)

Figure 2.6: Kettle reboiler flow pattern at (a) 10 kW/m^2, (b) 30 kW/m^2, (c) 70 kW/m^2

Figure 2.6 (b) and (c) show the flow patterns observed at heat fluxes of 30 and 70 kW/m^2 and a plume height of 40mm. Under these conditions the kettle reboiler was seen to contain two circulations. A region of lower circulation, comprising of bubbly flow, was observed in the shell. Compared to 10kW/m^2 this flow extended further down on the bottom rows. With increasing heat flux the strength of the circulation increases, and the entry of some bubbles is seen at the bottom of the bundle. In the frothy region at the top of the bundle an upper circulation, consisting of droplet flow, was observed. It was thought that the intersection of the upper and lower circulation flows had created a low

velocity region in the bundle centre. With increasing heat flux the bundle is filled totally with a highly bubbly or frothy mixture, which was the result of a higher nucleation rate.

For the second mode: a simulated submerged evaporator, the rig was filled totally with liquid. In this mode a two-phase mixture left the shell, whereas in the kettle reboiler mode only saturated vapour left.

Figure 2.7 shows the observed flow pattern for the submerged evaporator simulation at heat fluxes of 10, 30 and 70 kW/m^2. A cross flow was seen in the upper region of the tube bundle, as shown in Fig. 2.7 (a), due to a flow circulation pattern that was also observed in the first mode. A highly bubbly flow left the top of the bundle and moved downwards in the shell. For 30 kW/m^2 a similarity to the kettle reboiler mode was also observed with two circulation regions present between the bundle and shell wall, Fig. 2.7 (b). However, in contrast to the first mode, the upper circulation region consisted of frothy flow rather than droplet flow. The upper and lower circulation flows were equally strong, but the outlet quality was higher in the former. In the region between the columns a bubbly flow was seen, whereas between the tube rows it was mostly liquid that appeared. The upper circulation flow caused down-flow to the top of the bundle, and thus created a region of low velocity.

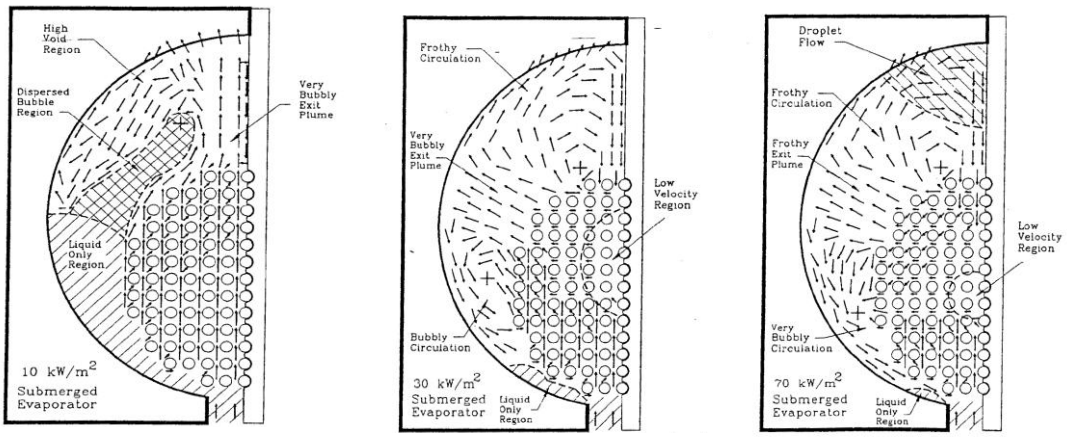

(a) (b) (c)

Figure 2.7: Submerged evaporator flow pattern at (a) 10 kW/m^2 (b) 30 kW/m^2 (c) 70 kW/m^2

At 70 kW/m^2, an increasing heat flux increases the frothy circulation region above the bundle, which allows down-flow to permeate the bundle's top three rows. This is shown in Fig.2.3 (c). As with the kettle reboiler mode, some bubbles re-entered at the base of

the bundle due to the lower circulation flow moving further down. The flow movement was largely horizontal from the bundle towards the shell.

A photographic study of the bubbles surrounding the tubes within the bundle was carried out by Cronwell and Shuller [14]. They observed that many bubbles grew as they slid along the tubes' sides. These bubbles originated from the main flow or nucleation sites underneath the tubes. The type of flow present at a heat flux of 20 kW/m^2 is shown in Fig. 2.8 (a), and, for comparison, Fig. 2.8(b) shows the flow characteristics around a tube under pool boiling operating at a heat flux of 50 kW/m^2. To calculate the velocity of the sliding bubbles a pseudostatic force balance was carried out by the authors. They assumed that the bubbles and liquid moved at constant velocities and that the rates of bubble growth were small in comparison to the translational velocity.

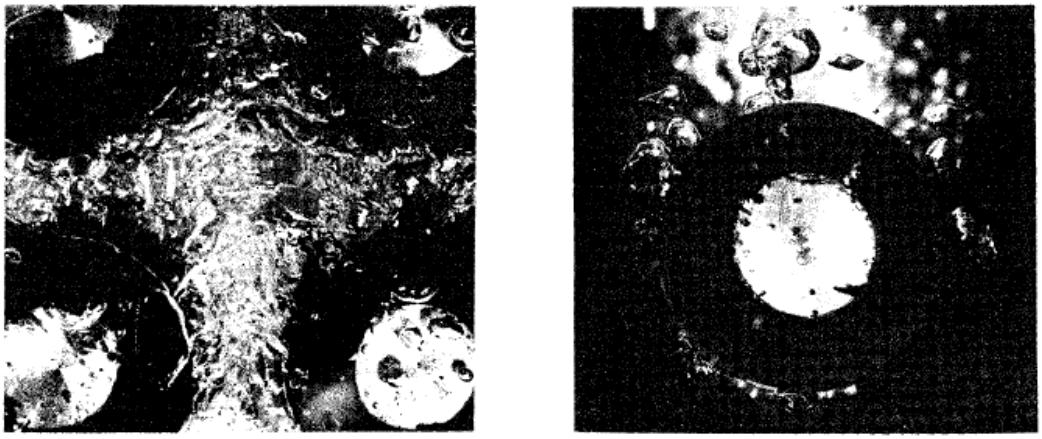

(a) Between upper tubes at 20 kW/m^2 (b) On a tube at 50 kW/m^2

Figure 2.8: Flow photographs of boiling, Cronwell et al. [14]

Shire [6] used a thin slice kettle reboiler to analyse the flow of boiling R113 at atmospheric pressure at heat fluxes ranging from 2 to 50 kW/m^2. The tube bundle contained 241 tubes with 19.0 mm diameter in 25.4 mm pitch square–in-line configuration. The transition from shell to vapour riser was through a 100 mm diameter hole in the back wall of the shell and a 90 degree elbow leading to the 100 mm diameter riser.

Small bubbles in the boiling flow were seen to circulate from the shell side towards the tube bundle. As the bubbles moved downwards through the shell some of them

condensed. The heat flux was found to determine the centre of the circulation flow, with an increasing value of heat flux causing the centre to move downwards in the shell and become close to the tube bundle. At low heat fluxes 10 kW/m^2 or below, the main movement of the flow is in the vertical direction from the bottom to the top of the bundle, as shown in Fig. 2.9 a-b.

At 20 kW/m^2, it was found that the foam of the R113 filled the shell above the bundle. As fluid moved up through the bundle the lateral flow increased, as shown in Fig 2.9c-f. It seemed that the extent of the vertical flow was reduced due to the formation of a vortex above the bundle, which caused a downward flow of liquid.

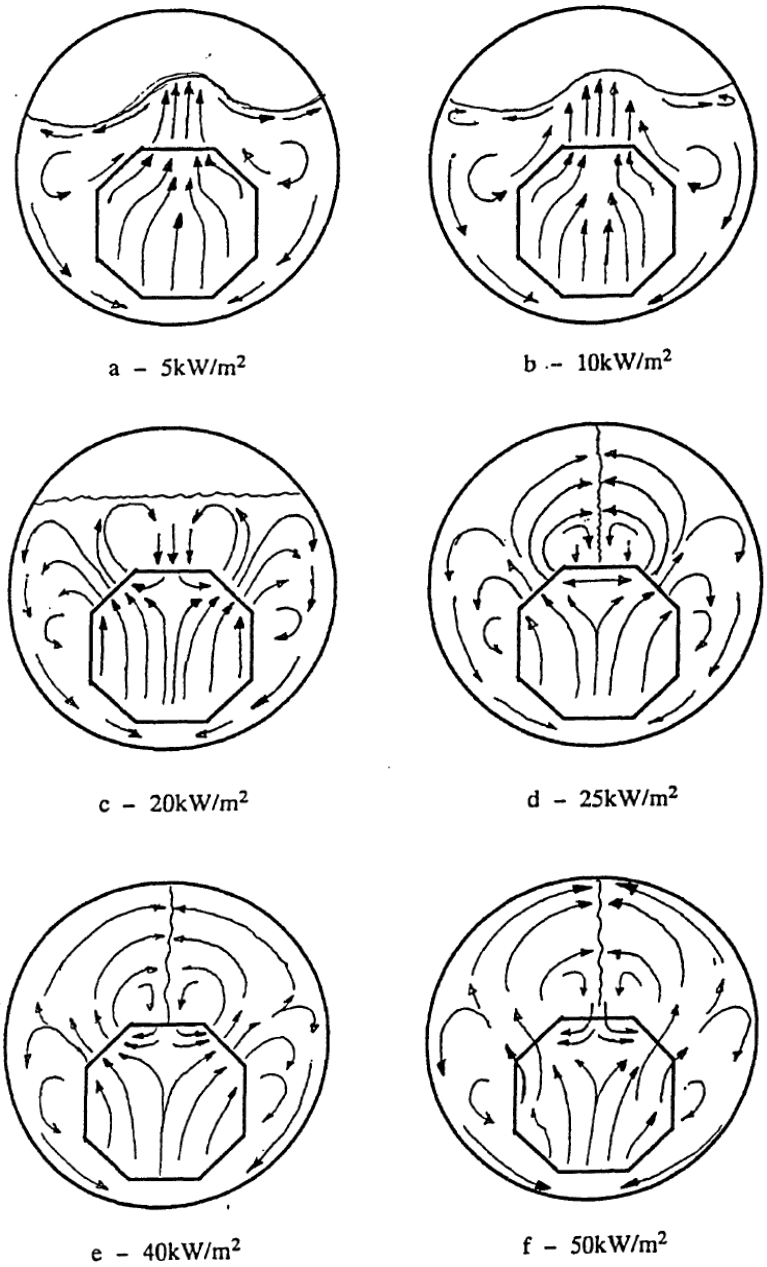

Figure 2.9: Fluid Flow Pattern [6]

To investigate the flow pattern in the thin slice kettle reboiler Miller [15] modified Shire's rig by changing the shape and dimensions of the vapour outlet. It was altered from a circular hole of diameter 100mm to a more elliptical shape with a cross-sectional area of 290 cm^2. This was connected to a 150 mm diameter riser, as shown in Fig. 2.10. The author claimed that this change improved the liquid-vapour disengagement, and therefore a lower quantity of foam was produced in the shell compared with previous studies. However, the author used n pentane instead of R113 as the working fluid, and it may have been this change that caused the foam quantity in the shell to be lower.

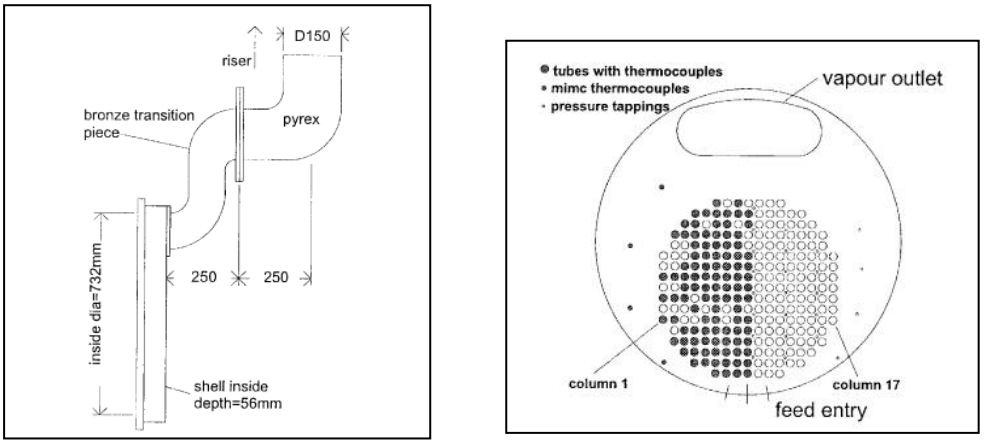

Figure 2.10: Kettle reboiler of Miller [15]

Burnside et al. [16] discussed Miller's flow patterns. It was noted that at a heat flux of 10 kW/m^2 the height of the foam exceeded the tube bundle by 100 mm. The direction of the flow movement was from the bottom to the top of the bundle, whereas lateral flow dominated at a heat flux of 50 kW/m^2. Figure 2.11 shows the pattern of flow at a heat flux of 50 kW/m^2 with the flow vapour leaving the bundle above row 3 (f).

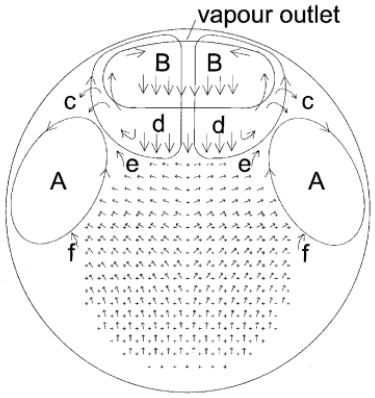

Figure 2.11: Flow pattern in the kettle reboiler at 50 kW/m^2, Burnside et al. [16]

Two flow vortices moving in opposite directions were observed above the bundle in area B. The horizontal movement of flow in the rows at the top of the bundle (e) was

caused by falling droplets of liquid from d. Two further vortices were also noted at the tube bundle's corners (A) and they were attributed to the gravitational unbalance.

Burnside et al. [2] stated that the vapour is prevented from separating from the liquid at the free surface by the two vortices above the bundle. Consequently two-phase flow moves to the bundle side horizontally resulting in 2-D flow. This flow pattern restricts circulation and so decreases the coefficient of heat transfer. An explanation of a similar nature for 2-D flow in the kettle reboiler was given by Shire [6] and King and Jensen [13].

The kettle reboiler's performance was analysed by examining the effect of the two vortices above the bundle. It was debated whether 2-D flow would actually be seen in the whole kettle reboiler and whether the thin slice kettle reboiler was the most appropriate model to use to model the whole reboiler (Burnside et al. [2]). To answer these queries the authors deemed it necessary to develop 2-D or 3-D thermo-hydraulic models of the kettle reboiler to give more accurate representations of the flow. A suggested starting point for the development of these models was to record the flow photographically. It was also recommended that greater observation of the flow field, especially in the bubbly flow area of the kettle reboiler, should be made. The authors' final conclusion was that it might not be appropriate to base the design of the real kettle reboilers on the results produced from the thin slice kettle reboiler at high heat fluxes.

2.2.1 Flow regimes

Noghrehkar et al. [17] state that roughly half of all process heat exchangers operate in two–phase flow, but that our understanding of this is unsatisfactory. Previous studies have shown that it is difficult to develop an accurate technique to investigate flow patterns. The main method for describing them has relied on visual observations. In tube bundles the models are limited by a lack of observations. The ability to accurately predict the flow patterns is necessary for relevant calculations to be developed.

Extensive work has been done for two-phase flow in a circular pipe [17], but few experimental studies focus on the two-phase flow across tube bundles. This is unsurprising given that it is difficult to make the measurements required to investigate patterns of flow within tube bundles. Most investigators have therefore had to use visual observation of the two-phase flow pattern from outside of the bundle.

The two-phase flow can take different geometric configurations known as flow patterns or flow regimes. Various flow patterns have been described for vertical up flow in tubes, these are: bubbly, slug/churn (intermittent flow) and annular flow (Taitel et al. [18]), as shown in Fig. 2.12.

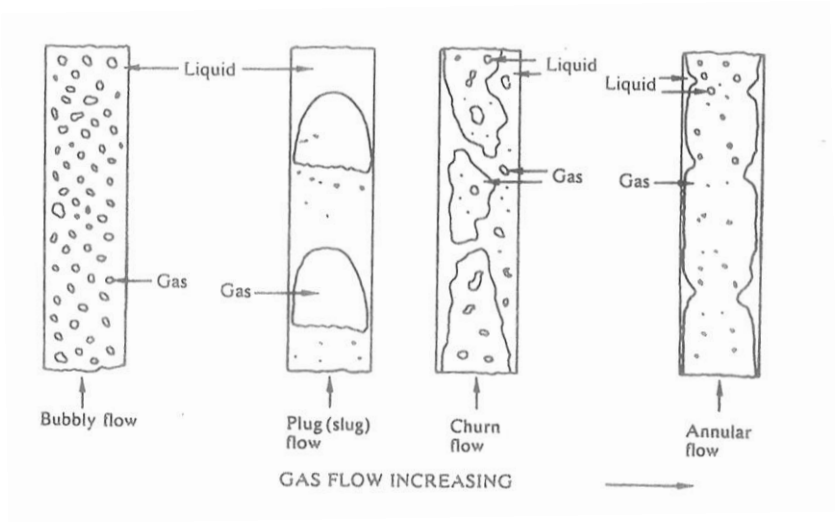

Figure 2.12: Flow patterns in vertical up-flow in a tube, Taitel et al. [18]

By visual inspection of air-water two-phase vertical up flow in horizontal tube bundles four types of flow patterns were identified by Noghrehkar et al. [17]. These flow patterns are defined below and illustrated in Fig. 2.13.

(a) Bubbly Flow: The liquid phase is continuous with gas phase dispersed as very small bubbles of approximately uniform size. The bubble concentration in the middle of the gap of the tube is higher in comparison to the rest of it. For all liquid flow rates bubbly flow takes place at a low superficial gas flow velocity (J_G < 0.4-0.8 m/s).

(b) Slug Flow: This is described by intermittent flow of relatively large slugs through a nearly continuous liquid phase. The shapes of the gas slugs are irregular and the small gas bubbles are distributed throughout the liquid flow phase.

(c) Churn Turbulent Flow: A more disordered form of slug flow, which is highly unstable and has an oscillatory nature. The liquid near the tube walls in the tube bundle oscillates up and down continuously. In this study, slug and churn flow regimes are grouped together under the term ‘intermittent flow’.

(d) Annular Dispersed Flow: This is described by upward wavy flow of separated gas columns through the tube bundle’s gaps. These gas columns contain entrained liquid

droplets and are separated by the liquid films flowing upwards on the walls of the tubes. For all liquid flow rates annular flow takes place at very high gas velocities.

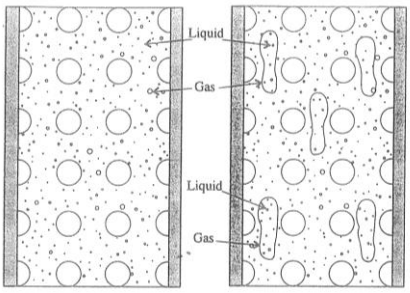

(a) Bubbly flow (b) Slug flow

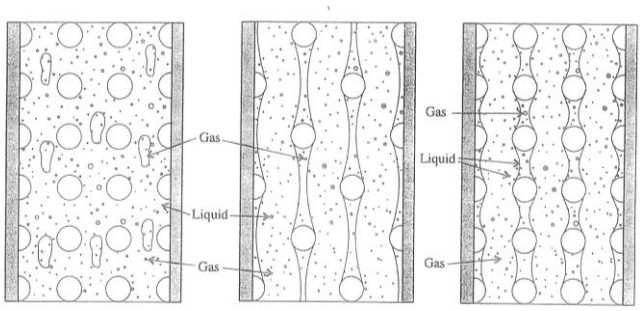

(c) Churn flow (d) Annular flow

Figure 2.13: Flow Regime in In-line Tube Bundles, Noghrehkar et al. [17]

Grant and Chisholm [19] reviewed the flow patterns using air/water mixtures in a transparent heat exchanger of rectangular cross section with a tube bundle. The shell contains 39 tubes of 19 mm outside diameter arranged on an equilateral triangular layout of 1.25 pitch/tube diameter ratio. Two types of mixing were used upstream of the model to generate air/water mixtures: (1) compressed air was injected into the water through a porous tube at high water flow rates, and (2) water was sprayed into the air through a nozzle at low water flow rates. Figure 2.14 shows the flow patterns, obtained by visual observation through the transparent exchanger. The patterns were classified as follows:

(a) Spray flow: Occurred at high mass flow qualities with liquid carried along by the gas as a spray.

(b) Bubbly flow: Occurred at low mass flow qualities with gas distributed as discrete bubbles in the liquid.

(c) Intermittent flow: Taking place where intermittent slug of liquid were propelled cyclically through the model by the gas.

(d) Stratified-spray flow: Type of flow where the liquid and gas were tending to separate with liquid flowing along the bottom of the model. The gas-phase was entrained as bubbles in the liquid layer and liquid droplets were carried along by the gas as spray.

(e) Stratified flow: The flow where the liquid and gas were totally separated.

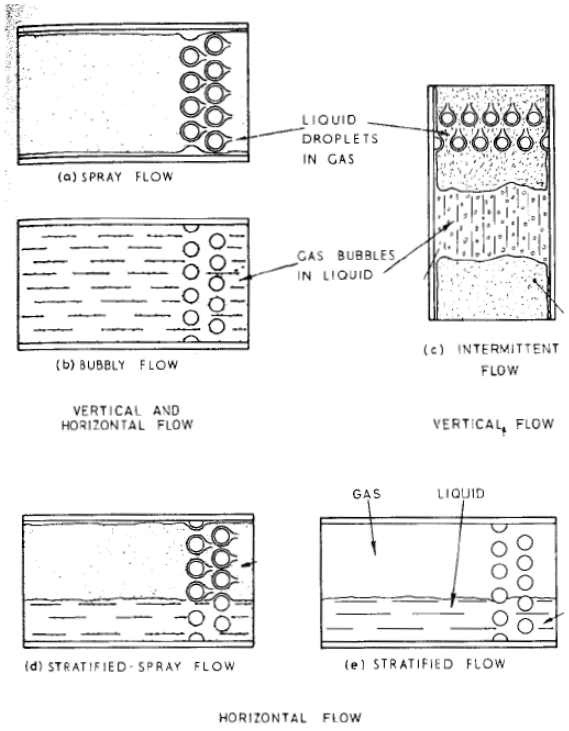

Figure 2.14: Shell-side two-phase flow patterns, Grant and Chisholm [19]

The authors noted that spray and bubbly flow occurred with their model orientated for either vertical up-and-down-flow or horizontal side-to-side flow. Intermittent flow only occurred with vertical up-and-down-flow and stratified-spray and stratified flow with horizontal side-to-side flow. Figure 2.15 shows the above regimes obtained from the flow pattern maps for both vertical and horizontal flow.

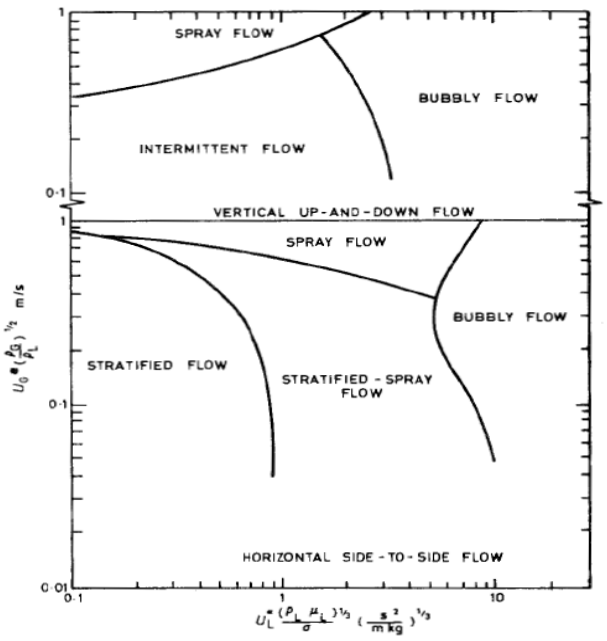

Figure 2.15: Shell–side flow pattern maps, Grant and Chisholm [19]

Pettigrew et al. [20] expressed the flow regime map of Grant in terms of the Martinelli parameter, X. and the dimensionless gas velocity Ug, Fig. 2.16. These dimensionless parameters are given as:

$$X = \left(\frac{1-\varepsilon_g}{\varepsilon_g}\right)^{0.9} \left(\frac{\rho_l}{\rho_g}\right)^{0.4} \left(\frac{\mu_l}{\mu_g}\right)^{0.1} \tag{2.1}$$

$$U_g = \frac{\dot{m}_{rg}}{[d_e g(\rho_l - \rho_g)]^{1/2}} \tag{2.2}$$

Where $\varepsilon_g$is the void fraction, $\rho$is the density, μ is the dynamic viscosity, $\dot{m}_{rg}$ is the gap mass flux of the gas phase, $d_e \approx 2(p-d)$ is the hydraulic diameter and g is the acceleration due to gravity. The subscripts g and l refer to gas and liquid, respectively.

Figure 2.16 shows the experimental data for several tube bundle layouts with various flow conditions plotted for comparison by Pettigrew et al. [20]. This data, classified on the basis of visual observation, is shown in the figure. When the value of the void fraction was below 90% bubbly flow was observed, whereas at higher void fractions intermittent flow was observed. The dashed line in Fig. 2.16 shows the boundary between bubbly and intermittent flow regimes.

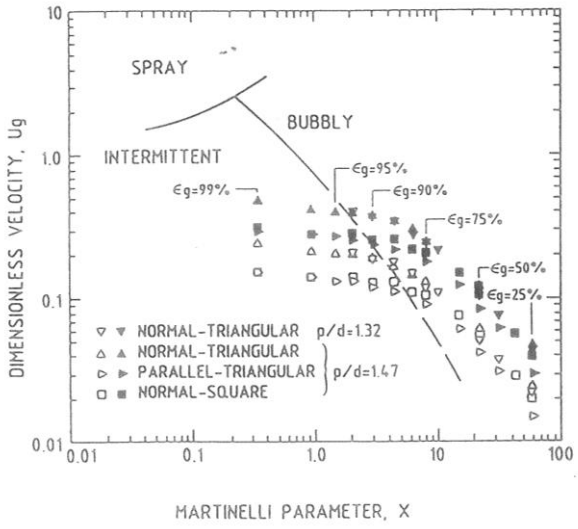

Figure 2.16: Flow regime map for different bundle configurations [20]

Ulbrich and Mewes [21] studied the vertical two-phase cross-flow on the shell side of a horizontal tube bundle. The tube bundle consists of 5 tubes with 20 mm diameter. The tubes were arranged in 10 rows on a square pitch with P/D =1.5 in a rectangular shell. The superficial velocity ranges of gas and liquid were (0.047-9.3 m/s) and (00.01-0.65 m/s), respectively.

After reviewing various articles on flow patterns and carrying out visual observations, for a wide range of gas and liquid volume fluxes, aided by photographic techniques and a video-camera, the flow patterns shown in Fig. 2.17 were observed and classified as follows:

Bubble (B) Small gas bubbles distributed in the liquid phase uniformly whose diameters were less than the characteristic spacing between the tubes. The bubble shape was found to be elliptical. The number of bubbles grows to fill the entire channel cross-section when the gas and liquid velocities increase. The shape of bubbles changed when the bubble size was larger than the tube clearance as the bubble pressed between the tube walls. It is very important that liquid flows as the continuous phases without any local oscillation.

Intermittent (I)-This flow was characterized by an irregular alternating motion of the liquid and gas. The direction of the liquid flow has been changed irregularly from up-flow to down-flow and vice versa. Liquid flows downward not only as a film, but also as units of liquid which occupy much of the cross-sectional area. Gas bubble shapes

were not only spherically or elliptically capped but also large flattened and irregular. The enlarged bubble height was several times greater than the tube diameter and their width was equivalent to the tube clearance.

Dispersed (D)- This flow was characterized by regular dispersed droplets which were carried by the gas, initially above the tube bundle, and then also between the tubes.

Intermittent-Dispersed (ID) flow had part of the liquid flow as irregular moving units.

Annular-Dispersed (AD) flow had liquid flow as a thin film, with surface waves occupying the tube wall or the shell wall. A pattern involving the the case where the entire flux of liquid flowing as droplets was possible but difficult to accomplish. A flow pattern map was constructed by plotting the superficial velocities of the gas and liquid with the respective flow pattern boundaries.

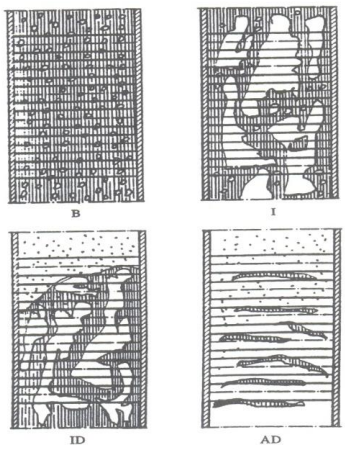

Figure 2.17: Flow patterns vertical upward flows across a tube bundle, Ulbrich and Mewes [21]

Hahne et al. [22] identified flow patterns aided by measurements of void fraction in two-phase flows of refrigerant R11 at 1 bar. A fibre optical probe was used to measure the local void fraction under pool boiling conditions in an 18 low-finned tube bundle with P/D=1.3 and 1.15. A Fast-Fourier-Transformation (FFT)-analyzer was used to identify the flow regimes inside the bundles by obtaining the probability density histograms of the local void fraction and their higher moments. From the statistical analysis of the local void fraction data, the first two-rows contained distributions of large quantities of small bubbles and are about the same size. For other rows the number of bubbles, big and small, were distributed according to a Gaussian curve. The top row favoured the formation of large bubbles. Hence, the authors observed only a bubbly

flow regime within the tube bundle, with no slug or annular flow regimes detected. The detection of only the bubbly flow regime may have been due to the limitation in flow condition or small gaps between the finned tubes, which could prevent formation of large vapour slugs

Xu et al. [23] made visual observations of vertical up, down and horizontal flow in a tube bundle. The following categorisation was given for a two-phase down-flow across the tube bundle, Fig. 2.18.

(a) Falling film: the superficial velocities of the gas and liquid were low, and a film around the tube wall and the inside wall of the shell was continuously formed by the liquid. Gas bubbles were absent from the film, and the gas flowed through free areas between tubes; the surface of the film was wavy and the gas contained very few or no liquid droplets;

(b) Intermittent: gas flowed at a higher velocity; waves travelling in the flow direction disturbed the gas liquid interface, and the continuous liquid film was intermittently cut off between the tubes by the gas. The gas phase was entrained as bubbles in the liquid when the velocity of the liquid increased;

(c) Annular: an annular liquid film covered the tube wall and inside wall of the shell, and some liquid was entrained as droplets in the gas at a high gas velocity;

(d)Bubbly: similar to the falling film, but the liquid film thickened and contained small dispersed air bubbles. The film also flowed faster.

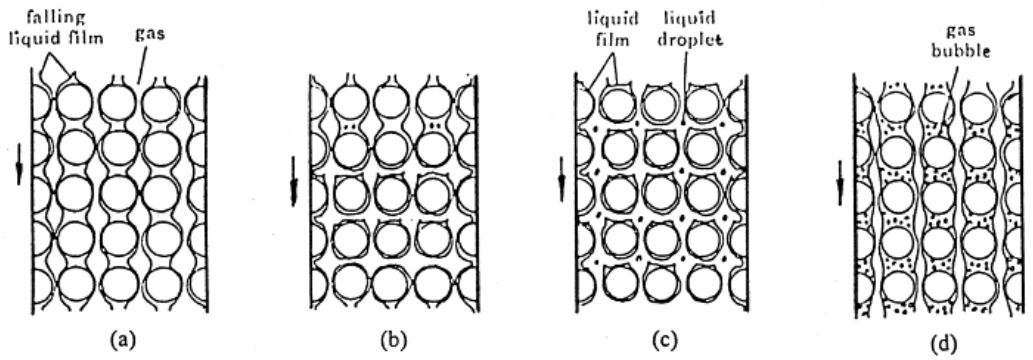

Figure 2.18: Flow patterns in vertical down-flow across a horizontal tube bundle: (a) falling film flow; (b) intermittent flow; (c) annular flow; and (d) bubbly flow [23]

The schematic diagrams for up flow are displayed in Fig. 2.19 and the flow patterns are classified as:

(a) Churn flow: this type of flow was more chaotic, was controlled by the gravitational force and took place at low superficial velocities of liquid and gas;

(b) Intermittent flow: this type of flow was more unstable, when a pulse appeared an annular film wetted parts of tubes and discrete bubbles filled the other parts;

(c) Annular flow: this type of flow had a similar behaviour to down-flow;

(d) Bubbly flow: the gas phase was uniformly distributed in the form of discrete bubbles in a continuous liquid phase.

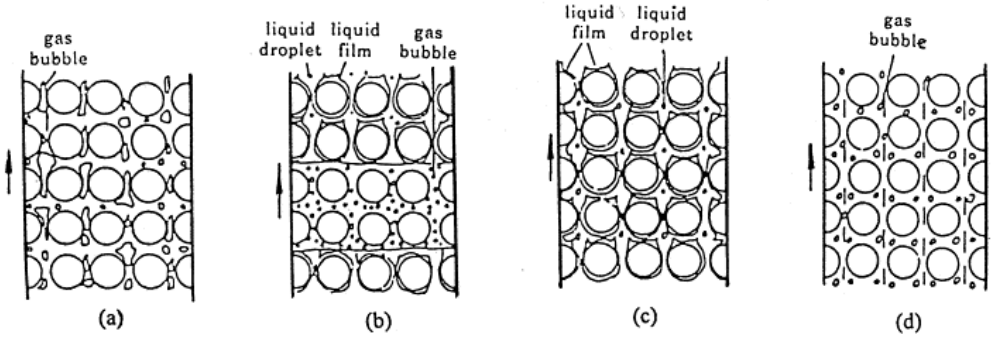

Figure 2.19: Flow patterns in vertical up-flow across a horizontal tube bundle: (a) churn flow; (b) intermittent flow; (c) annular flow; and (d) bubbly flow [23]

For horizontal flow, Xu at el. [23] discussed the differences between the type of the flow pattern annular, bubbly, intermittent and stratified flows. The experimental observations were presented in terms of liquid and gas superficial velocities and the flow pattern maps for vertical up and vertical down-flows were constructed, Fig. 2.20.

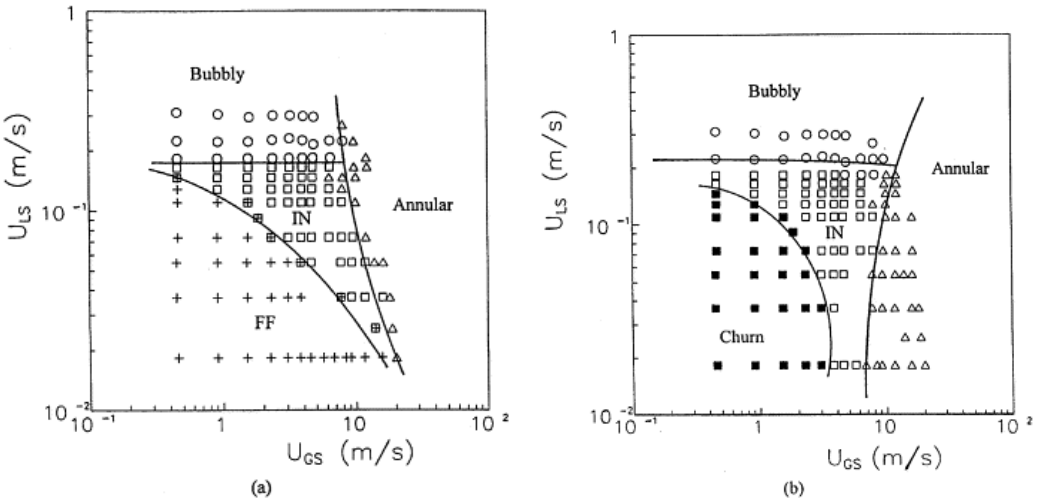

Figure 2.20: Flow pattern map: (a) vertical down-flow; and (b) vertical up-flow [23]

Flow pattern in horizontal staggered tube bundles with three different pitch to diameter ratios (1.4, 1.28, 1.28) were investigated by Kondo and Nakajima [24]. The experimental superficial velocities of air and water had ranges of 1.5-50 (cm/s) and 0.032-0.32 (cm/s), respectively. Four flow patterns, bubbly, slug, forth and spray, Fig. 2.21 were classified by the authors on the basis of visual observation and a photographic technique. Figure 2.21 (a) shows the bubbly flow pattern: the flow at low air flow rates, the bubbles are uniformly distributed in the water phase, are much smaller in diameter than the tube diameter and have an elliptical shape. The slug flow is shown in Fig 2.21 (b). Here, the air flow rate increased and some of the bubbles coalesced and filled up the tube clearance, which made the height and length of the bubbles comparable to the pitch of the tube. This type of flow contains different bubbles size. Figure 2.21(c) shows the fourth flow, the flow at high air flow rates, where the height of the large bubbles are several times the pitch of the tube and their width is equal to the tube clearance.

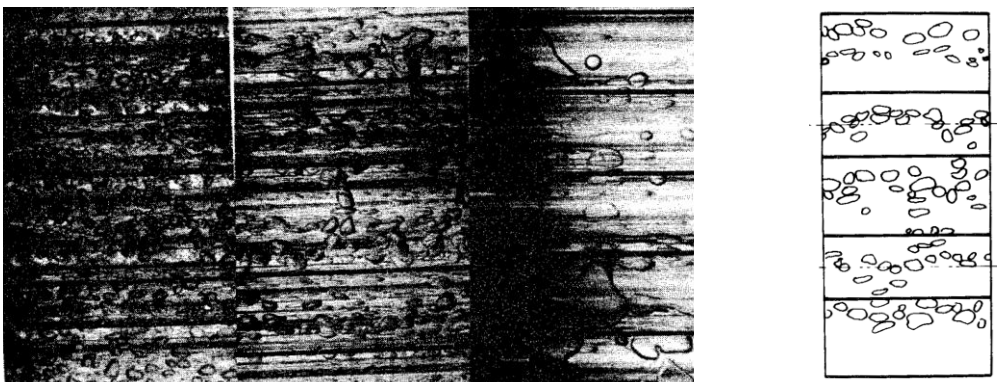

(a) **Sketch (a)**

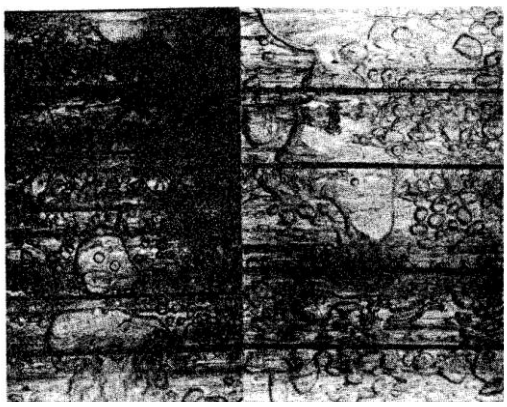

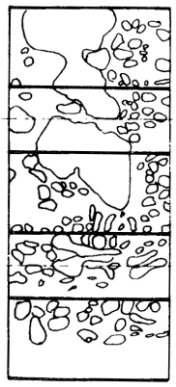

(b) **Sketch (b)**

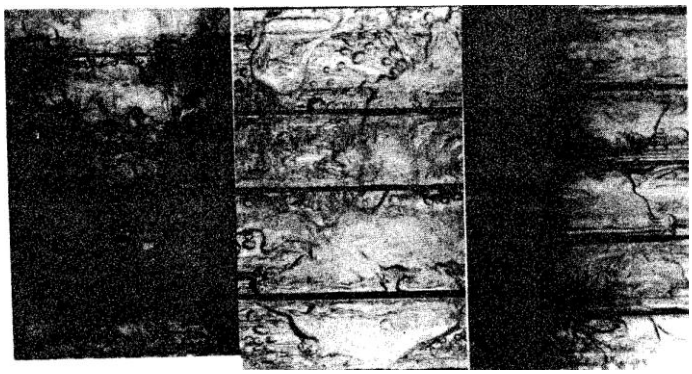

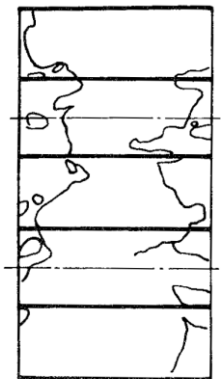

(c) **Sketch (c)**

Figure 2.21: Flow patterns (a) bubbly flow (b) slug flow (c) forth flow, Kondo and Nakajima [24]

Burnside and Shire [25] performed experiments in which R113 was boiled at atmospheric pressure with flow restricted to the vertical direction. The boiler, shown in Fig. 2.22, was adapted from a 732 mm internal diameter thin slice kettle reboiler by the addition of two brass walls. These sealed off a space of rectangular cross-section, 102 mm wide and 52 mm deep, between the reboiler black plate, and its toughened glass viewing window. The reboiler contained 17 rows and 5 columns with 25.4 mm squared pitched bundle and 19 mm diameter tubes made of 90 Cu: 10 Ni. The tube bundle was heated electrically at fluxes of 10-65 kW/m^2.

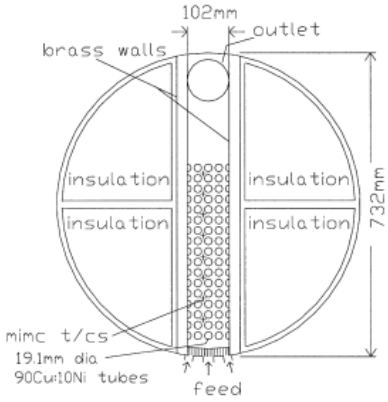

Figure 2.22: Kettle reboiler used by Burnside and Shire [25]

To characterise their data the authors used the flow pattern map given by Grant and Chisholm [19]. This classified all their data in the bubbly flow regime, which conflicted with the authors' observations. They had also seen intermittent and annular flow regime at higher qualities and lower flow rates. To obtain a better agreement with their observations the Xu et al. [23] flow pattern map was used. At fluxes of 10 and 20 kW/m^2, the data were in the bubbly flow regime. At 40 kW/m^2 and a low Reynolds number, the data were in the intermittent region at low quality, extending into annular flow regime at large quality. At 50 and 65 kW/m^2, the data were in the bubbly flow regime at lower qualities while at higher qualities, the data were in the annular flow regime.

Vertical two-phase flow patterns have been studied experimentally by Aprin et al. [26]. They investigated the boiling across a horizontal tube bundle for three hydrocarbons (n-pentane, propane and iso-butane) under saturated conditions. The tube bundle consisted of 54 copper tubes with 9 rows x 6 columns with 19.05 mm outside diameter in a staggered layout with a pitch-to-diameter ratio (p/d=1.33) as shown in Fig. 2.23.

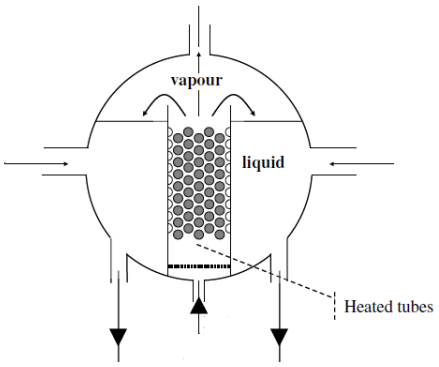

Figure 2.23: Boiler used by Aprin et al. [26]

The local void fraction was measured using an optical probe. A probability density function (PDF) of void fraction fluctuation was used to determine three different flow regimes (bubbly, intermittent and annular flow) as shown in Fig. 2.24.

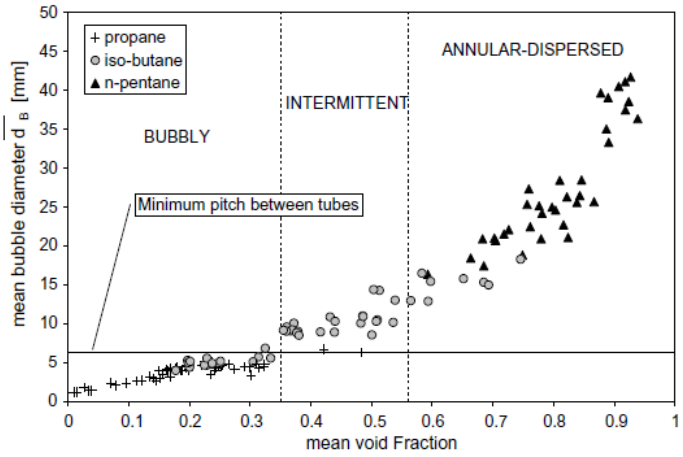

Figure 2.24: Flow regime using void fraction by Aprin et al. [26]

When the values of a void fraction were lower than 0.35 the bubbly flow regime occurred. At void fraction values between 0.35 and 0.56 intermittent flow occurred, and for larger values than this an annular-dispersed flow occurred. The flow regimes given by the authors are shown in Fig. 2.25. Bubbly flow is defined as a vapour phase distributed discretely in the continuous liquid phase, Fig. 2.25 (a). Annular-dispersed flow is characterized by a continuous gas phase in which the liquid droplets are carried, Fig. 2.25 (b). Intermittent flow is defined as a combination of bubbly and annular-dispersed flows.

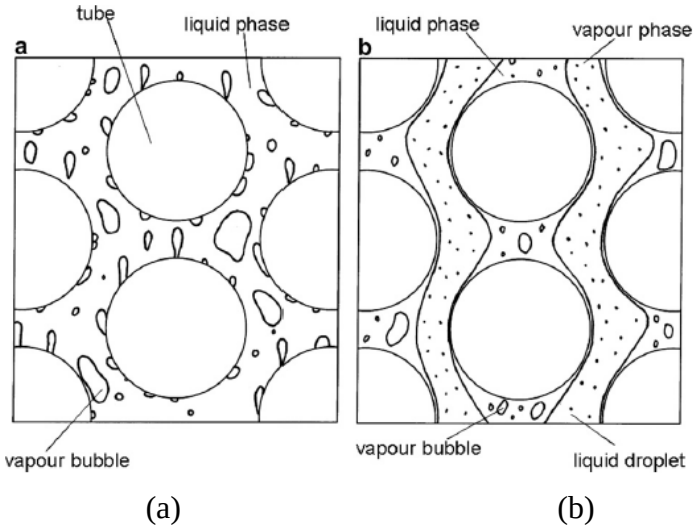

(a) (b)

Figure 2.25: Flow patterns in the boiler Aprin et al. [26] (a) Bubbly flow (b) Annular-Dispersed flow

A comparison between the authors' flow map and that of Noghrehkar et al. [17] showed that, in the former, a transition in the flow boiling conditions occurred at a lower superficial vapour velocity. This is shown by the solid lines in Fig. 2.26.

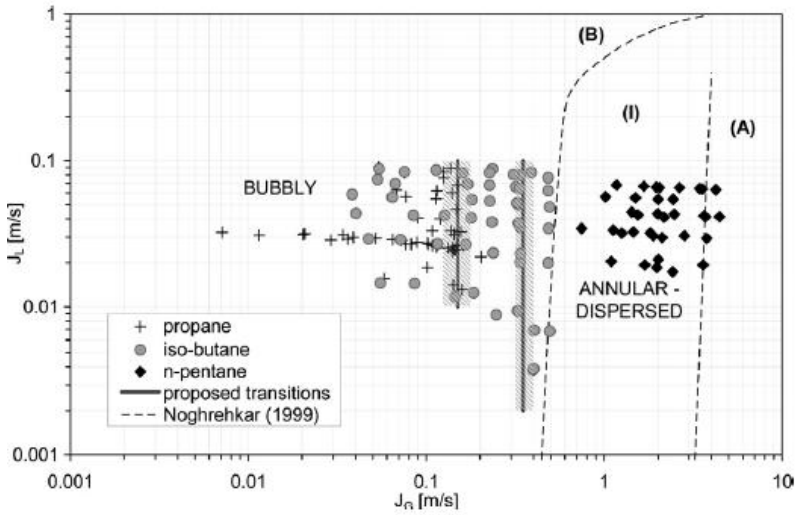

Figure 2.26: Flow pattern map using superficial velocities by Aprin et al.[26]

The authors also noted that the width of the intermittent regime for their boiling flow was smaller than adiabatic two-phase flow observed by Noghrehkar et al. [17].

The flow pattern of air-water two-phase flow in in-line tube bundles was investigated with the use of a high speed camera by Hong and Liu [27]. The authors used two tube bundles: a 10x4 in-line tube bundle with P/D=1.8, and a 10x6 in-line tube bundle with P/D=1.3. For both types the tubes had a length of 65mm and a diameter of 20mm. Three different flow patterns were observed from visual inspection: bubbly, intermittent and spray flow. Bubbly flow occurred at low superficial gas velocities ($U_{SG} < 0.08\, m/s$) and was characterized as a continuous liquid phase with gas distributed as discrete small bubbles. It was noted that increasing superficial liquid velocities reduced the size of the bubbles. As superficial gas velocity increased, the intermittent flow pattern was observed. This was characterized as a continuous gas or large slugs in the liquid phase with small bubbles also distributed in the liquid phase. At a high superficial gas velocity the spray flow pattern was observed. This occurred when the liquid phase flowed upwards both as a thin liquid film and in the form of drops entrained in the gas, Fig. 2.27.

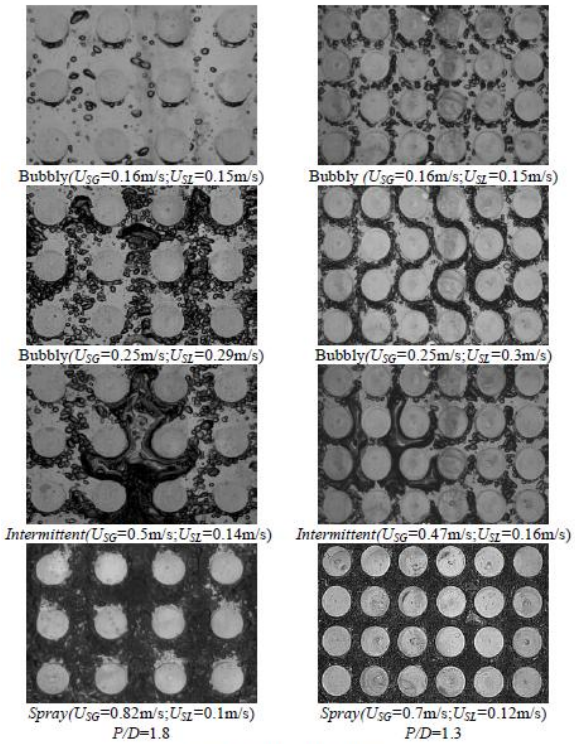

Figure 2.27: Two-phase flow pattern, Hong and Liu [27]

The authors created flow pattern maps for both tube bundles (P/D=1.3 and 1.8) using the coordinates of superficial gas against liquid velocities. These maps are shown in Fig. 2.28. The figure also shows how the authors' flow pattern maps compare with those of Ulbrich and Mewes [21], Noghrehkar et al. [17]and Xu et al. [23].

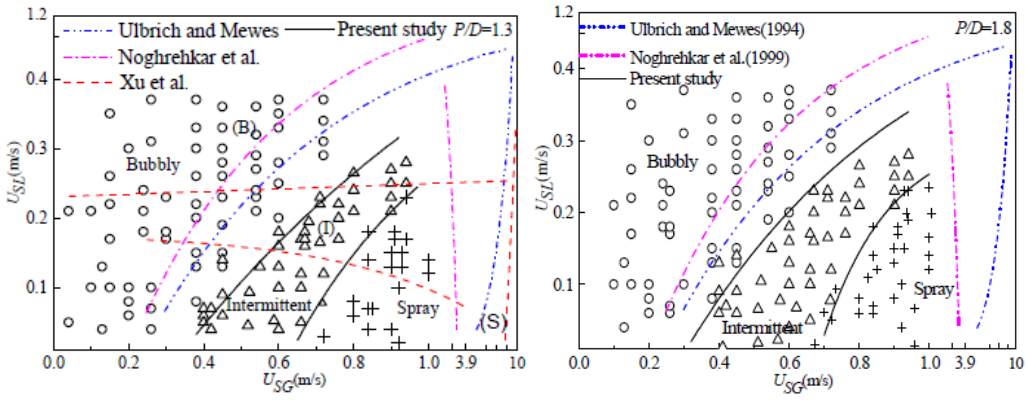

Figure 2.28: Two-phase flow pattern maps, Hong and Liu [27]

2.2.2 Summary of Flow Pattern

- The relationship between the heat transfer process and the hydrodynamics of the flow across the bundle is complicated [10]. It exists as a result of the heat transfer for the tubes within the bundle and is a function of the local flow conditions. Flow patterns inside a kettle reboiler depend on the applied heat flux value.
- Flow patterns can be distinguished using a range of different techniques such as visual observation and photographic or video recordings, gamma and X-ray attenuation, absolute and differential pressure transducers, electrical resistive and impedance void probes and fibre optic probes.
- A plume of two-phase fluid is observed at the top of the bundle when the boling occurs within the kettle reboiler. The plume's size increases with increasing heat flux.
- The driving force for the recirculation, and thus the reboiler's performance, is influenced by the pattern of downward recirculating flow at the sides of the bundle. It is also dependent on the extent of the vapour-liquid separation near to vapour-liquid interface (above and to the sides of the tube bundle).
- The following pattern is apparent from visual observation of the boiling flow in the kettle reboiler: bubbly flow at the bundles' bottom rows of tubes, and a transition to a frothy flow pattern where vapour rises to the bundle's top rows [11].
- An inspection of the boiling flow in the upper tubes in the bundle shows that high voidage flow occurs between the tubes' vertical gaps and liquid flow between the tubes' horizontal gaps [22].
- The majority of investigations of the flow pattern in tube bundles show that three different flow patterns can be recognised: bubbly, intermittent, and annular or dispersed.
- Kettle reboilers have usually been designed on the principle that the recirculating flow within the tube bundle can be modelled as one-dimensional [28]. A two-dimensional model has recently been developed to take into account the two-dimensional nature of the recirculating flow inside and outside of the tube bundle [8].
- A two-dimensional model is needed in order to analyse the general flow pattern within the kettle reboiler [7].

- Many of the maps of flow patterns that have been used are just a plot of the maximum superficial gas velocity against the maximum superficial liquid velocity.
- Previous studies suggest that most maps of flow patterns within the tube bundle were developed by simulated two-phase flows with air-water mixtures because of the cost and difficulty associated with testing in vapour-liquid mixture.
- Flow pattern changes occurred largely as a result of changes to the value of superficial gas velocity; the superficial liquid velocity had a relatively small effct on the flow pattern.
- A comparison between the flow maps for boiling and adiabatic conditions in the tube bundles showed they are different.
- A greater understanding is needed about the boiling flow in reboilers in order to further investigate the flow pattern across the tube bundle.

2.3 Recirculation velocity

To design kettle reboilers, the heat transfer coefficients required an accurate estimate of the rate at which flow recirculates through the bundle [29]. The circulation of fluid is caused by the difference in density between the liquid that surrounds the bundle and the two-phase mixture within it. A number of studies have been done to find the rate of recirculation flow across the tube bundle. In the study by Cornwell et al. [11], the flow in the reboiler was observed by placing paper disks in the moving liquid. It was assumed that the difference between the paper and liquid velocities was not significant as the acceleration of the liquid and the paper mass were small. A frame-by-frame analysis of cine-films was used to calculate the velocity and direction of the liquid at heat fluxes of 10, 20 and 50 kW/m^2, Fig. 2.29. The location of the circulation centres and the general geometry of the flow are also shown in Fig. 2.29.

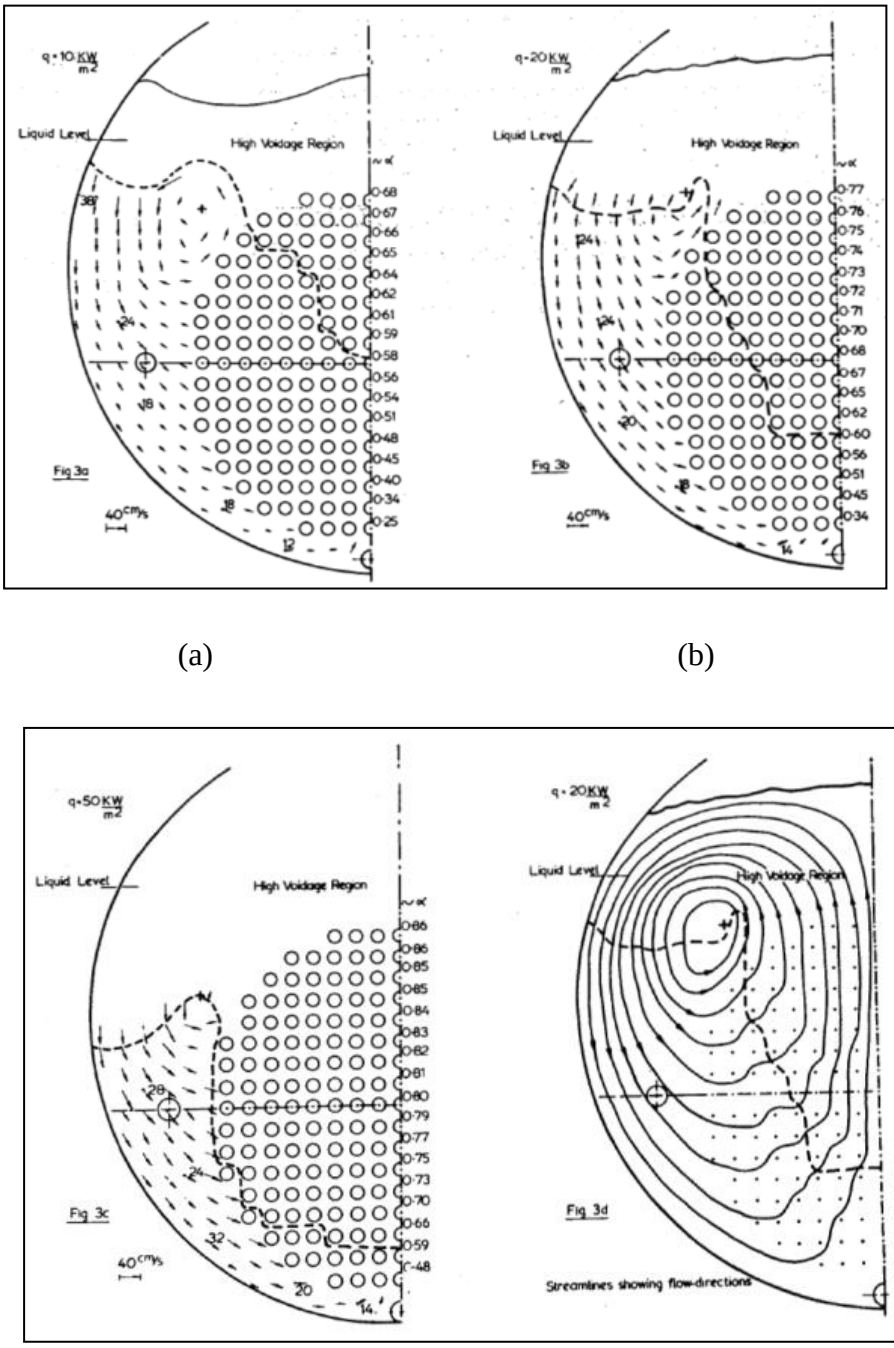

(a) (b)

(c) (d)

Figure 2.29: Flow direction and velocities across the kettle reboiler [11]

(a) 10 kW/m^2 (b) 20 kW/m^2 (c) 30 kW/m^2 (d) 40 kW/m^2

Shire et al. [29] used a laser Doppler anemometry system (LDA) to measure the velocity of the liquid. R113 was used as the working fluid in the kettle reboiler used by

Cornwell et al. [11]. LDA was used to measure horizontal and vertical velocity along the lines 1-1 to 10-10, Fig. 2.30 at all the heat fluxes used (5, 20, 40 and 50 kW/m^2).

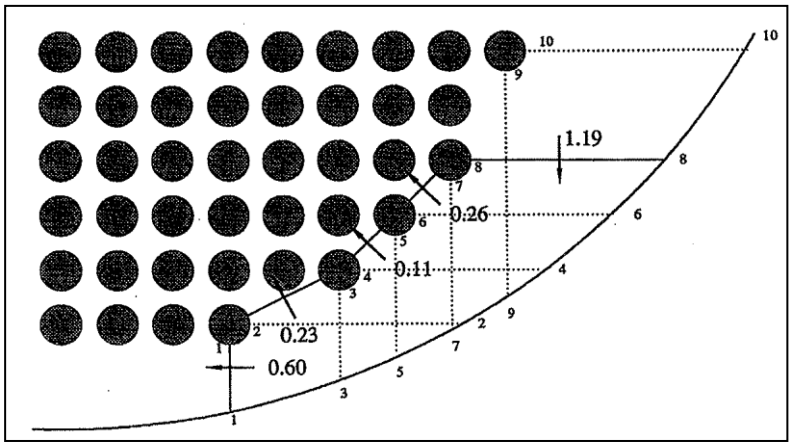

Figure 2.30: Positions of the planes used for calculating mass flux, Shire et al. [29]

Figure 2.31 shows a vector plot of the circulation velocity at a heat flux of 20 kW/m^2. The velocities ranged from 0.25-0.28 m/s at this heat flux.

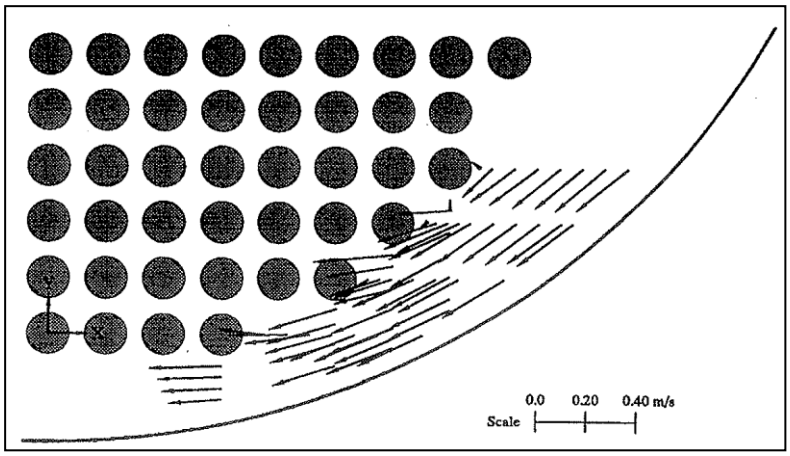

Figure 2.31: Velocity Vector Plot at 20 kW/m^2, Shire et al. [29]

At 40 kW/m ^{2} the velocities ranged from 0.20 - 0.4m/s, and the range changed to 0.16 - 0.4 m/s at 50 kW/m^2. The velocities measurements and liquid mass fluxes across the boundaries 1-1 and 2-2, 3-3 and 4-4, 5-5 and 6-6, and 7-7 and 8-8 were computed and compared. To calculate the mass fluxes the velocity measurement profiles were integrated across the boundaries, Fig. 2.30. The error in the results, obtained by continuity checks, is given in Table 2.1.

Table 2.1: Mass flux differences over boundaries, Shire et al. [29]

Boundaries Compared	Heat Flux (kW/m^2)			
	5	20	40	50
1-1 & 2-2	-4	+6	+16	+14
-3-3 & 4-4	-10	-1	-10	-7
5-5 & 6-6	-22	+20	-21	-17
7-7 & 8-8	-6	-16	-38	-36
9-9 & 10-10	-	-	-42	-39

Error values in the calculated mass flux values ranging from 1- 42% were found. These errors were dependent on the heat flux values and the positions of the planes; the authors attributed them to the periodic variation of flow conditions between the shell and the bundle. Thus it is not sufficient to take single component LDA measures to obtain precise velocity values; a simultaneous measurement of the two main velocity components is required.

Miller [15], working with the same kettle reboiler as Shire et al. [29], and with n-pentane as the working fluid, used a Particle Image Velocimetry (PIV) technique to make liquid velocity measurements. At all the heat fluxes used (10, 20, 30, 40 and 50 kW/m^2) the horizontal and vertical velocities were measured by PIV along the lines shown in Fig. 2.32.

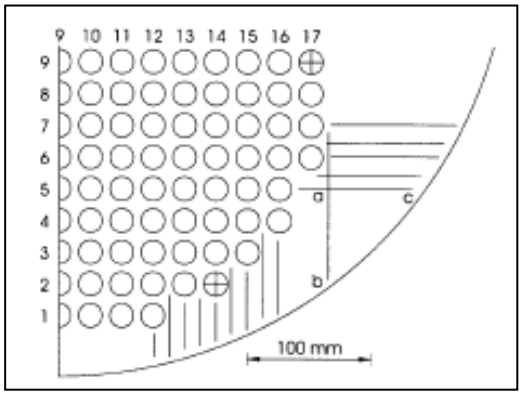

Figure 2.32: Positions of the planes used for calculating mass flux, Miller. [15]

The velocity measurements and liquid mass fluxes across the boundaries a-c and a-b, were determined and compared. To calculate the mass fluxes the normal components of

the velocity measurement profiles were integrated across the boundaries, Fig. 2.32. Table 2.2 displays the error in the mass flux values, as determined by continuity checks.

Table 2.2: Mass flux differences across planes ab and ac, Burnside et al. [2]

Heat flux (kW/m^2)	$\dot{m}_{ab}$	$\dot{m}_{ac}$	Error %
10	0.485	0.444	-2
20	0.522	0.654	-16
30	0.397	0.575	-31

Figure 2.33 shows the velocity profiles at a heat flux of 20 kW/m^2. The origin of x is centred on the tube in row 2, column 14 of the bundle, while the origin of y is centred on the tube in row 9, column 17. Both origins are marked in Fig. 2.33. The inclination of flow to the horizontal (θ) is defined in Fig. 2.33. Figure 2.33 (a) shows the velocity profiles across the horizontal planes beside the rows 5-7. At the side of the bundle, the velocity had a maximum value close to the shell wall, which decreased to a minimum close to the bundle edge. For row 7, the velocity decreases from 400 to 100 mm/s. Figure 2.33 (b) shows the velocity profiles across the vertical planes below the columns 12-17. At column 17, the velocity decreases from 250 mm/s close to the bundle to 150 mm/s towards the shell, then increases to 350 mm/s close to the shell wall.

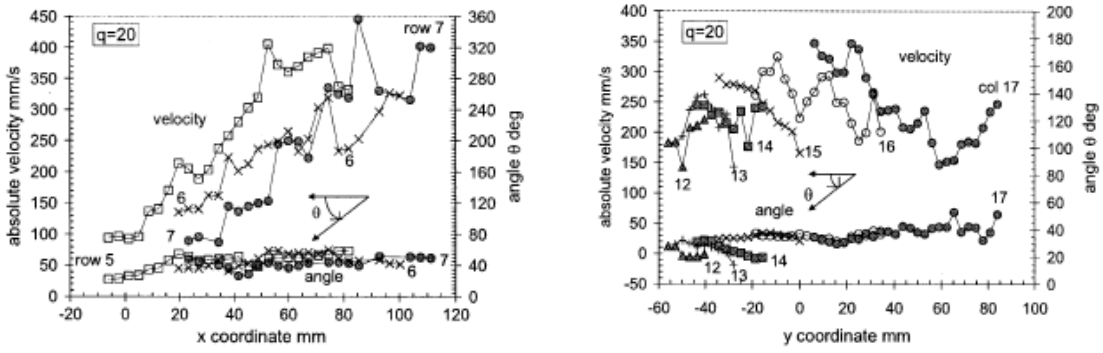

(a) (b)

Figure 2.33: Profiles of velocity and angle around bundle, Burnside et al. [2]
(a) across horizontal planes (b) across vertical

Figure 2.34 shows the measured mass flow rate passing through horizontal planes beside of the bundle ($\dot{m}_y$) and through vertical planes below the bundle ($\dot{m}_x$). Fig 2.34 (a) shows that between rows 6 and 7 the mass flow rate ($\dot{m}_y$) is approximately 0.7 kg/s. Below row 6, $\dot{m}_y$ decreases at 10 and 30 kW/m^2, but did not change significantly at 20 kW/m^2. At all heat fluxes the mass flow rate ($\dot{m}_x$) decreases towards the bundle centre line, Fig. 2.34 (b).

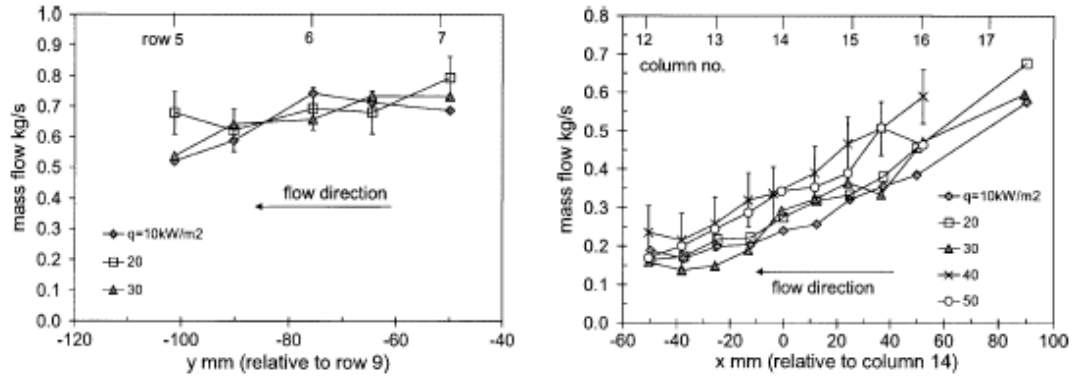

(a) (b)

Figure 2.34: Mass flow rates through the planes, Burnside et al. [2]

(a) Horizontal planes beside the bundle $\dot{m}_y$ (b) Vertical planes below the bundle $\dot{m}_x$

It is concluded by the authors that the application of PIV to making measurements in the kettle reboiler was successful, but that close to the bundle edges and the separation vortex region measurements were difficult.

2.3.1 Summary of recirculation velocity

- To model the kettle reboiler, the recirculation flow rate within it must be predicted accurately.
- A number of different techniques have been used to measure the recirculation flow rate including: photographic, laser Doppler anemometry and Particle Image Velocimetery. The results obtained by using these techniques were fairly similar, with those taken at high heat fluxes being less accurate due to periodic variation of the flow condition between the shell and bundle [2].

- The flow condition (velocities, void fraction, qualities) and heat transfer coefficients within in the bundle may vary considerably as a result of variation in the intensity of the recirculating flows.
- The heat flux is important in determining the recirculation flow rate in the kettle reboiler.

2.4 Void Fraction

The void fraction, or the volume fraction of gas, is one of the most important parameters used to characterize two-phase flows. It is the key physical value for determining various other important parameters, such as two-phase density, two-phase viscosity and the relative average velocity of the two phases. It is also of fundamental importance in models that predict flow pattern transition, heat transfer, pressure drop and flow-induced tube vibration. Therefore, an accurate prediction of void fraction is needed to better understand the two-phase flow phenomena [24].

The term, void fraction is defined as the ratio of local gas volume to the volume of liquid-gas mixture at a certain cross section [30]. From this definition, the cross section void fraction, ε, and velocity ratio, S, defined as the ratio of gas to liquid velocity, can be related by a linear combination of the continuity equation for each phase. To give:

$$\varepsilon = \frac{1}{1 + s\left(\frac{\rho_g}{\rho_l}\right)\left(\frac{1-x}{x}\right)} \tag{2.3}$$

The homogenous void fraction can be obtained by substituting the velocity ratio of gas to liquid, S = 1 in Eq. (2.3) assuming that both phases are well mixed.

Several investigators such as Schrage et al. [31], Dowalti et al. [32,33] and Feenstra et al. [41] have found the void fraction to be lower than that predicted by the homogenous model. The reason has been found to be that there is slip between the phases i.e. S≠1. The validity of this assumption depends on the degree of the mixing between the phases. The void fraction data tend to approach the values predicted by the homogenous model at high mass velocity and lower vapour quality. At low mass velocity and especially at low vapour quality, where buoyancy effects are significant, the velocity difference between the phases is considerable [31].

Kondo and Nakajima [24] measured the void fraction of upward two phase, air-water mixtures across horizontal staggered tube bundles with equilateral triangular pitches. Three different pitch to diameter ratios (1.4, 1.28, and 1.08) and six different configurations of the tube rows (7, 9, 11, 13, 15, and 20) were tested**.** Tests were carried out for flow rates of mixtures with mass velocities over 60 kg/m^{2}s, a range of quality: 0.005 to 0.9 and a range of superficial air and water velocities of 1.5-50 cm/s and 0.032-0.32 cm/s respectively. The experimental data indicated that the void fraction increases with superficial air velocity, whereas the superficial water velocity does not affect the void fraction. Based on these results, they proposed a simple empirical correlation to predict the mean void fraction i.e.,

$$\varepsilon = K\left(\frac{V_g}{\sqrt{P\,g}}\right)^{1/3} \tag{2.4}$$

where K depends on the dimensions of the tube bundle, determined from

$$K = 1.0\left(\frac{P_T}{L}\right)^{5/6}\sqrt{\frac{g}{L}}\left(\frac{{P_T}^2 Sin60^0}{{P_T}^2 Sin60^0 - 0.25\pi d^2}\right) \tag{2.5}$$

in which P_T is the tube pitch, V_g is the superficial vapour velocity and L is the tube length.

Their experimental void fractions are compared with the calculated values from Eq. (2.4) in Fig. 2.35. The authors stated that the Eq. (2.4) is valid for bubbly, slug and frothy flows and for the given experimental ranges.

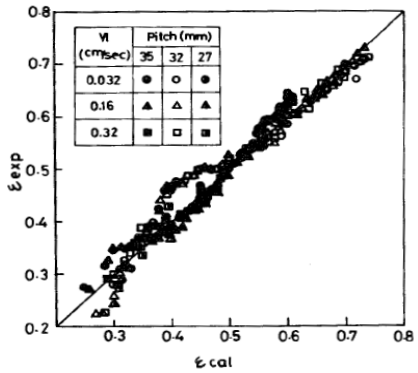

Figure 2.35: Comparison of predicted void fraction with experimental results Knodo and Nakajima [24]

Chan and Shoukri [30] measured void fraction profiles in tube bundles boiling R113 driven through the test section by natural circulation. A gamma ray densitometry technique was used to measure the variation of void fraction in both the 3x3 and 3x9 tube bundles under pool boiling conditions. Figure 2.36 shows the data of the small bundle (3x3) with all tubes heated. The data show that the void fraction increased in the columns and then decreases slightly at the top of the bundle. The decrease was caused by an increase in vapour velocity as the two-phase mixture emerged from the bundle. Above the bundle, the void fraction increased as the two-phase mixture rose, indicating lateral dispersion of vapour in the pool.

Figure 2.37 describes typical observed flow patterns for high and low heat flux. As the heat flux was increased, the void fraction profile exhibited two local minima, Fig. 2.38, one close to the bundle and the other near the free surface. This suggests a complicated recirculation pattern. However, the void fraction increased fairly uniformly through the large bundle and increased rapidly towards the free surface, Fig. 2.38 and near the top of the bundle, the void fraction did not decrease.

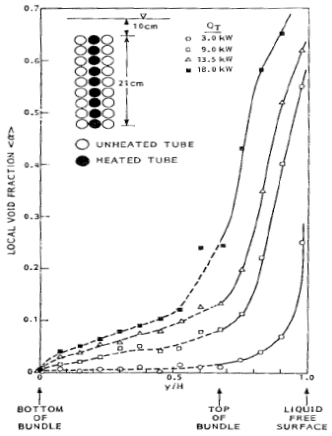

Figure 2.36: Void distribution data bundle 3x3 bundle, Chan and Shoukri [30]

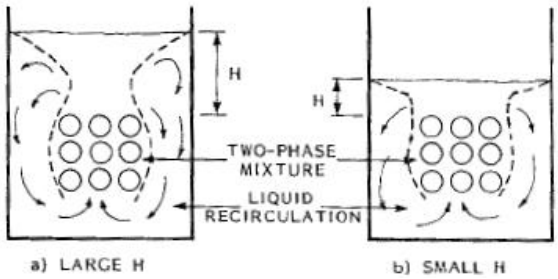

Figure 2.37: Observed flow patterns, Chan and Shoukri [30]

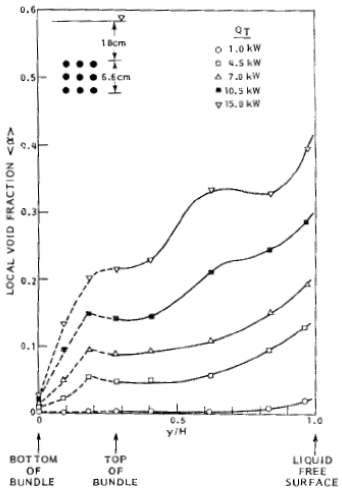

Figure 2.38: Void distribution data 3x9 bundle, Chan and Shoukri [30]

Gebbie and Jensen [34] measured the void fraction of boiling R113 in a half boiler using hotwire anemometry. The half bundle comprised of 75 tubes arranged in a square in-line configuration, Fig. 2.39. The distribution of horizontal and vertical void fractions was obtained for heat fluxes of 10, 30, 50 and 70 kW/m^2.

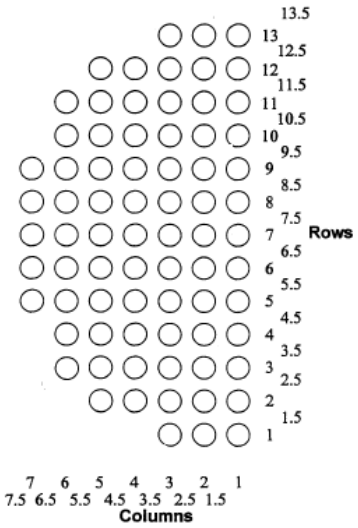

Figure 2.39: The test section of the tube bundle of Gebbie and Jensen [34]

The horizontal void distributions across the tube bundle for heat fluxes of 10, 30 and 70 kW/m^2 are displayed in Fig. 2.40. With increasing heat flux the void fraction in the lower rows of the bundle increases rapidly, with a slower change in the upper rows. Figure 2.40 shows that the highest values of void-fraction occurred either above the tubes or in the inter-column region, depending on the flow pattern. A maximum occurring in the inter-column region was indicative of vertical flow caused by the generation of vapour at both sides of the lower tubes. Maxima occurring above the tubes

were indicative of lateral flow. At the lowest row (1.5) and for all heat fluxes, the void fraction distribution decreases towards the left edge of the bundle. For the between-tube void fraction measurements, little horizontal variation was found and maxima generally appeared to be absent, Fig. 2.40.

The uniform void fraction between tubes resulted from the small change in vapour generation in this region. For some rows, the void fraction distribution decreases beyond the left edge of the bundle at all heat fluxes.

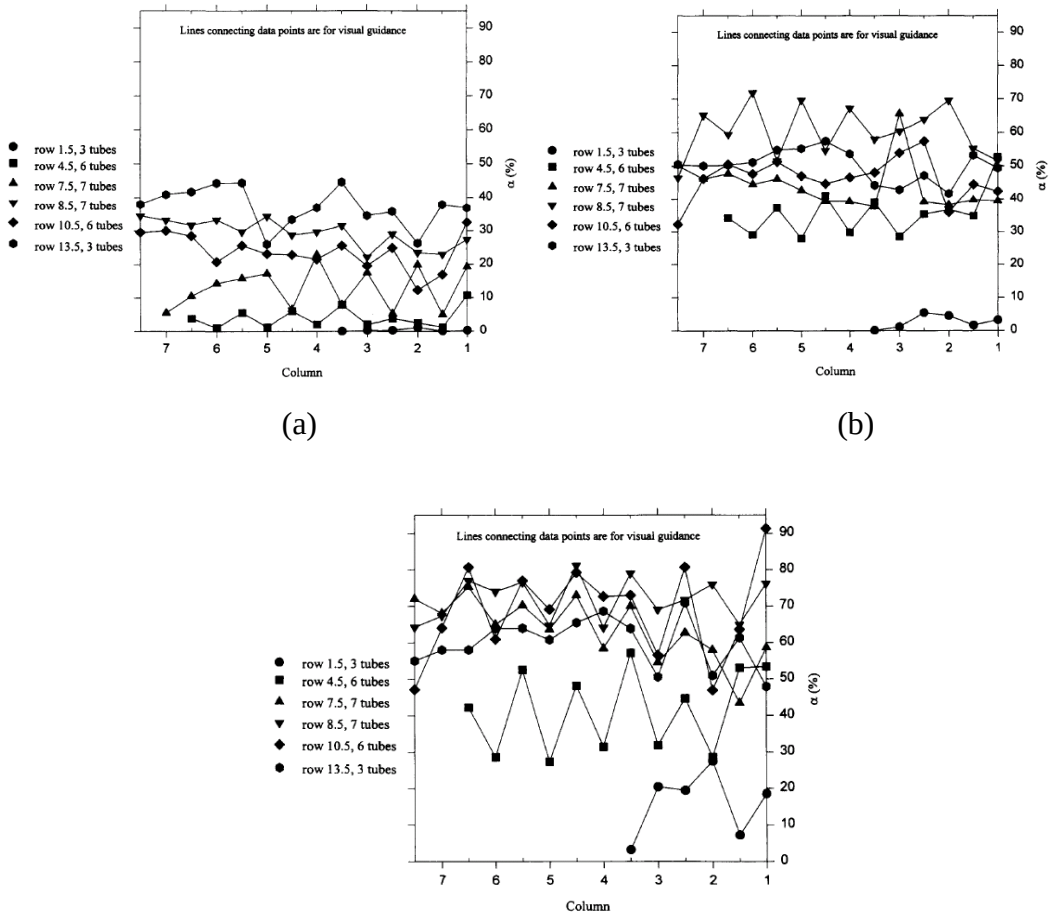

Figure 2.40 : Tube bundle void fraction above the tubes, Gebbie and Jensen [34]

(a) at 10 kW/m^2 (b) at 30 kW/m^2 (c) at 70 kW/m^2

Hinata et al. [35] investigated the mechanism of nucleate boiling heat transfer by conducting void fraction distribution profile measurements around a horizontal cylindrical copper surface. A copper rod, 20 mm in diameter and 100 mm long, was heated in a pool of Freon 11. The copper rod had a hole, 7 mm in diameter, on the

centre axis and a sheathed electrical heater wound on a stainless steel pipe was inserted in it as shown in Fig. 2.41. The distribution of local void fraction was measured by a miniature optical-fiber probe, which consisted of two optical fibers with a 45-degree surface at each end for detecting the response of the liquid or gas phase, Fig. 2.41.

The void fraction profiles in the radial direction at different angular positions were captured and are shown on the right hand side of Fig. 2.42. Bubbles generated at locations below the mid-point (i.e. $\theta<90^o$) slid along the wall and joined other bubbles. Beyond the mid-point, some bubbles separated from the wall and rose vertically. At about $\theta = 135^o$, Bubbles no longer slid along the wall. The authors reported this as the formation and separation of a bubble boundary layer. The left hand side of Fig. 2.42 shows the lines of constant void fraction around the cylinder. There are two region of high void fraction. The first is in the "wake" of the cylinder, through which region most of the generated bubbles pass. The second is the bubble boundary layer separation point at about the $\theta = 135^o$ point. These results indicate where to locate the probes to measure void fraction in the tube bundle of the kettle boiler.

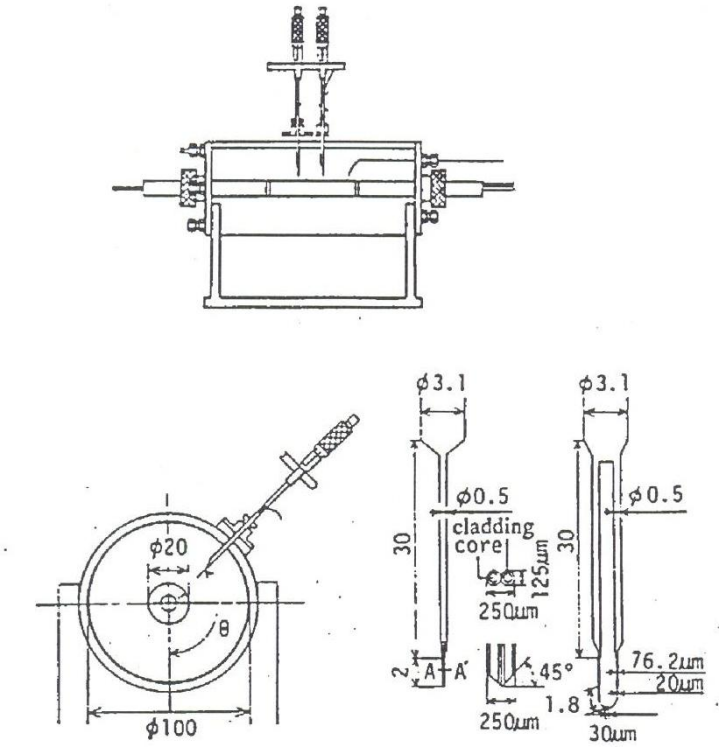

Figure 2.41: Schematic diagram of experimental setup and detail drawing of miniature optical-fibre sensor and micro thermocouple, Hinata et al. [35]

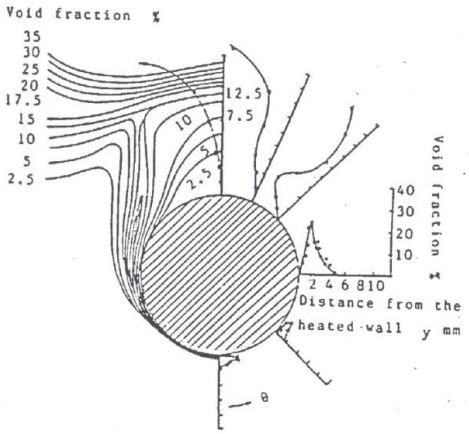

Figure 2.42: Local void fraction distribution and constant void fraction curves around a head wall, Hinata et al. [35]

Hahne et al. [36] measured the local void fraction distribution across a tube bundle using an optical probe, Fig. 2.43. R11 as the working fluid was heated under pool boiling conditions using finned copper tubes with pitch-to-diameter ratios, P/D=1.3 and 1.15. The distributions of measured void fractions within the bundle for P/D=1.3 and 1.15 are shown in Fig. 2.44 (a) and (b), respectively. With increasing heat flux and increasing bundle height from the bottom to the top, there is an increase in the local void fraction. The local void fraction distribution across the bundle top is shown in Fig. 2.45; the maximum and minimum values occur, respectively, between and behind the tubes. The inline bundle configuration had a higher rising void fraction between the tubes than the staggered bundle, Fig. 2.45.

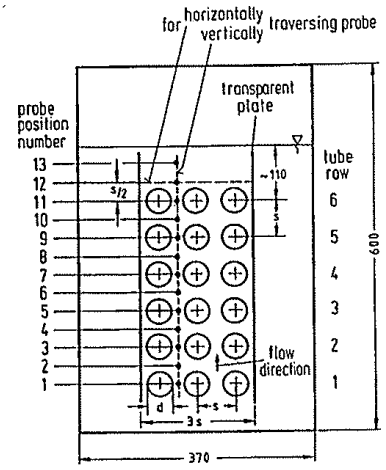

Figure 2.43: Tube bundle evaporator, Hanhe et al. [36]

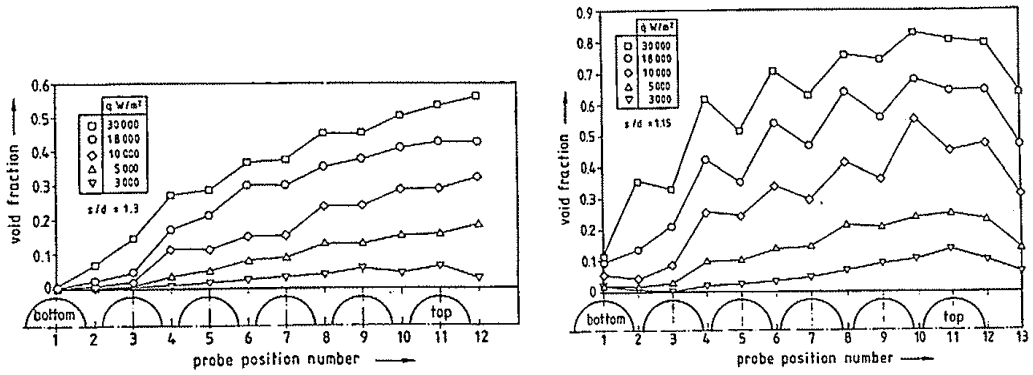

(a) In-line configuration P/D=1.3 (b) In-line configuration P/D=1.15

Figure 2.44: Vertical void fraction distrbution within the bundle,Hahne et al. [36]

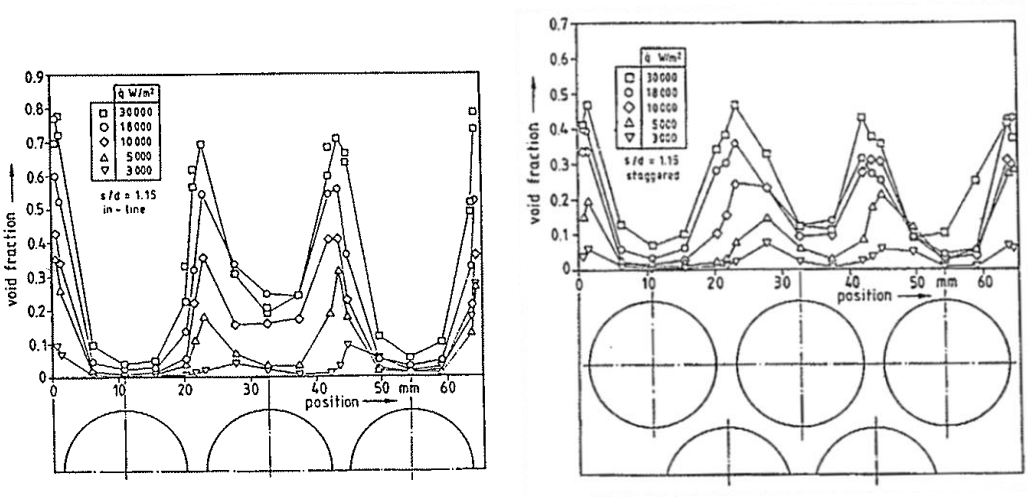

(a) In line configuration (b) Staggered configuration

Figure 2.45: Horizontal void fraction distribution above bundle exit (P/D=1.15) [36]

Suzuta et al. [37] measured the local void fraction using HCFC123 fluid under boiling conditions, in which the two-phase flow moved upwards across the horizontal tube bundle. The bundle had a cross section of 165×162.7mm and consisted of thirty rows and five columns in an in-line configuration. The tube diameter and pitch were 22.23mm and 32.54mm respectively, Fig. 2.46.

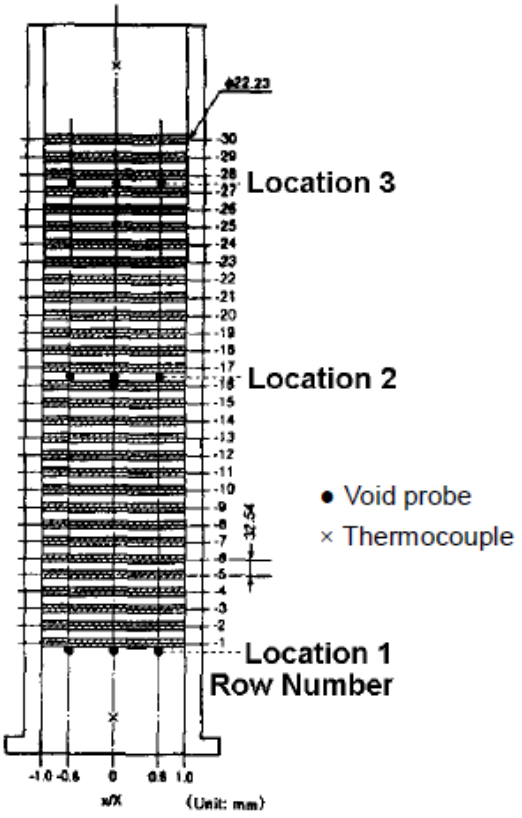

Figure 2.46: Tube bundle with void fraction measurements locations, Suzuta et al. [37]

Void fraction measurements were made with optical probes at three locations along the direction of flow in the bundle: the inlet, centre and outlet. Fig. 2.47 shows the test results and conditions. The local void fraction distribution was found to be non-uniform across the tube bundle; the void fraction has a higher value behind the tubes compared to the gap between them. According to the authors, this was a consequence of gas trapped by the centrifugal separation that takes place behind the tubes.

x/X*(-)	-0.6	○
	0	□
	0.6	△

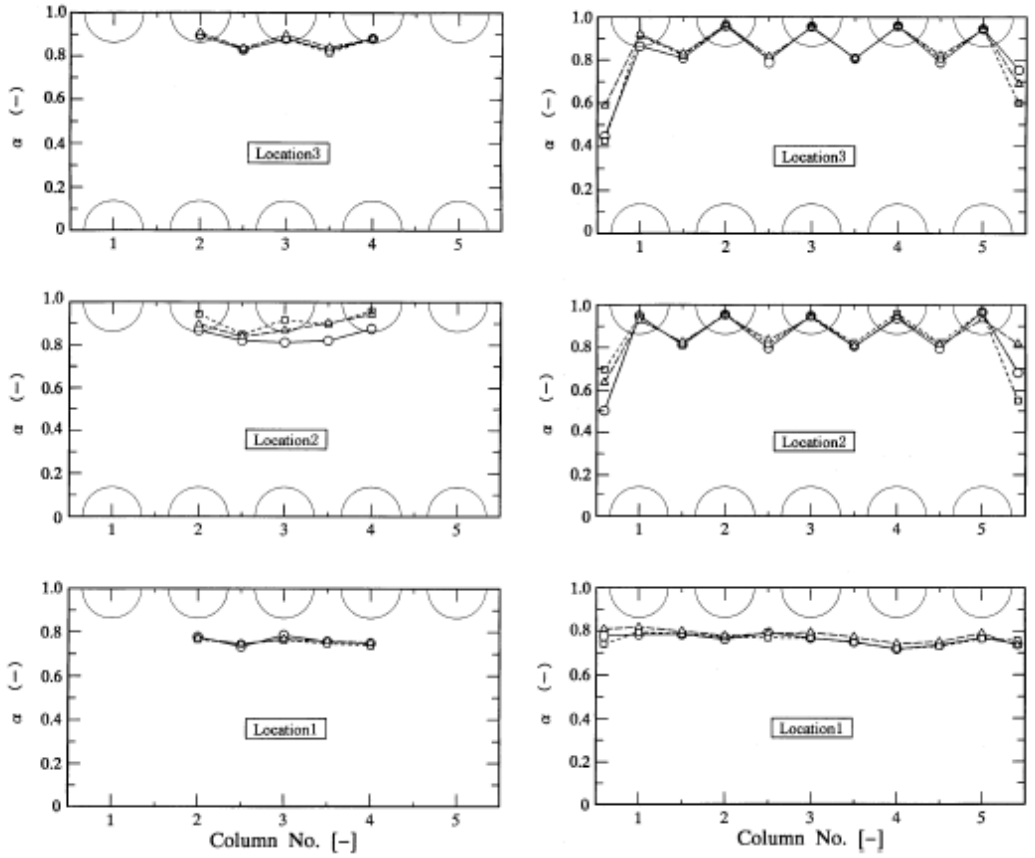

(a) (b)

x/X^* corresponding to the locations shown in Fig .2.1

Figure 2.47: Void fraction distribution for (a) (J_G=3.1 m/s ,J_L=0.35 m/s ,P=0.40 MPa) , (b) (J_G=3.1 m/s ,J_L=0.35 m/s ,P=0.76 MPa), Suzuta et al. [37]

Schrage et al. [31] investigated shell side void fraction experimentally for two-phase air/water mixtures flowing vertically across a horizontal tube bundle. The tests were conducted under adiabatic flow conditions and empirical correlations were developed for the void fraction. The test section consists of a tube bundle containing 27 rows of 7.94 mm diameter tubes with five tubes in each row. The tube arrangement was an in-line, square array with a pitch-to-diameter ratio of 1.3. To obtain volume-average void fractions, quick-closing plate valves were used to isolate the tube bundle. The range of mass velocity was 55 to 680 kg/m^{2}s and the range of vapour quality was 0.0003 to 0.68, at pressures of 1 and 3 atm. Figure 2.48 shows the ratio of void fraction data to the homogeneous value at pressures of 1 and 3 atm. As can be seen, the homogeneous void fraction model over predicts the void fraction data for all quality and mass velocity levels.

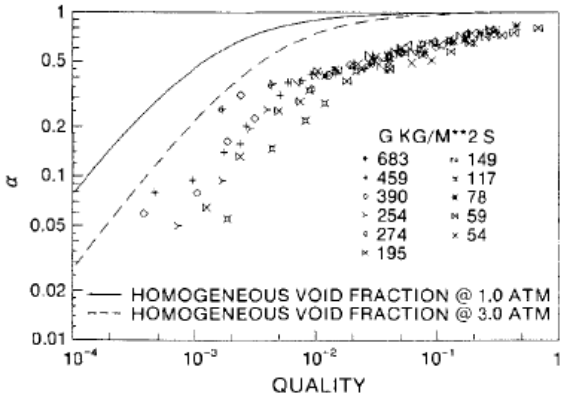

Figure 2.48: Comparison data with homogenous void fraction, Schrage et al. [31]

To eliminate the effects of pressure, a reduced void fraction, α / α_H , the ratio of the measured void fraction, α , to the homogeneous void fraction, α_H , was used, as shown in Fig. 2.49.

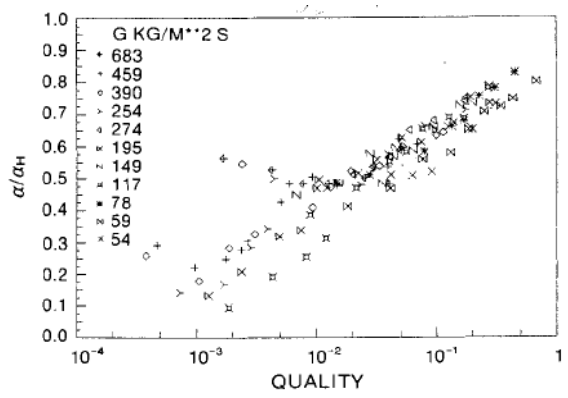

Figure 2.49: Effects of mass velocity on reduced void fraction, Schrage et al. [31]

Figure 2.49 shows that the reduced void fraction increased with increasing mass velocity and vapour quality and, at large mass fluxes, the experimental void fraction approached the homogenous value. Also as the quality approaches unity, the reduced void fraction, α/α_H, tends towards unity. However, if the trend in data is extrapolated to approach zero quality, the data trend indicates that α/α_H will approach zero at some finite quality, which is not possible. The authors argued that, as quality tended to zero, the vapour phase is present in the form of very small bubbles and that the flow would behave essentially as a homogenous flow. Therefore, α/α_H would approach unity. The authors were unable to fit the various combinations of quality and mass velocity at which the minima in α/α_H would occur. Therefore for correlation purposes, a minimum value of α/α_H was assumed to be 0.1.

The reduced void fraction data were correlated as

$$\frac{\alpha}{\alpha_H} = 1 + 0.123\ Fr^{-.191} \ln x \tag{2.7}$$

where $Fr = \dfrac{G}{\rho_l \sqrt{gD}}$ and G was the total mass velocity based on the minimum flow area in the bundle. The correction was valid for $\alpha/\alpha_H > 0.1$ and was accurate to ±20%.

Dowalti et al. [32] examined void fraction using the phenomenological approach developed by Zuber and Findlay [38], commonly referred to as the drift flux model. Based on the drift flux model, Zuber an Findlay [38] derived the following general expression for the weighted mean vapour velocity, $\bar{u}_g$,

$$\bar{u}_g = C_0 \langle j \rangle + \bar{V}_{gj} \tag{2.8}$$

Where $\langle j \rangle$ is the mixture mean velocity based on the total volumetric flow rate and the minimum flow area and $\bar{V}_{gj}$ is the weighted vapour drift velocity. This expression accounts for non-uniform velocity and void fraction profiles through the distribution parameter C_0 and the effect of local relative velocity between the phases through the drift velocity. The weighted mean vapour velocity is related to the void fraction using the area-averaged superficial vapour velocity,

$$\langle \varepsilon \rangle = \frac{\langle j_g \rangle}{\bar{u}_g} \tag{2.9}$$

Substituting (2.8) into (2.9) gives the average void fraction as:

$$\langle \varepsilon \rangle = \frac{\langle j_g \rangle}{C_0 \langle j \rangle + \bar{V}_{gj}} \tag{2.10}$$

Dowalti et al. [39] applied the drift flux model to their air-water tube bundle void fraction data from six different tube bundle geometries. The bundle consisted of 20 rows with 5 columns. A gamma ray densitometer was used to measure the void fraction. The following fit line was obtained for air-water data using linear regression:

$$\bar{u}_g = 1.1040 \langle j \rangle + 0.33 \tag{2.11}$$

Here, both the average gas velocity and mixture mean velocity are specified in m/s. The values of C_0 are close to unity, indicating a fairly uniform void fraction profile across the tube bundle. The average deviation between the correlated and their experimental data was found to be 11.1%, Fig. 2.50.

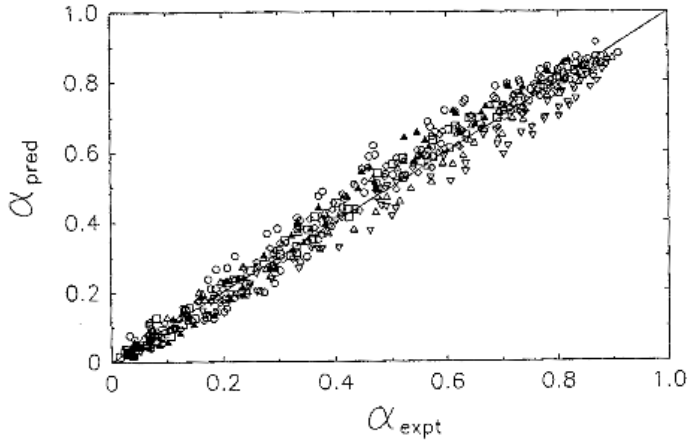

Figure 2.50: Comparison of predicted and measured void fractions, Dowalti et al. [32]

Although Zuber and Findlay proposed equations for determining $\bar{V}_{gj}$ for different flow patterns in a tube, these equations were not found to be applicable to the Dowalti et al. data set. One reason may be that $\bar{V}_{gj}$ is generally considered a function of the terminal rise velocity of a bubble in a stagnant liquid column. Obviously, this velocity would be

different for a tube bank, especially a staggered one. The authors suggest that more data, using other fluids, were required before a general expression could be proposed for the determination of $\bar{V}_{gj}$ in a tube bundle.

Dowalti et al. [33] extended their previous works to study void fraction variation across a horizontal tube bundle using R113. The tube bundle consisted of 100 copper tubes arranged in an in-line square array of 5 columns by 20 rows, on a pitch-to-diameter ratio of 1.3. The tubes were 12.7 mm in outside diameter with wall thickness of 1.24 mm and a tube length of 108 mm. The tube bundle was heated by the flow of hot oil inside the tubes. Void fraction measurements were taken with a gamma-ray densitometry at the four vertical locations shown in Fig. 2.51. The R113 tests were conducted under the following conditions: mass velocity range 50-790 kg/m^{2}s, quality 0-50%, Inlet subcooling between 3-20 K, heat fluxes upto 80 kW/m^2 and the range of pressure of 103-155 kPa. Figure 2.52 shows the void fraction data plotted against quality for R113 and Fig. 2.53 shows the void fraction data against quality for air-water in a similar tube bundle geometry, Dowalti et al. [33]. It is clear from Figs. 2.52 and 2.53 that for a given quality the data show a strong mass velocity effect, with a higher void fraction obtained at larger mass velocities. Similar to the air-water data, the measured void fractions for R113 are lower than the values predicted by the homogenous flow model. These figures also indicate that the homogenous flow model for R113 is below that for the air-water system because of the larger liquid to vapour density ratio. For the conditions used in this study, the density ratio for R113 is approximately four times that of air water.

Figure 2.54 compares the correlation developed for air water experiments in Dowalti et al. [39] with the R113 data,

$$\alpha = 1 - \frac{1}{\sqrt{1 + C_1 j_g^* + C_2 j_g^{*2}}} \tag{2.12}$$

The constants C_1 and C_2 in Eq. (2.12) were found to be 10 and 1, respectively, for R113 data to give an absolute average deviation 15.6% between the predictions and the measurements. For air-water, C_1 and C_2 were found to be 35 and 50. Since the air-water and R113 experiments were conducted under similar conditions of the mass velocity and pressure, the authors suggested that the discrepancy between the two data sets was in part attributable to the large difference between the vapor densities. They also suggested that more experiments were required to determine the dependence of C_1 and

C_2 on other properties, such as the liquid density and surface tension. The following best fit curve was obtained for the R113 tube bundle void fraction data for the drift flux model:

$$\bar{u}_g = 1.076\langle j \rangle + 0.85 \tag{2.13}$$

The average deviation of the prediction to the data was 12%. The higher drift velocity for R113 indicates significantly greater slip in comparison to the air-water data. The authors concluded that there are no reliable models to predict C_o and $\overline{V}_{gi}$ in a tube bundle, hence, these two parameters needed to be empirically determined.

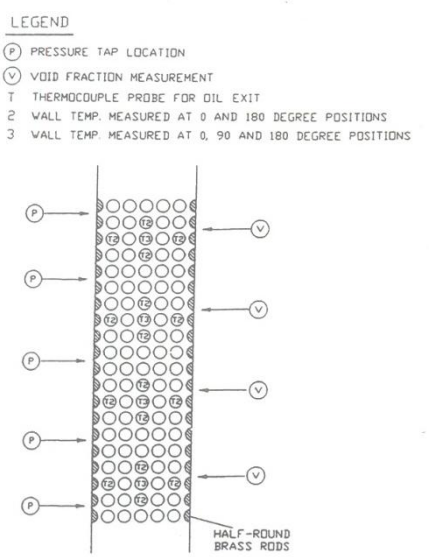

Figure 2.51: Tube bundle layout and location of instrumented tubes, Dowalti [33]

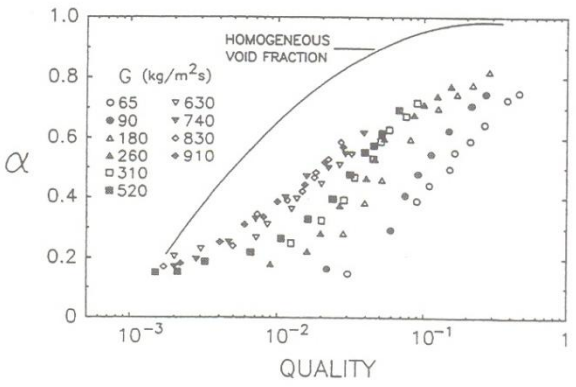

Figure 2.52: Void fraction data and mass velocity effect for R-113, Dowalti et al. [33]

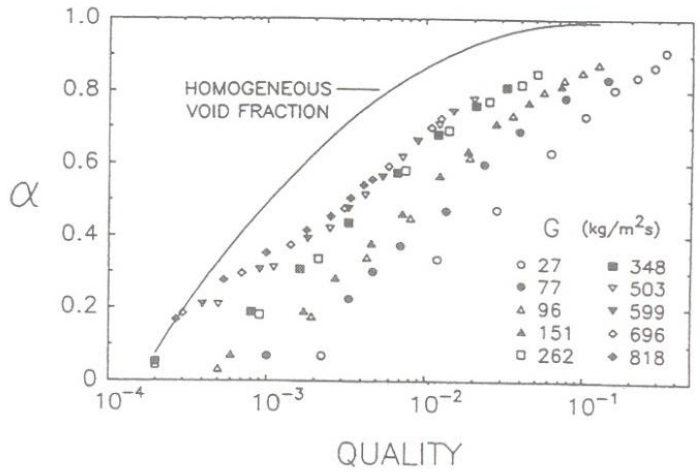

Figure 2.53: Air-water void fraction data for In-line rod bundle (P/D=1.3), Dowalti et al. [33]

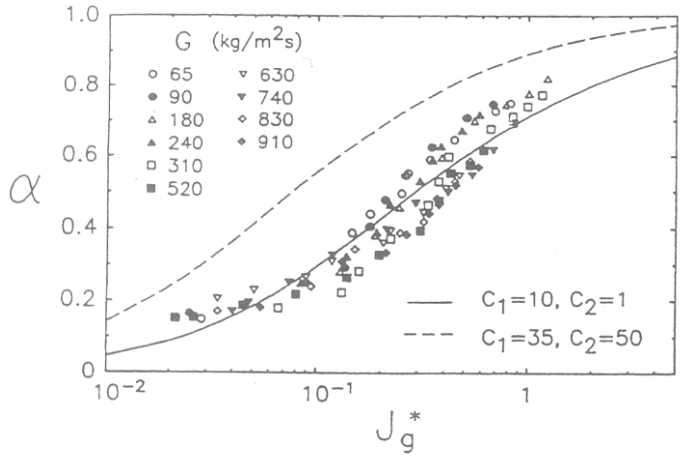

Figure 2.54: Correlation of R-113 void fraction data with j_g^*, Dowalti et al. [33]

Xu et al. [40, 23] measured the void fraction using quick-closing valves. They measured the void fraction for vertical air-water flows across a horizontal, in-line, 5x20 tube bundle with a pitch-to-diameter (P/D) ratio of 1.28. The void fraction values at high quality were found to be equal for down-flow and up-flow. However, when the vapour quality was low, the down-flow void fraction values exceeded those for up-flow. This difference may be due to the two directions of flow having different characteristics. It was also found that the measured void fraction values were significantly smaller than those predicted by the homogenous flow model and contained a strong mass velocity effect, Fig. 2.55.

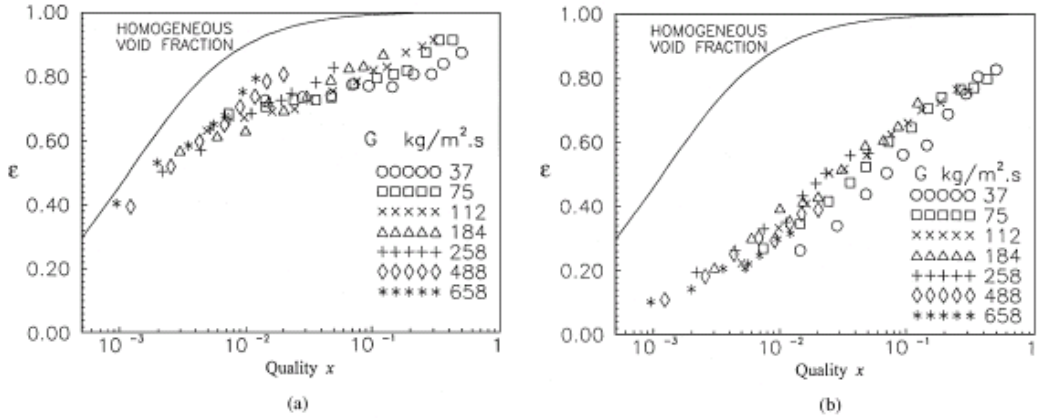

Figure 2.55: Void fraction and mass velocity effect: (a) vertical down-flow; and (b) vertical up-flow

The authors derived an equation for predicting the shell side void fraction. The equation is specified according to the Martinelli parameter, X_{tt}, and the liquid Froud number, Fr_{LO} , through

$$\frac{\varepsilon}{1-\varepsilon} = C_1 . {Fr_{LO}}^{C_2} . X_{tt}^{-C_3} \tag{2.14}$$

where

$$X_{tt} = \frac{\Delta P_L}{\Delta P_G} = \left(\frac{1-x}{x}\right)^{0.9} \left(\frac{\rho_G}{\rho_L}\right)^{0.5} \left(\frac{\mu_L}{\mu_G}\right)^{0.1} \tag{2.15}$$

and

$$Fr_{LO} = \frac{G^2}{(\rho_L^2 \; g \; D)} \tag{2.16}$$

The values of $C_1 = 1.95$, $C_2 = 0.18$ and $C_3 = 0.833$ produced the best fit to their air-water and air-oil horizontal flow data [40]. For down-flow $C_1 = 1.95, C_2 = 0.36, C_3 = 0.44$ and for up flow $C_1 = 1.07, C_2 = 0.138, C_3 = 0.645$ [23]

Feenstra et al. [41] used gamma ray densitometry to measure the void fraction for upward cross-flow through horizontal tube bundles. The authors developed a correlation for the void fraction, ε, which was derived from the combination of the continuity equations for the liquid and gas phases and accounted for the slip ratio, S and vapour quality, x through

$$\varepsilon = \left(1 + S\frac{\rho_g}{\rho_l}\left(\frac{1}{x} - 1\right)\right)^{-1} \tag{2.17}$$

Dimensional analysis was used to show that the velocity ratio was controlled by four dimensionless groups. Feenstra et al. [41] found that the following equation produced a good fit to their experimental data.

$$S = 1 + 25.7(R_i \times Cap)^{0.5}(P/D)^{-1} \tag{2.18}$$

where R_i is the Richardson number, defined as

$$R_i = \Delta\rho^2\, ga/G^2 \tag{2.19}$$

in which G is the mass velocity, based on the minimum gap between the tubes, and a is the distance between the tubes.

Cap is the capillary number, found from

$$Cap = \mu_l\, u_g/\sigma \tag{2.20}$$

Where μ_l is the dynamic viscosity of the liquid, σ is the surface tension and $u_g\ is$ the gas velocity,i.e.

$$u_g = \frac{x\, G}{\alpha\, \rho_g} \tag{2.21}$$

The gas velocity u_g requires a known void fraction. Hence the void fraction must be calculated using an iterative method.

The authors compared the predictions from this correlation with their void fraction measurements and with the data of Dowlati et al. [32], Noghrehkar et al. [17], Schrage et al. [31] and Axisa et al. [42]. These measurements varied in terms of the geometries (P/D of 1.3, 1.44, 1.75), the working fluids used (R11, air –water mixtures, R113 and steam-water) and the wide range of mass flux and qualities. Good agreement was found between the prediction of ε and nearly all of the data sets (Figs. 2.56, 2.57, 2.58 and 2.59). The exception was the data of Schrage et al. [31], shown in Fig. 2.58 (b). Ribatski and Thome [43] stated that the Feenstra et al. [41] correlation was the most suitable predictive correlation of void fraction in tube bundles in their review of the correlations proposed in the literature.

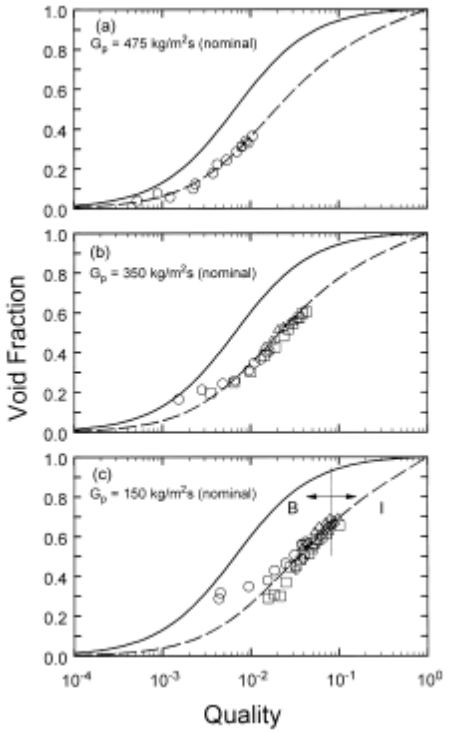

Figure 2.56: Void fraction vs. quality for R-11 data, P/D=1.44, Feenstra et al. [41]

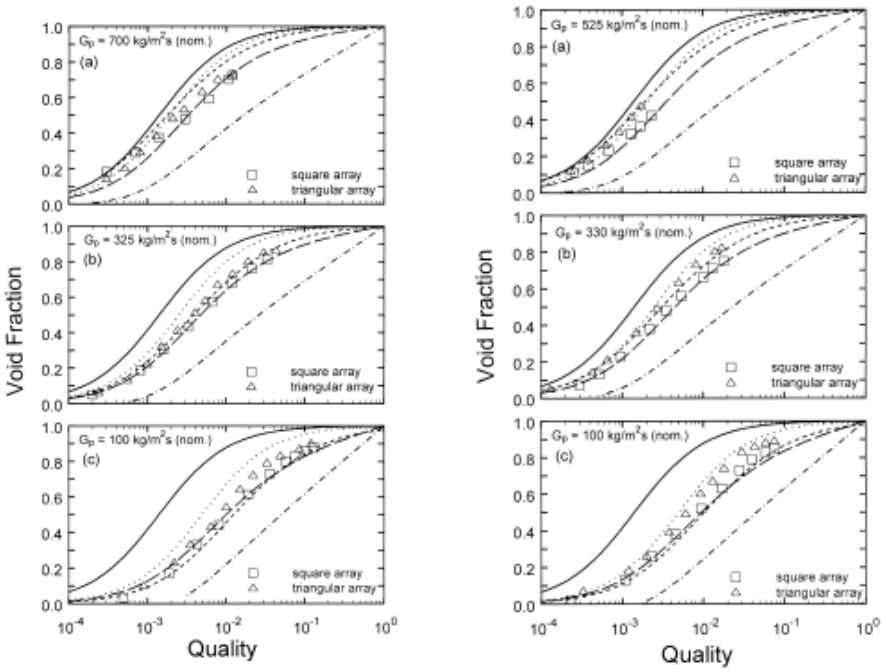

(a) (b)

Figure 2.57: Void fraction vs. quality for (a) air-water of Dowlati et al. (1992) P/D=1.3,(b) air-water Dowlati et al. (1992) P/D=1.75, Feenstra et al. [41]

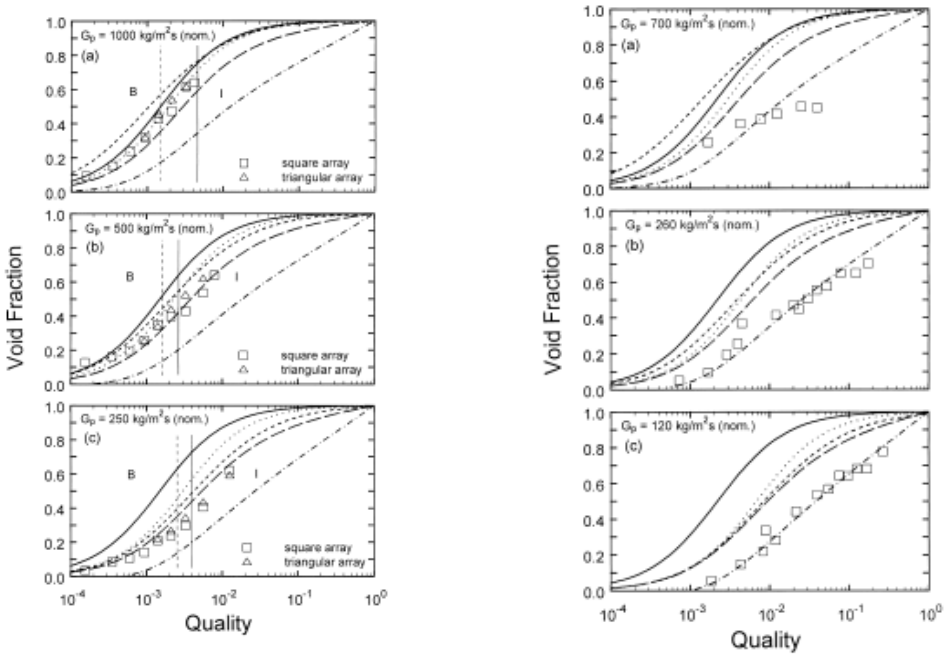

Figure 2.58: Void fraction vs. quality for (a) air-water data of Noghrehkar et al. (1996) P/D=1.47, (b) air-water data of Schrage et al. (1988) P/D=1.3 , Feenstra et al. [41]

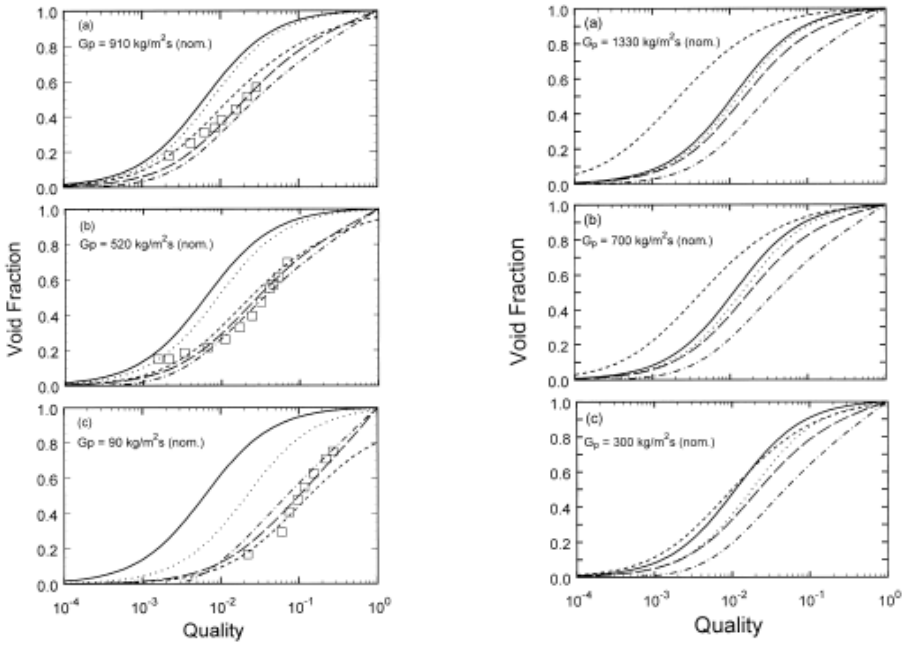

Figure 2.59: Void fraction vs. quality for (a) adiabatic R113 data of Dowlati et al. (1996) P/D=1.3,(b) steam-water data of Axisa et al. (1985) P/D=1.44, Feenstra et al. [41]

Consolini et al. [44] investigated the accuracy of the different void fraction correlations for the tube bundle using the correlations of Schrage et al. [31], Xu et al. [23], Feenstra et. al. [41], and the homogenous model. From these correlations the authors predicted the summation of the static and momentum components of pressure drop with refrigerants R-410a, R-507A and R-507A. These refrigerants were boiled in a tube bundle that contained three kinds of tubes, plain, low-finned and enhanced boiling tubs, Fig. 2.60. It was found that the Feenstra et al. [41] correlation gave the best agreement with the authors' measurements. This finding was attributed to the fact that the Feenstra et al. [41] correlation was developed using different types of data and a more general method to determine the slip ratio's functional dependency.

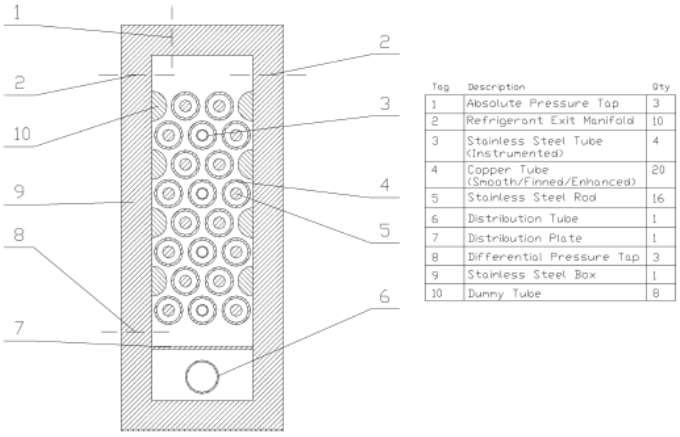

Tag	Description	Qty
1	Absolute Pressure Tap	3
2	Refrigerant Exit Manifold	10
3	Stainless Steel Tube (Instrumented)	4
4	Copper Tube (Smooth/Finned/Enhanced)	20
5	Stainless Steel Rod	16
6	Distribution Tube	1
7	Distribution Plate	1
8	Differential Pressure Tap	3
9	Stainless Steel Box	1
10	Dummy Tube	8

Figure 2.60: The tube bundle test section, Consolini et al. [44]

Taylor et al. [45] compared the available void fraction correlations with their measurements of the void fraction distribution across a tube bundle. Their bundle comprised of 33 stainless steel tubes that were 609 mm long, 12.7 mm in diameter on a 19.05 mm pitch in a triangular layout with a pitch-to-diameter ratio of 1.5, as shown in Fig. 2.61. Void fraction measurements were taken over a wide range of flow rates, using Freon 134a, at three power levels, 50, 200 and 400 kW. The measurements were made with optical probes located at three different locations along the tubes and two locations around their circumference, as shown in Fig. 2.62(a) and (b). Figure 2.63 (a) displays the void fraction distribution along the length of the tube. When the flow rate increased, the measured void fraction values at position 3 in the tube C-1 were lower than those predicted by the models. A nearly constant void fraction was measured at position 2 in the same tube, and the average void fraction measurements at the positions lay between those predicted by the Smith and drift-flux models. The average local void fraction value was over-predicted by the homogenous model and under-predicted by the Schrage

model. A comparison of the void fraction measurements around the tube c-1, between the underside and the side of the tube, cp and sp, respectively, is displayed in Fig. 2.63 (b). At the side of the tube the measured void fractions were greater than those under the tube. Hence, the void fraction around the tubes was radially non-uniform. From Fig. 2.63 (c) it is seen that the void fraction increases from the bottom to the top of the bundle. The authors attribute this effect to either the pressure falling as the flow moves upward across the tube bundle or the bundle tending to holdup the liquid phase as the flow moves up towards the bundle top. It was concluded that the best fit for the authors' measurements of void fraction was given by the drift –flux and Smith models.

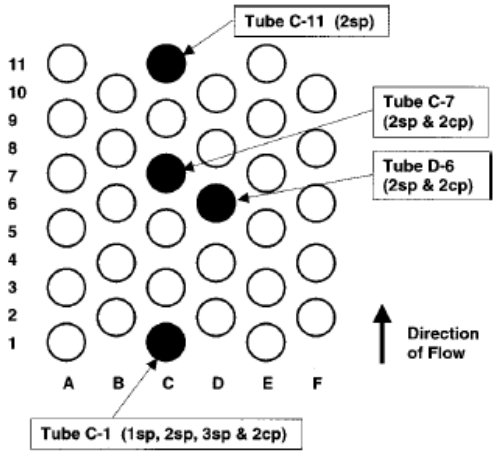

Figure 2.61: The tube bundle with optical probes positions, Taylor et al. [45]

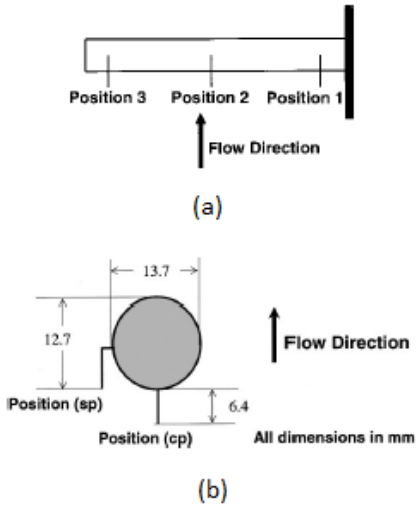

Figure 2.62: Optical probes positions (a) along a tube (b) around tube circumference, Taylor et al. [45]

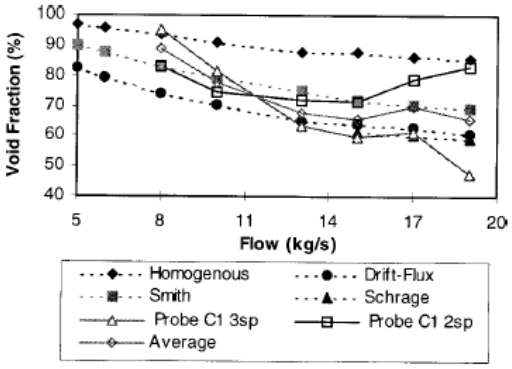

(a)

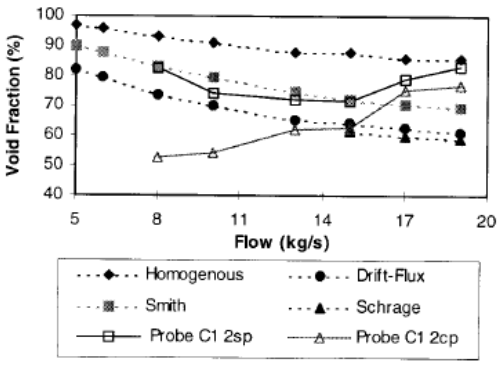

(b)

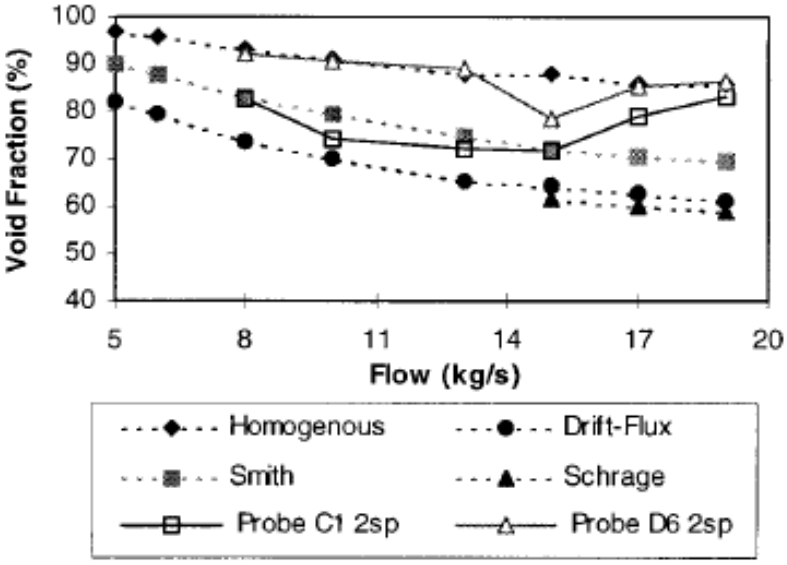

(c)

Figure 2.63: Void fraction distribution (a) along a tube (b) around a tube (c) through the bundle, Taylor et al. [45]

2.4.1 Summary of Void fraction

- In order to make improvements to the design of heat exchangers it is essential to understand the void fraction. This is because the void fraction is needed to find the hydrostatic head and accelerational pressure drop. Additionally, it is required for the average flow density and velocity to be found [41].
- The majority of investigations of void fraction have been made in adiabatic, air-water, two-phase flow in bundles, and therefore the existing correlations do not account for the two-phase problem's complexity. The currently available models are only applicable to certain bundle configurations and working fluids [26].
- The general trend in the void fraction distribution within the kettle reboiler was for it to be low at the base of the bundle and increase significantly vertically. In contrast, only small increases in the void fraction distribution were observed horizontally across the bundle.
- It was found that the effect of the pitch-to-diameter ratio on the void fraction measurements for the in-line tube bundle were not significant.
- The assumption of homogeneous flow is that the gas and liquid phases flow with equal velocities. This is not appropriate for tube bundles. Drift and slip models shown, the flow velocities of the phases to be different [41].
- The void fraction measurements in the bundles are over-predicted by the homogenous flow model because of the large ratio of the gas to liquid velocities that exist in the data.
- The most reliable correlation for predicting the void fraction for flow moving upward across the bundle is thought to be the Feenstra correlation.

2.5 Two-Phase Friction Multiplier

Ishihara et al. [46] reviewed the available correlations for the prediction of the two-phase friction multiplier across both horizontal and vertical flow. They proposed that the two-phase friction multiplier could be modelled using a correlation based on the Martinelli parameter. This correlation was given by Chisholm and Laird [47] as:

$$\emptyset_l^2 = \frac{\Delta P_{2\emptyset}^F}{\Delta P_L^F} = 1 + \frac{C}{X_{tt}} + \frac{1}{X_{tt}} \tag{2.22}$$

where

$$X_{tt}^2 = \left(\frac{1-x}{x}\right)^{2-m} \left(\frac{\rho_g}{\rho_l}\right) \left(\frac{\mu_l}{\mu_g}\right)^m \tag{2.23}$$

$\Delta P_{2\emptyset}^F$ is the two-phase flow friction pressure drop and ΔP_L^F is the liquid phase only friction pressure drop. C=8 and m=0.2 were found to give the best fit to data available from previous studies, as shown in Fig. 2.64.

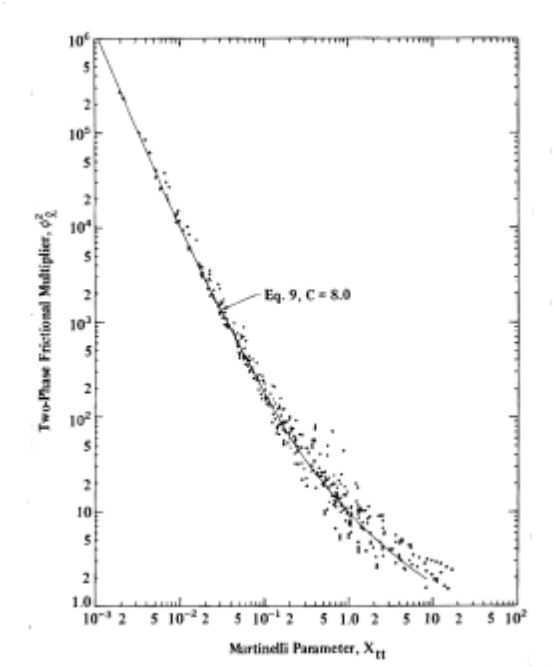

Figure 2.64: The two-phase friction multiplier correlation, Ishihara et al. [46]

Figure 2.64 shows that for $X_{tt} < 0.2$, the proposed correlation predicts the measured data relatively accurately, but that for $X_{tt} > 0.2$, the predicted and actual data values diverge considerably. The cause of this difference was attributed to not taking into account the changing flow pattern when obtaining the constant C.

Schrage et al. [31] determined the friction pressure drop by subtracting from the total pressure drop, the static and momentum pressure drop components, found from the experimental void fraction data. The two-phase friction multiplier they derived is shown in Fig. 2.65 and is strongly affected by the mass flux.

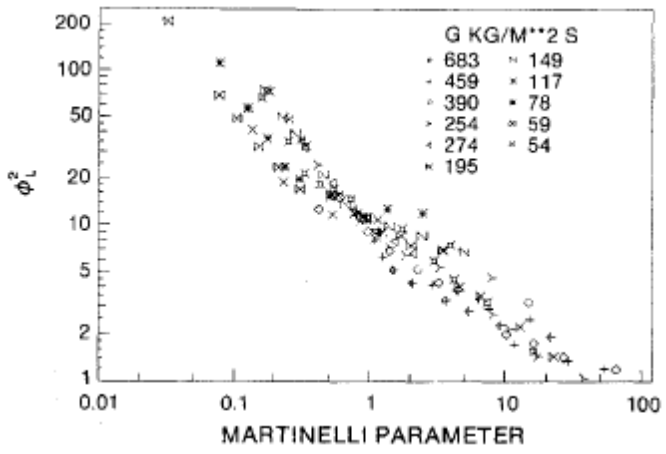

Figure 2.65: Two-phase friction multiplier data, Schrage et al.[31]

For $X_{tt} \leq 0.9$, the values of $\emptyset_l^2$ increased with increasing mass velocity and for $X_{tt} > 0.9$ the converse occurred. A comparison was made between the data and the two-phase friction multiplier correlation of Ishihara et al. [46] with C=8. The authors noted that their data were over predicted, on average, by 17% and they attributed this difference to the change in flow regime. They classified their data using the Grant and Chisholm [19] flow pattern map. It was suggested that correlation (2.24) could be used to fit their data, Fig. 2.66 if the C factor was expressed as:

$$C = (C_1 G^{C_2}) \ln X_{tt} + C_3 G^{C_4} \tag{2.24}$$

To achieve the best fit to their data, the authors suggested that an additional factor (C_5) be incorporated into the Ishihara et al correlation:

$$\emptyset_l^2 = 1 + \frac{C}{X_{tt}} + \frac{C_5}{X_{tt}^2} \tag{2.25}$$

The values of the coefficients C_1 to C_5 depend on the flow regimes and are given in Table 2.3

The authors concluded that the spray and slug flow patterns values should only be used when the value of the mass flux is greater than 43 kg/ m^{2}s. For a mass flux less than 43 kg/m^{2}s, and $\emptyset_l^2 < 1$, the Ishihara et al. [46] correlation should be used.

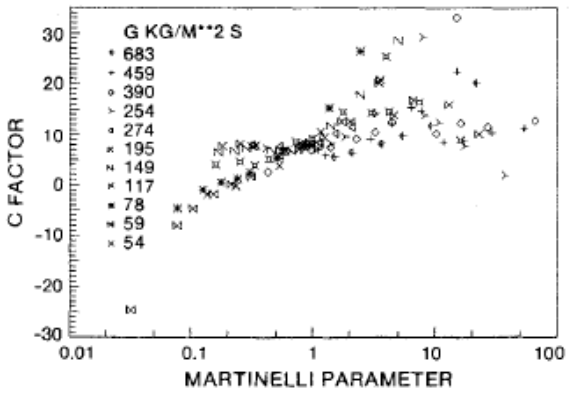

Figure 2.66: C factors reduced using Martinelli-type model, Schrage et al. [31]

Table 2.3: Coefficients in non dimensional two-phase friction multiplier correlation, Schrage et al. [31]

Flow pattern	C_1	C_2	C_3	C_4	C_5
Bubbly	0.036	1.51	7.79	-0.057	0.774
Slug	2.18	-0.643	11.6	0.233	1.09
Spray	0.253	-1.50	12.4	0.207	0.205

Dowlati et al. [48] investigated how the two-phase multiplier was influenced by the pitch-to-diameter ratio (P/D). They studied the two-phase multiplier for adiabatic air-water flows across in line, 5x20 tube bundles with P/D ratios of 1.3 and 1.75. They found that when the bundle had P/D=1.3 and the mass velocity was greater than 260 kg/m^{2}s, the Ishihara et al. [46] correlation with C=8 produced the best fit to their data. For a mass velocity less than 260 kg/m^{2}s a strong mass velocity was seen, Fig. 2.67.

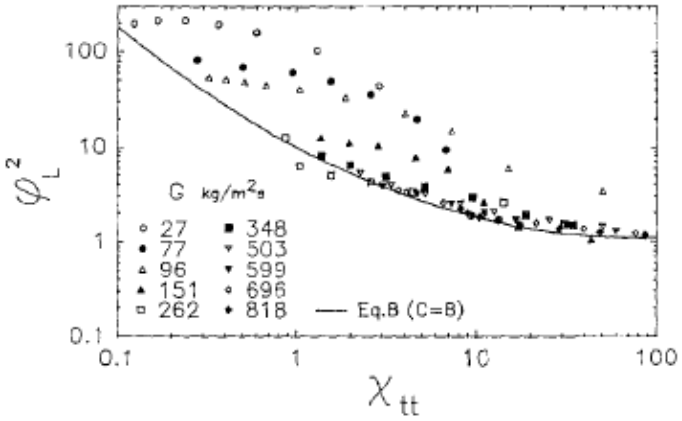

Figure 2.67: Liquid only two-phase friction multiplier data and Martinelli parameter P/D=1.3, Dowlati et al. [48]

For the bundle with P/D=1.75, and a mass velocity greater than 200 kg/m^{2}s, the Ishihara et al. [46] correlation with C=50 produced the best curve fit to their data. However, when the mass velocity was lower than 200 kg/m^{2}s, a strong mass velocity was observed, Fig. 2.68.

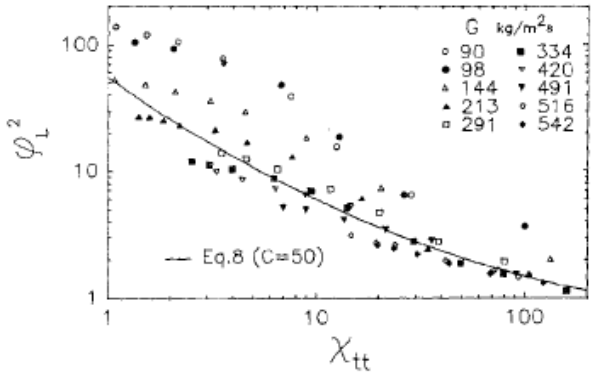

Figure 2.68: Liquid only two-phase friction multiplier data and Martinelli parameter/D=1.75, Dowalti et al. [48]

A comparison between the bundles with P/D=1.3 and 1.75 at a given X_{tt} clearly showed that the two-phase friction multiplier was greater for a larger P/D. With decreasing X_{tt} this effect increased.

The authors also discussed the effect of P/D on the two-phase friction pressure drops as shown in Fig. 2.69. This figure shows the ratio of the large P/D friction pressure drops for the bundle to the smaller P/D value against the Martinelli parameter, X_{tt}, for different Reynolds numbers. For $X_{tt} > 50$, the value of the void fraction (α) is less than 0.2, and the two-phase friction pressure drop for the larger P/D ratio bundle is less than that for the bundle with the smaller P/D ratio. With $\alpha < 0.2$, the flow behaviour is single-phase and the single-phase friction pressure drop is approximately smaller for the larger P/D ratio bundle.

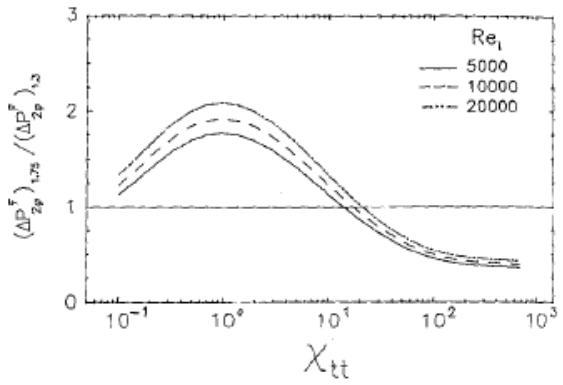

Figure 2.69: Effect of P/D ratio on the two-phase friction multiplier, Dowlati et al. [48]

As X_{tt} decreases below 50 and the value of α increases above 0.2, the value of the two-phase friction pressure drop for the large P/D ratio bundle increases to a maximum at $X_{tt} \approx 1$ and $\alpha \approx 0.8$. The two-phase friction pressure drop for the large P/D ratio bundle is consistently higher until $X_{tt} = 0.05$. With a further decrease in the value of X_{tt} to below 0.05 ($\alpha > 0.8$), the flow changed to the dispersed droplet flow regime and again behaves similar to a single-phase flow.

Dowalti et al. [39] also investigated how the two phase multiplier ($\emptyset_l^2$), was affected by changing the pitch-to-diameter ratio (P/D). They studied the two-phase multiplier for vertical air-water two-phase flow across two staggered tube bundles with P/D=1.3 and 1.75. The data for the two-phase friction multiplier for both bundles were plotted against the Martinelli parameter, shown in Fig. 2.70. The Chisholm and Laird [47] correlation with C=20 was used to obtain the best curve fit two-phase multiplier for both bundles. Figure 2.70 shows that for $G \geq 200$ kg/m^{2}s, both bundles follow the same pattern as the Chisholm and Laird [47] correlation. However, when $G < 200$ kg/m^{2}s, strong mass velocity effects were observed for a range of values of X_{tt}, Outside of this range the data still follow the trend of the Chisholm and Laird [47] correlation.

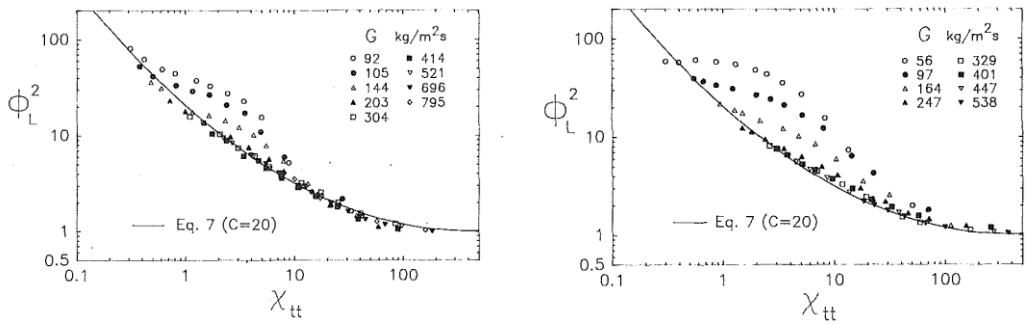

(a) (b)

Figure 2.70: Liquid-only two-phase friction multiplier data and Martinelli parameter for staggered bundle with (a) P/D=1.3 (b) P/D=1.75, Dowalti et al. [39]

The authors used the staggered and an in-line bundle data to investigate how the two-phase friction pressure drop was affected by the bundle geometry. For P/D=1.3, it was found that the two-phase friction pressure drop, within a certain void fraction range, was larger for the staggered bundle than the in-line bundle. The opposite effect was seen for P/D=1.75.

Dowlati et al. [49] also investigated the two-phase friction multiplier for boiling R113 flowing vertically upward across a tube bundle. The tube bundle consisted of 5x20 tubes in a square in-line configuration with P/D=1.3. When the authors plotted the two-phase friction multiplier data against the Martinelli parameter they found that the best fit curve to their data was the Chisholm and Laird [47] correlation with C=8, Fig. 2.71. This figure shows that for G>100 kg/m^{2}s , the data follow the trend of the correlation (Eq. 2.22). For G≤100 kg/m^{2}s, a mass flow velocity effect, exists below the predicted values.

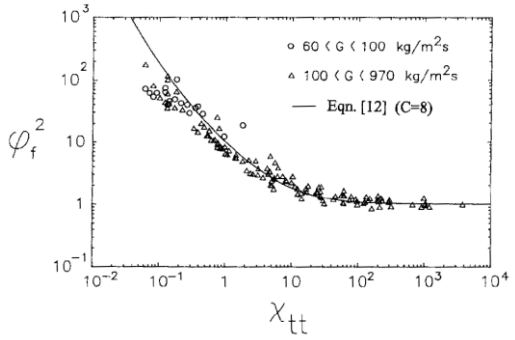

Figure 2.71: Two-phase friction multiplier data and Martinelli parameter, Dowlati et al. [49].

Xu et al. [40] described the results of tests that used adiabatic vertical down and up two-phase flow of air-water mixtures across an in-line, 5x20 tube bundle with P/D=1.28. The two-phase friction multiplier was correlated in terms of the Martinelli parameter, Eq. (2.22), Fig. 2.72. For X_{tt}> 0.2, a strong mass velocity effect was observed and the values of $\emptyset_l^2$ decreased as the mass velocity increased. For X_{tt}< 0.2, however, the mass velocity effect was unclear.

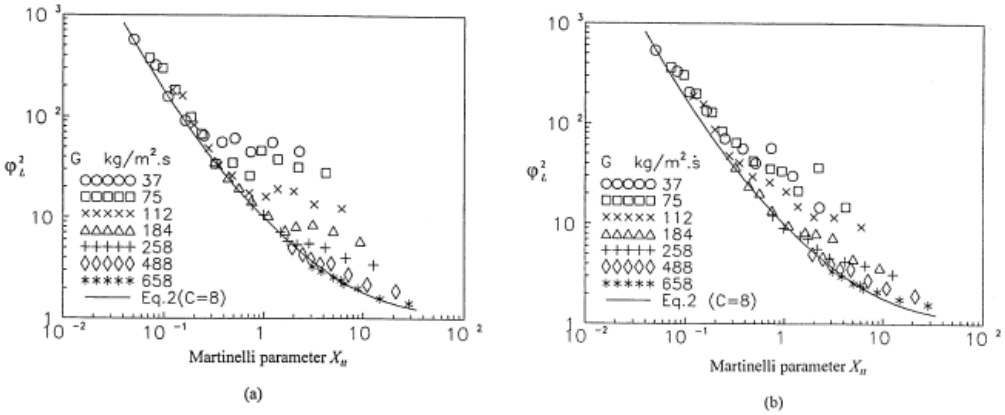

Figure 2.72: Liquid-only two-phase friction multiplier and Martinelli parameter

(b) Vertical down-flow (b) vertical up-flow , Xu et al.[23]

The authors found that they could not obtain a good fit to their data using the Chisholmand Laird [47] correlation with C=8. They suggested using a C factor that is a function of the dimensionless superficial gas velocity, of gas U_{GS} , and $^{x}/_{(1-x)}$

$$C = A\, U_{GS}^{B} \left(\frac{X}{1-X}\right)^{F}$$

For up-flow, A=24.45, B=-0.654 and F= 0.336. For down-flow A=22.5, B=-0.723 and F=0.340.

2.5.1 Summary of two-phase friction multiplier

- The two-phase friction multiplier and void fraction are functions of mass velocity and flow pattern.
- The most reliable correlation for representing the two-phase friction multiplier is the Ishihara et al. [46] correlation.
- For the Ishihara et al. [46] correlation, different values have been suggested for C if the mass flux is less than 260 kg/m^{2}s. Otherwise C=8.
- An in-line tube bundle with a larger P/D ratio has a greater two-phase friction multiplier. However, the effect of the P/D ratio on the two-phase friction multiplier was negligible for staggered bundles.
- For a bundle with a small P/D ratio, the two-phase friction pressure was greater for the staggered bundle than the in-line bundle. The opposite is true for a bundle with a larger P/D ratio.
- Further tests of the flow through the bundle with different fluid types are needed to facilitate the development of more reliable correlations for void fraction and the two-phase friction multiplier.

2.6 Pressure Drop

One of the most important parameters in the successful design of reboilers and condensers in two-phase flow is the pressure drop. The total pressure drop, ΔP_t, across a system consists of three components (a) a pressure differential due to frictional losses, ΔP_f, (b) a pressure differential, ΔP_m, due to the change of momentum, (c) a static pressure difference ΔP_s, due to the density and elevation of the fluid, that is

$$\Delta P_t = \Delta P_f + \Delta P_m + \Delta P_s \tag{2.26}$$

In order to analyse any two-phase heat exchanger, these components need to be known. Evaluation of the fractional pressure drop needs the two-phase frictional multiplier to be identified while the gravitational and acceleration pressure drops requires the void fraction to be known. The details of void fraction and the two-phase multiplier have been discussed in previous section. The total pressure drop models and correlation used by different researchers is discussed in the following.

Gas–liquid, two-phase (air-water) pressure drops across two horizontal tube banks was measured by Diehl [50]. The tube bundles had 2x16 tubes arranged in a 45-degree staggered bundle configuration tubes with D=19.05 mm and P/D =1.33 and 5x17 tubes arranged in an in-line layout with D=12.7 mm and P/D =1.25.

The effect of pressure drop was investigated by introducing the ratio of the vapour to liquid densities and void fraction as a parameter, i.e:

$$\frac{\Delta P_t}{\Delta P_G} = f\left(\alpha_H \Big/ \left(\frac{\rho_g}{\rho_l}\right)(\mathrm{Re}_G)^n\right) \tag{2.27}$$

The obtained data was plotted on a log-log diagram as shown in Figs. 2.73 and 2.74. The index n was found through non-linear regression analysis to be 0.5 for the staggered bundle and 0.2 for the inline bundle. The effect of liquid viscosity on the two-phase pressure drop across the staggered and inline tube bundles was discussed. Figure 2.73 indicates no effect on the two-phase pressure drop for the liquid viscosity range of 0.2 to 3 centipoises. However, as the viscosity of the liquid increases further the data lie on a curve with a steeper slop and so two distinct curves were developed for the staggered tube bundle, as shown in Fig. 2.75. In the case of the in-line tube bundle, just one curve

was proposed because the experiments were carried out solely with air-water mixtures, Fig. 2.74. The authors concluded that their correlation was valid for all of the data to within a maximum deviation ±35%, with 90 percent of the data falling within a deviation of ± 20%.The average deviation was 10 %.

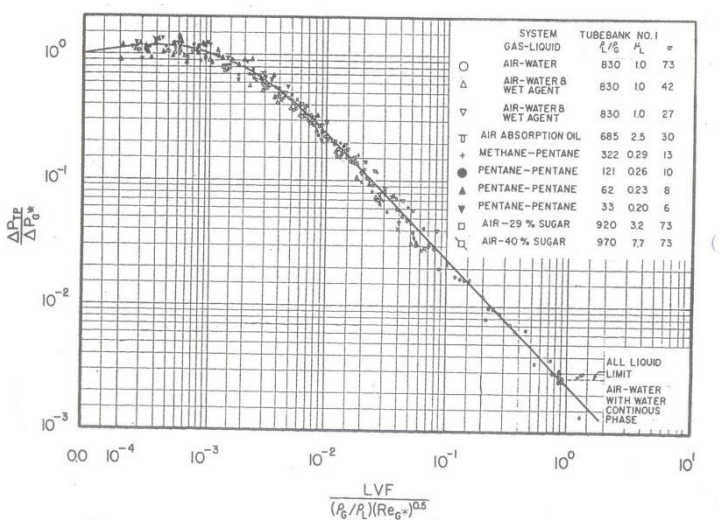

Figure 2.73: Correlation of two-phase pressure drop for turbulent down-flow through a bank staggered tube, Diehl [50].

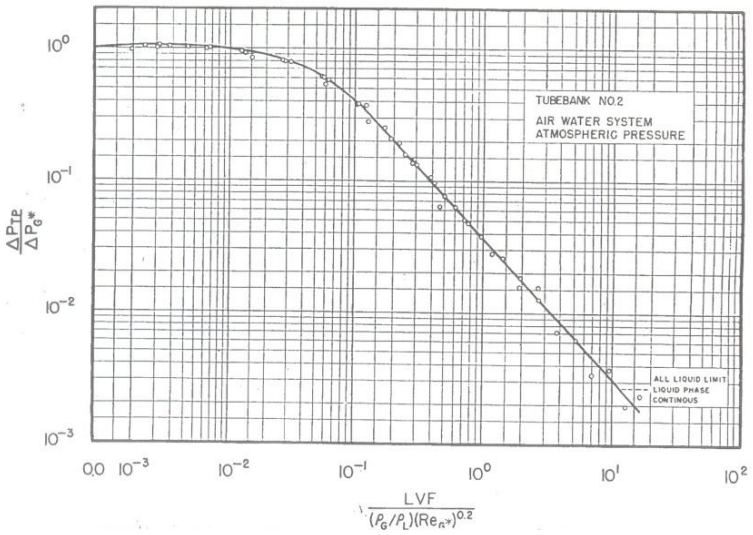

Figure 2.74: Correlation for two-phase pressure drop for turbulent down-flow through a bank of inline tubes, Diehl [50].

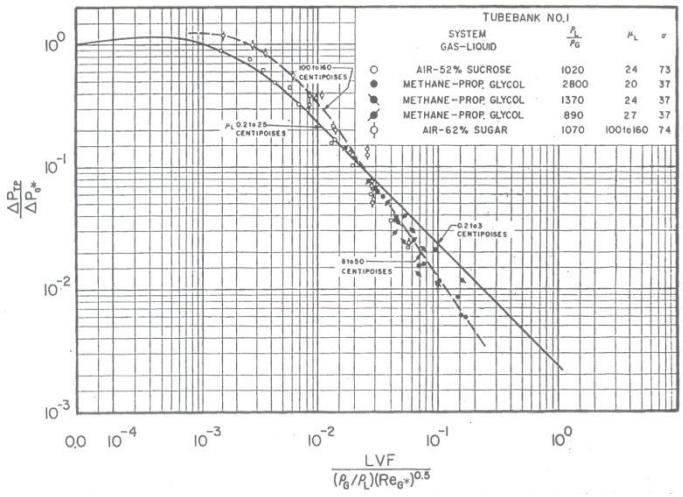

Figure 2.75: Effect of high liquid viscosity on two-phase pressure drop for down-flow through a bank of staggered tubes, Diehl [50]

The pressure drop data for the R113 experiments of Hsu and Jensen [51] have been investigated by Schrage et al. [31]. The predicted pressure drop data was calculated using the Martinelli parameter with m=0.2 in Eq. (2.25). The constants in the equations, C and C_5, were dependent on the type of pattern, determined from the Grant and Chisholm flow map. Table 2.3 shows the values of constants and ranges of applicability. The single phase fraction factor was calculated using a Blasius type correlation.

$$f = 35\,\mathrm{Re}^{-0.674} \quad \text{for } 1250<\mathrm{Re}<7000 \tag{2.28}$$

$$f = 35\,\mathrm{Re}^{-.191} \quad \text{for } 7000<\mathrm{Re}<20600 \tag{2.29}$$

The average absolute deviation between the prediction and the experimental data was 9.8%. The average ratio of predicted to experimental total pressured drop was 0.99, with reasonable agreement for x < 0.1, as shown in Fig. 2.76. The authors noted that the shift in mass velocity when x > 0.1 was due to the map flow used, which did not, in general, predict the flow pattern for R113 since it was originally developed for air-water flows.

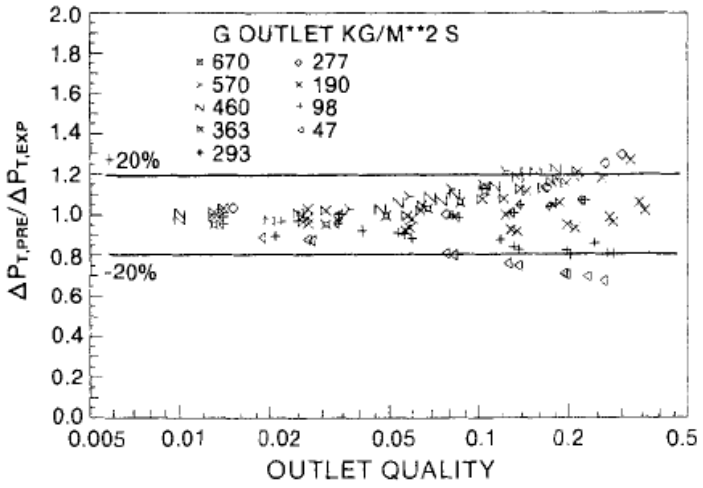

Figure 2.76: Predicted and experimental R-113 adiabatic total pressure drop data, Schrage et al. [31].

Dowalti et al. [48] analysed the two phase pressure drop data of Hsu [52] in order to test the validity of the equations for the friction multiplier (Eq. 2.22) and void fraction (Eq. 2.12). The test conditions of Hsu [52] were an in-line 5x27 tube bundle with 7.94 mm OD tubes and P/D=1.3; R113 was used as the working fluid and the ranges of pressure and mass velocities were 200-500 kPa, and 50-700 kg/m^2 s, respectively. The value of C = 8 for G $\geq$ 260 kg/m^{2}s, C = 35 for 260 > G > 90 kg/m^{2}s and C = 70 for G < 90 kg/m^{2}s were used in two-phase multiplier equation 2.22.

To calculate the accelerational pressure drop, ΔP_{acc}, Eqs (2.30-2.31) were used based a large variation in quality across the bundle occurred. The separated flow model gives.

$$\Delta P_{acc} = G^2 (v_2' - v_1') \tag{2.30}$$

where

$$v' = \frac{(1-x)^2}{(1-\alpha)\rho_l} + \frac{x^2}{\alpha \rho_g} \tag{2.31}$$

and G was based on the minimum flow area. The void fraction was evaluated from Eq. (2.12).

Figure 2.77 shows the ratio of the experimental overall pressure drop Hsu [52] to the predicted pressure drop against the average quality between the two elevations considered. The authors reported that 90% of the predicted values were within ±20% of the measurements.

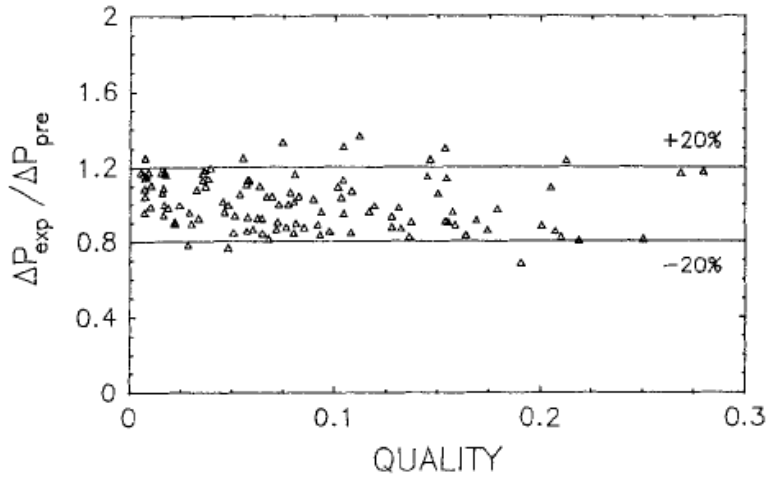

Figure 2.77: Prediction of overall pressure drop data obtained by Hsu [52] In Freon boiling experiments, Dowalti et al. [48]

Dowalti et al. [39] also compared their predicted pressure drop for flow of R113 across a staggered tube bundle with P/D=1.3, with the experimental overall pressure drop of Reinke [53], Fig. 2.78.

In this case, C=15 for G≥ 200 kg/m^{2}s and C=20 for G≤ 200 kg/m^{2}s is used in Eq. (2.22) for ϕ_l^2. To calculate X_{tt}, the value of m in Eq. (2.23), was derived from single phase friction factor data, as given by Reinke, which is in good agreement with Zukauskas [54]. The authors noted that their correlations were successful in predicting 90% of the data to within ± 20%. Even though the present correlations were derived from experiments performed with air-water two-phase flows at near atmospheric pressures, Fig. 2.78 shows that correlations work reasonably well for predicting the total pressure drop for R113 with a slight modification in the C- values of Eq. (2.22) at elevated pressures.

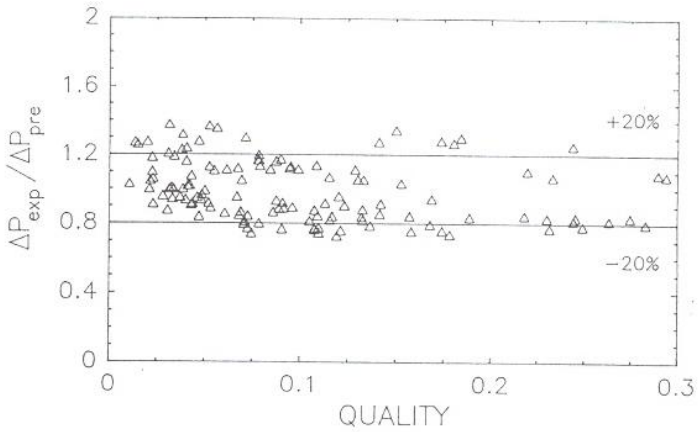

Figure 2.78: Prediction of overall pressure drop obtained by Reinke [53] in R-113 boiling experiments, Dowalti et al.[41]

Dowalti et al. [33] developed a correlation from their pressure drop data from a square in-line tube bundle with 12.7 mm diameter tubes and P/D=1.3 to flow boiling R113 in vertically upward flow. They compared the obtained correlations with Hsu's data. In this case C=8 was used in the two-phase friction multiplier equation (2.22) and m = 0.2 in the Martinel parameter equation (2.23). The single-phase friction factor for two different flow ranges was observed from the following Blasius type correlations:

$$f = 0.811\mathrm{Re}^{-.087} \quad \text{for} \quad 3500<\mathrm{Re}<2\mathrm{x}10^{4} \tag{2.32}$$

$$f = 21.4\mathrm{Re}^{-.513} \quad \text{for} \quad 700<\mathrm{Re}<3500 \tag{2.33}$$

The local void fraction was determined from Eq. (2.12) with the constants C_1=10 and C_2=1. The accelerational pressure drop term was calculated using the separated flow model. Figure 2.79 indicates the ratio the experimental overall pressure drop from Hsu's data to the predicted pressure drop from the Dowalti et al. correlation plotted against the average quality between the two elevations considered. The authors noted that the correlations predicted about 90% of the data points to within ±20%.

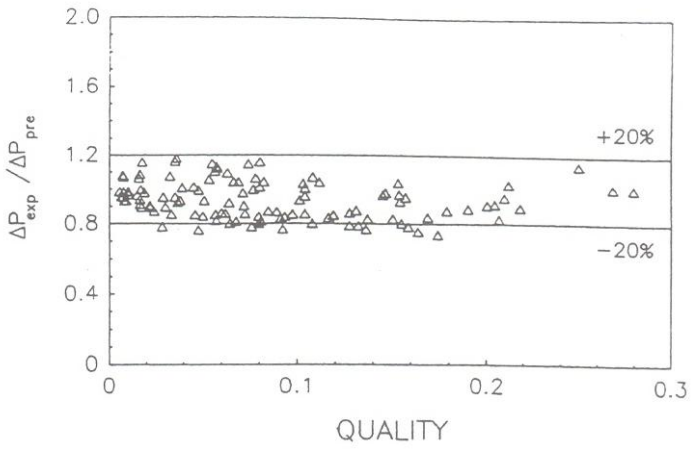

Figure 2.79: Prediction of overall pressure drop data obtained by Hsu [52], Dowalti et al. [33]

The pressure distribution across the tube bundle of a kettle boiler for heat fluxes of 10, 30, 50 and 70 kW/m^2 was measured by Gebbie and Jensen [34] and their respective data for these heat fluxes are shown in Fig. 2.80 (a),(b),(c) and (d). At all heat fluxes there is a decrease in pressure variation as the row number increases from the tube bundle's bottom to top. This pattern was attributed to the movement of flow in the same direction. The pressure value for row 4.5 and column 6.5 exceeds that at row 4.5 and column 1.5 for all heat fluxes, Fig 2.80, while the pressure value at row 9.5 and column 1.5 is higher than at row 9.5 and column 6.5, Fig 2.80. This pattern of values suggests that flow recirculation in the kettle boiler is counter-clockwise. Figure 2.80 (c) shows the pressure variation at 50 kW/m^2, where there is an increase in pressure two regions along column 6.5. Region one was between rows 2.5 and 4.5 and region two between rows 9.5 and 13.5. The authors did not consider the pressure increase in the first region to be consistent with the direction of flow in the bundle, which was in contrast to the second region where the rise in pressure was consistent. There was not a significant change in the pressure variation from 50 to 70 kW.m^2, Fig. 2.80 (d).

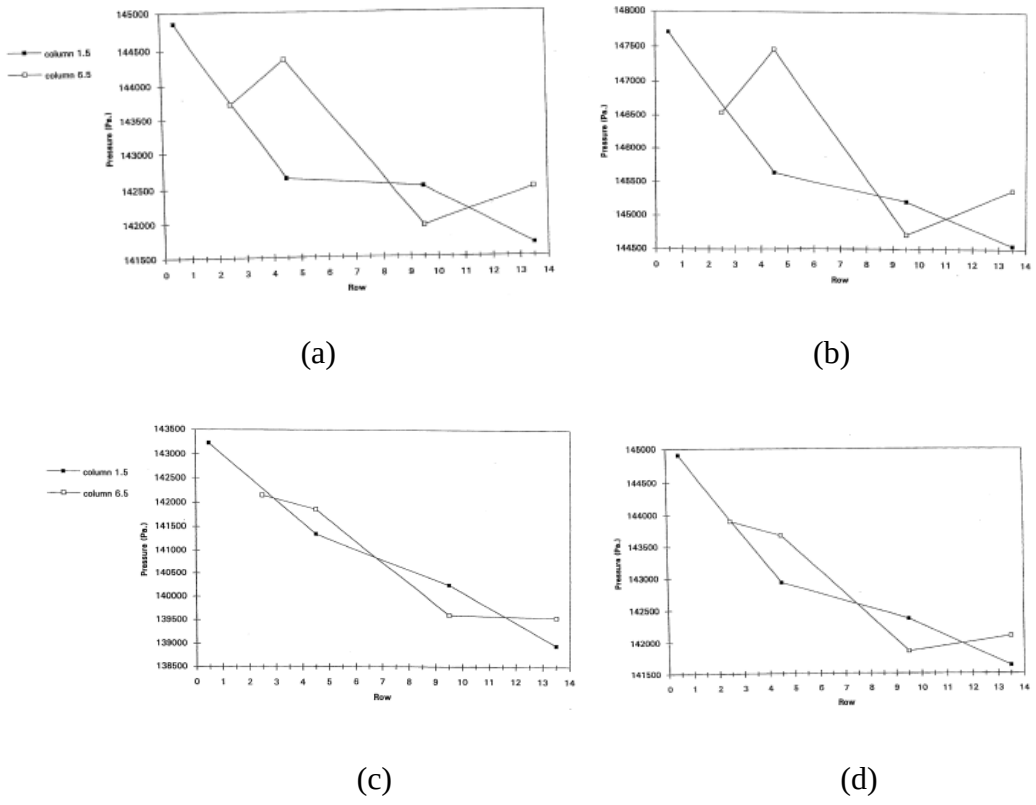

Figure 2.80: The tube bundle pressure variation at (a) 10 kW/m^2 (b) 30 kW/m^2 (c) 50 kW/m^2 (d) 70 kW/m^2, Gebbie and Jensen [34]

The overall drop in pressure across the tube bundle between the lower and upper tap along column 1.5 is shown in Fig. 2.81. The pressure drop decreases with increasing heat flux. This trend was claimed to be the result of the increasing void fraction value in the shell causing the hydrostatic pressure to decrease.

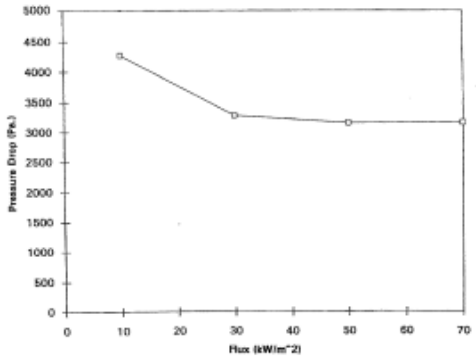

Figure 2.81: Average cross bundle pressure drop, Gebbie and Jensen [34]

Shire [6] studied the pressure distribution for the flow of boiling R113 at 1.01 bar in a kettle reboiler containing 241 tubes with a diameter of 19.05 mm. The arrangement of the tubes was 17 rows and 17 columns on in-line layout with a square pitch of 25.4 mm, Fig. 2.82. All pressure drops were measured relative to the bottom tapping in the central column, with the pressure drop value calculated by subtracting the reading for the adjacent tapping. Measurements of the pressure drop were taken between the tapping for the bundle's central column at heat fluxes of 10, 20, 25, 40 and 50 kW/m^2. The static head pressure drop was 751 Pa.

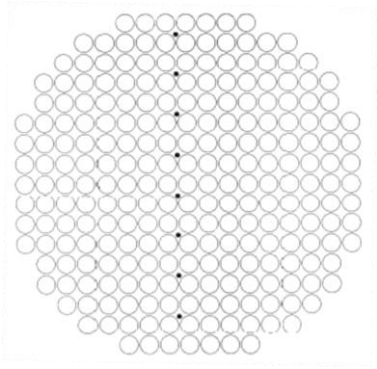

Figure 2.82: Kettle reboiler with pressure tapping positions used by Shire [6]

At heat fluxes of 5 and 10 kW/m^2, shown in Fig. 2.83 (a) and (b) respectively, there was little variation in the pressure drop along the central column and it remained almost constant at the static head value. It was claimed that this was due to a reduction in the gravitational pressure drop cancelling with the increasing friction pressure drop. At 20 kW/m^2, Fig. 2.83 (c), the pressure drop slowly decreased until row 10 then fell rapidly. With heat fluxes increasing above 20 kW/m^2 a significant decrease in the pressure drop along the central column was seen, Fig. 2.83(d-f).

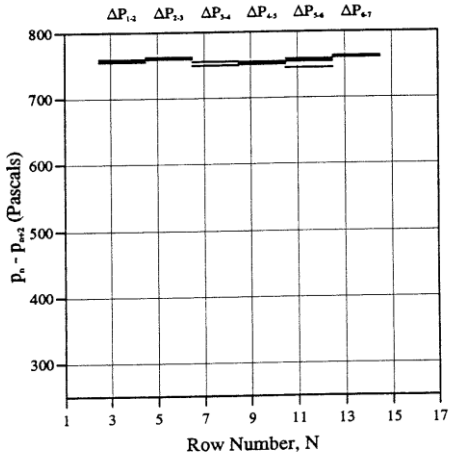

(a)

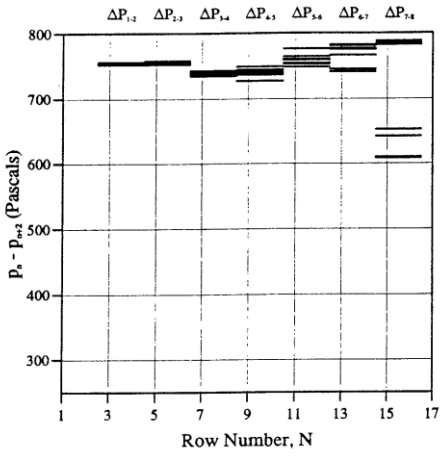

(b)

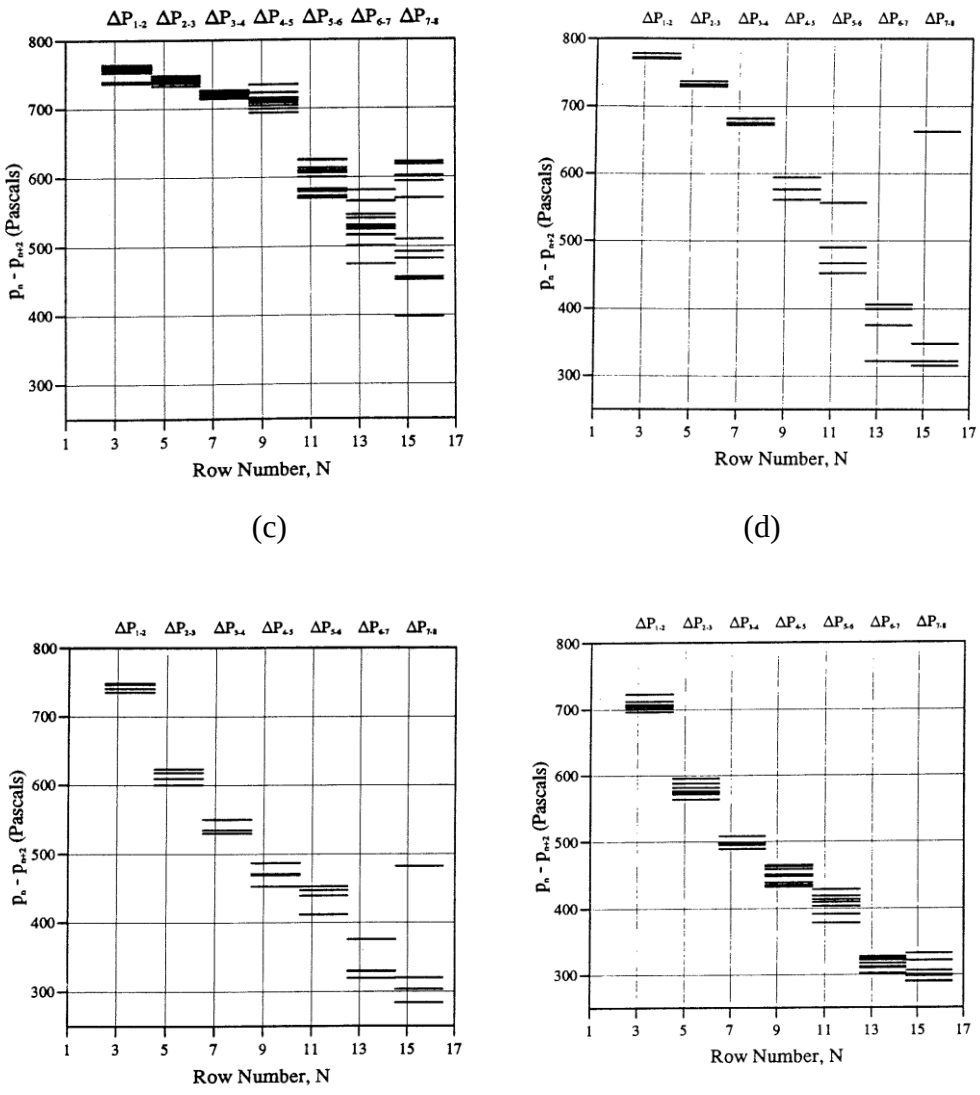

Figure 2.83: Variation of pressure drop across Adjacent Pressure Tappings at (a) 5 kW/m^2 (b) 10 kW/m^2 (c) 20 kW/m^2 (d) 25 kW/m^2 (e) 40 kW/m^2 (f) 50 kW/m^2 [6]

Shire and Burnside [55] measured the pressure drop in a flow of boiling R113 using the same kettle reboiler as in the previous investigation [6]. However, in this investigation, the boiler was modified by adding two brass walls. This limited the flow to upward movement through a vertical column layout that consisted of 5 columns with 17 rows, Fig. 2.84. The pressure drop was recorded heat fluxes of 5, 10, 20, 40 and 50 kW/m^2 and a mass velocity range of $200 \leq G \leq 700$ kg/m^{2}s. A comparison was made between the pressure drop values obtained and those predicted by the correlations given by Dowalti et al. [49], Dowalti et al. [49] (a drift flux model), Schrage et al. [31] and modified Schrage et al. [31]. Dowalti et al. [49], used Eq. (2.12) with C_1=10 and C_2=1,

and Dowalti et al. [49], used Eq. (2.10) with C_0=1.076 and $\bar{V}_{gi} = 0.85$. Schrage et al. [31] used Eq. (2.25). This comparison is displayed in Fig. 2.85. The pressure drops obtained from the correlations over predicted those measured by Shire, and a best fit was obtained with the Dowalti et al. [49](drift flux model).

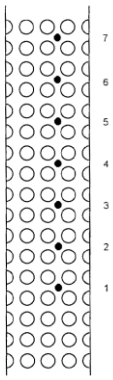

Figure 2.84: Vertical column rig with pressure tapping positions used Shire and Burnside. [55]

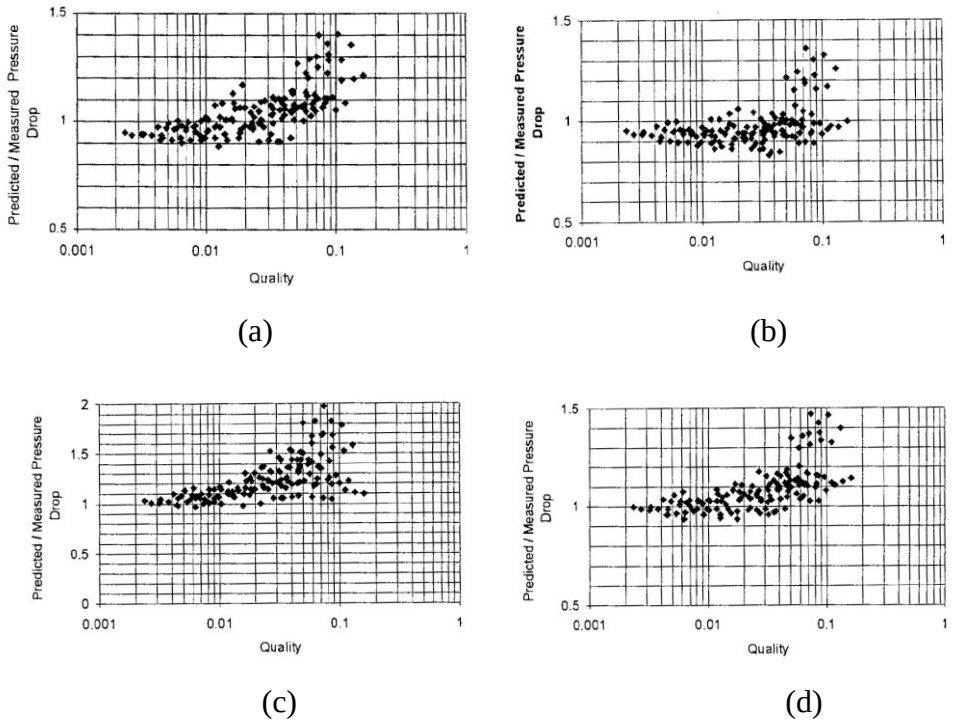

Figure 2.85: Comparison of measured pressure drop with (a) Dowalti et al. [49] (b) Dowalti model (Drift model flux) [49] (c) Schrage et al. [31] model (d) Modified Schrage et al. [31] model

The pressure drop for boiling pentane was measured by Burnside et al. [56] in the same kettle reboiler used by Shire [6]. A modification was made to the shape of the vapour outlet from the shell: it was changed from a hole with a diameter of 100mm to an elongated hole with a 290 cm^2 cross-section. This provided a vapour outlet with an area four times greater than that of Shire [6] and was done in order to improve disengagement. All the pressure drops were measured relative to the bottom tapping in the centre column and the pressure drops were found by subtracting the readings form adjacent tappings. Pressure drop measurements were made between two adjacent tapps at heat fluxes of 10, 20, 30 and 40 kW/m^2. The tapping locations within the kettle reboiler are shown in Fig. 2.86 and the pressure drop measurements in columns 9, 12, 15 and shell for all heat fluxes are given in Fig. 2.87. At 10 and 20 kW/m^2, the pressure drops measurements remained nearly constant and equal to the static head pressure drop (304 Pa) from the column bottom to the top of the bundle. For heat fluxes greater than 20 kW/m^2, there was a decrease in the pressure drop with increasing height towards the top of the bundle. No significant differences were found between the measured pressure drops and static liquid head for column 15 at any of the heat fluxes used. This was attributed to the decrease in the gravitational pressure drop, as the void fraction increases towards the top of the bundle, being balanced by the increase in the frictional pressure drop. A comparison was made between the measured pressure drops and those reported by Gebbie and Jensen [34] at 30 kW/m^2. The authors noted that for Gebbie and Jensen's middle central column (row 6), the pressure drop was about 33 % of the liquid head of R113 over the same height. However, in their study in the middle column (row 10), Fig. 2.87 (a), the pressure drop was approximately equal to the liquid head of the pentane. This was attributed to a greater exit of vapour from the authors' reboiler . The pressure drop was roughly equal to the static liquid head for both studies in the outside column. The authors concluded that pressure drop and recirculation flow pattern in the kettle reboiler were affected by the shape of the shell's vapour outlet.

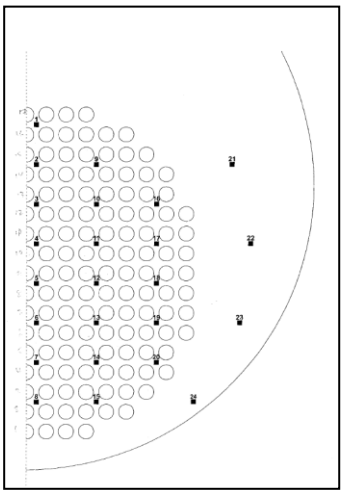

Figure 2.86: Kettle reboiler with pressure tappings positions used by Burnside et al. [56]

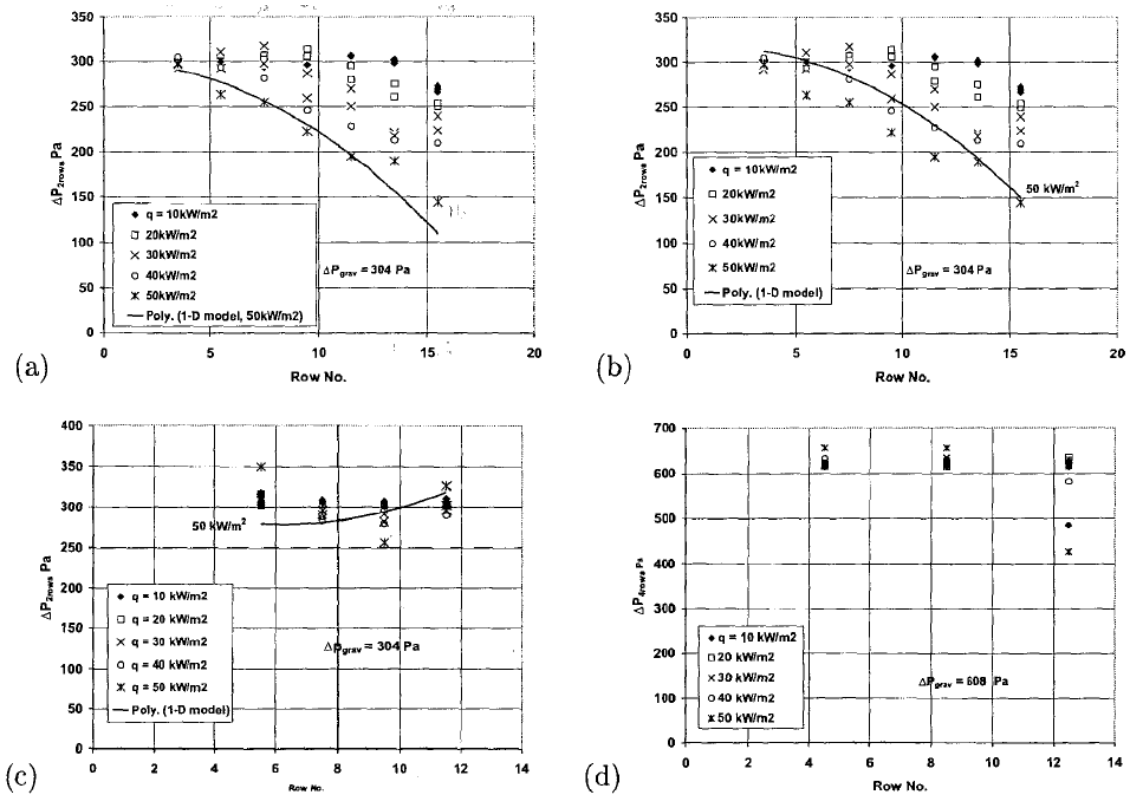

Figure 2.87: The tube bundle pressure drop distribution at (a) column 9 (b) column 12 (c) column 15 (d) shell. The 1-D model prediction at 50 kW/m^2 was also plotted.

2.6.1 Summary of pressure drop

- In order to develop equations that describe boiling more accurately there is a need to accurately calculate the pressure variation in the upward flow over the tube bundle.
- At a higher heat flux, the pressure drop is smaller in the in-line bundle relative to a staggered layout bundle. At lower heat fluxes the converse occurs.
- For heat fluxes lower than 20 kW/m^2, the pressure drop measurements in a kettle are nearly constant and equal to the static liquid head from the bottom to the top of the bundle. At higher heat fluxes the pressure drop decreases with increasing height towards the top of the bundle.
- A reduction in pressure drop with the vertical position in the tube bundle indicates that the direction of upward flow movement through the bundle is changing from one-dimensional to two-dimensional.

2.7 Numerical studies

2.7.1 One-dimensional model

A number of researchers have incorporated a simple 1-D model of liquid circulation in the kettle boiler into its design [57, 56, 28, 4, 8]. The flow through the bundle is assumed to be uniform and circulate in such as way that it enters the base of the bundle and flows upwards towards the top. When the flow reaches the free surface there is a separation of the vapour from the liquid with the latter flowing back to the bundle's base. This is illustrated in Fig. 2.88.

To calculate the flow rate of the re-circulating liquid in the kettle reboilers it is assumed that there are three components of the two-phase pressure drop that occurs inside the tube bundle: frictional, accelerational and gravitational. These components sum to a value that is equal to the hydrostatic head of the liquid outside the bundle. The shell side frictional and acceleration pressure drops are taken to be negligible. The fountain effect at the free surface, that results from a high flow velocity, is also neglected in the analysis because the movement of the flow towards the shell is at a sharp angle [57].

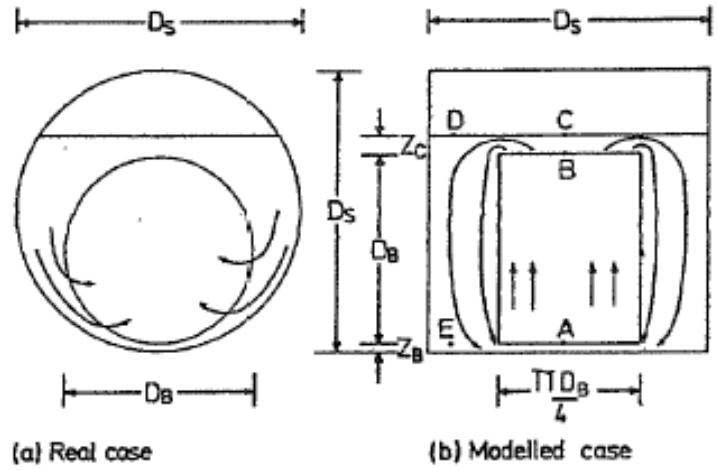

Figure 2.88: 1-D simple model for a kettle reboiler, Brisbane et al. [57]

Jensen [28] modified the 1-D model by accounting for the impact of the frictional and accelerational pressure drop in the shell side. The behaviour of the re-circulating flow in the reboiler was observed to vary with the applied heat flux and weir height, Fig. 2.89. It was noted that the re-circulating flow rate increased with increasing heat flux up to a maximum then decreased. For a lower heat flux in the bundle, a low quality level and dominant hydrostatic head were observed. With increasing heat flux the flow rate rose

as a result of the hydrostatic head decreasing more rapidly than the increase in the frictional pressure drop. However, the frictional pressure drop becomes dominant at higher heat fluxes. With further increases in heat flux the flow rate decreased due to the rapidly rising frictional and acccelerational pressure drop. The effect of weir height was insignificant at low heat fluxes as a result of the liquid hydrostatic pressure being dominant. At higher heat fluxes as the weir height increases the re-circulating flow rate increases. An additional observation was that the effects of the frictional and acceleration pressure drop in the shell side were negligible.

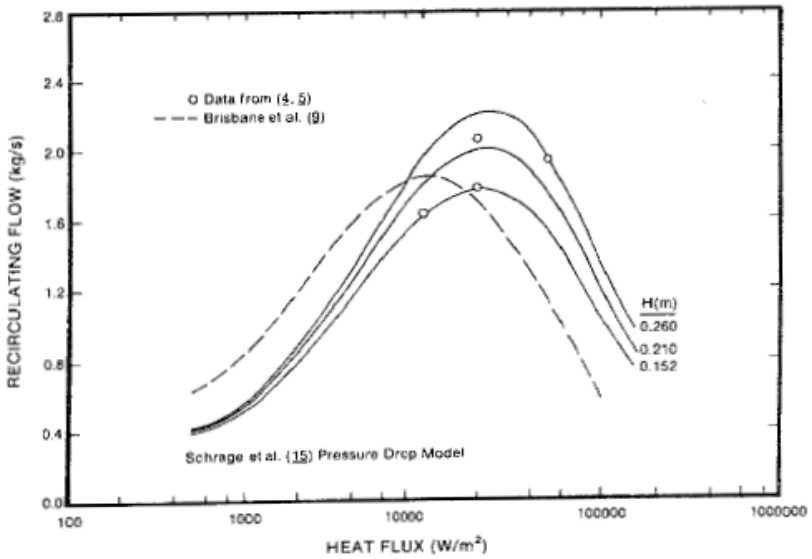

Figure 2.89: Effect of weir height and heat flux on the recirculating flow rate, Jensen [28].

Jensen compared his modified 1-D model with those previously constructed, Fig. 2.90. Comparing the Jensen model to that of Brisbane et al. [57] revealed that both have similar characteristics, Fig. 2.90.

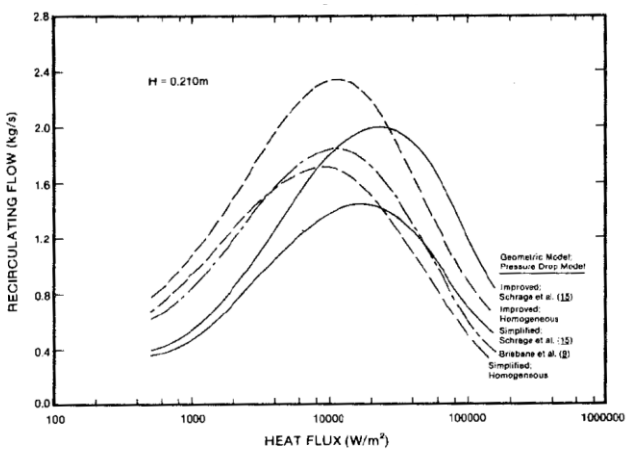

Figure 2.90: Comparison of various circulation models with Jensen model, Jensen [28]

In both models the recirculation flow rate increases with increasing heat flux to a maximum then decreases with further increases in heat flux. A peak of recirculation rate is predicted by both models, but is higher in the Jensen model [28], and the heat flux corresponding to this maxima is also greater.

Models for the design and analysis of the circulation rate and heat transfer in kettle reboilers have been put forward by Kumar et al. [4]. In the authors' proposed model, liquid is assumed to enter the bundle through the base and sides and flow vertically, Fig. 2.91.

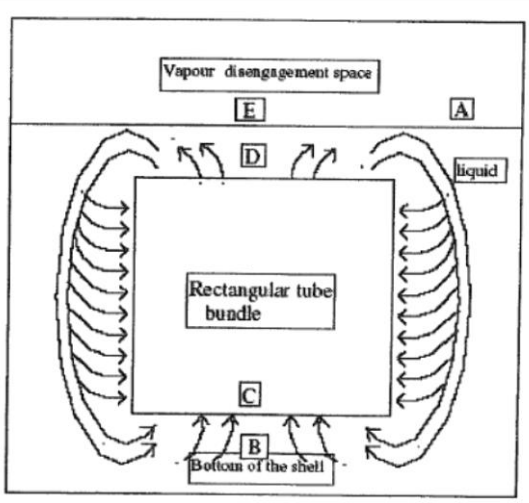

Figure 2.91: Schematic view of reboiler with assumed rectangular tube bundle, Kumar et al. [4]

The unreliable assumption of homogeneous flow for the two-phase mixture of liquid and vapour in the bundle was considered for the model.

2.7.2 1.5-D model

The previously described 1-D model was used by Burnside et al. [16] to predict the pressure drops of boiling pentane at atmospheric pressure in a 241 tube bundle kettle reboiler at heat fluxes of 10, 20, 30, 40 and 50 kW/m^2. The authors found that the measured pressure drop values were only predicted correctly by the model at low heat fluxes; the model was unable to make the correct predictions at higher heat fluxes. This was indicated by the decrease in pressure drop with row height, Fig. 2.92, and was due to the bundle's top rows having a greater lateral flow.

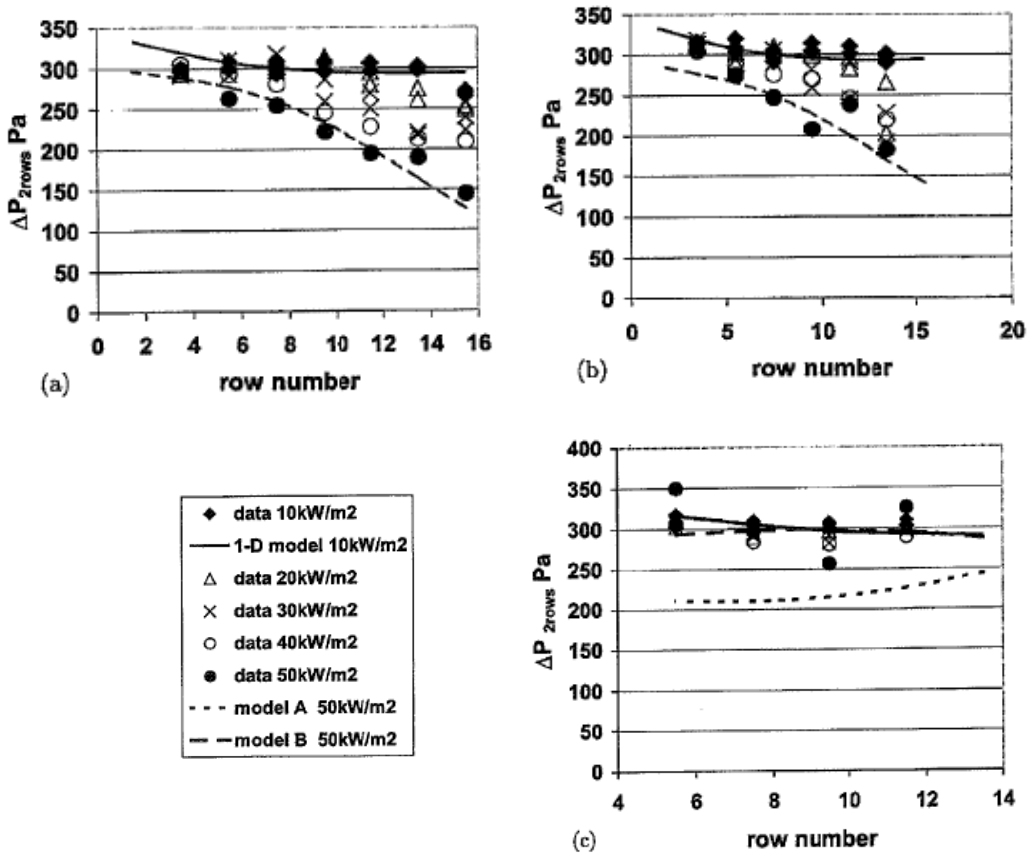

Figure 2.92: Two-phase pressure drop data for different models. (a) column 9, (b) column 12, (c) column 15 , Burnside et al. [16].

To predict the pressure drop values at higher heat fluxes, a 1.5-D model was constructed that took account of lateral flow. The vertical mass flux was decreased linearly along the channel from a row at which the lateral flow started (identified from video) until it reached a value of zero one pitch above the top of the bundle. The pressure drop and void fraction were calculated according to the mass flux. This model did not consider the lateral pressure forces which led to its designation as 1.5-D. To calculate the mass flux the static head pressure in the shell was balanced with the two-phase pressure in the bundle. The shell's static head pressure (foam in that region) was smaller than the static pressure for pure liquid. The 1.5-D model's predicted pressure drop values were compared to the measured data at 50 kW/m^2 for columns 9, 12 and 15. There was good agreement between the predicted and measured values for columns 9 and 12, Fig. 2.92 (Model A), but not for column 15. To obtain a good agreement for the latter column the vertical mass was altered accordingly (Model B).

2.7.3 One-fluid model

A one-fluid, or algebraic slip, model was used by McNeil et al. [5] to simulate two-phase flow in the kettle reboiler. The model was used to predict the pressure drops and mass flux of boiling R113 and n-pentane, over varying heat fluxes, at atmospheric pressure in the kettle reboiler of McNeil et al. [5]. Figure 2.93 shows that the bundle's shape was taken to be octagonal. The model used a static liquid boundary condition for the bubbly flow regime, but for the intermittent flow regime the flow pattern change determined the boundary pressure, and this was deduced from the critical Kutateladze number. The correlations developed by many investigators for void fraction and the force on the fluid from the tubes form the basis of this model. It was found that the predicted pressure distribution was compatible with the measured results of McNeil et al. [5]; however, at higher heat fluxes, or other bundle configurations, the predicted and measured data did not agree very well. The authors also made a comparison between their predicted vertical mass flux and the prediction made by the one-dimensional model. They found that both models gave similar results before the change in flow pattern. In contrast, the one-dimensional model significantly over-predicted the values after the flow pattern changes. Consequently the authors recommended that a two-fluid model be constructed in order to surmount the difficulties of analysing two-phase flow in the kettle reboiler.

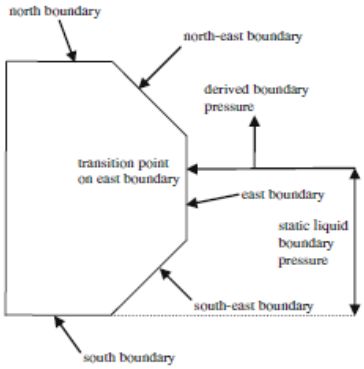

Figure 2.93: Boundary conditions used in the simulation of the kettle reboiler, McNeil et al. [5]

2.7.4 Two-dimensional model

An algebraic slip model and two-fluid model have been used to analyse two-phase flow in the kettle reboiler. For the algebraic slip model it was assumed that liquid and vapour

move in the same direction at different speeds. By contrast, the two-fluid model assumes that the directions of movement differ. The two-phase flow has been taken to be homogenous, by Carlucci et al. [59], or separated, by Edwards and Jensen [60]. From observation of the flow within the kettle reboiler in experiments, Burnside et al. [8] recommended that kettle reboiler simulations should use separated flow models with the appropriate void fraction correlation.

The separated algebraic slip model was used by Burnside [8] to simulate the experimental kettle reboiler used by Shire [6]. The bundle's shape was taken to be rectangular and comprised of 17 tubes rows and 9 tubes columns with a square pitch configuration of 19 mm diameter tubes and 1.33 pitch diameter ratio placed in a pool of saturated liquid, Fig. 2.94. All liquid variation in static pressure was applied to the sides of the tube bundle in this model, and the conditions in the shell side did not affect the flow over the tube bundle.

The two-fluid model uses conservation equations for mass, momentum and energy for each phase. These equations are solved simultaneously with closure equations that describe the interaction in the tube bundle between the phases and between the phases and the tubes. To solve the closure equations the key forces required are interfacial drag force and the force the tubes exert on the fluid. These forces significantly affect the void fraction and the pressure drop of the phases. The flow in the tube bundle and shell has been analysed by applying this model. The strength of the two-fluid model is dependent on the precision of the interfacial drag force and the force on the fluid by the tubes for the flow through tube bundle. These forces are not well developed for this model.

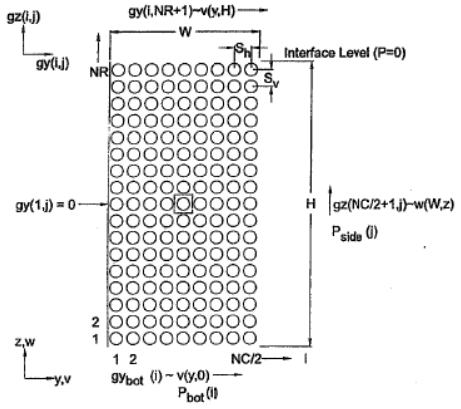

Fig. 1. 2-D reboiler model.

Figure 2.94: 2-D Kettle reboiler model based on Burnside [8]

Carlucci et al. [59] modelled homogenous two-phase re-circulating flow in the kettle reboiler using a finite difference technique, Fig. 2.95. It was not possible to predict the separation of liquid and vapour above the bundle in this geometric model. This was because the model used was homogenous and thus simulates separation by the reintroduction of the liquid flow at the top of the weir. The feed flow was maintained at the level needed for the vaporized flow to be replenished. The experimental kettle reboiler of Cornwell et al. [11], with boiling R113 at 1atm at a heat flux of 20 kW/m^2, was modelled by the authors.

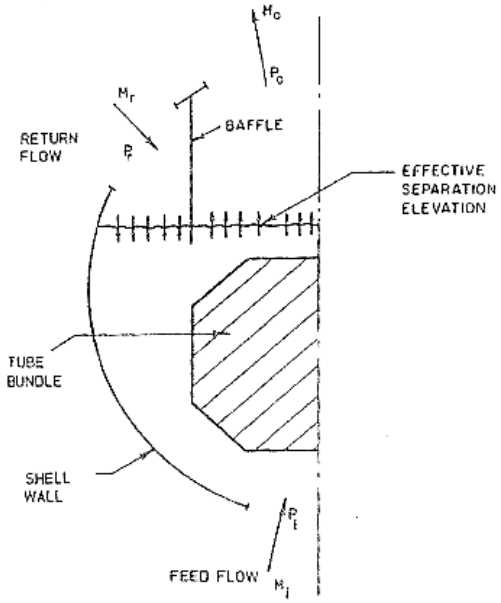

Figure 2.95: A Kettle reboiler model of Carlucci et al. [59]

The tube bundle was modelled as a momentum sink (due to friction pressure drop) and on interphase mass source (due to vaporization of the liquid). This model used the porous media approach, which assumes that the domain consists of solid, liquid and gas fractions. The correlations of Butterworth [61] were used to derive the bundle friction factor and this factor was introduced as a momentum sink in the homogenous momentum equation. The solution region was divided into a cylindrical coordinate grid using a staggered mesh to solve vector and scalar variables. A hybrid upwind/central difference discretization scheme was used to approximate the convection-diffusion flux and the SIMPLE algorithm of Patankar and Spalding [62] was used to deal with the pressure-velocity coupling. The model could predict the velocity field observed by Cornwell et al. [11], but the recirculation mass velocity exceeded the experimental data of Cornwell et al. [11] and Shire [6] as a result of the assumption of homogenous two-phase flow.

Edwards and Jenson [60] produced a two-dimensional model that used a finite difference technique in the PHOENICS CFD code, to predict the two-phase flow in the kettle. The two-phase flow across the tube bundle was treated using the porous media approach. For modelling, the authors used the experimental kettle reboiler of Cornwell et al. [11] in which R113 was used as the working fluid. To eliminate the requirement to solve the energy equation, the model described a saturated mixture with constant properties entering the reboiler.

The flow feed at the centre of the base of the reboiler is proportional to the amount of vapour generated in the kettle reboiler,

$$m_{in} = C_0\, q/h_{fg} \tag{2.34}$$

The overflow factor C_0 was assumed to be 1.0 .The term q/h_{fg} indicates the total rate of vapour generation in the reboiler. The frictionless non porous wall was used because its effect on the recirculation flow rate was assumed negligible.

From the form of Lahey et al. [63], the interfacial drag source terms, which represent a force per unit volume acting on a phase due to the relative velocity between the liquid and vapour, was determined using the following equation

$$F_{gl} = -F_{\mathrm{lg}} = \frac{3}{8}\alpha_g \rho_l \frac{C_D}{R_P}(u_g - u_l)\left|u_g - u_l\right| \tag{2.35}$$

Where the value of the drag coefficient C_D was calculated using three different analyses (a) Wallis " dirty water" model, (b) a simple model using the PHOENICS model, and (c) different values of drag coefficients, 100, 50, 20, and 10. The reboiler model was based on a finite difference solution governed by a simplification of the continuity and momentum equations by Lahey and Drew [64].

A discretization scheme was developed in which each tube in the bundle occupied one grid cell as shown in Fig. 2.96. This was done to reduce the duration of the computation time.

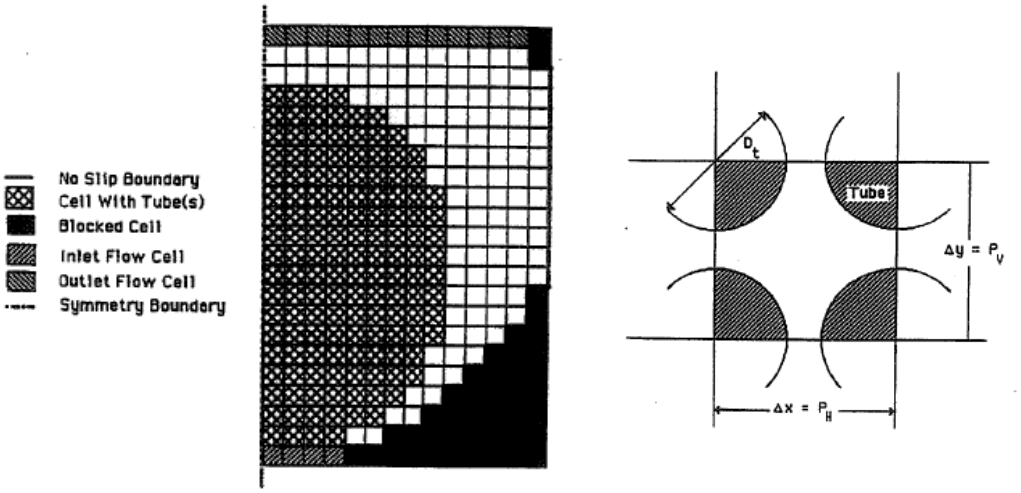

Figure 2.96: Mesh configuration used by Edwards and Jenson [60]

An investigation of grid size variation showed that the results were only affected by 2%. It was found that the results were dependent on the choice of the drag coefficient model. When the drag coefficient of the Wallis model and the PHOENICS model were used, the authors observed that the experimental void fraction values could not be accurately predicted, with a deviation of 80% from the measured data. However, when a constant drag coefficient was assumed for the whole field by using different values of 100, 50, 20, and 10 (third model), the measured void fraction values could be approached. For a drag coefficient of 10, there was a 30% difference between the predicted and measured data. Convergence problems were observed for drag coefficients of less than 10. A trend similar to the experimental data of Cornwell and coworkers was predicted by the model, particularly at a heat flux of 10 W/m^2, Fig. 2.97. However, the use of a constant value of drag coefficient in the entire flow analysis of the kettle reboiler resulted in poor predictions at higher heat flux values. Fig 2.97(c) shows the predicted void fraction at 15^o C wall super heat, which was extremely and unexpectedly high, approaching the value of 0.98 in the middle of the bundle.

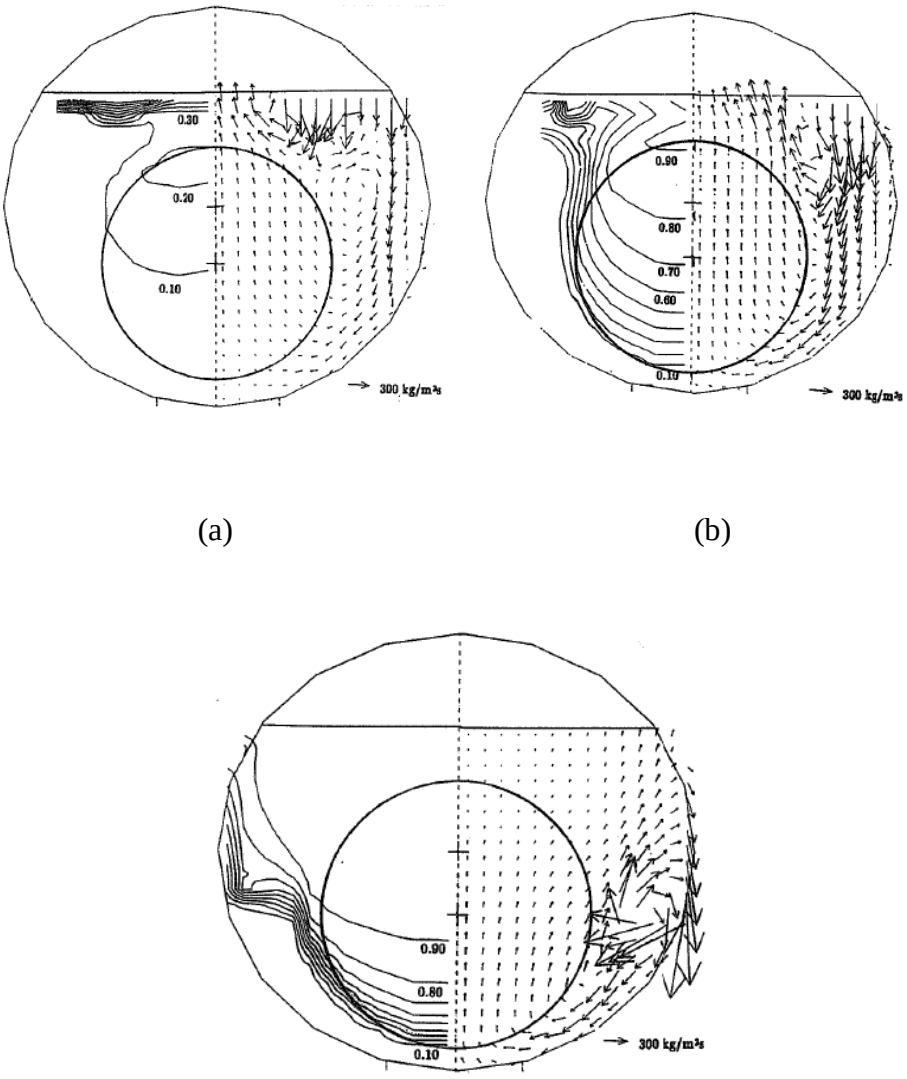

Figure 2.97: mass flux and void fraction contour plot for constant wall super heat. (a) 4^{o} C (b) 10^{o} C (c) 15^{o} C, Edwards and Jenson [60].

Rahman et al. [65] gave a correlation for the interfacial drag coefficient in vertical two-phase flows across tube bundles, horizontal in-line and staggered. To determine the interfacial drag coefficient correlation the air-water experimental data of Dowlati et al. [39], and Schrage et al. [31] were used. It was assumed that the resistance between the tube walls and the gas or vapour phase was negligible as the only phase in contact with the bundle's tubes was the liquid. A power law dependence between drag coefficient and Reynolds number was estimated. The Reynolds number was defined as:

$$R_e = \frac{\rho_m v_r \delta}{\mu_l} \tag{2.36}$$

Where ρ_m , v_r , δ , μ_l are the two-phase mixture density, the vapour relative velocity, the product of porosity and transverse pitch, and dynamic viscosity of the liquid phase respectively. Fig. 2.98 (a) and (b) show that the drag coefficient variation with Reynolds number for in-line and staggered bundles, respectively. It was observed that the variation of C_D with Re consists of two regions of differing slope that were distinguished based on the change in flow pattern. Transition occurred at $C_D \approx 4$, for the upper region, $C_D > 4$ and for lower region $C_D < 4$.

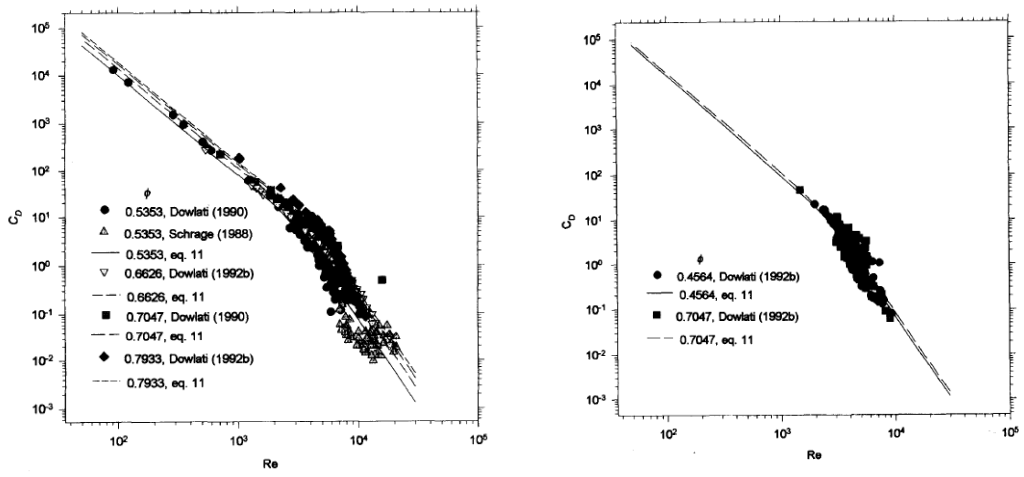

a) In-line tube bundle b) Staggered tube bundle

Figure 2.98 : Interfacial drag coefficient by Rahman et al. [65]

The lower portions comprise the region of high liquid mass flow and moderate to high mixture densities, which produced high Reynolds numbers. Bubbly and slug flow regimes resulted from the conditions in this region. The upper portions were associated with low liquid mass flows and mixture densities, and produced low Reynolds numbers and hence churn and spray/annular type flows. These two portions are shown in Fig. 2.98 (a) and (b).

The total drag coefficient was the combination of the drag coefficients at upper and lower regions via

$$C_D = (C_{D_u}^{-4} + C_{D_l}^{-4})^{-0.25} \tag{2.37}$$

Where C_{D_u} and C_{D_l} represent the upper and lower region values. The drag coefficients were calculated based on the equation:

$$C_{D_{l\,or\,u}} = e^{E}\phi^{\beta}\,\mathrm{Re}^{n} \tag{2.38}$$

Values for the constants E , β and n are given in Table 2.4 for in-line and staggered bundles.

Table 2.4: Constant for Rahman's correlation

	E	β	n
Upper/ in-line	19.91	1.63	-2.1
Lower/in-line	33.49	3.49	-3.68
Upper/staggered	20.17	0.31	-2.22
Lower/staggered	31.97	0.53	-3.72

It was concluded that the void fraction in the kettle reboiler with an in-line tube bundle was better predicted by the two-dimensional model based on the newly developed drag coefficient than in previous investigations, Fig. 2.99. The flow in the bundle was seen to move towards the centreline and, additionally, two distinct vector plot regions (high and low void fraction) of the tube bundle (Fig. 2.99) were noted. Flow in the high void fraction region moves vertically upwards with a high velocity, whereas in the low void fraction region the flow's velocity was lower and its direction has a greater horizontal component.

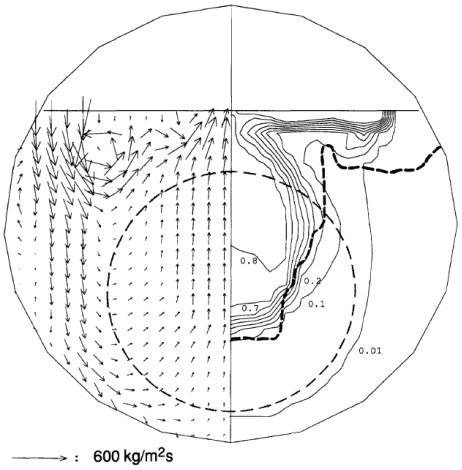

Figure 2.99: Void fraction contour plot and mass flux obtained at heat flux 20 kW/m^2 using the interfacial friction correlation [65]

A set of two interfacial drag coefficient correlations were developed by Stevanovic et al. [66], Stosic and Stevanovic [67], Stevanovic et al. [68] and Pezo et al. [69]. These correlations described the bubbly and churn flow regimes of two-phase flow across the tube bundles and were given for bubbly flow:

$$C_D = 0.267 D_P \left(\frac{g\Delta\rho}{\sigma} \right)^{0.5} \left(\frac{1+17.67(1-\varepsilon)^{9/7}}{18.67(1-\varepsilon)^{3/2}} \right)^2 \tag{2.39}$$

and for churn flow:

$$C_D = 1.487 D_P \left(\frac{g\Delta\rho}{\sigma} \right)^{0.5} (1-\varepsilon)^3 (1-0.75\varepsilon)^2 \tag{2.40}$$

Equation (2.39) has been obtained by using the correlation of Ishii and Zuber [70], which was developed for two-phase pipe flow and applied to bubbly flow across the tube bundles. To account for the reductive effect of the varying bubble shape on the drag coefficient the Ishii and Zuber [70] correlation was multiplied by 0.4. Equation (2.39) was used to determine the ratio of drag coefficient C_D to the particle diameter, D_P, for two-phase bubbly flow across a tube bundle. Churn flow was determined using Eq. (2.40). Fig 2.100 shows the result of both Eqs. (2.39) and (2.40). Equation. (2.40) shows that increasing the void fraction will result in C_D/D_P decreasing markedly. This is

suggested by the authors to be due to the gas-liquid interfacial area concentration. The coefficient used in the above correlations were derived from the void fractions measured of Dowlati et al [39] for air-water mixtures. The resulting correlations therefore agree well with the experimental data, Fig. 2.101.

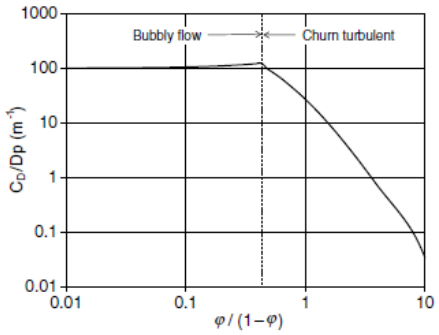

Figure 2.100: Relationship between the void fraction for two-phase flow across a tube bundle and C_D/D_P as calculated for bubbly and churn flow.Simovic et al. [71]

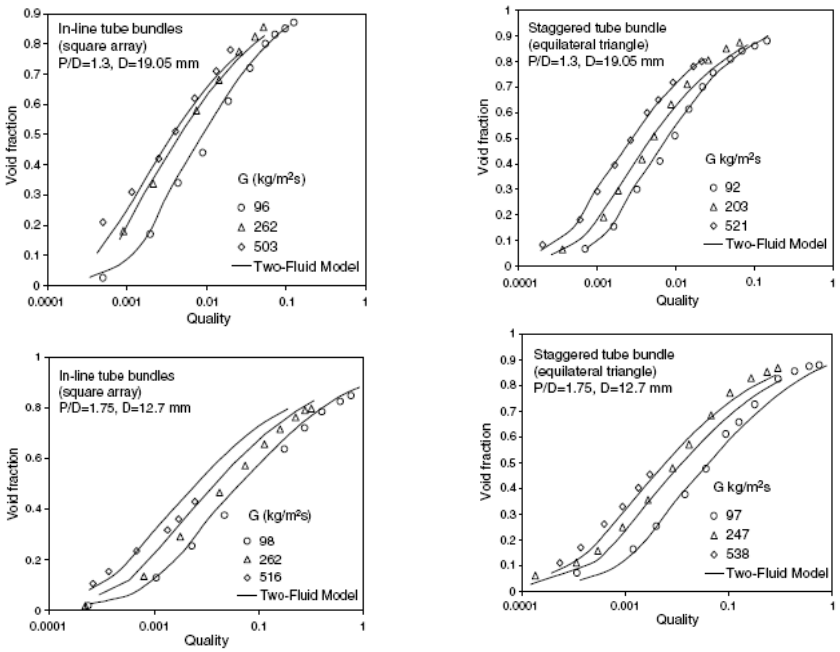

Figure 2.101: Comparison of the measured void fraction by Dowalti et al. [39] with predicted by Stevanovic et al. [68]

These drag coefficient correlations have been applied to the two-fluid model of boiling flows in horizontal steam generators and kettle reboilers. The boundary condition in the north face of the model was difficult to determine so Pezo et al. [69] tried modelling the

kettle reboiler using two different conditions. For the first boundary condition, which was similar to that of Rahman et al. [65], a horizontal plane boundary where fluid exited at constant pressure was used at the free surface. In the second boundary condition the pressure was ignored and the liquid vertical velocity component was taken to be zero, to model the recirculation of liquid at the free surface. Additionally, the vapour vertical velocity gradient and liquid and vapour horizontal gradients were considered to be zero. Only vapour was allowed to re-enter through this boundary as shown in Fig. 2.102.

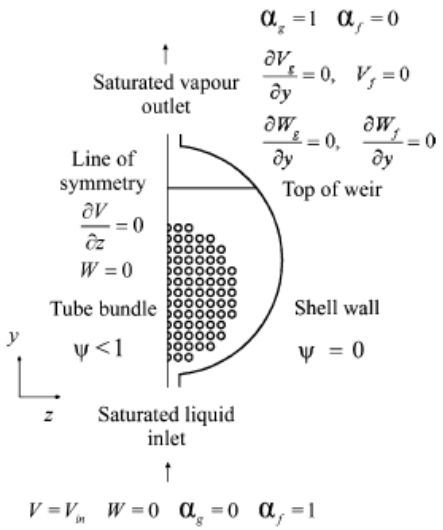

Figure 2.102: Boundary condition of the kettle reboiler model used by Pezo et al. [69]

It was concluded by the authors that better results were achieved from the application of the first boundary condition, as the second boundary condition predicted the void fraction of 0.7 at a heat flux of 20 kW/m^2. This high value of void fraction would be expected for higher heat flux values. A comparison has been made between the predicted results of the void fraction using the first boundary condition and the measured data for the kettle reboiler of Gebbie and Jensen [34]. This comparison has verified the conclusion of Pezo et al. [69]. In contrast the numerical flow patterns generated with the first boundary condition did not agree with the experimental results of Cornwell et al. [11] and Gebbie and Jensen [34]. The data is shown in Figs. 2.103 and 2.104.

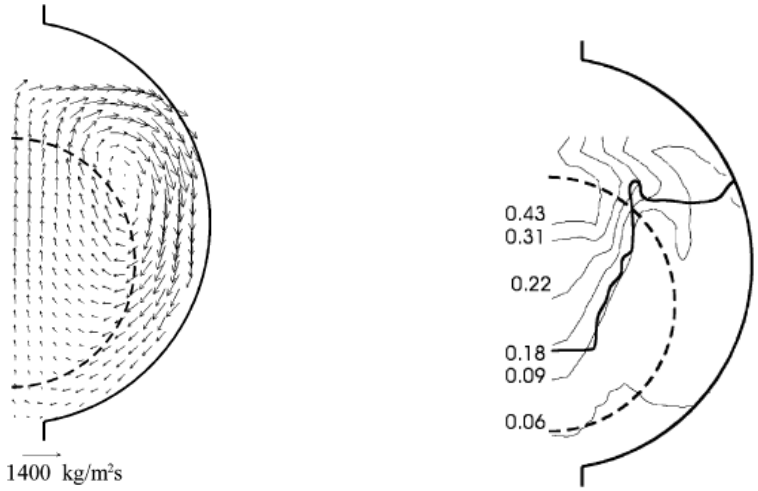

Figure 2.103: Mass flux vectors and Void fraction distribution based on first boundary condition at 20 kW/m^{2}obtained by Pezo et al. [69]

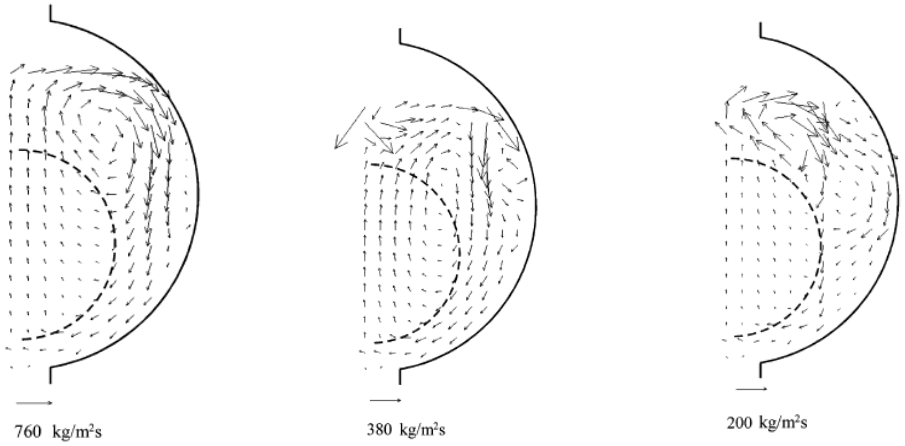

(a) (b) (c)

Figure 2.104: Mass flux vectors of two-phase flow based on first boundary condition at (a) 10 kW/m^{2,} (b) 30 kW/m^{2,} (c) 70 kW/m^{2}obtained by Pezo et al. [69]

A two-dimensional two-fluid model for two phase flow within a kettle reboiler was developed by McNeil et al. [7]. The porous media concept was used in the model and the empirically based, one-dimensional model was used to determine the drag coefficient and tube wall force. It was found to be difficult to deduce the boundary condition to apply at the free surface of the pool, which is necessary in order to specify the intra-tube bundle flow regime. An isobaric with entrainment boundary was used. This simulated bubbly flow when only liquid was allowed to re-enter across the boundary. When it was largely vapour that re-entered, intermittent flow was simulated.

The two-fluid model was used to model boiling R113 in the kettle reboiler. For the correctly chosen boundary condition at the model's free surface there was good agreement between the predicted flow pattern and pressure drop values and the experimental data of McNeil et al. [58]. In order to construct models that are more accurate the authors advised that future work measured the void distribution in the tube bundle and the turbulence level in the shell. It was recommended additionally that the velocity distribution and drag coefficient in the tube bundle and shell be deduced or measured.

2.7.5 Summary of numerical studies

- Out of all the models available, the one-dimensional model provides the simplest simulation of two-phase flow in a kettle reboiler.
- In the one-dimensional model it is necessary to know the void fraction and two-phase friction multiplier correlation, while the influence of frictional and acceleration pressure drop on the shell side are not considered.
- At low heat fluxes there is a close correspondence between the pressure drop predicted by the one-dimensional model and the experimental values. At high heat fluxes there is more deviation between the predicted pressure drop values and the experimental values. Hence, the one-dimensional model for the kettle reboiler is effective for use at lower values of heat flux.
- Extensive analysis of flow process in the kettle reboiler has led to the development of a two-dimensional model for the purpose of industrial design.
- 2-D flow within the kettle reboiler has been simulated using a one fluid model (algebraic slip) and a two fluid model .
- The one fluid model has been used to simulate flow in the tube bundle. To construct a one fluid model, the void fractions, pressure distribution around the bundle and the tube bundle flow resistance must be known.
- A two-fluid model has also been used to simulate flow in both bundle and shell. The conservation equations for mass, momentum and energy for liquid and vapour are required for constructing this type of model. These equations are solved together with closure equations that express the interaction between the phases and between the phases and the tubes in the bundle.
- The predicted flow pattern in two-phase flow models is not clearly specified in the literature that is available to review.

2.8 Conclusion and Scope of the Investigation

A careful review of the literature has shown that there is insufficient data available to provide a complete quantitative description of the two-phase flow regime, pressure drop, void fraction and mass flux inside the reboiler. The literature survey has also identified the need for an enhanced numerical model for kettle reboilers. The existing models, including those in one and two dimensions, do not accurately predict the recirculating flow or local flow condition within the kettle. Developing a model which can accurately predict the two-dimensional, two-phase flow in the kettle reboiler would facilitate the design of more efficient reboilers. The tools required to construct such a model are principally the pressure drop, void fraction and velocities which must be investigated experimentally and developed numerically.

One of the aims of this study is to further develop the model of McNeil et al. [7] and to analyse the two-phase flow of boiling pentane in the kettle reboiler. An additional aim is to develop a new model to accurately predict two-phase flow behaviour in a kettle reboiler in which only the tube bundle is modelled. This approach simplifies the problem and reduces the computational time required to solve it. These two models are two-dimensional two fluid models with pentane as the boiling fluid. The most recent pressure drop, void fraction and velocities correlations are used in these models in order to best predict the two-phase flows within the kettle reboiler. The fluid equations are solved using the ANSYS, CFX CFD package.

The development of these models includes a description of the tube bundle resistance forces, the drag coefficient correlations, the boundary conditions and a technique to guarantee the tube bundle flows are in the correct flow regime. To validate the predicted results two type of experimental have been carried out.

- Measurement of the pressure drop throughout the tube bundle.
- High speed camera visualisation of the flow movements between the tubes to investigate the flow patterns.

Further verification of the modified model is achieved by comparing the predicted liquid velocities and mass flow rates within the pool with the 2-dimesional instantaneous velocity fields obtained by Particle Image Velocimetry (PIV), and recorded Burnside et al. [2]. Additionally the predicted results of void fraction and mass flux are compared to predicted results from the one fluid model of McNeil et al. [5].

CHAPTER 3

Experimental Apparatus and Procedure

In this chapter, the flow loop characteristics, kettle reboiler, data measurement techniques and experimental procedure (used to analyse the two-phase flow pattern and pressure drop) are discussed.

3.1 Flow loop characteristics

The description of the kettle reboiler used in this study is discussed briefly here. More details are given in Miller [15]. The kettle and the respective flow loops are illustrated in Fig. 3.1.

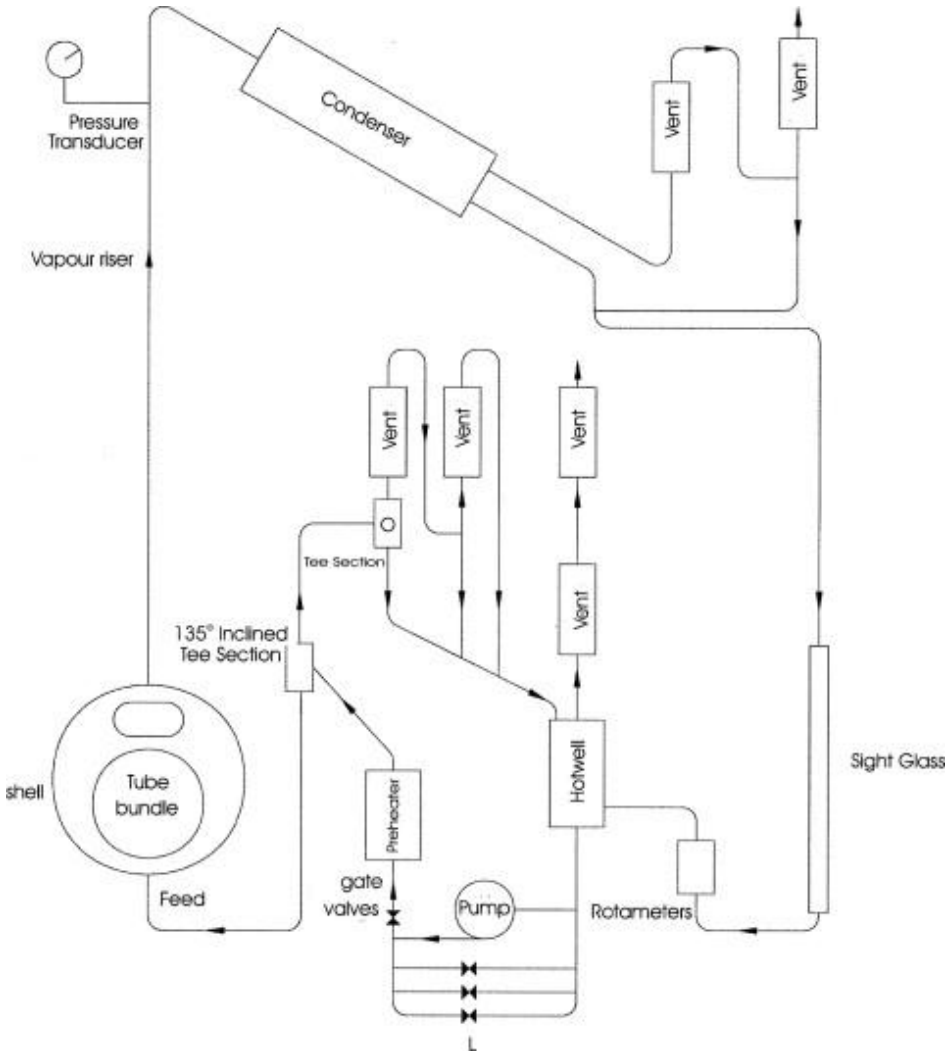

Figure 3.1: Kettle reboiler experimental rig [15]

The liquid was moved by natural circulation from the hotwell tank (19.5 × 19.75 × 36.25 cm) through one rotameter of three in parallel (metric series 7×, 14× or 24×) and entered through the electrical preheater. One of three different gate valves was utilised to control the fluid entering the kettle reboiler. To maintain the temperature of the inlet fluid near to the saturation temperature, the flow passed through a preheater and a tee section with an angle of 135º. The liquid flow entered the kettle reboiler through three holes at the base of the shell. The liquid was boiled by electrical heating inside the tube bundle. After leaving the kettle reboiler, the vapour passed to the condenser, where chilled water was used to condense it. By using the effect of gravity the liquid was taken back to the hotwell and the cycle was completed. Fibre glass insulation was used in the flow loop to reduce heat losses.

3.2 The kettle reboiler

In the kettle reboiler, the shell was made from brass with an internal diameter of 732 mm and 56 mm deep. The centre of the shell was located 110 mm higher than the bundle centre line. The bundle contained 241 tubes, made of a 90 Cu: 10 Ni alloy, 19 mm in diameter, and arranged in 17 vertical and horizontal lines with a square in-line layout and a pitch of 25.4 mm. At 310 mm above the shell centre, the exit port for vapour is located. To visualise the flow patterns and distribution, a transparent window was fixed to the front of the shell. PTFE discs separated each tube from the front window. To carry the vapour out of the shell, an elongated bronze transition pipe of 290 cm^2 y-sectional area and a Pyrex elbow of internal diameter 150 mm was used. The vapour outlet is shown in the Fig. 3.2.

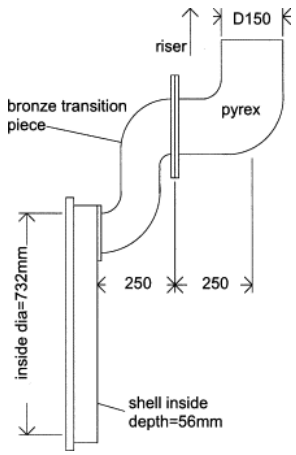

Figure 3.2: Arrangement of vapor outlet [16]

Each tube contained a 51mm length of electrical cartridge heater with an external diameter of 9.5 mm. At 240 V, the maximum power of 250 W was supplied to the heater. The 241 heaters were divided into 18 banks of tubes. In each bank, 13 to 14 tubes were placed. By using nine variable control transformers or variacs, the power to the heaters was controlled, with each transformer controlling two tube banks.

3.3 Preheater

The preheater consisted of 72 horizontal electrically heated and nickel plated mild steel tubes (19 mm diameter) and was fixed in a rectangular sectioned tank. The tank dimensions were 275 mm length × 153 mm width × 354 mm in height, and the flow passed vertically over the tubes. Tubes with a 30° staggered arrangement and transverse pitch of 25.4 mm were used. Heating was done by Grimwood cartridge heaters, 254 mm long × 12.7 mm in diameter. The 250 V and 250 W cartridge heaters were used and the power to the heaters was controlled by six 25 A variable transformers. To avoid overheating, wall thermocouples were installed in five tubes to act as temperature controllers. If vapour was generated in the preheater it was condensed using 2 × 50 mm diameter corning QVF condensers vented to the atmosphere.

3.4 Condenser

A single pass condenser with condensation on the tube side acted as a heat exchanger (Serck ZA396). For cooling the working fluid, cooling water with a flow rate of 85 lpm was available in the condenser. An external circuit valve was used to set the cooling water temperature to any desired value.

3.5 Power

A portable electronic wattmeter (Siemens B4305) was used to measure the supplied power. A switch that controlled the current to heater was closed, to prevent the interruption of power to the heaters and the wattmeter was plugged into one of 18 sockets, one per heater bank. The wattmeter activated a 24 V dc and switched the current through the wattmeter. The uncertainty in measurement of the heat flux ranged from ± 6% and 1.7% for heat fluxes 10 and 20 kW/m^2, respectively (Miller [15]).

3.6 Instrumentation

3.6.1 Temperature measurement

For measuring and monitoring the temperatures, twenty Mineral Insulated Metal Clad (MIMC) thermocouples were fixed in the kettle reboiler. The thermocouples were fixed in different places within both the bundle and shell. In the present study, only six thermocouples were used. Thermocouples were used to monitor the temperature, to avoid tube overheating and to keep the inlet temperature at its saturation value. To check the tubes' surface temperatures in the bundle, three thermocouples were sited at various levels. The fluid temperature in the bundle was checked with two thermocouples. The flow temperature at the shell inlet was checked with the remaining thermocouple

3.6.2 Pressure measurement

For measuring the pressure distribution in the shell and tube bundle, 24 pressure tappings were fixed in the kettle reboiler as shown in Figure 3.3. Eight, seven and five pressure tappings were located in channels 9.5, 12.5 and 15.5, respectively. The remaining 4 pressure tappings were placed in the shell. In the vertical channel of the tube bundle every two adjacent tappings were separated by 50.8 mm (two tube pitches). In the shell the two adjacent tappings were separated by 101.6mm (four tube pitches). The pressure tappings were 2BA screws with 1.2 mm diameter holes.

The pressure drop across the shell and the tube bundle was measured using a Rosemount differential pressure transmitter (E1151 DP). The low pressure side of the pressure transmitter was joined to tapping 8 while the remaining tappings were joined, via valves, to the transmitter's high pressure side. The pressure difference measurement between any tapping and tapping 8 at the bottom of the central channel was measured by manipulating the PTFE valves shown in Fig. 3.4 An additional Rosemount E1151DP pressure transmitter was connected between tapping 8 and atmosphere which allowed the gauge pressure to be measured. All inter-connections were made by thin PTFE tubing. The pressure measuring circuit could be completely filled with the working fluid from a 1.5 litre glass vessel reservoir placed 1.7 m above the pressure transmitter so that no air was present.

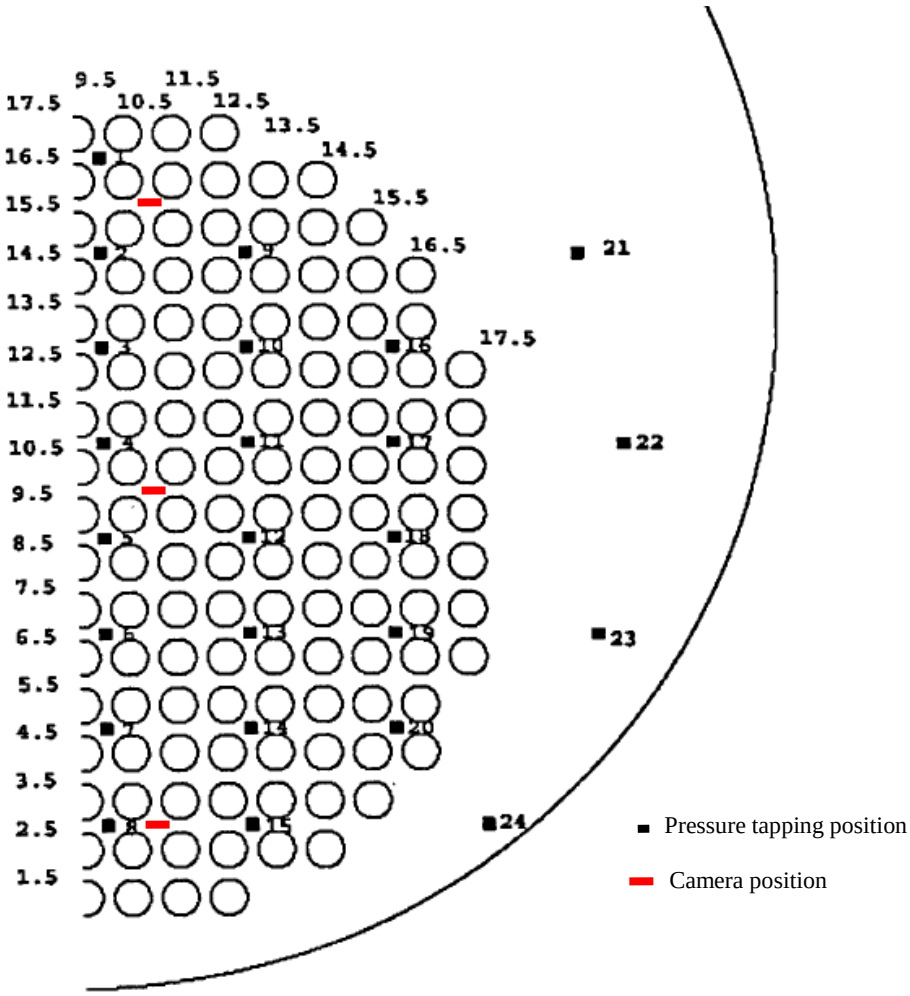

Figure 3.3: The pressure tapping and camera position

The two row pressure drops were calculated by subtracting the readings from two adjacent tappings.

The pressure drops, P_i-P_j, between tapping i and j were measured by converting the voltage measurements through the following equation:

$$\Delta P = P_i - P_j = \rho_l g z - \Delta P_{trans} \quad (3.1)$$

where

$$\Delta P_{trans} = 625\ (V_R - 0.9925) \quad (3.2)$$

and z is the vertical distance between the tapping i and j connected to the transmitter, ρ_l is the density of the working fluid at atmospheric pressure(i.e. pentane Pa) and V_R is the voltage drop. The gauge pressure can be determined from:

$$\Delta P = 1000\ (V_R - 0.9925) \quad (3.3)$$

Between the two tappings the accuracy of the pressure measurement was ±10 Pa and that of the gauge pressure was ± 81 Pa, [10].

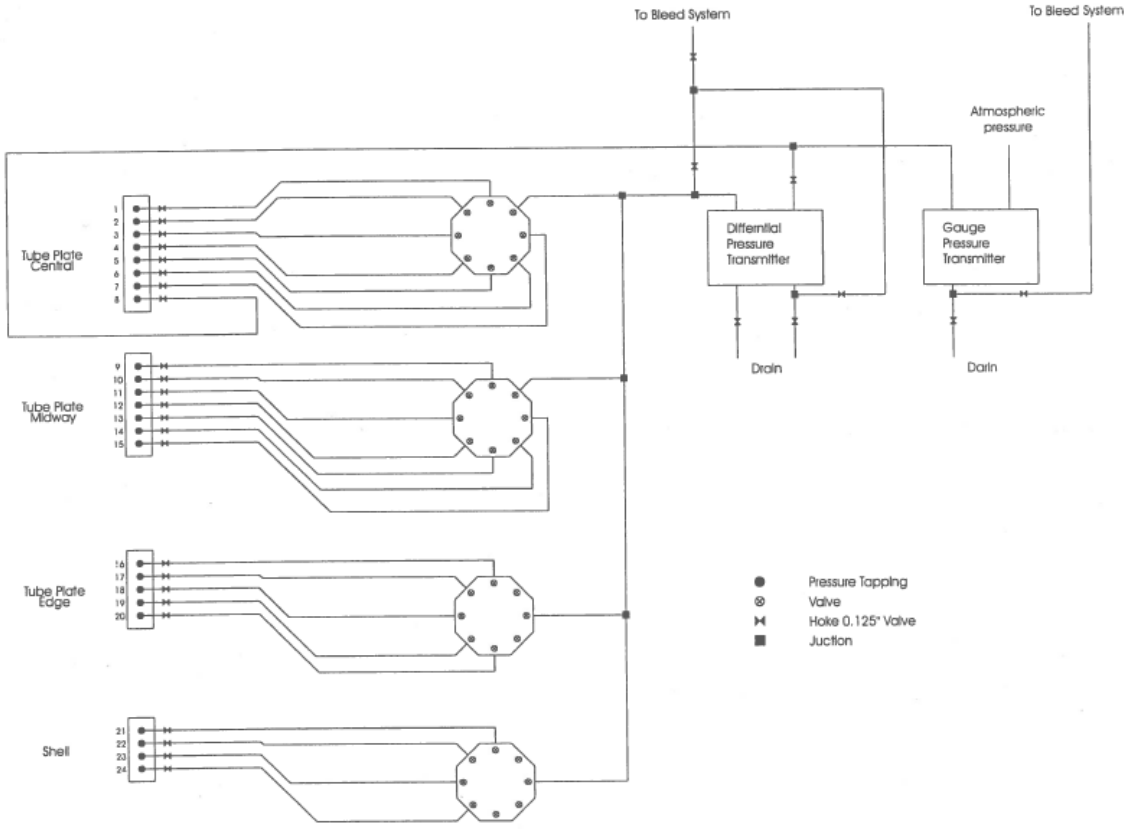

Figure 3. 4: Pressure tapping connections valves [15]

3.6.3 Data acquisition

A data acquisition system was used to collect pressure drop measurements. Via a RS-232 wire, a computer with an HP-IB interface card was linked to a HP 75000 series B (model: E1300A) processor.NT-4 Windows was the PC operating system and HP VEE software was utilized to construct a program for data collection and storage. A large number of readings and the frequency of data acquisition were recorded with this program.

3.6.4 High speed camera

In order to investigate the flow between the tubes, a high speed camera was used. The Kodak micro-motion 1000 high Speed Camera had a variable framing rate from 10 to 10,000 f.p.s (Hz). Shutter speed is dependent on the lighting system used, and here light

was provided by two flash sources. The camera and light system are shown in Fig. 3.5. The motion of the working fluid and the flow pattern in the kettle reboiler were captured by a Cosmicar lens which allowed magnifications of 1.8 to 22 and had a 12.5 to 75 mm field of view. The camera was connected by a cable to a motion recorder analyzer, on which the images were stored. The images were later transferred to the computer.

Figure 3.5: High speed video camera and the lighting systems

3.7 Experimental Procedure

The condenser cooling water was turned on and the test section was filled with working fluid from the storage tank. The fluid was added to a height just over the top of the tube bundle. Before switching of the main power supply, the flow loop was checked for any leakage. Nine variacs (variable transformers) were used to adjust the power to the eighteen heater banks. The tube surface and fluid temperatures were monitored to avoid tubes overheating. Slowly increasing the power supply allowed the required value to be achieved. Approximately two hours were needed to complete all the procedure described above. The power supply of the preheaters was adjusted using four variacs (variable transformer) to ensure that the liquid entered the kettle reboiler close to the saturation temperature. After reaching steady state conditions, the relevant data were collected, either flow data or photographic data

3.7.1 Flow data

All the temperature, flow rate and power data were recorded manually. The pressure drops were measured at the pressure taps, which were located between tubes in the bundle, as shown in Fig. 3.3. A data logger was used to store the pressure drop measurements. Air or vapour was removed from the pressure transducer lines by purging with a small quantity of working fluid before recording any pressure drop

readings. To ensure reliable average pressure drop data for each pressure tapping, at least three hundred measurements were taken at 50 ms intervals. Heat flux values of 10, 20, 30 and 40 kW/m^2 were used for the operation of the kettle reboiler. For each heat flux, pressure drop measurements were recorded twice to ensure good reliability of the data.

3.7.2 Photographic data

The camera was mounted on a tripod, placed at the front window of the kettle reboiler and focused on the gaps between the tubes in the central channel in three locations (bottom, middle and top) of the tube bundle, as shown in Fig. 3.3. During the tests, the camera frame rate was set at 240 frames per second at a resolution of 720 x 480 pixels. Two flash sources provided the illumination that the camera required to record clear images of the two-phase flow. The flash sources were fitted to the front of the test section with a flexible hanger and illuminated the gaps between tubes. Flow images were recorded at heat flux values of 10, 20 and 30 kW/m^2.

CHAPTER 4

Assessing the Use of an Optical Fibre Probe for Measuring Void Fraction in a Tube Bundle

4.1 Introduction

Over the last 40 years, revolutionary advancements in measuring void fraction in two-phase flow in heat exchangers have occurred. Different techniques have been developed to measure the local void fraction in a flowing mixture. These are usually based on the detection of difference between the physical properties of the phases. The absorption of X and γ rays has been widely used. Probes based on the thermal and electrical properties of the flow have been used extensively and, recently, fibre optical sensors have been used, (Morris et al.[72] and Hamad et al.[73]). Aprin et al. [26] used an optical probe for their void fraction measurements and found that this technique was easy to use, provided high precision, was compatible with hydrocarbon fluids, worked effectively at high temperatures and did not encounter the problems of corrosion that can be associated with electrical and thermal probes.

Several types of fibre optical probes can be used to measure two-phase flow characteristics such as local void fraction, bubble diameter, bubble frequency and bubble velocity. A probe with Glass rod systems was used by Miller and Mitchie [74], U-shaped fibre systems were utilized by Danal and Delhaye [75] and Abuaf et al. [76] used a Monofibre system. Optical probes are based on measuring the difference in refractive indices between the liquid and gas.

Therefore, based on the literature survey, an optical fibre probe measurement technique was chosen to measure the void fraction of the two-phase flow within tube bundles. So far, optical techniques have been widely used in pipes or vertical columns for phase detection, but rarely in tube bundles.

This chapter describes the development of an optical probe that can measure the void fraction distribution inside the tube bundle of the heat exchanger. The description will also include the operating principals of optical probes and the previous work done to develop signal analysis techniques that are applicable to two-phase flow. The design and development of the optical fibre probe is discussed in the following sections.

4.2 Optical probes

Optical fibres can be classified into two types: step-index and graded (gradient) index fibres. This classification provides the user with the refractive index profile of the fibre: how the refractive index changes across the cross-section of the fibre.

4.2.1) Step index fibres

Figure 4.1 (a): This type of fibre consists of a glass or silica core surrounded by cladding, usually made from a different glass material. The core and cladding have different refractive indices, denoted by n_1 and n_2, respectively; the refractive index of the core is higher. The main purpose of the cladding is to provide a constant refractive index at the core-cladding interface, which allows light to be transmitted down the core by total internal reflection. It also provides the fibre with structural support.

4.2.2) Graded index fibres

Figure 4.1 (b): Graded index fibres differ from step index fibres in the nature of their refractive index profile. The core of the graded index fibre has a parabolic refractive index profile, in contrast to the constant refractive index in the core of the step index fibre. The refractive index of the fibre core changes as a function of the radial distance across it. Light is transmitted through the fibre by total internal reflection at the core-cladding interface. Optical sensors are characterised by their numerical aperture (NA); this is defined as the maximum angle of acceptance, θ_{max} of the fibre for light guidance, Fig. 4.1 (c). The numerical aperture thus indicates the light-collecting ability of the fibre. With reference to Fig. 4.1 (c), and using Snell's law:

$$n_1 \text{ Sin } \theta_1 = n_2 \text{ Sin } \theta_2 \qquad (4.1)$$

It can be shown that:

$$\text{NA} = n \text{ Sin } \theta_{max} = \sqrt{(n_1^2 - n_2^2)} \qquad (4.2)$$

Where n is the refractive index of the medium outside the fibre, and the refractive indices of the core and cladding are n_1 and n_2, respectively.

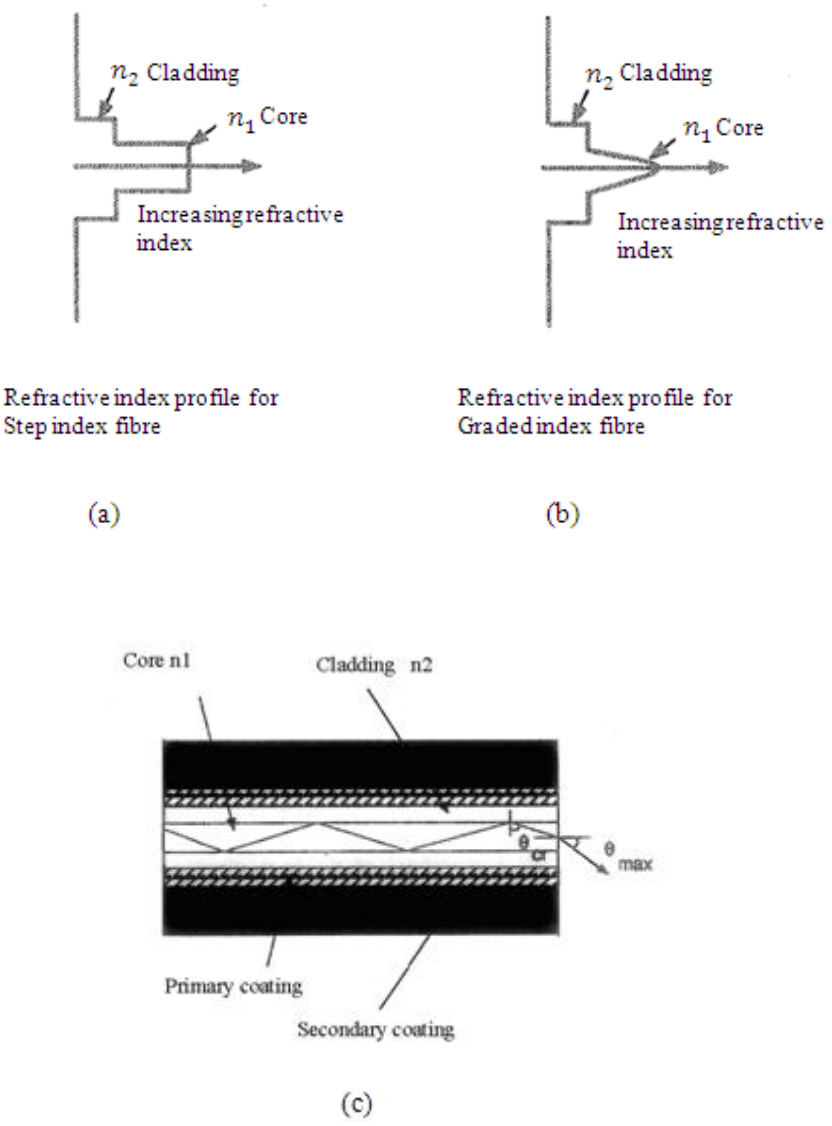

Figure 4.1: Step index fibre and Graded index fibre

4.3 Principles of operation

Optical probes are used to indicate the phase change at a point in the flow. Their function is based on the principle of total internal reflection. Miller and Mitchie [74], and Abuaf et al [76], applying the principle of total internal reflection, have used cone-tipped optical probes to differentiate between the air and liquid phases. Immersion of the probe tip in the liquid phase causes the ray of light to be refracted out of the tip. If the tip is surrounded by the gaseous phase, total internal reflection occurs and a significant amount of the light is reflected back through the fibre.

Total internal reflection occurs at the probe tip if $\theta_1 \geq 45^o$ and the tip angle is 90º, Fig. 4.2. From Snell's law (Equation 4.1) it can be determined that Sin $\theta_1 \geq \frac{1}{2}\sqrt{2}$ and $n_1 \geq n_2 \sqrt{2}$. If the value of n_1 is taken to be 1.48 (the refractive index for silica), then the medium must have a refractive index: $n_2 \leq 1.05$ for total internal reflection to occur.

Water and air have refractive indices of 1.33 and 1.00, respectively, therefore using the previous method an optical probe with a cone tip (90º tip angle) will work successfully in liquid-air flows, as shown in Fig. 4.2.

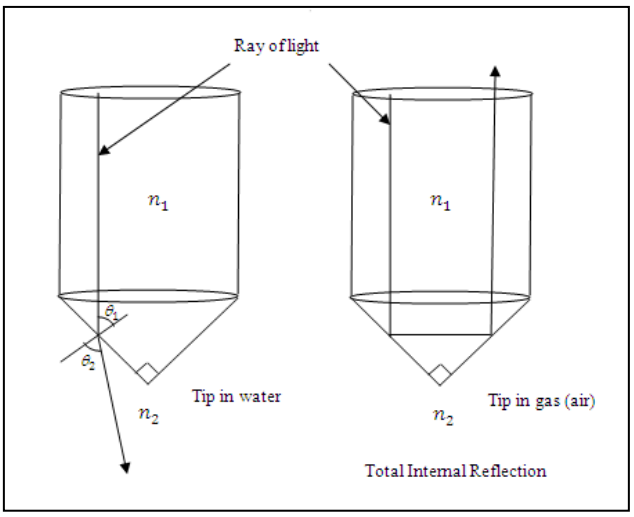

Figure 4.2: Operating principle for cone/prism ended optical probe

A cleaved (straight-cut) optical probe, shown in Fig. 4.3, has been found to discriminate between air and water by Morris et al. [72]. The principle of its function is the variation in the reflection coefficient (the Fresnel coefficient) at the probe tip with the index of each fluid (Morris et al. [72]). For a normal light incidence at the interface between the fibre and the surrounding fluid, the Fresnel coefficient (*R)* is:

$$R = \left(\frac{n_2 - n_1}{n_2 + n_1} \right)^2 \tag{4.3}$$

Where n_1 is the refractive index for the optical probe and n_2 is the refractive index of the surrounding fluid.

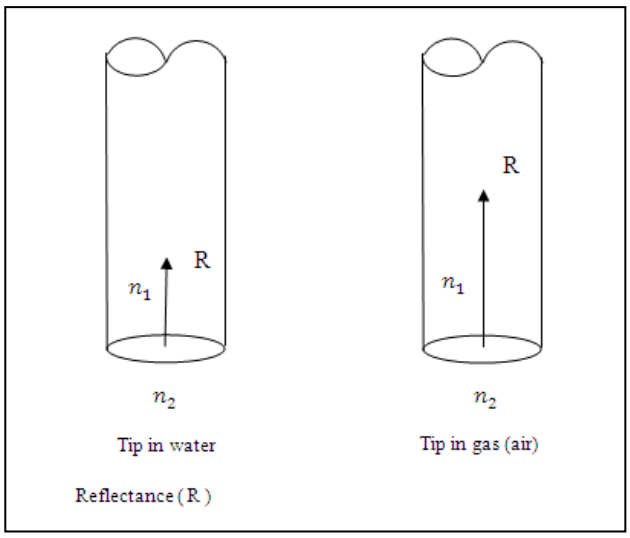

Figure 4.3: Operating principle for cleaved ended optical probe

In this study a normal reflection probe was developed, with the tip surface cut at a right angle to the fibre axis, so as to make the tip flat. Two investigations of gas-liquid flows and one of liquid-liquid flow with this probe type have been described by Sekoguchi et al. [77], Morris et al.[72], and Hamad et al.[73]. The current investigation measured the void fraction using the normal cut optical probe tip in gas-liquid flow (water-air flow).

4.4 Signal analysis techniques

This section explains how void fraction has been calculated from optical signals in previous research.

4.4.1 Void fraction analysis

Moujases and Dougall [78] analysed optical signals by choosing a suitable threshold to separate the air bubbles and the continuous phase. A schematic optical signal in vertical air-water flow is shown in Fig. 4.4. A problem described by Moujases and Dougall was choosing a threshold level that represented an appropriate value of the local void fraction. They noted that there was a finite rise and fall time in the optical signal for the probe to penetrate the film thickness of the bubble and to overcome the surface tension effects. This effect did not depend on the speed of the signal-changing response of the electronics, but was due to hydrodynamic effects and the rate of the bubble interaction

with the optical probe. The threshold level was calculated by taking the average of the two voltage levels V_1 and V_2:

$$V_{av} = \frac{(V_1 + V_2)}{2} \tag{4.4}$$

The void fraction was given as:

$$\alpha = \frac{\sum V \geq V_{av} N_d}{\sum_{Ntotal} N} \tag{4.5}$$

Where N_d is the number of data points collected in the bubble phase and N is the total number of data points in the complete signal trace.

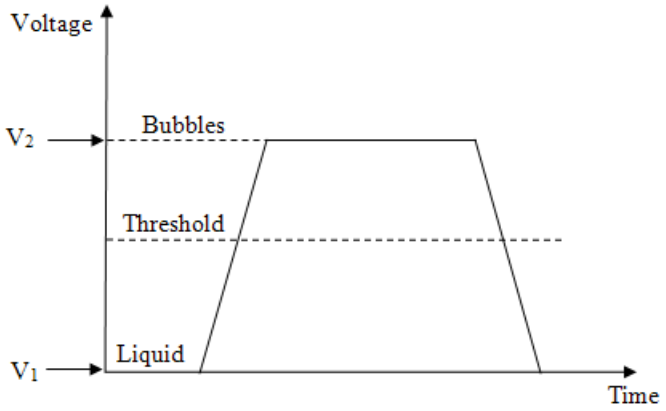

Figure 4.4: Detection threshold level used by Moujaes and Dougall [78]

Gartellier [79] investigated the characterisation and performance of an optical probe in air-water flows, and described two different techniques for analysing the optical signal. The first technique was the most common method, where a signal threshold was set as shown in Fig. 4.5. The start and finish points of a bubble are determined by the intersection of the threshold level with the optical signal. The second technique used two distinct threshold levels. The first threshold level acts on the rising slope of the signal and determines the start of the bubble, as shown in Fig. 4.6.

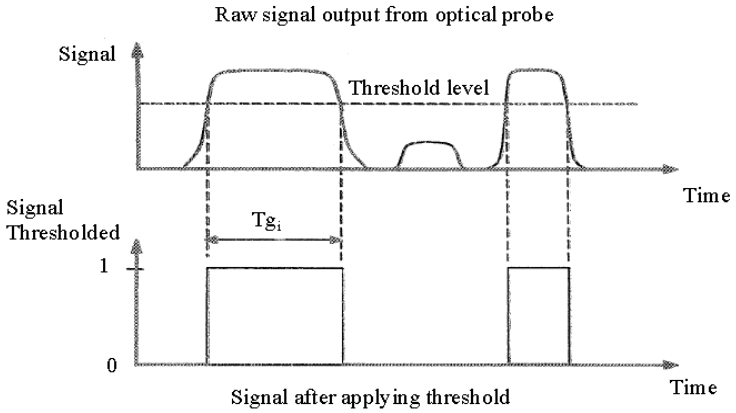

Figure 4.5: Threshold detection level used by Gartellier [79]

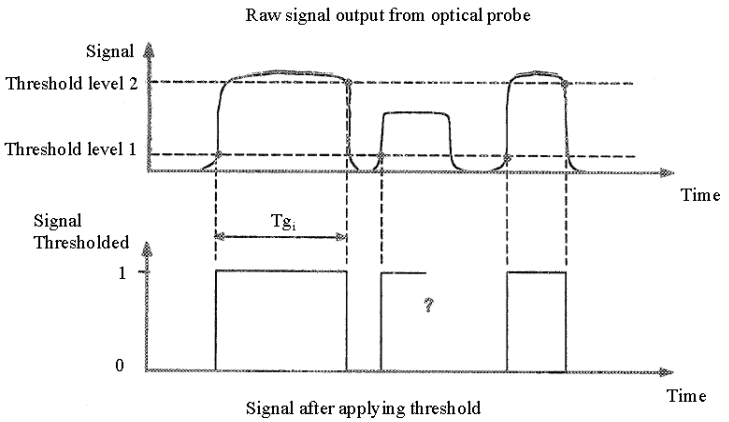

Figure 4.6: Double threshold level detection used by Gartellier [79]

The second threshold level acts on the falling slope and defines the end of the bubble. Gartellier calculated the local void fraction, using Serizaewa's definition, given by:

$$\alpha_i = \frac{\sum T_{gi}}{T} \tag{4.6}$$

Where T_{gi} is the time period the probe is in the gaseous phase, and T is the total time.

The local void fraction can be measured, using the definition given by Hamad et al. [73], with the dispersed-phase density function $X_G(x, t)$ defined as:

$$X_G(x, t) = \begin{cases} 1 & \text{if x is in the dispersed phase at time t} \\ 0 & \text{otherwise} \end{cases} \quad (4.7)$$

For statistically stationary conditions the local void fraction $\alpha = \alpha(x)$ can be defined by:

$$\alpha(x) = \lim_{T\to\infty}\left(\int_t^{t+T} X_G(x,t')\, dt'/T \right) \quad (4.8)$$

A time averaging procedure can also be used to determine the local void fraction as:

$$\alpha(x) = \lim_{T\to\infty}\left(\sum_{T\to\infty} {}^{T_G}\!/_{T} \right) \quad (4.9)$$

Where $\sum T_G$ is the total time the dispersed phase occurred at the selected measuring point, and T is the total measurement time.

The definitions of the void fraction given by the Moujases Equation 4.5, Serizawa Equation 4.6 and Hamad *et al.* Equation 4.9 have been used by other authors, but the selected threshold level varies. In this study, Equation 4.9 was used to determine the local void fraction $\alpha(x)$.

4.5 The Optical Probe-Assembly and Initial Tests

4.5.1 Optical probes:

A fibre probe with a normal cut fibre tip and with core and cladding diameters of 600 μm and 830 μm, respectively, was used in this research. This fibre was selected because of its ability to transmit light at a sufficiently high power, and also because of its small size. The optical fibre was a multi-mode fibre with a graded refractive index profile, and it was used as a mono-fibre; i.e. the transmission and receipt of light occurred through the same fibre. A photo-coupler was used to connect this mono-fibre to the light source and photo-diode. The optical fibre equipment that was used is shown in Fig. 4.7. The

optical fibre was placed inside a stainless steel tube with diameter 2.26 mm, which was used to hold the fibre rigid, as shown by Fig. 4.8.

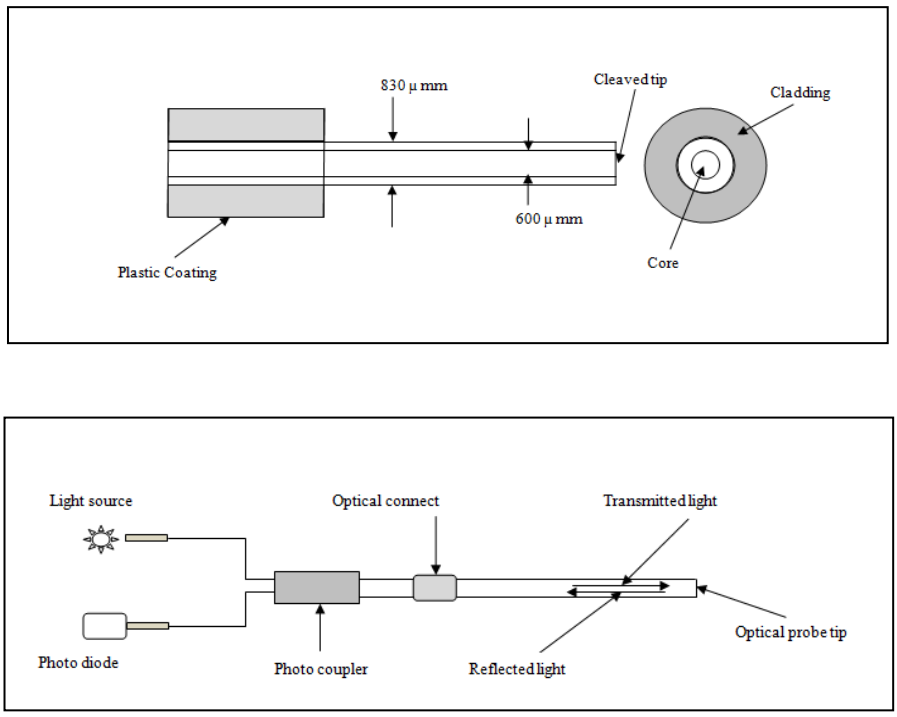

Figure 4.7: Diagram of optical probe equipment

Figure 4.8: Photograph of the optical probe.

4.5.2 Electronics for the optical probes

The electronics used for the optical probes are illustrated in Fig. 4.7. A Fibre Optical Laser Diode Source (0.1mW) was used to produce infrared light. This light was transmitted through the photo-coupler to the fibre tip, where reflection occurred, and light was transmitted back through the fibre to the photo-coupler. The photo-coupler transmitted the reflected light to the photodiode (detector) located on the other side of the coupler. The photo-diode used a two stage process to convert reflected light to current. The first stage was the conversion of current to a voltage; the second stage was

the amplification of the voltage. The complete system was connected to a computer through a data acquisition card: NI USB-9162 and the voltage signal was digitised using LabView 8.5. The LabView program was built and used to record the signals at 10 kHz and, at the same time, output results for storage in the file for further data processing. More details of the LabView program can be found in Appendix E

More light was reflected when the tip was inside the gas phase and the fibre tip only detected the bubbles that touched its surface.

4.5.3 Initial optical probe tests

To eliminate any problems associated with interpreting probe performance, and to become more familiar with its use, pre-testing was undertaken. After the construction of the optical probe was completed, tests were undertaken in a small circular rig that was 20 cm in diameter and 60 cm in height and was built to carry out visual low, velocity tests. These tests allowed errors in the positioning of the probe and the measurement of its signal to be understood. A vertical circular section was made from Perspex and was filled with water to various levels. Air was injected through a 3mm nozzle located at its base. The motion of the air bubbles in the circular rig, and their interaction with the probe tip, are shown in Fig. 4.9.

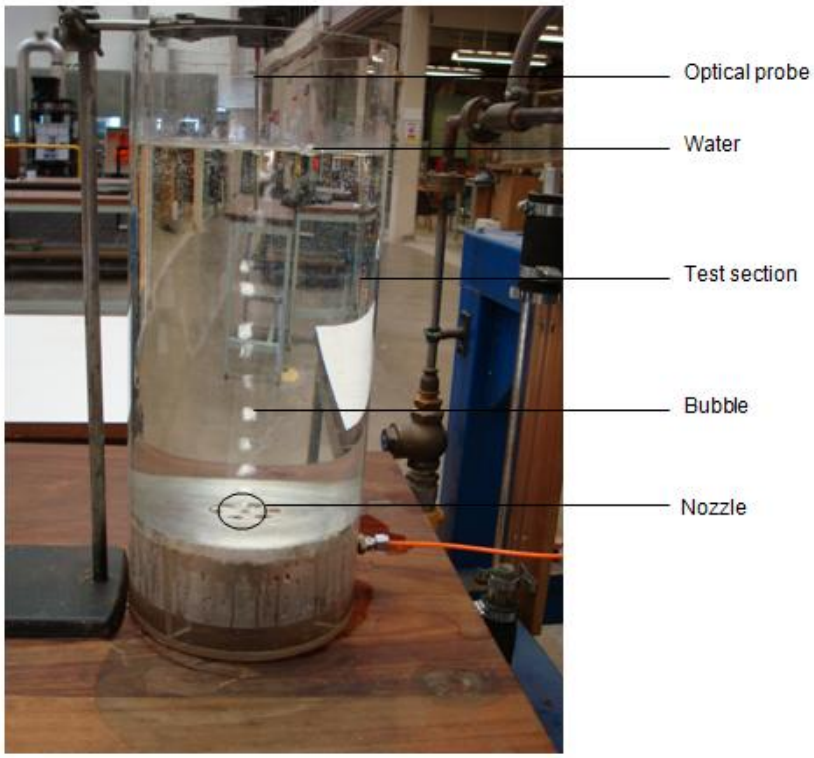

Figure 4.9: small rig (test section)

4.5.4 Optical probe test

A test was performed to measure the output signal from the optical probe during penetration of air bubbles. Air bubbles were injected throughout the base of the rig; the results were stored on a PC data file, and the output signal was viewed on the monitor. A typical optical signal measured during an interaction between the probe tip and an air bubble is shown in Fig. 4.10. The difference between the levels of the air and water signals was approximately 0.2 volts, with the former having a value of -4.8 volts and the latter having a value of -5 volts.

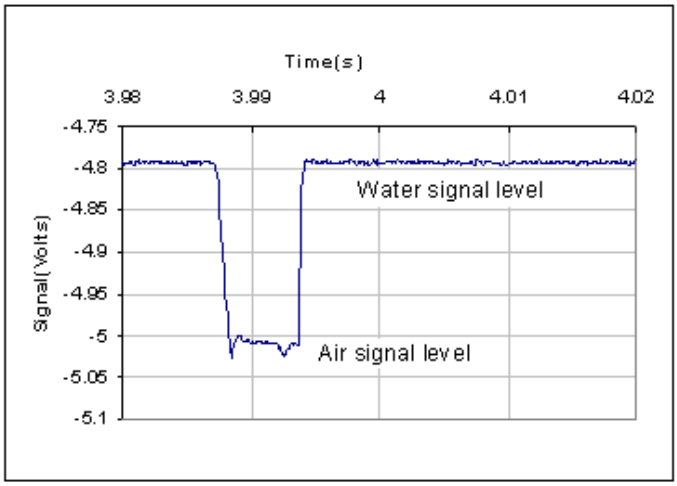

Figure 4.10: Detection of an air bubble passing an optical probe

The difference in signal amplitude between the water and air was lower than expected. This was due to the 'wetting 'effects on the probe tip. It is assumed that when a fibre tip is wetted by a fluid a thin layer will always be present on the tip, and this will alter its reflective properties.

4.5.5 Determination of the void fraction

Information about the flow was produced by analysing the collected optical probe data. This was used to calculate the void fraction. In the two-phase, vertical, air-water flow in the rig, as air bubbles impact on the probe, an output signal from the probe, X(t), was observed. A typical signal is shown in Fig. 4.11. This illustrates the residence time, T_{di}, of each bubble. The time averaged local void fraction, $\bar{\alpha}_j$, at a single position, j, in the flow, is given by:

$$\bar{\alpha}_j = \frac{\sum_{i=1}^{N_J} T_{dij}}{T} \tag{4.10}$$

Where T_{dij} is the residence time for each bubble, T is the total averaging time, and N_j is the number of bubbles passing the optical probe tip.

To calculate the air void fraction from the experimental optical signals, the start and finish of each air bubble had to be determined. The dispersed and the continuous phases were defined by using a threshold technique. The choice of the threshold level was determined by the maximum value from the water signal, and taking values above this to be in the air phase. The threshold level varied as a function of the probe position and time; therefore, individual threshold levels were calculated for each position in the flow.

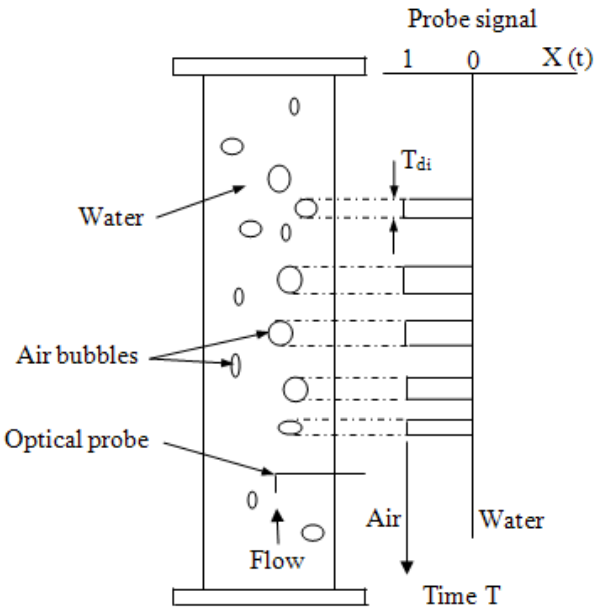

Figure 4.11: Schematic diagram to show determination of void fraction.

Figure 4.12 shows a selected threshold level, which was used to determine the start and finish points of passing bubbles. The start of a bubble was defined as the time at which the optical signal dropped below the threshold level and the subsequent rise of the signal above the level defined the end point of the bubble. The sum of the time periods between the start and finish points, the time spent in the dispersed phase, was divided by the total sampling time to calculate the air void fraction. The averaged air void fraction is given by Equation 4.10.

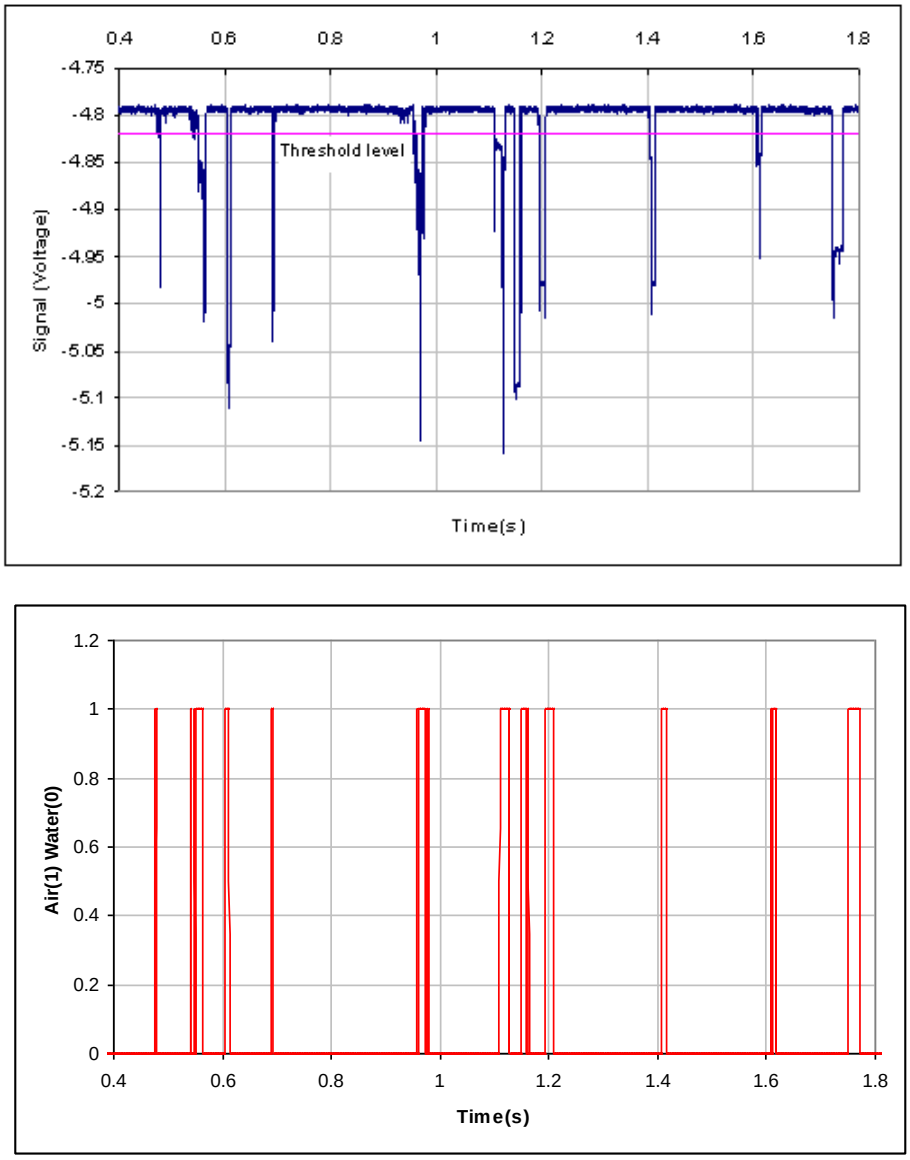

Figure 4.12: Typical voltage signal obtained before and after the threshold line was drawn for the circular test rig.

4.6 Experimental test and Calibration

A gamma-ray densitometer was used to calibrate the optical probe. This was carried out in the flow loop using a two-phase mixture of water and air. The flow loop details and the calibration process are described in this section.

4.6.1 Experimental setup

A schematic of the flow loop and test section is displayed in Fig. 4.13 (a). Water was passed from the supply tank to the pump, where it could be transferred to the test section or returned, via the re-circulation line, to the tank. Water was moved through one of four nozzles with different diameters in a parallel arrangement. The nozzles allowed the flow rate to be measured to an accuracy of ±1%. The water flow rate's magnitude was controlled using a manual valve located in the re-circulation line.

The delivery of compressed air from the supply vessel to the test section was facilitated by one of two flow rotameters and valves. Measurements of the air flow rate supplied to the test section was made by the flow rotameters with ranges of 0-0.0039 and 0-0.034 kg/s to an accuracy of ±1.6%.

The movement of the two-phase mixture was upwards across the test section to a separator by way of the convergent section. Water was returned to the supply tank from the separator and the air was released to the atmosphere.

The test section contained five separable sections: a bubble generator, a convergent section, a settling length, the tube bundle and a second converging section, as shown in Fig. 4.13 (b). For observing the flow in the test section, a 12mm thick Perspex sheet attached by bolts was used.

The bubble generator contained two pieces of porous tube each with a length of 110 mm, an outside diameter of 50 mm, and a pore size of 206 μm. These tubes were positioned in a rectangular Perspex box 224 mm in height x 100 mm in depth x100 mm in width. The box received water through its base. Air was supplied from both sides of the porous tube. In this way a reasonably even two-phase flow mixture was produced. Entry of the two-phase flow mixture to the tube bundle was via the first convergent section and the 224 mm settling length.

The tube bundle comprised of 10 rows, with one full tube in the middle column and half tubes located on the walls for the purpose of reducing bypass leakage. The tubes were 50 mm in length, 38.0 mm in outside diameter and were arranged in an in-line layout with a pitch to diameter ratio of 1.32.

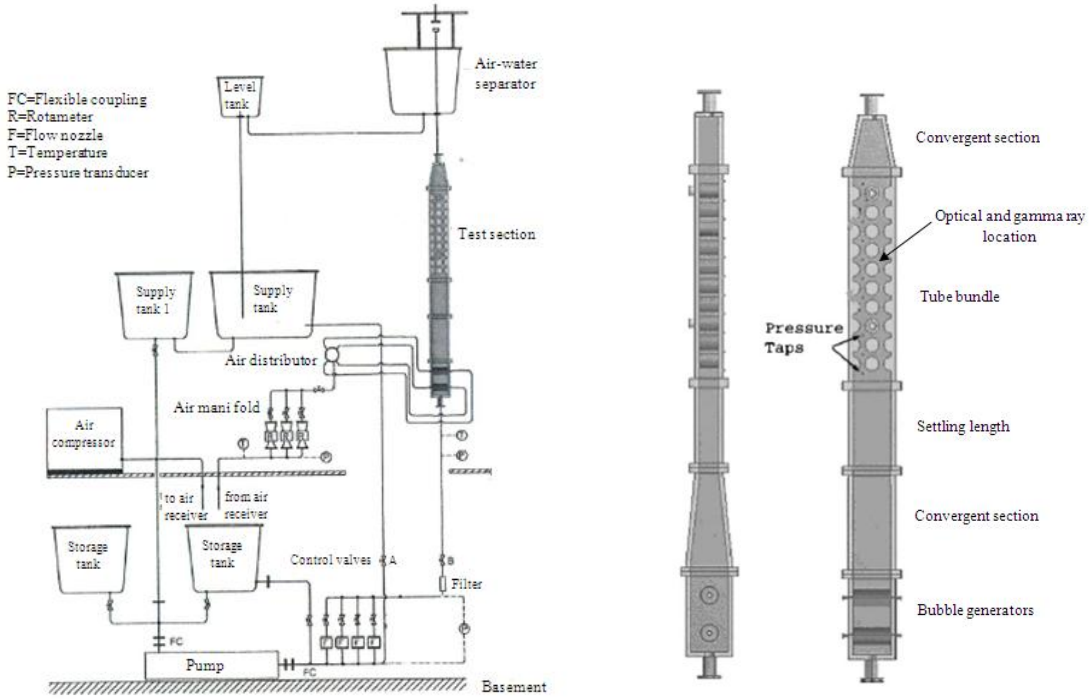

(a) **(b)**

Figure 4.13: Test flow loop layout and test section [80]

Measurement of the void fraction during the two-phase mixture test was conducted using a single-beam, gamma-ray densitometer, which contained the isotope Americium (Am) 241. The densitometer was positioned in the gap south-east of the central tube in row 7 of the tube bundle. A beam 10 mm in diameter was projected into the flow parallel to the tubes from the collimated low-energy source. The beam from the test section was incident on a photomultiplier tube where the radiation was measured using a PC card-based, electronically controlled pulse counter [80].

At the same flow conditions, the optical fibre probe was placed in the same position as the gamma-ray densitometer inside tube bundle and this permitted its calibration.

4.6.2 Experimental data

A number of tests were carried out to obtain void fraction data. Each data set contained gamma-ray and optical probe void fraction measurements that were obtained under the same nominal conditions. The tests were performed for a fixed total mass flow rate, so that for increasing gas mass flow rate, the liquid mass flow rate was decreased. For each data set nine gas mass flow rates were used.

The tests were carried out by adjusting firstly the water flow rate, and secondly the air flow rate to achieve the desired conditions. Measurements of the mass flow rates were then taken. Manuel readings of the air-flow rate were made, while the water mass flow rate was measured through a data logger connected to PC controlled by Lab VIEW software. Following this, and dependent on the data set used, the void fraction was measured.

4.6.3 Void fraction tests

Prior to carrying out the experiment, the gamma-ray densitometer was positioned in the gap south-east of the central tube on row 7. Background readings, I_B , were recorded before the Am241 source was installed . After installation, the air-only readings, I_G, were recorded. The water–only readings, I_L, were recorded after the water flow was set. The two-phase mixture readings, I, were recorded once the experimental conditions had been established. All readings were recorded via the densitometer's software, using the electronic counter inside the PC. Each point was the average of one hundred readings taken during a sampling period of 100s.

The void fraction, α, is defined as the ratio of the flow area occupied by gas to the total flow area and was calculated from these measurements using Chan and Banerjee [81]:

$$\alpha = \frac{\ln(I - I_B) - \ln(I_L - I_B)}{\ln(I_G - I_B) - \ln(I_L - I_B)} \tag{4.11}$$

For the data recorded using the optical probe the void fraction was calculated by the same procedure as in the initial test of circular rig, using Equation 4.10.

4.7 Results and discussion

Figure 4.14 compares the measurements of void fraction against quality for the gamma–ray densitometer and optical probes. With increasing quality, the void fraction increases. A notable observation is that similar void fraction profiles are obtained using both measurement instruments when the threshold line for the optical measurements is chosen to be -4.37 V.

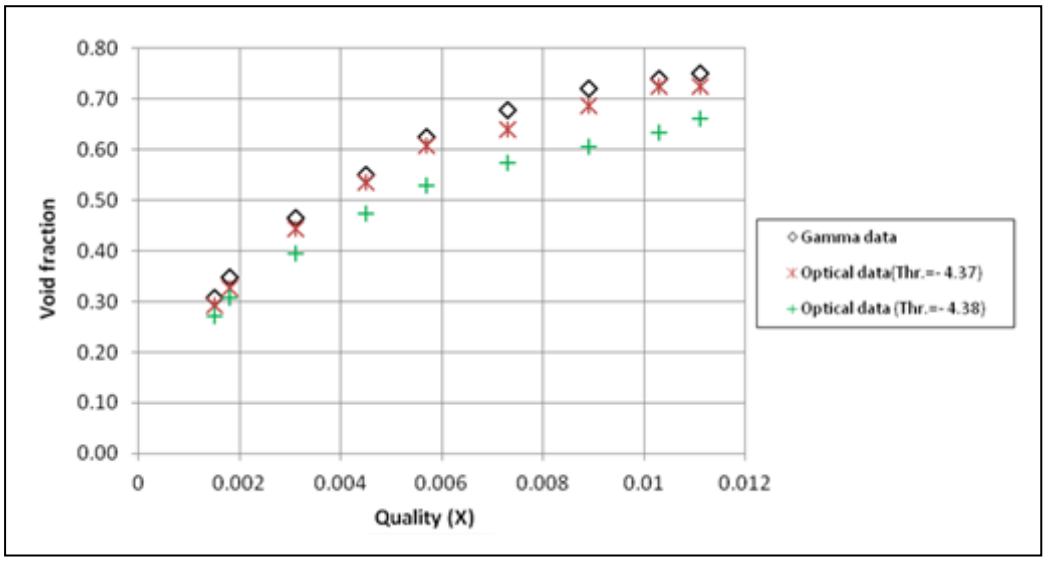

Figure 4.14: Comparison of void fraction measurements made with the optical probe and gamma ray densitometer under the same flow conditions.

This present experiment has shown that the optical probe is suitable for measuring the void fraction in two-phase flow. It will be necessary to further develop the geometry of the probe to allow it to be used to make measurements of the void fraction in boiling fluid inside the kettle reboiler. The central issue that arose in using the optical probe was deciding how the threshold level for the analysis of optical void fraction data should be determined. The construction of the tube bundle in the water-air rig test from Perspex facilitated the use of gamma rays. It was thus straightforward to compare void fraction measurements from the gamma ray and the optical probe to determine the threshold level (the transition between air and water) needed for the optical probe. To determine the effect of threshold line selection on the void fraction measured by the optical fibre probe two thresholds levels were chosen (-4.37 V and -4.38 V) in the experiment. Figure 4.15 illustrates a typical signal pattern obtained from the tube bundle

in the water-air test rig. A threshold line is indicated in Fig. 4.15 (a) whereby all data values higher than the line were set to one (gas-phase), and those lower were set to zero (liquid phase), as shown in Fig. 4.15 (b). As discussed earlier the void fraction data were calculated using Equation (4.10). When the value of threshold line was set at -4.37 V a good agreement was obtained between the void fraction measurements from the optical probe and the gamma ray method. However, when the threshold was decreased by just 0.01 V to a value of -4.38 V a large divergence between the measurements was observed. When the threshold value of -4.38 V was used the void fraction measured by the optical probe is lower than that by gamma rays, and this difference increases with increasing void fraction. Hence, a higher threshold level (-4.38 V) leads to a smaller void fraction as smaller bubbles are not counted. Therefore the accuracy of the void fraction measurement obtained from the optical probe is strongly dependent on the threshold line chosen. For measuring the void fraction in the kettle reboiler, gamma rays were ineffective because the back and side walls of the boiler were metallic. The walls did not allow the passage of gamma rays to the receiver, and therefore void fraction measurements could not be made or compared to those made using the optical probe. It is recommended that the walls of the kettle reboiler be constructed out of transparent materials so that accurate void fraction measurements can be obtained.

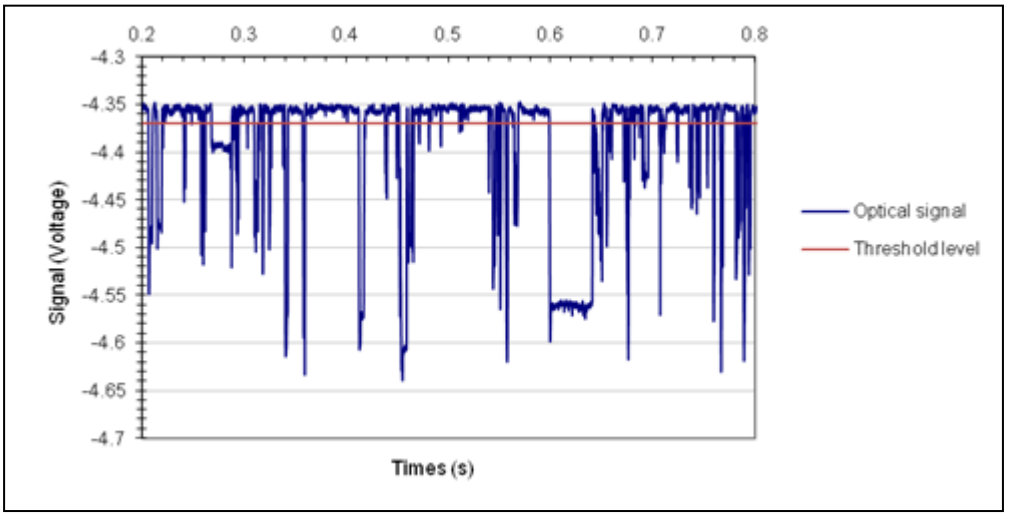

(a)

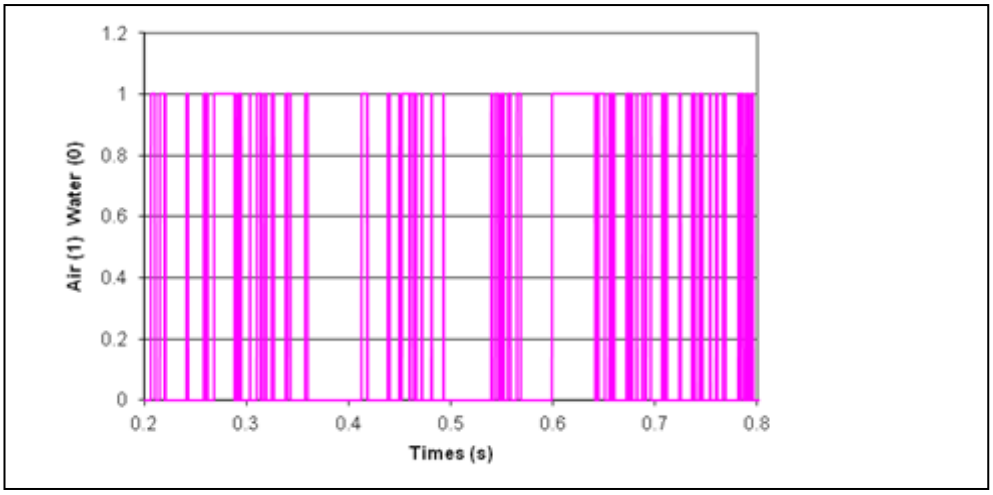

(b)

Figure 4.15: Typical voltage signal obtained before (a) and after (b) the threshold line was drawn for the air-water test rig.

It is worth noting that in previous studies optical probe measurements have also been calibrated by a comparison to those obtained from other instruments, e.g. Spindler et al. [82] calibrated the void fraction measurements they obtained with an optical probe using those measured by the gamma ray method. Morris et al. [72] have demonstrated that optical probes are suitable for making void fraction measurements by validating them with quick closing valve measurements. Hammad et al. [73] have compared the void fraction measurements made by the optical fibre probe to those measured using the thermal probe technique of X-hot wire anemometry.

4.8 Summary

An optical fibre probe has been developed and applied to measure void fraction in gas–liquid flows in a bubble circular rig and water test rig. The operating principle of these probes is based on the difference in refractive indices between the gas and liquid phases. If the probe tip is immersed in vapour or air then the probe's light is reflected back into the fibre. By contrast, in the presence of liquid, light exits the tip of the probe. The most important aspect of this work was to study the response of the optical probe in controlled situations. In order to improve the design of the probe, and accurately interpret the data it provides, it is necessary to develop a better understanding of how the optical probe interacts with bubbles. Threshold level analysis techniques have been used to analyse the optical signal. These techniques are based on specifying stable

signal levels that correspond to either of the phases. The set of experiments in these tests has shown the suitability of a normal cut fibre optic probe for measuring the local void fraction and the calculation of this property has been discussed. Testing of the optical probe has been performed in a tube bundle with an air-water mixture, and the void fractions obtained are comparable with those obtained using a gamma-ray densitometer under similar conditions. The present study shows that the accuracy of the void fraction measurements obtained by the optical probe was significantly dependent on the threshold level that was chosen to function as a discriminator between the liquid and gas phases.

4.9 Suggestions for future work

It is necessary for more work to be carried out to improve the use of the optical probe developed in this study for accurately measuring void fraction. A wetting film develops infrequently on the tip of the optical probe. This requires further investigation to get a clearer view of the difference between the gas and liquid signals. The use of an optical probe to measure the void fraction of boiling fluid in the complex geometry of the kettle reboiler requires an appropriate method to determine the threshold level procedure to analyse the data. Therefore, void fraction measurements taken with the optical probe will have to be verified, or calibrated, possibly using the gamma ray densitometer inside the kettle reboiler to determine the threshold level for optical void fraction data. After selecting a threshold level technique, the experimental work must then focus on selecting different positions in the kettle reboiler to which the optical probe will be fixed. A large number of two-phase experiments will need to be carried out to investigate the void fraction and flow pattern within the tube bundle and in the region of the shell. The void fraction data obtained can be compared with previous two-phase void correlations to check the match and to help develop a new void fraction correlation for the tube bundles. These results can then be compared with the data obtained from the CFD model in order to examine its capability.

CHAPTER 5

Experimental Results and Analysis

5.1 Introduction

Flow boiling tests were carried out in the kettle reboiler using pentane at atmospheric pressure with a boiling temperature of 36.1 ^{o}C, at uniform heat fluxes of 10, 20, 30 and 40 kW/m^2. These tests were done to investigate the flow regimes and pressure drop within and across the bundle.

5.2 Flow pattern

In gas-liquid two-phase flow, various flow regimes exist. These are known as flow patterns. The impact of the different flow patterns can significantly affect the pressure distribution for the same mass flow rate within the tube bundle. To improve two phase flow design, designers should identify and differentiate the flow regimes properly. Within the tube bundle, the two-phase flow regime can vary with position and it is very important to know which regions of the bundle are in what flow regime. There has been considerable work done on two-phase flow in circular tubes. However, in bundles few experimental studies have investigated two-phase patterns. This is because the local measurements required for flow regime identification in the tube bundle are not easy to make. Consequently, the experiments have mainly involved visual observation of two-phase flow regime from outside of the bundle. In the present study, the flow patterns were observed by visual observation of pentane two-phase vertical upflow across a horizontal tube bundle. These flow patterns are described and illustrated below.

5.2.1 Flow pattern at 10 kW/m^2

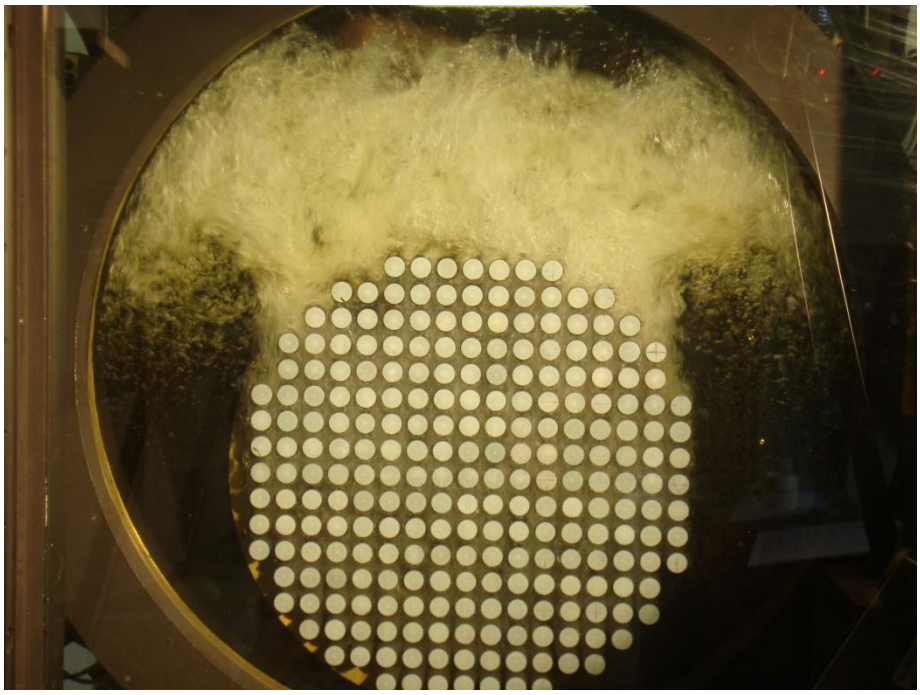

Figure 5.1: The kettle reboiler at heat flux 10 kw/m^2

Figure 5.1 shows the flow of pentane boiling at a heat flux of 10 kW/m^2.The flow within the bundle is mainly vertical. Above the bundle, there is a high voidage region (foam) whose width decreased with the bundle width before expanding to fill the width of the shell. It does not reach the top of the shell. The fluid exiting the top of the bundle causes a recirculating entrainment vortex near the top corners of the bundle. The entrainment vortex was found to move up and down in the boiler and was in phase with the foam oscillation. The liquid is separated from the vapour above the bundle and moves down between the bundle and shell. The liquid recirculation entrained very little vapour and the fluid at the sides of the shell is predominantly liquid. In the gap between shell and tube bundle most of the fluid is in a liquid state. Vapour is generated from the bottom row and the spaces between tubes are mainly filled with vapour.

5.2.2 Flow pattern at 20 kW/m^2

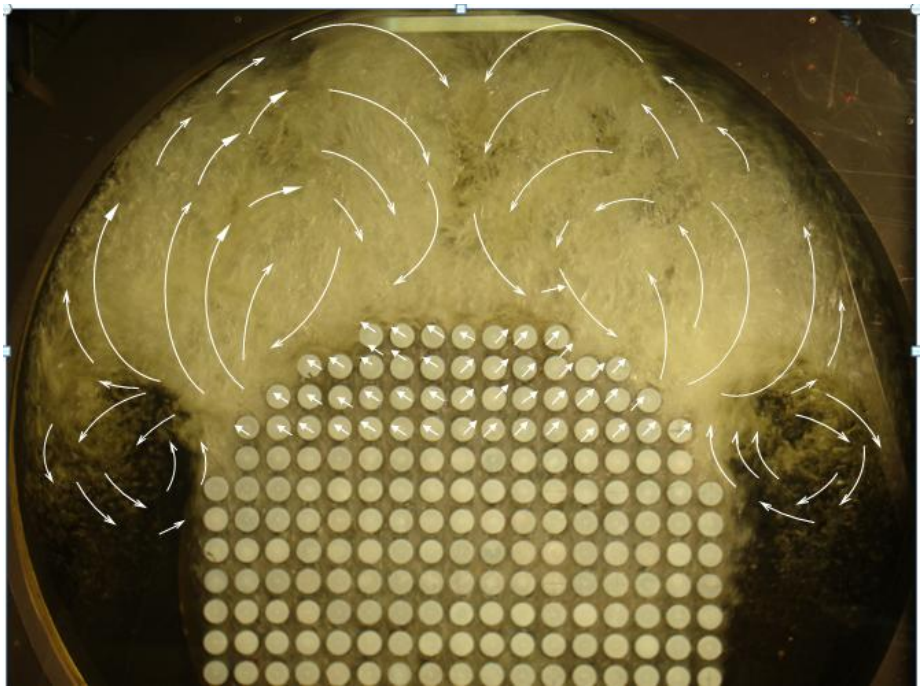

Figure 5.2: The kettle reboiler at heat flux 20 kw/m^2

The flow pattern for a heat flux of 20 kW/m^2 is shown in Fig. 5.2. In this case, there is no longer a vertical flow observed in the middle column of tube bundle. Towards the top rows of the bundle, lateral flow was caused by the separation that occurs between the vapour plume and liquid such that the liquid moves across the bundle. The main flow moves to reach the top shell corners, leaving from above row 14. Because of this phenomenon, a large vapour plume is produced above the tubes bundle. In comparison with the 10 kW/m^2 case, a larger foam quantity is observed above the bundle and occupied all of the space above it. In both bundle corners, the formation of two circulations is clearly observed, with the centres of these circulations close to the bundle's top corners.

A down-flow was observed between the bundle and shell. This flow vortex occurs because of the variation in density between the two phase flow in the tube bundle and shell [58]. At the sides of the bundle, the vortices are much further down to about row 10. The liquid was recirculated towards the centre of the bundle below the vortex. During the test the directions of the flow were captured using a video camera and drawn as white curved arcs in the upper part of the kettle reboiler. In this way the flow regime was detected.

5.2.3 Flow pattern at 30 kW/m^2

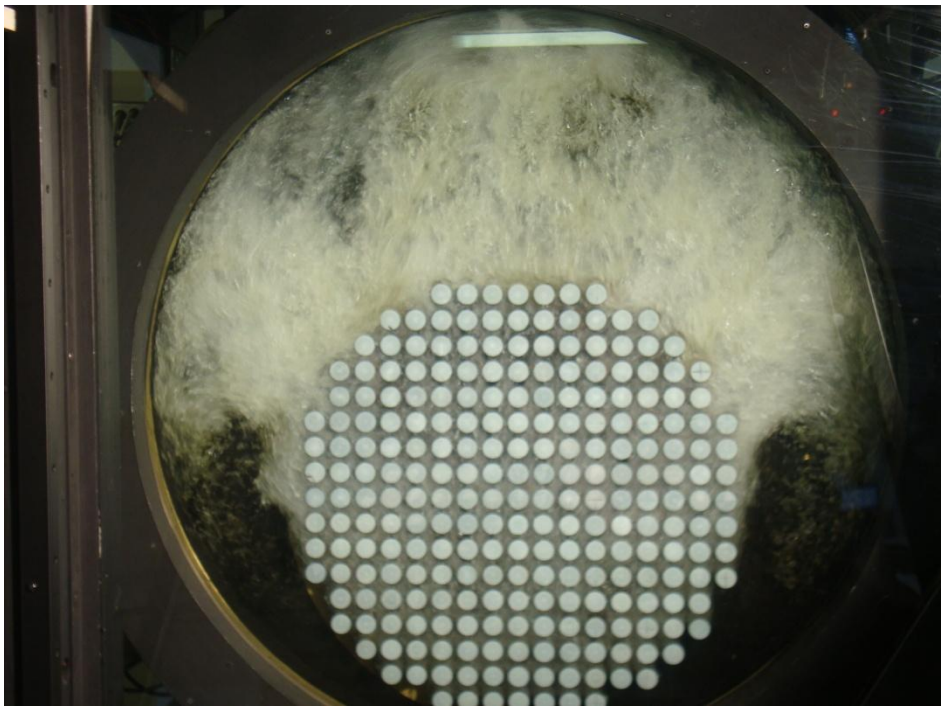

Figure 5.3: The kettle reboiler at the heat flux 30 kw/m^2

Figure 5.3 shows the flow pattern for a heat flux of 30 kW/m^2. A highly chaotic flow is shown above the bundle, which is totally filled with foam. There are two re-circulation regions contained two vortices in opposite directions. Roughly from row 12, fluid leaves the bundle and separates into two streams at the shell wall, developing two vortices, one moving upwards and one downwards. The upwards portion from each side of the bundle couple together at the top and fall down onto the bundle, creating streams that move around the top rows until they reach about row 9. In this region, the two streams are connected with the flow coming from the bottoms rows then moving towards the shell wall. The downwards portion of the flow produces entrainment vortices at approximately row 7. The liquid phase flows with few bubbles, extending downwards from row 10.

5.2.4 Flow pattern at 40 kW/m^2

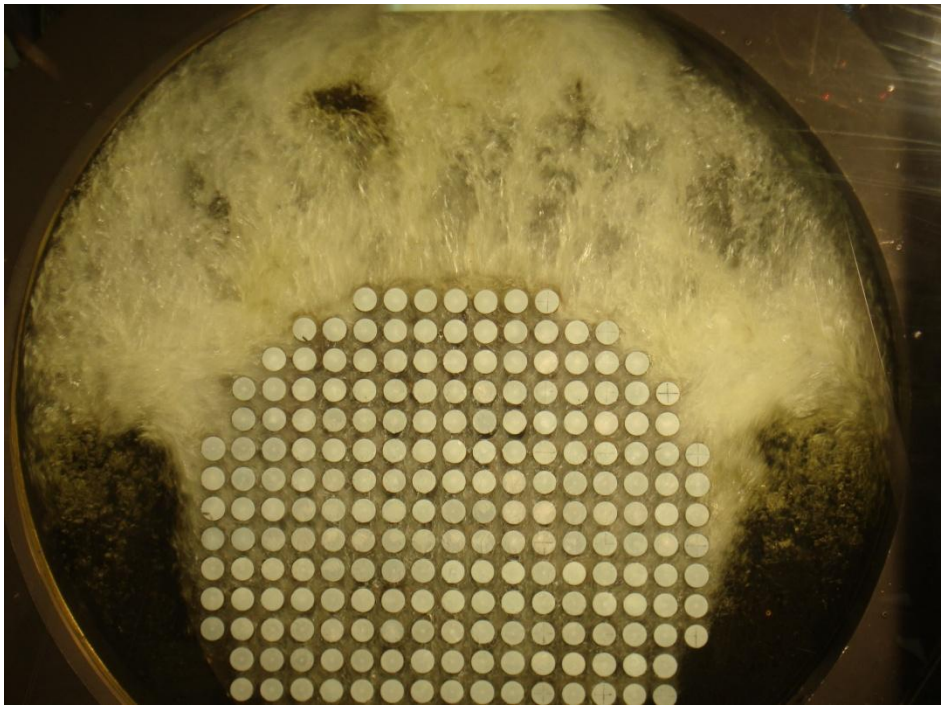

Figure 5.4: The kettle reboiler at a heat flux of 40 kW/m^2

Figure 5.4 displays the flow pattern at a heat flux of 40 kW/m^2. This has approximately the same flow behaviour as the pattern seen at 30 kW/m^2. The foam fills the space above bundle with high flow intensity which creates more recirculation above and at the side of the bundle. The recirculation rates are observed to be more than the previous cases at the bottom of bundle. The recirculation entrainment vortex is now at row 7. Below this the space between the bundle and shell wall is filled with liquid with few bubbles.

5.2.5 Flow pattern between bundle tubes

A photographic study was made in the kettle reboiler between tubes within the bundle. A high speed camera was used to investigate these flows. A Kodak high speed camera with a variable framing rate from 10 and 10,000 fps was used in this study. This camera enabled the motion of the working fluid and the flow pattern inside the kettle reboiler to be studied. The local flow patterns at heat fluxes of 10, 20 and 30 kW/m^2 were recorded. Many video sequences were taken at different heights within channel 10.5 see Fig. 3.3. Figure 5.5 (a) displays the image taken, between row 2 and 3, at a heat flux of 10kW/m^2. Bubbles are present in this region. The movements of the bubbles were mainly vertical. Generation of bubbles from the tube walls is clearly visible. Their

movement continued towards the rows above as a result of the influence of buoyancy. Figure 5.5 (b) shows a large flow of small bubbles existing between rows 9 and 10. Figure 5.5 (c) shows the flow between rows 15 and 16. The bubbles' motion became stronger, and they collide with other bubbles and the tube walls. This was predominantly because of the effect of higher turbulence on the flow following collisions. The bubbles followed the tube surfaces and circulation does not occur in this region. This was due to the large influence of buoyancy on the two-phase flow. The type of flow pattern observed throughout the bundle at a heat flux of 10 kW/m^2 was a bubbly flow.

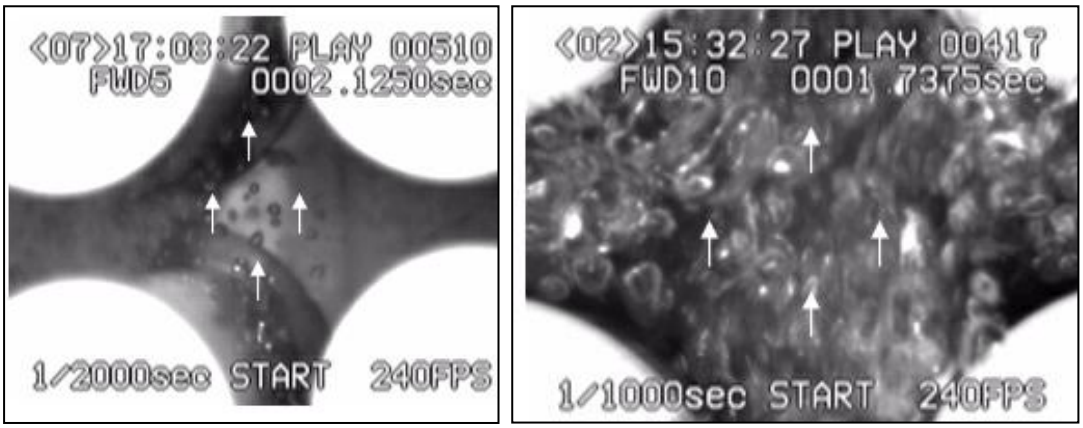

(a) Between rows 2 and 3 **(b)** Between rows 9 and 10

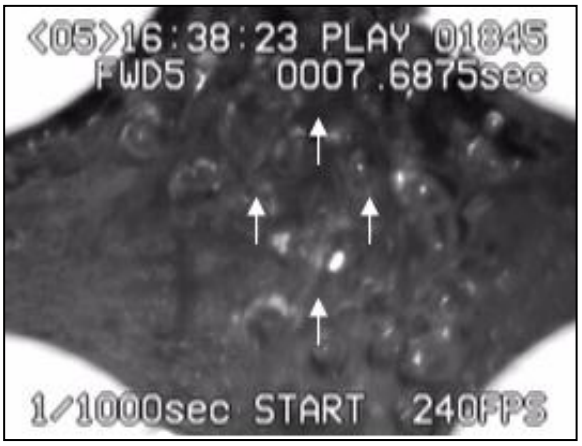

(c) Between rows 15 and 16

Figure 5.5: Flow between in the vertical channel 10.5, of the bundle, at 10 kW/m^2 .

The gas distribution was roughly uniform, with the bubbles having the shape of separate spheres within the liquid.

This result is consistent with the observation of McNeil et al.[58]. They showed that the static liquid pressure at the edge of the tube bundles controlled the two-phase flow when the flow was bubbly.

The following observations were made at a heat flux of 20 kW/m^2: Bubbles in the bundle's middle region became larger and elliptical in shape, as shown in Figure 5.6 (a). As the flow turbulence increased bubbles accumulated behind the tubes and the bubbles were appeared to circulate in flow that in these regions. Bubbles were not uniformly distributed in the cross-sectional area between the tubes, as shown in Fig. 5.6 (a).

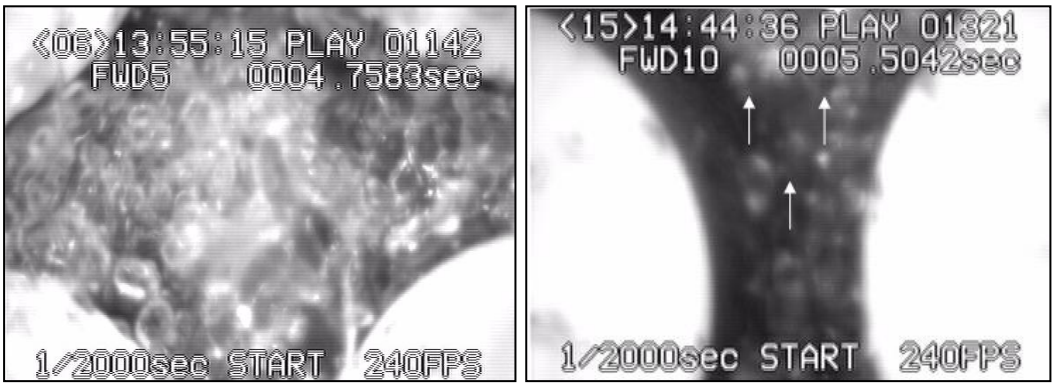

(a) Between rows 9 and 10 (b) Between rows 15 and 16 (up)

(c) Between rows 15 and 16 (down)

Figure 5.6: Flow between in the vertical channel 10.5, of the bundle, at 20kW/m^2.

By raising the heat flux, the gas velocity became higher and the tube surfaces together with the area between them were coated by a thin layer of liquid and a quantity of liquid was carried by the vapour as small drops.

In this case, the flow could be described as a chugging flow, due to its composition of very large bubbles, or slugs, and smaller bubbles. Above the bundle, a large frothy circulation existed and, due to droplet flow from the plume, a strong liquid down flow into the top of the bundle occurred. This flow can be described as an intermittent flow. This down flow seemed to change the direction of the flow from up to down in this region, as shown in Fig. 5.6 (b) and (c). A quantity of flow appears to move horizontally towards the shell; possibly because of the low magnitude of the drag force experienced by the liquid from the gas during the high oscillation condition. In other words, the lateral flow may be caused by the flow pattern being altered to intermittent from bubbly. McNeil at al.[58] asserted that the alteration to intermittent from bubbly flow coincided with a change from constant to declining column pressure. These photographs confirm this.

The following observations were made at 30 kW/m^2. The bubbles look even more ellipsoidal, as illustrated in Fig. 5.7 (a). Extremely turbulent flow developed inside the tube bundle and as the bubbles grew, they slid over the tube circumferences. At the tubes' cross section the distribution of bubbles was more extensive, and behind the tube bundle the liquid single–phase area decreased. These bubbles may be produced by the tube itself or the main flow.

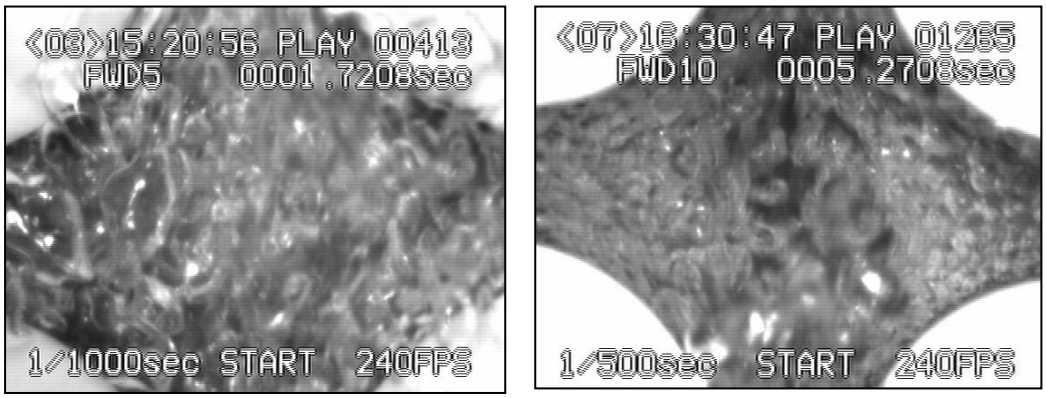

(a) Between rows 9 and 10 (b) Between rows 2 and 3

Figure 5.7: Flow in the vertical channel 10.5, of the bundle, at 30kW/m^2

The flow between tubes was observed to oscillate vertically, consistent with intermittent flow. In the upper region of the bundle, liquid emerged above the rows of the top tubes and reached a certain height then, due to gravity, dropped down again.

As a result of the falling liquid on the tube tops, films developed at the bottom. At a higher heat flux the two-phase flow became unstable, and the presence of a pulse suggests the existence of an intermittent flow. Two regions were observed in the tube walls, one covered by a film of liquid and the other region was filled by small separated bubbles, as shown in Fig. 5.7 (b).

Dry out may occur with very poor heat transfer, and thus a large oversized shell is used to separate the liquid droplets from outgoing vapour. This leads to the complete prevention of liquid evaporation without carryover.

A complete understanding of the details of the actual flow pattern has yet to be achieved. There is a need for more information about the void fraction distribution in the kettle reboiler.

5.3 Pressure drop

The two-phase pressure drop is considered an essential parameter required for effective kettle reboiler design. An accurate prediction of the pressure drop of boiling fluid is needed in determining the pumping power, pressure profiles, allowable pressure drop for a given design, and other design factors. In this study, pressure drop measurements were made between the bottom centre tapings (number 8), and the other tapings as shown on Fig. 3.3. From these measurements, the pressure drop between adjacent tapings can be calculated over two tube rows. Pressure tappings in three locations, 9.5 (between columns 9 and 10), 12.5 (between columns 12 and 13) and 15.5 (between columns 15 and 16), where used for the measurements, which can be seen in Figure 3.3. With this arrangement, the gravitational pressure drop of a column of saturated pentane, at atmospheric pressure, between adjacent tappings for two rows was 304.3 Pa. These pressure drop measurements are described and illustrated below.

5.3.1 Pressure drop at 10 kW/m^2

The measured two-row pressure drop against row number at a heat flux 10 kW/m^2 is shown in Fig. 5.8. The pressure drops in centre column 9.5, Fig. 5.8 (a), were found to be almost constant and close to the static liquid value of 304.3 Pa until row 14 and then decreased with row number. In this central column, the uniform pressure drop took place with increasing void fraction. The minor changes in pressure drop occurred due to variations in the gravitational pressure drop term, (ΔP_{grav}) and the frictional pressure drop term (ΔP_{fric}). Near the central column, the experimental pressure data agreed well with the predicted pressure drop from the 1-D model, see Fig. 5.8 (a) within the uncertainty of ±10Pa. In column 12.5, Fig. 5.8 (b), the pressure drop slightly fluctuates near the static head from row 3 to 14. In column 15.5, Fig. 5.8 (c), the pressure drop also maintains an almost constant value, close to the static pressure drop after row 9 minor variations occurred

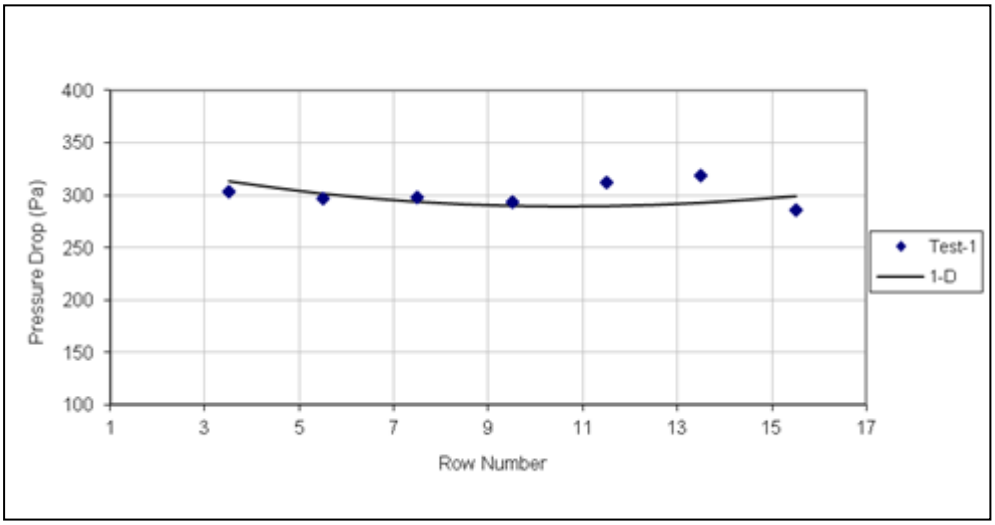

(a) Column 9.5

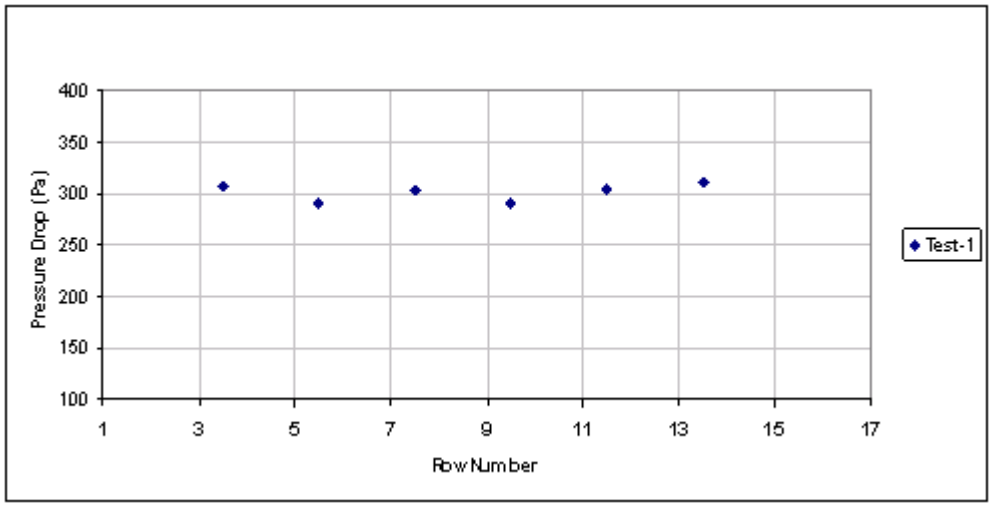

(b) Column 12.5

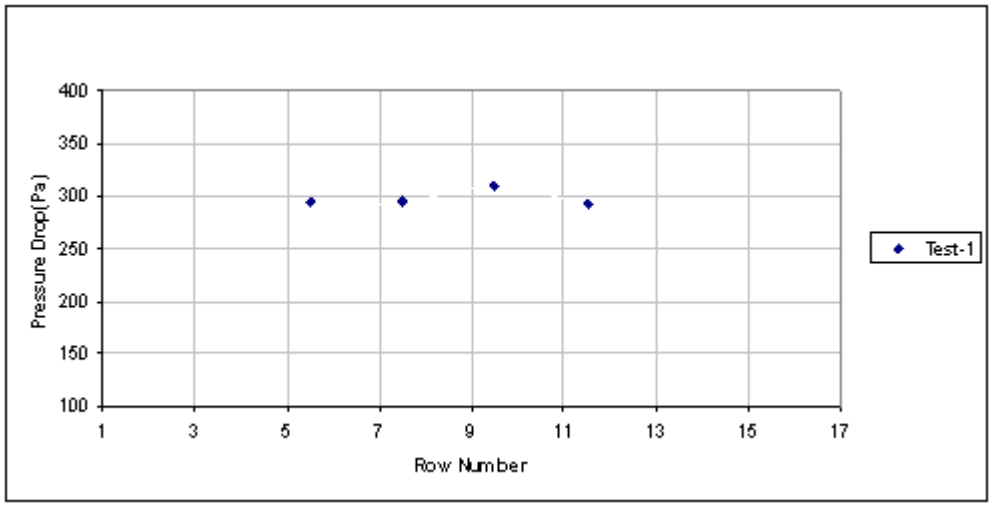

(c) Column 15.5

Figure 5.8: Pressure drop in the kettle reboiler at heat flux of 10 kW/m^2

5.3.2 Pressure drop at 20 kW/m^2

Figure 5.9 shows the measured two-row pressure drop distribution in the three columns for heat flux of 20 kW/m^2. Figure 5.9 (a) shows the behaviour of the pressure drop in column 9.5. The pressure drop up until row 12 is shown to be roughly equal to the static liquid pressure drop. Thereafter it decreases. In the bundle, the 1-D model assumes that mass fluxes in all columns result from a balance between the static liquid pressure head in the shell and the sum of the bundle's pressure drop components, gravitational (ΔP_{grav}) and frictional (ΔP_{fric}). After row number 12, the vertical mass flux would have to give a

reduced pressure drop. This would decrease and result in flow deviating towards the shell [58]. The reduction in the pressure drop indicates that the behaviour of the flow is two- dimensional as shown in the Fig. 5.2. Hence, the 1-D model is not able to predict the pressure drop accurately in the upper rows. In column 12.5, Fig. 5.9 (b), the pressure drop decreases and immediately changes to a constant trend after row 6, the pressure drop values are close to the static liquid pressure head. It may start to decrease after row 14. The minor variation in pressure drop up the channel was again due to variations in the frictional pressure drop (ΔP_{fric}) and the gravitational pressure drop component (ΔP_{grav}). Figure 5.9 (c) shows that the column 15.5 two-row pressure drops are approximately equal to the liquid static head. This might be due to lateral flow being prevented from moving further to the shell side. This obstruction of the lateral flow maintains the pressure drop almost constant in this column.

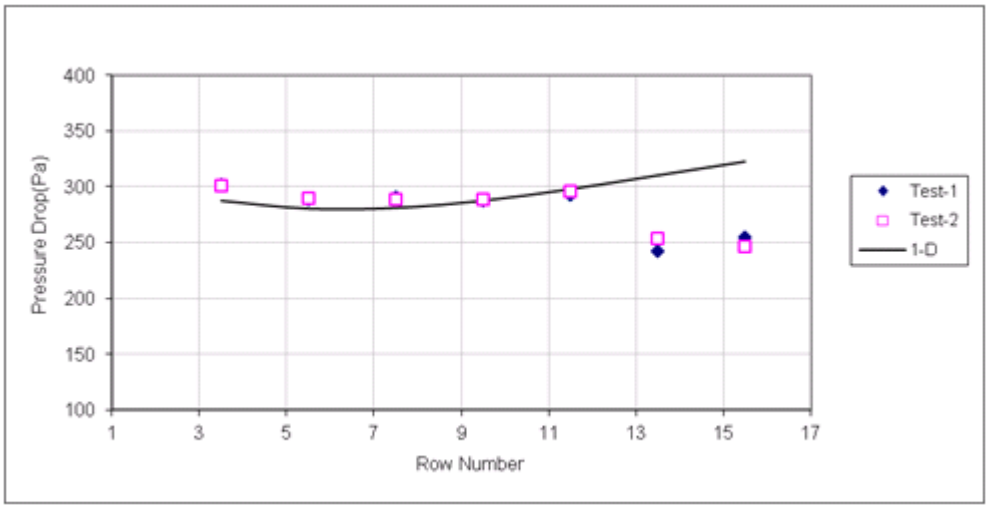

(a) Column 9.5

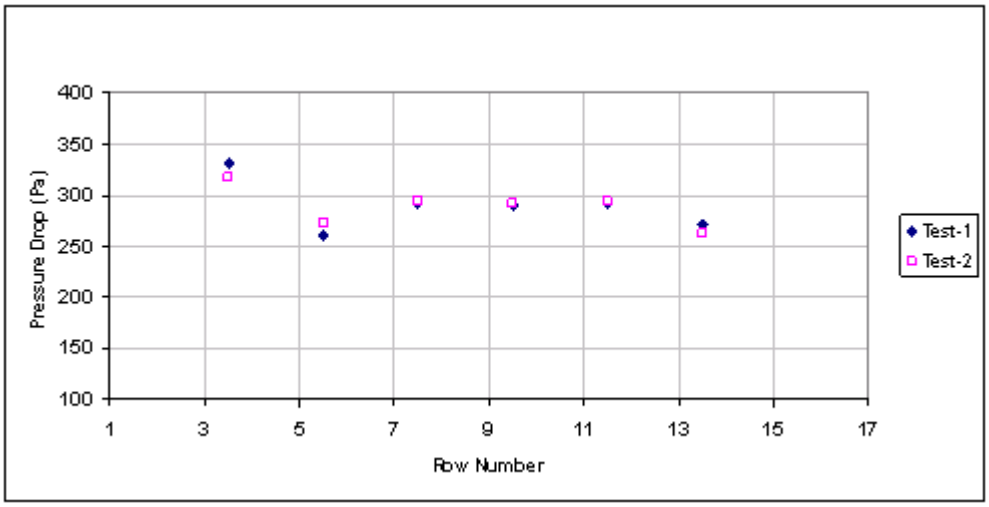

(b) Column 12.5

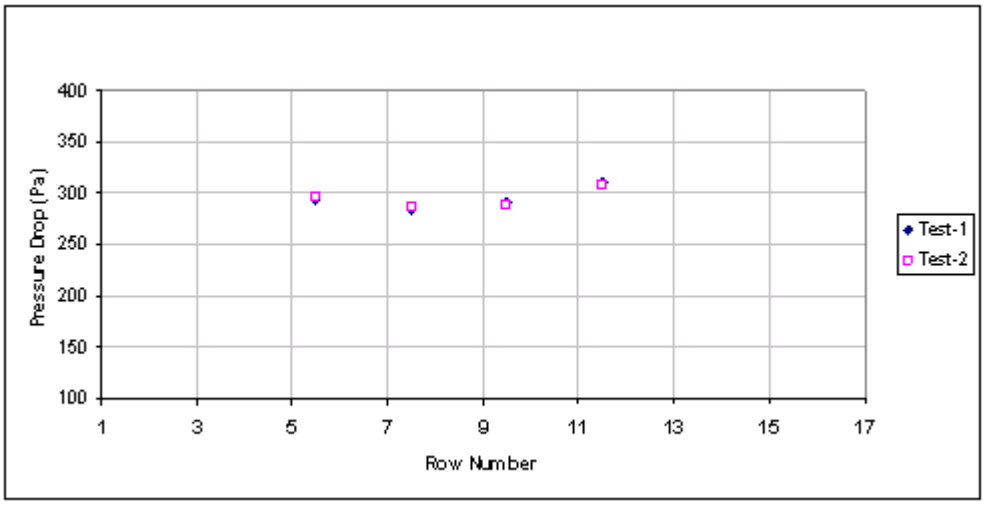

(c) Column 15.5

Figure 5.9: Pressure drop in the kettle reboiler at heat flux 20 kW/ m^2

5.3.3 Pressure drop at 30 kW/m^2

Figure 5.10 shows the experimental two-row pressure drop distribution in the three columns at a heat flux of 30 kW/m^2. Stronger boiling occurred and have led to the increased scatter observed in of the data, relative to those at lower heat fluxes. Figure 5.10 (a) shows the pressure drop decreasing with increasing row number in column 9.5. This decreasing trend of the pressure drop at 30 kW/m^2 is more significant than that which occurred at 20 kW/m^2. The pressure drop reduction with increasing row number indicates that more horizontal flow towards the shell is happening. As a result lower vortices were observed in the shell, as shown in Figure 5.3. In column 12.5, Fig. 5.10 (b), the pressure drop suddenly reduced at row 6 before decreasing more slowly until row 16. The change in the pressure drop was due to the effect of entrained vapour, and leads to a decrease in the gravitational pressure drop, $\Delta P_{grav.}$ In the case of column 15.5, Fig. 5.10(c), a very small change in the two-row pressure drop along the channel was observed. Again it is approximately the static liquid value 304.3 Pa.

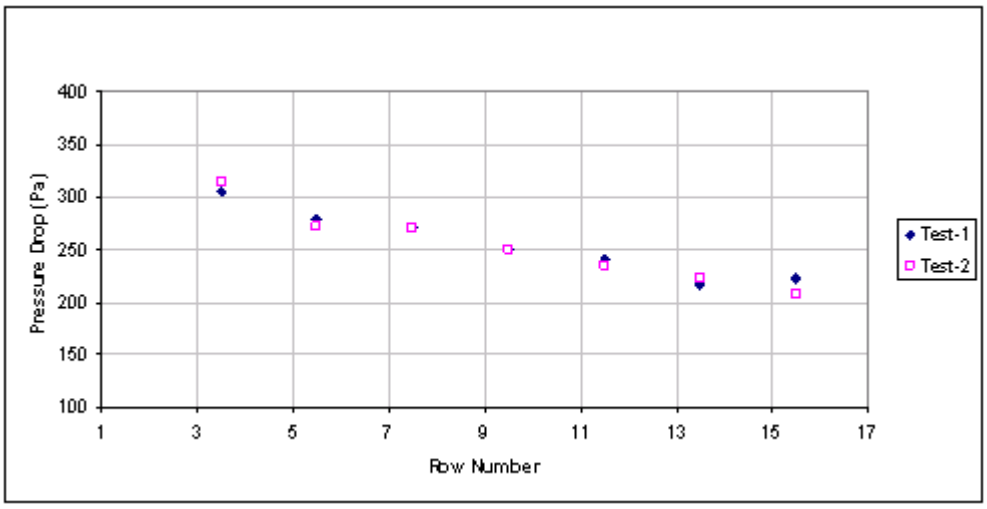

(a) Column 9.5

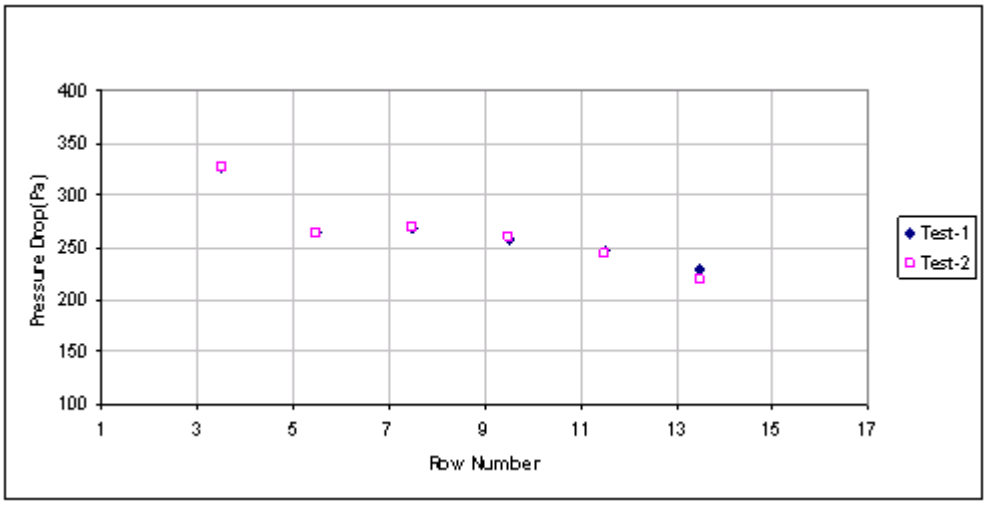

(b) Column 12.5

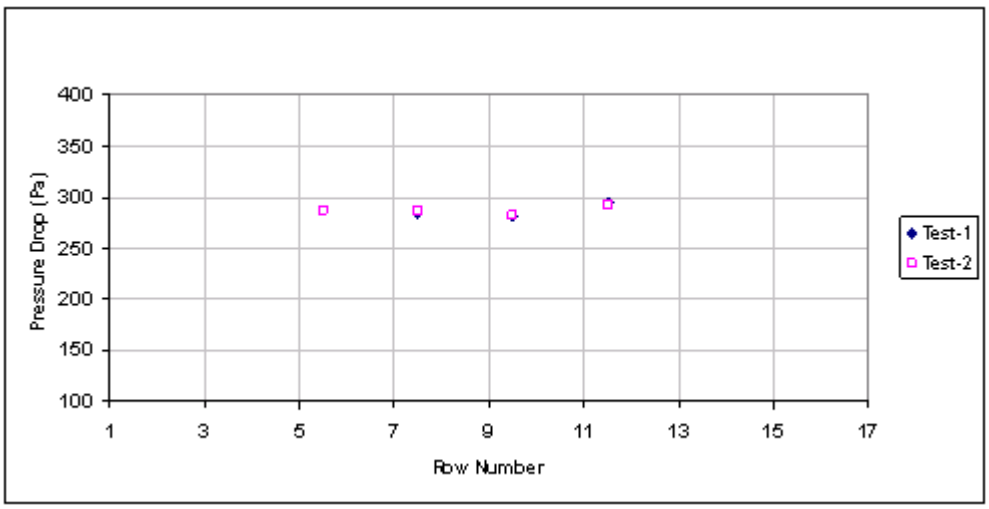

(c) Column 15.5

Figure 5.10: Pressure drop at heat flux of 30 kW/m^2

5.3.4 Pressure drop at 40 kW/m^2

Figure 5.11 displays the measured two-row pressure drop distribution at a heat flux of 40 kW/m^2. For columns 9.5, 12.5 and 15.5, Fig. 5.11(a), (b) and (c) respectively, the general trend is a decreasing pressure drop with increasing row number. This corresponds to more lateral flow towards the shell than in previous cases. Within the central column 9.5 the larger pressure drops are caused by the pentane in this region having a higher void fraction and so producing a larger drop of the gravitational head, $\Delta P_{grav,}$ and hence the overall pressure drop was also decreased. In channel 15.5, the pressure drops decrease more slowly than in the other channels and this may be caused by the flow's interaction with the fluid located between the bundle and the shell wall. The reduction in the pressure drop that was observed for this case is greater than previous heat fluxes values. This indicates more predominant 2-D effects. The cause of pressure drops in the upper rows of the bundle was due to an increase in the foam levels on the bundle's top and sides. Therefore, the foam reduces the gravitational pressure drop, ΔP_{grav} and it is greater than the rise in ΔP_{fric} that further reduces the overall pressure drop.

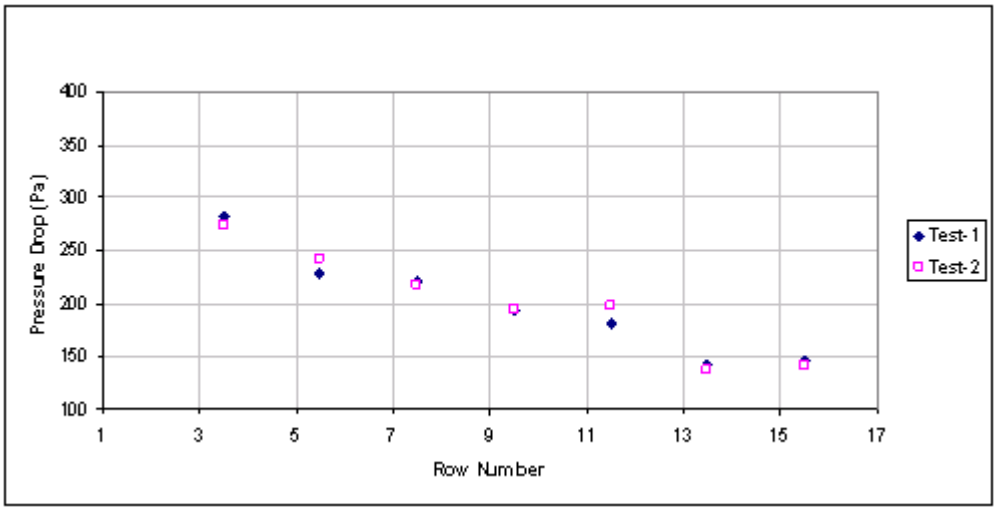

(a) Column 9.5

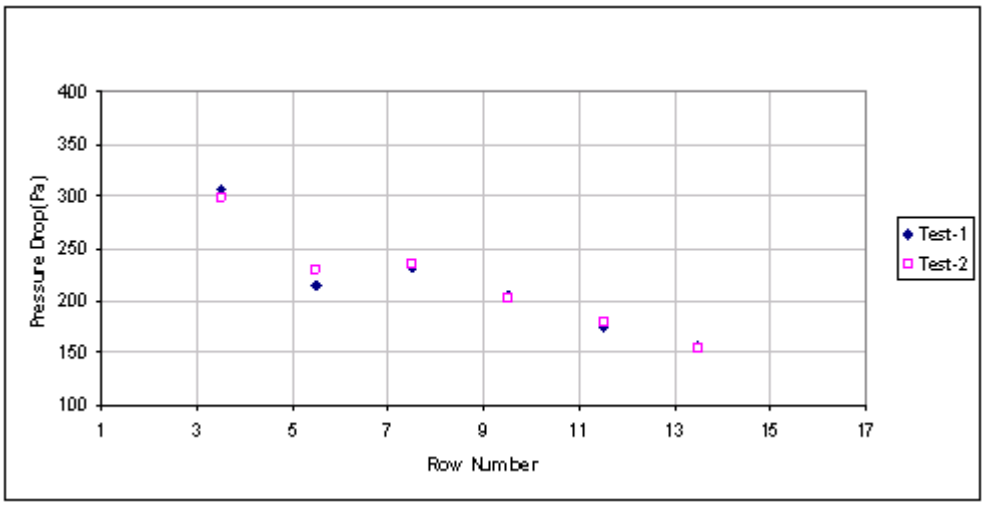

(b) Column 12.5

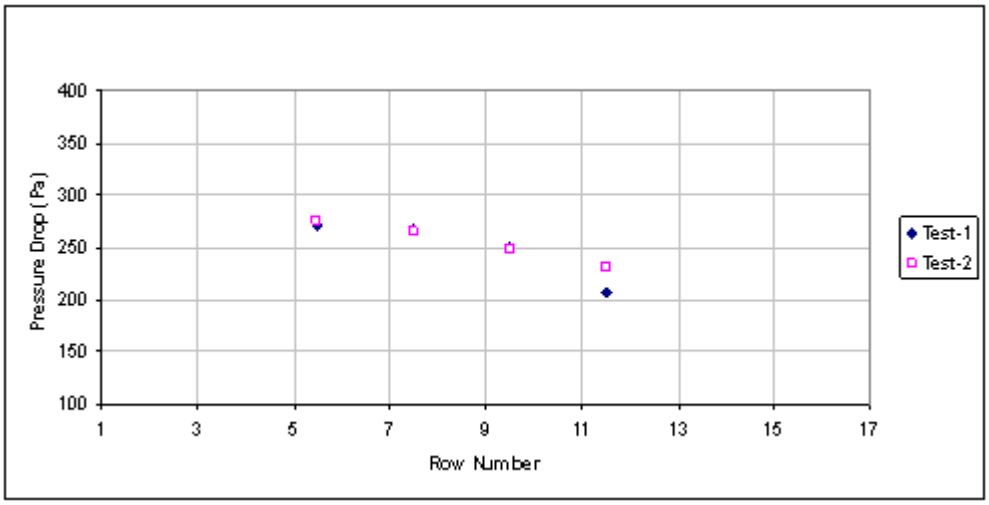

(c) Column 15.5

Figure 5.11: Pressure drop in the kettle reboiler at heat flux of 40 kW/m^2

5. 3.5 Comparison with previous investigations

Miller [15] has analysed the pressure drop measurements made across the same tube bundle and showed that within the centre columns the pressure drops were roughly uniform up the bundle and the data was very near to the static liquid pressure drop (304.3 Pa) at a 10 kW/m^2 heat flux. At a heat flux of 20 kW/m^2, the pressure drops were roughly uniform in the first ten rows, and then decreases with increasing row number.

The present study shows a good agreement with Miller's study as can be observed from Fig. 5.12.

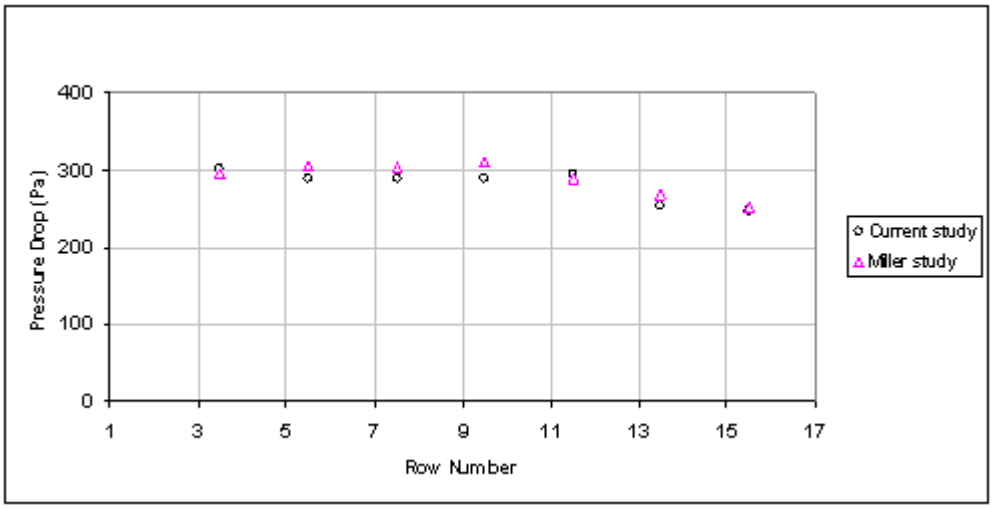

Figure 5.12: Comparison between pressure drop from current and Miller study at 20 kW/m^2

Figure. 5.13 shows a comparison of Miller's data and the data from this study at a heat flux of 40 kW/m^2. A significant reduction in the pressure drops of the current data is shown relative to Miller's study. The difference was caused by taking a larger sampling time than in Miller's study. It proves that Miller's sampling time was too short to achieve a true average. However, both data sets show that the pressure drops decrease significantly, again demonstrating a large increase in lateral flow. Shire [6] and Miller [15] argued that the reduction in the pressure drop in the kettle reboiler was related to the decrease in gravitational pressure drop being higher than the rise in frictional pressure drop. They pointed out that the existence of a lateral flow reduces the pressure drop because as the net vertical mass flow rate is reduced, it mainly affects the contribution of the frictional and the gravitational pressure drops.

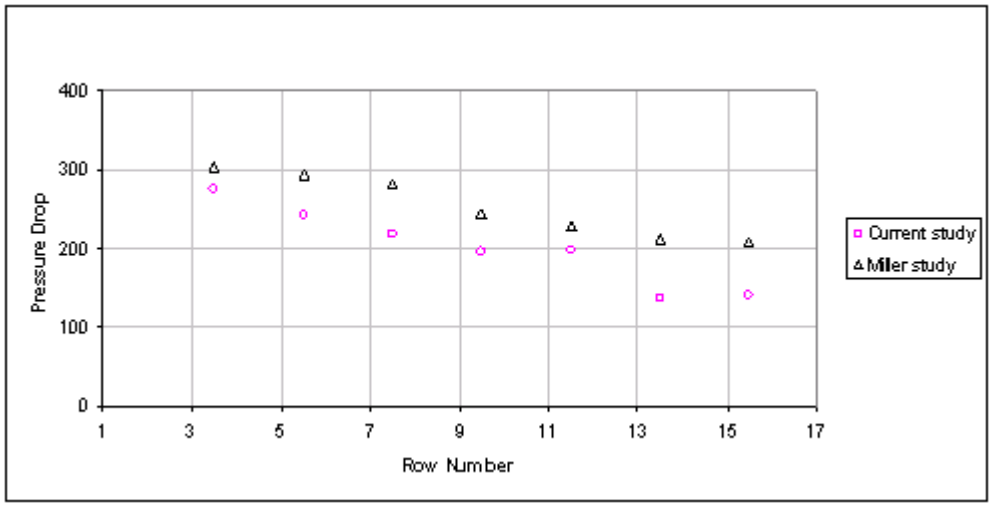

Figure 5.13: Comparison between pressure drop from current and Miller study at 40 kW/m^2

Bamardouf [10] investigated the pressure drop across the tube bundle using R113 in the same test section. He also observed that the pressure drop was uniform at a heat flux of 10 kW/m^2, and close to the static liquid value. At a heat flux of 40 kW /m^2, the pressure drop decreased significantly from the static pressure drop of 750 Pa, similar to the results from this study. Bamardouf [10] compared his results with Miller's n-pentane data and suggested that the difference was due to differences in the working fluids' properties causing a lower reduction in pressure drops and a similar quantity of foam. Gebbie and Jensen [34] used R113 to measure the pressure in a half shell kettle reboiler. In the bundle's lower rows, the pressure in the central channel was lower than the pressure on the bundle's edge. At the top rows of the bundle, this trend was reversed. In this present study, a similar experimental trend was observed. The present experimental pressure drop data were different from Gebbie and Jensen pressure drop measurements. At 30 kW/m^2 the central channel's pressure drop in the present study (over row 8) was found to be 260.5 Pa, or 86% of the static liquid pressure drop of pentane. Whereas Gebbie and Jensen observed that the pressure drop in central column (over row 6) as 600 Pa, about 33% of the static liquid pressure drop of R113 over the same height. Similarly, the two-phase flow patterns of Gebbie and Jensen [34] were found to be different to the present experimental studies. In Gebbie and Jensen's [34] studies, entrained vapour bubbles at the shell side reached a level lower than those observed in the current work. Gebbie and Jensen [34] also noted that at 10 kW/m^2, bubble movements were observed at rows in the shell, around 60% of the bundle height. In the 30 kW/m^2 case, some of the bubbles entrained at the tube bundle's base. The current

work found that the movement of bubbles was noted at the 12th row of the shell for 10 kW/m^2, which is around 30% of the bundle height. In addition to that, the penetration of the bubbles from the bottom was not observed. The reason for the greater downward movement of the bubbles in Gebbie's kettle is probably due to the smaller size of their tube bundle (i.e. short pitch and fewer rows). The height of their tube bundle was 310 mm, compared to the 431.8 mm height used in this study. These configuration variations not only shift the movement of the bubbles, but also reduce the pressure drop in Gebbie's kettle. Burnside et al. [56] argued that the reason for the more downward direction of the bubbles' movement, together with the pressure drop reduction of Gebbie's reboiler, was caused by the reboiler outlet shape: a straight pipe. During boiling, this straight pipe outlet was not efficiently allowing the liquid separation from vapour compared to wide outlet of the present bundle.

5.4 Summary

- In general, the amount of the foam, the intensity of the recirculation and size at the bundle's top and sides varied based on the heat flux values and type of working fluid. Also the observed two-phase flow pattern in the shell indicated that down flow into the top of the tube bundle affects the movement of fluid from the centre column of the bundle.
- The pressure drop was generally found to decrease below the all-liquid value, as the height of the bundle increased, particularly in the centre column, due to increasing void fraction. This pressure drop was found to increase with an increasing value of the heat flux. In general, a change in the pressure distribution up the tube bundle from roughly constant to decaying with height results from flow regime variation.
- Flow regime observation and measurement of the pressure drop inside the kettle reboiler showed that the flow in the tube bundle must be two-dimensional above 10 kW/m^2.
- Various flow patterns have been identified within the bundle: bubbly and intermittent. When the heat fluxes are low, the smooth and stable flow of the two phase flow pattern is generally described as bubbly flow. For higher heat fluxes (> 10 kW/m^2), there was an unstable two phase flow that was observed to oscillate up and down. In this case, the high velocity flow emerged from the top

of the tube bundle and attained a certain height above the tube bundle before falling due to gravity. This upward and downward movement of the liquid were observed clearly in the upper tubes of the bundle. This behaviour was caused by a low drag force on the liquid from gas and was normally observed at high heat flux value (> 10 kW/m^2). Because of the above-described phenomenon the vapour slugs developed due to bubble coalescence. This kind of flow behaviour could be described as intermittent flow.

CHAPTER 6

Two-Fluid Model Development

6.1 The two-fluid model

From the literature review, it has been observed that there is a need to improve the accuracy of models that can effectively predict the overall performance as well as the local flow conditions in a kettle reboiler. In this chapter, a two-dimensional kettle reboiler model is developed and used to predict the flow patterns, pressure drop, void fraction and mass flux.

In the present research work, a two-dimensional model is considered instead of a three dimensional model of the reboiler. It is assumed that the two-dimensional vertical cross-section of a thin slice of the reboiler can be used to predict the three-dimensional flow within a kettle reboiler. The effect of changes in the fluid flow in the z- direction, is negligible, when compared to flow changes in the other directions. Apart from this, the selection of the two-dimensional model has several advantages over a three-dimensional model. It requires much less computational time and allows for simplification of the boundary conditions. Also, the experimental results are given as two- dimensional and this two-dimensional model provides a better comparison for the present two-dimensional data.

6.2 Description of the model

As a basic model for investigation and comparison, a two-dimensional slice of a kettle reboiler with a geometry identical to that used in the experiments was selected using a similar approach to McNeil et al.[7]. The shell diameter was 732 mm and the depth was 56 mm. The tube bundle, centre line was 110 mm below the shell centre. It contained 241 tubes, 19 mm in outside diameter and 56 mm in length arranged in 17 vertical and horizontal lines with an in-line arrangement and $P/D = 1.34$. Each tube bundle row consisted of a number of tubes. The number of tubes and distribution in each row is shown in Fig. 6.1 and Table 6.1. In this model, tube columns are numbered from the left shell wall to the right and tube rows are numbered from the bottom to top. An octagonal

shape was chosen for the bundle because it represented the bundle area simply and very well. This geometry is shown in Fig. 6.2.

Table 6.1: Number of tubes per row in the reboiler model

Tube Row (from the bottom of the bundle)	Number of Tubes
1,17	7
2,16	11
3,15	13
4,5,13,14	15
6,7,8,9,10,11,12	17
Total number of tubes	241

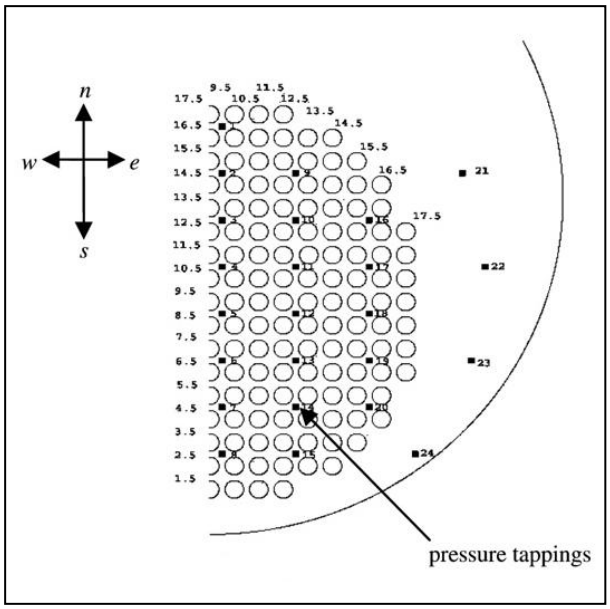

Figure 6.1: Tube and pressure tap distribution

6.3 Modelling approaches

To model the flow inside the kettle reboiler in 2D, various assumptions are presented. The kettle reboiler contains three regions, the tube bundle, the pool and the separation zone. The bundle is located in the middle of the kettle reboiler with the pool

surrounding its bottom and sides and the separation zone on top of it. All three regions form a single flow domain for which boundary conditions are specified. Based on the symmetrical nature of the domain, a symmetrical half of the kettle reboiler is used for analysis. Everywhere inside the kettle reboiler, the flow is a saturated liquid /vapour mixture. This condition eliminates the need to solve the energy equation [69]. For modelling the 2-phase fluid inside the bundle, a porous media is utilized. The modelled geometry and the applied boundary conditions are shown in Fig. 6.2.

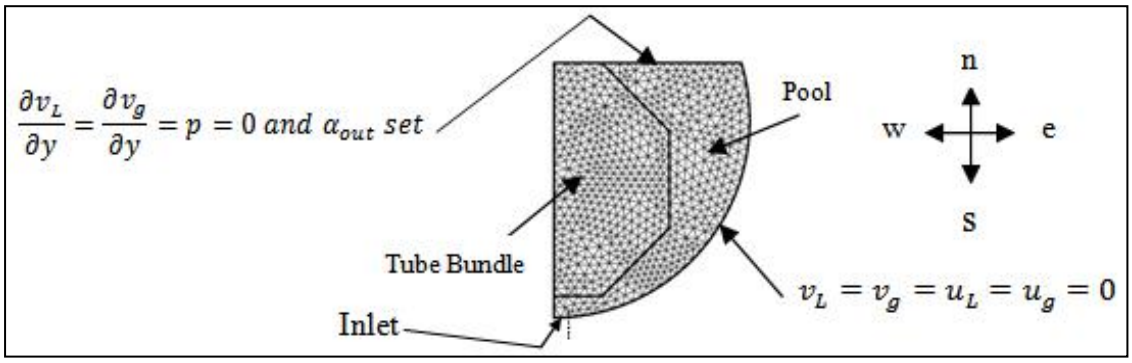

Figure 6.2: Mesh used in simulations

6.4 Boundary conditions

There are four boundary conditions, which need to be defined in the two-fluid model. These boundary conditions are symmetry, the shell wall, the inlet and the outlet flow boundaries.

- The west boundary is a symmetry plane at the centre line of the shell. It is modelled using the default boundary condition which allows no mass or momentum to cross the boundary.
- The east boundary is the shell wall with a smooth surface so there is no slip velocity for the liquid and vapour. On this face, both u and v components of both phases are set to zero.
- The inflow south boundary is set at the shell bottom. At the centre of the shell the liquid entering is specified as saturated to simulate the actual feed flow entering the kettle reboiler

- The outflow north boundary cannot be easily defined. The boundary pressure is set to be atmospheric. Yet the flow does not have a regular form. In this case the vapour and liquid exit through this boundary and liquid re-enters through it. Based on the pressure of the node adjacent to the boundary, the movement of liquid or vapour is determined. If the node pressure is higher than atmospheric, both liquid and vapour exit across the boundary from the regions of higher pressure to regions of lower pressure. Otherwise, saturated liquid will be forced to enter the domain across the boundary. This happens when strong recirculation occurs in the separation region. This makes the liquid forced out of the separation region to re-enter the north boundary [7]. Different methods have used to consider this north boundary [7]. Rahman et al. [65] suggested a horizontal surface with non-varying flow pressure. Similar conditions were suggested for leaving flow by Pezo et al. [69], or it was assumed that $v_L = \frac{\partial v_g}{\partial y} = 0 \; and \; \frac{\partial u_L}{\partial x} = \frac{\partial u_g}{\partial x} = 0$. Also, flow re-entering across the north face was taken to be gas. Based on their second assumptions Pezo et al. [69] obtained good predicted data. Somehow, the boundary conditions needs to be specified for this boundary.

6.5 Governing equations

6.5.1 The tube bundle

In the present two-fluid model of the tube bundle, the fluid is considered to be a mixture of saturated liquid and vapour. The amount of vapour produced in the bundle, M_g, is a result of mass transfer between phases due to boiling. This can be calculated as:

$$M_g = \frac{ND\pi L\, q}{h_{fg}} \tag{6.1}$$

Where N is the number of tubes to which heat flux q is applied, D is the tube diameter, L is the tube length and h_{fg} is the latent heat of fluid vaporization. This quantity, M_g leaves across the north face of the bundle. Through the south boundary, the amount of liquid, M_l, is also given by Equation (6.1). Within the bundle q is constant so the liquid to vapour transition is modelled by assuming an invariant generation rate of vapour per

unit volume of domain. The vapour rate is obtained by dividing equation (6.1) by the tube bundle sub-domain volume. A mass sink of equal magnitude with the reverse direction is set for the liquid. The forces caused by phase transition are ignored. For simulating the 2- phase fluid inside the bundle, a porous sub domain is considered. The model assumes that the sub-domain volume consists of three phase fractions. These fractions are solid, liquid and gas: ε_s, ε_l and ε_g, respectively. The total volume fraction is given as:

$$\varepsilon_s + \varepsilon_l + \varepsilon_g = 1 \tag{6.2}$$

The vapour and liquid volume fraction in the tube bundle is defined as:

$$\phi = \varepsilon_g + \varepsilon_l = 1 - \varepsilon_s \tag{6.3}$$

where ϕ is the porosity of the tube bundle.

The solid volume fraction, ε_s, for the square in-line tube bundle is found from;

$$\varepsilon_s = \frac{\pi}{4}\left(\frac{D}{P}\right)^2 \tag{6.4}$$

The tube bundle's porosity is given by:

$$\phi = 1 - \frac{\pi}{4}\left(\frac{D}{P}\right)^2 \tag{6.5}$$

where P is the tube pitch.

The liquid and vapour volume fractions are found through:

$$\alpha_l = \frac{\varepsilon_l}{\phi} \text{ and } \alpha_g = \frac{\varepsilon_g}{\phi} \tag{6.6}$$

For each phase, the continuity and momentum equation are applied in the two-fluid model.

For the sub-domain of the tube bundle, the vapour mass conservation equation is

$$\frac{\partial}{\partial x}\left(\varepsilon_g \rho_g u_g\right)+\frac{\partial}{\partial y}\left(\varepsilon_g \rho_g v_g\right)=\frac{M_g}{V} \tag{6.7}$$

Where u_g and v_g are the components of the vapour's velocity in the horizontal and vertical directions respectively. Vapour density and volume of the porous subdomain are represented by ρ_g and V respectively. The momentum equation for vapour in the x and y directions can be written as:

X-direction:

$$\varepsilon_g \rho_g\left(\frac{\partial u_g}{\partial t}+u_g\frac{\partial u_g}{\partial x}+v_g\frac{\partial u_g}{\partial y}\right)=-\varepsilon_g\frac{\partial p}{\partial x}+F_{Lg}^{x}+F_{sg}^{x} \tag{6.8}$$

Y-direction:

$$\varepsilon_g \rho_g\left(\frac{\partial v_g}{\partial t}+u_g\frac{\partial v_g}{\partial x}+v_g\frac{\partial v_g}{\partial y}\right)=\rho_g g-\varepsilon_g\frac{\partial p}{\partial y}+F_{Lg}^{y}+F_{sg}^{y} \tag{6.9}$$

where p is the pressure, g is the acceleration due to gravity, F_{sg} is the force on the vapour by the tubes per unit volume of domain, with superscripts x and y indicating the force components in the x and y directions respectively, and F_{Lg} is the interfacial drag force per unit volume of domain. This interfacial force influences the void fraction and relative velocity of the phases, and can be calculated from

$$F_{gL}=\frac{3}{4}\phi\rho_L\alpha_g\frac{C_D^{tb}}{D_B}(\vec{s_g}-\vec{s_L})\left|\vec{s}_g-\vec{s_L}\right| \tag{6.10}$$

where ρ_L is the liquid phase density, C_D^{tb} is the drag coefficient in the tube bundle region, D_B is the bubble diameter and s_g and s_L are the vector sums of the horizontal and vertical velocity components of the vapour and liquid phases.

Similarly, for the sub-domain of the tube bundle, the mass conservation equation for the liquid phase is given as:

$$\frac{\partial}{\partial x}\left(\varepsilon_L \rho_L u_L\right)+\frac{\partial}{\partial y}\left(\varepsilon_L \rho_L v_L\right)=-\frac{M_g}{V} \tag{6.11}$$

where u_L and v_L are the components of the liquid's velocity in the horizontal and vertical directions respectively. The momentum equations for the liquid in the x and y directions can be written as;

X-direction:

$$\varepsilon_L \rho_L \left(\frac{\partial u_L}{\partial t} + u_L \frac{\partial u_L}{\partial x} + v_L \frac{\partial u_L}{\partial y} \right) = -\varepsilon_L \frac{\partial p}{\partial x} + F_{gL}^{x} + F_{sL}^{x} \tag{6.12}$$

Y-direction:

$$\varepsilon_L \rho_L \left(\frac{\partial v_L}{\partial t} + u_L \frac{\partial v_L}{\partial x} + v_L \frac{\partial v_L}{\partial y} \right) = \rho_L g - \varepsilon_L \frac{\partial p}{\partial y} + F_{gL}^{y} + F_{sL}^{y} \tag{6.13}$$

where F_{sL} is the force on the liquid by the tubes per unit volume of domain and $F_{gL} = -F_{Lg}$. Values of F_{Lg}, F_{sg} and F_{sL} are required in order to model the flow inside the tube bundle. According to Rahman et al. [65], there is no significant contact between the vapour phase and the tube walls. Therefore, F_{sg} is neglected.

6.5.2 The drag coefficient in the tube bundle

To obtain F_{Lg}, C_D^{th} and D_B need to be determined for Equation (6.10). The methodology to obtain drag coefficients is based on the approach of McNeil et al. [7]. The drag coefficient is obtained by using void fraction and pressure drop correlations for fully developed models of 1-D flow. The momentum equation for the one-dimensional model of the fully developed flow is

$$\frac{\partial p}{\partial y} = -\rho_{tp} g + F_{sL} + F_{sg} \tag{6.14}$$

In Equation (6.14), F_{sg}, is neglected. By using the two-phase multiplier correlation of Ishihara et al. [46], Bamardouf and McNeil [3] proposed a relation for the force on the fluid by the tubes in the kettle reboiler. The force on the liquid by the tubes is given by:

$$F_{sL} = \frac{f_l}{2} \rho_l \; j_{lo}^2 \, \phi_l^2 \tag{6.15}$$

where, j_{lo} is the liquid velocity when the liquid fraction flows alone in an unrestricted flow area, f_l is the bundle friction factor obtained in the same situation and obtained by ESDU [83], and ϕ_l^2 is the two-phase multiplier, and is obtained from:

$$\phi_l^2 = 1 + \frac{8}{X_{tt}} + \frac{1}{X_{tt}^2} \tag{6.16}$$

where X_{tt} is the Martinelli parameter, calculated from:

$$X_{tt} = \left(\frac{1-x}{x}\right)^{0.9} \left(\frac{\rho_g}{\rho_l}\right)^{0.5} \left(\frac{\mu_l}{\mu_g}\right)^{0.1} \tag{6.17}$$

where, x is the gas mass fraction, and μ_g and μ_l are the viscosities of the vapour and liquid phases, respectively.

The slip ratio, S, for kettle reboiler is obtained from the Feenstra et al. [41], correlation given by:

$$S = 1 + 25.7(R_i\, Ca)^{0.5} \left(\frac{D}{P}\right) \tag{6.18}$$

where Ca is the capillary number, defined as:

$$Ca = \frac{\mu_L\, j_{g\max}}{\sigma};$$

and is R_i the Richardson number, given by:

$$Ri = (\rho_L - \rho_g)^2 \frac{g(P-D)}{m_{\max}^2} \tag{6.19}$$

The maximum mass flux, $m_{\max}$, is found from

$$m_{\max} = \frac{MP}{(P-D)L} \tag{6.20}$$

where M is the amount of vapour and liquid flowing up between the tubes, with $(P-D)L$ being the smallest gap between tubes multiplied by the tube length.

The maximum gas velocity, $j_{g\max}$, is given by:

$$j_{g\max} = \frac{x m_{\max}}{\alpha_g \rho_g} \tag{6.21}$$

Thereafter, the void fraction is obtained from an iterative procedure and is given by:

$$\alpha_g = \frac{x\rho_L}{(x\rho_L + S(1-x)\rho_g)} \tag{6.22}$$

The fully-developed, 1-D, two-fluid model momentum equation for the gas phase is

$$\varepsilon_g \frac{\partial p}{\partial y} = -\varepsilon_g \rho_g g + F_{Lg} + F_{sg} \tag{6.23}$$

In Equation (6.23), the value of F_{sg} is ignored.

The gas fraction, ε_g ($i.e.\ \varepsilon_g = \alpha_g \phi$) and the pressure gradient, $\frac{\partial p}{\partial y}$ is obtained from the one-dimensional model. The only unknown parameter is the drag force, F_{Lg}, which can be determined from Equation (6.23).

In a one-dimensional, fully developed flow, the drag force and the drag coefficient are related according to Equation (6.24),

$$F_{Lg} = \frac{3}{4}\phi\rho_L \alpha_g \frac{C_D^{tb}}{D_B}(v_g - v_l)\left|v_g - v_L\right| \tag{6.24}$$

From Equation (6.24), C_D^{tb}/D_B can be determined, the value of which can allow F_{Lg}, Equation (6.10), to be obtained. By this procedure the drag coefficient for pentane flows were obtained similar to the one-dimensional model, the mass fluxes were found at a particular gas-mass fraction for a static liquid pressure drop over a tube. A tube bundle with an in-line arrangement of tubes with a 19 mm outside tube diameter and P/D=1.34 was assumed, similar to the tube bundle illustrated in Fig. 6.1. Pentane data are obtained

at atmospheric pressure, similar to the operating condition of the kettle reboiler. The drag coefficient correlation was found from the resultant plot of drag coefficient versus void fraction as shown in Fig. 6.3.

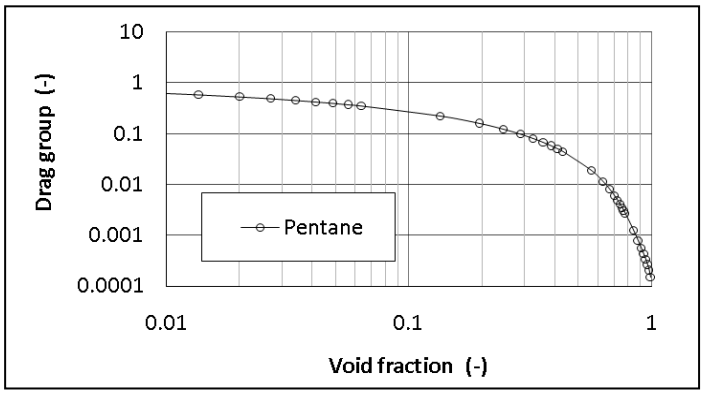

Figure 6.3: Change in drag group with void fraction

This pentane drag coefficient was correlated by:

$$C_D^{th} = 1\times10^{-4}\sqrt{E_0}\left(1.227 - 2.212\alpha_g + 19.37\alpha_g{}^2 - 32.37\alpha_g{}^3 + 14.84\alpha_g{}^4\right)e^{6.595(1-\alpha_g)} \qquad (6.25)$$

where, E_O is defined as

$$E_O = \frac{g(\rho_L - \rho_g)D_B^2}{\sigma} \qquad (6.26)$$

This correlation gives the ratio C_D^{tb}/D_B as required in equation (6.10) and is independent of D_B

6.5.3 The force on the liquid by the tubes

In the bundle zone, the main force on the fluid is due to the tube wall, F_{sL}. Similar to the one-dimensional model approach, this force (F_{sL}) is modelled as given by Equations (6.15-6.17). F_{sL} was implemented as a momentum loss term by modifying the Ishihara et al. [46] technique similarly to McNeil et al. [7]. The 1-D technique is used here by presuming that F_{sL} is in the same direction as the liquid velocity. The two-phase multiplier, ϕ_l^2, is then based on the vapour velocity component, also in this same direction, as illustrated in Fig. 6.4. Equation (6.15) was used to calculate F_{sL}. In Force

Equation (6.15), the liquid only velocity is used alone, and in the ESDU [83] Reynolds number the value of x in Equation (6.17) was calculated as:

$$x = \frac{\alpha_g \rho_g s_g \cos\theta}{(\alpha_g \rho_g s_g \cos\theta + \alpha_L \rho_L s_L)} \tag{6.27}$$

where θ is the angle between the vapour and liquid velocity vectors and θ_g and θ_L are the angles of the vapour and liquid velocity vectors with respect to the x-axis The expression for θ, θ_g and θ_L are given by:

$$\theta = \left| \theta_g - \theta_L \right| \tag{6.28}$$

$$\theta_g = \tan^{-1}\left(\frac{v_g}{u_g}\right) \text{ and } \theta_L = \tan^{-1}\left(\frac{v_L}{u_L}\right) \tag{6.29}$$

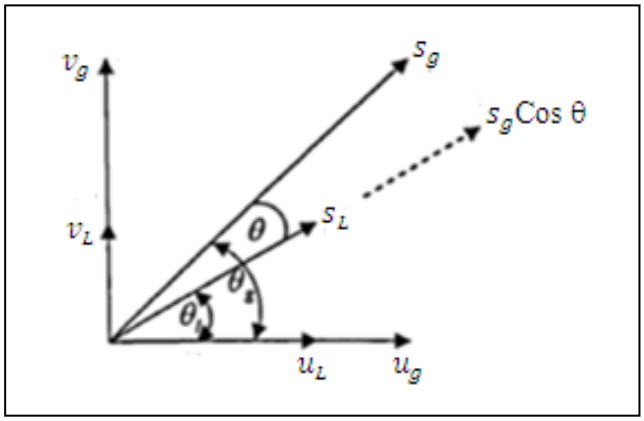

Figure 6.4: The gas velocity used to calculate the quality

6.6 The pool

The pool is taken as a fluid domain where between the two phases, there is no mass transfer. Therefore, mass conservation equations. (6.7) and (6.11) are used here with the value of $M_g = 0$. Momentum equations (6.8, 6.9, 6.12 and 6.13) are altered by substituting using the viscous forces for those that the tubes exert on the fluid and taking $\emptyset = 1$. These viscous forces are found, from the k-ε turbulence model with

turbulence enhancement from Sato and Sekoguchi [84]. Grace's drag coefficient is applied in the pool, i.e. [85]:

$$c_D^{pl} = \frac{4}{3}\frac{g\,D_B\left(\rho_L - \rho_g\right)\alpha_L^n}{\rho_L\, v_t^2} \tag{6.30}$$

where for one bubble, the terminal velocity, v_t, is determined as;

$$v_t = \frac{\mu_L\left(J - 0.852\right)}{\rho_L D_B M_O^{0.149}} \tag{6.31}$$

where M_O is the Morton number, given by:

$$M_O = \frac{\mu_L^4\, g\left(\rho_L - \rho_g\right)}{\rho_L^2\, \sigma^3} \tag{6.32}$$

and J is a parameter defined as:

$$J = 0.94H^{0.751}\ For \quad 2 < H < 59.5 \ \ or \quad J = 3.42H^{0.441}\ For \quad H > 59.5 \tag{6.33}$$

In equation (6.33), H is a parameter given by:

$$H = \frac{4}{3}\frac{E_O}{M_O^{0.149}}\left(\frac{\mu_{ref}}{\mu_L}\right)^{0.14} \tag{6.34}$$

The reference viscosity, μ_{ref}, was $0.0009 Ns/m^2$. The exponent n of the power law liquid volume fraction term is used to correct for the presence of other bubbles. The range of values for the exponent n is given between -0.5 and 4. The exponent 3 is used here. The correlation is reasonably independent of diameter. A bubble diameter of 1 mm was used.

6.7 Separation region

Two techniques to model the separation region above the tube bundle have been used by McNeil et al. [7], both of which use a plane horizontal isobaric surface. This simulated plane surface coincides with the position of the weir in the actual kettle

reboiler. In the first technique the surface was located directly above the tube bundle, to exclude flow modelling in the separation region. In the second case flow modelling was permitted in this region as the surface was located 100 mm above the tube bundle. The weir was represented using the north boundary condition, illustrated in Section 6.4. At this boundary, the value of void fraction for any fluid re-entering across it must be specified, and three re-entry void fraction values (α_{out}) were used. These void fraction values were given only for the fluid re-entering the pool; with the leaving fluid having the local predicted void fraction. McNeil et al. [7] reported that the predicted void fraction values did not correspond to those observed in the actual kettle reboiler when the second location for the surface was used. An inaccuracy in the predicted void fraction distribution results in errors to the predicted pressure drop and mass flux distribution in the kettle reboiler model. Positioning the surface immediately above the tube bundle removes these problems. McNeil et al. [58] also found that experimentally changing the pool height (liquid level above the tube bundle) did not influence the pressure distribution within it.

Finally, the time-averaged shape of the free surface due to level swell formed from the production of vapour inside the tube bundle is extremely turbulent and not easy to model (Fig 5.1). As a result of these circumstances, the height of the swell is located to roughly balance the pressure on the same horizontal plane across the pool and tube bundle, with the additional gravitational effect of the liquid head dissipated by the turbulent activity. This can be achieved by having a plane surface at the top of the bundle and assuming equal pressure under it [7]. Therefore the low liquid level model is considered to be an appropriate choice for simulating the tube bundle in the kettle reboiler.

Consequently a plane interface was selected at zero height above the tube bundle for the north boundary for modelling purposes. Above the north boundary, separation between the liquid and the vapour phase occurs. This boundary allows vapour and liquid to exit and only liquid to re-enter. An opening with static pressure with intermittent flow was set at this boundary. This sets the pressure and the vertical velocity gradients of any incoming fluid to zero. Different values of the vapour volume fraction, or re-entry void fraction, of any incoming fluid were set for this boundary, see Chapter 7.

6.8 Fluid Parameters

To solve the two-fluid model, the working fluid properties need to be defined. A kettle reboiler is used in a wide range of applications. In most of the applications, the working fluid is a mixture of various fluids, commonly hydrocarbons. However, in this study, pentane was the working fluid and is therefore used in this model to compare with the measurements made. The properties of pentane change with pressure and temperature. In this application the fluid properties are considered to be constant through the fluid and porous domains. This simplifies the solution. This assumption can be justified because the system pressure varies only slightly in the reboiler as the fluid is saturated in most of the regions with only a small portion of sub cooling liquid pressure at the bottom of the bundle near the inlet that can be ignored. The thermo physical properties of pentane at an atmospheric pressure of 1.013 bar are given in Table 6.2.

Table 6.2: Thermo physical properties of pentane

Liquid properties	Units	Value	Vapour or gas properties	Units	Value
Thermal conductivity	W/mK	0.1095	Thermal conductivity	W/mK	0.01555
Density	kg/m^3	610.5	Density	kg/m^3	2.978
Entropy	J/kgK	-1101.7	Entropy	J/kgK	48.14
Specific heat at constant pressure	J/kgK	2376.2	Specific heat at constant pressure	J/kgK	1759.2
Viscosity	Ns/m^2	0.000194	Viscosity	Ns/m^2	0.00000719
Molecular weight	kg/mole	72.15	Molecular weight	kg/mole	72.15
Saturation pressure	bar	1.01300	Saturation temperature	^OC	36.1
Enthalpy of evaporation	kJ/kg	355.5	Isentropic index	(-)	1.070
Surface tension	N/m	0.01428			

6.9 Convergence criteria

The meshed geometry used for the kettle reboiler is shown in Fig. 6.2. The CFD code used to solve the equations was Ansys CFX version 11.

When the flow re-entering across the north face was small, values of $\alpha_{out} \leq 0.5$, steady state solutions were achieved by solving the equations of momentum until RMS values of residuals were less than $1x10^{-5}$ and solving the volume and turbulence equations until the RMS values of the residuals were less than $1x10^{4}$. When values of $\alpha_{out} \geq 0.5$, flow vortices were observed close to the north face. These produced transient solutions, for which a time step of 0.02 s was used. Convergence was difficult to achieve in these circumstances.

6.10 Grid Sensitivity

Grid sensitivity tests were carried out by comparing the results of the model for different grid sizes from 10 mm to 2 mm. In the first stage, both domains of the kettle reboiler (bundle and pool) used a cell size of 10 mm. The model, with a constant heat flux of 10 kW/m^2 was used for the comparison. The grid refinement was accomplished by using smaller grid sizes of 8, 4 and 2 mm. Results for the grid size of 10 mm were compared to results from the smaller grid sizes. It was observed that the pressure drop, void fraction, vertical mass flux profiles and velocity distribution varied by no more than 4% within the tube bundle region, Fig. 6.5. These results show only minor differences between the model with coarse and finer grids in the bundle region. In the pool region variation was shown between the 4 and 2 mm grid in Figs. 6.6 and 6.7. Hence, a coarse grid size of 10 mm was imposed on the bundle region while the pool region used a finer grid size of 2 mm.

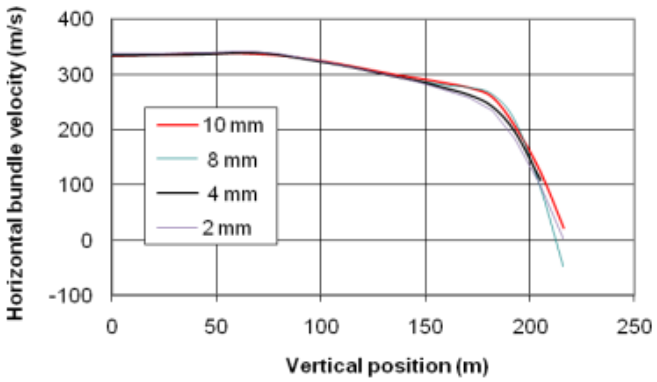

Figure 6.5 : The bundle velocity distribution with varying grid size.

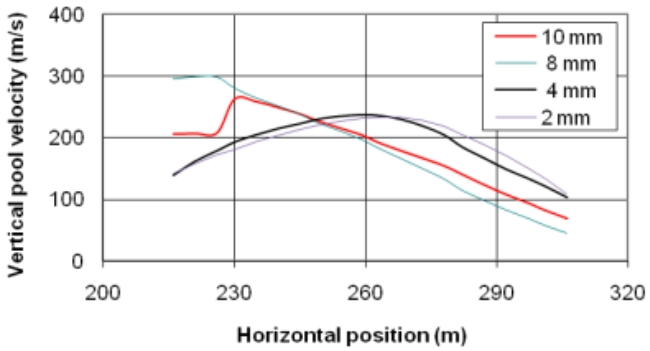

Figure 6.6: The pool sides velocity distribution with varying grid size.

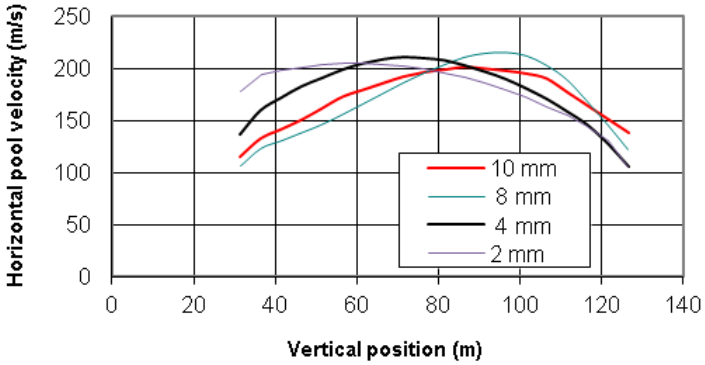

Figure 6.7: The pool bottom velocity distribution with varying grid size.

CHAPTER 7

Results of Simulations of 2-D Two-Fluid Model

7.1 Introduction

In this chapter, the simulation results of the 2D two-fluid model presented in Chapter 6 are analyzed and discussed in detail. In this study of applying the two-fluid model, clarification of the magnitude of the re-entry void fraction for the fluid that returns via the north boundary is made. The results are validated by comparing predictions with experimental data and with predictions from the one-fluid model at heat fluxes of 10, 20, 30 and 40 kW/m^2. The predicted void fraction contours and liquid and vapor velocity vectors are compared to the observed flow patterns, and the predicted pressure drops are compared with the pressure drop measurements discussed in Chapter 5.

Since test data are not available for the void fraction or for the velocities of the flow within the tube bundle, predicted vertical mass flux and void fraction distributions are compared with the prediction from the one fluid model. This comparison of two-fluid and one-fluid models will give a good indication of the ability of the two-fluid model to predict mass flux and void fraction, since the one-fluid model is empirically based

7.2 Heat flux of 10 kW/m^2

7.2.1 Flow pattern observation

For a heat flux of 10 kW/m^2, the flow regime observed in the kettle reboiler is illustrated in Fig. 7.1. Within the tube bundle, the two-phase flow mainly consists of bubbly flow moving vertically between the tube columns. The bubbly flow moves vertically outwards from the top, north east and north west surfaces of the tube bundle. This flow is accelerated quickly and is dispersed along the top of the pool. Flow moves downwards near the shell wall to form a circulation around the upper corners of the tube bundle. This circulation causes the liquid at the pool side to move towards the bottom of the bundle. The space between the pool wall and the bundle is occupied with liquid, except near the pool top where the vapour penetrates into the pool.

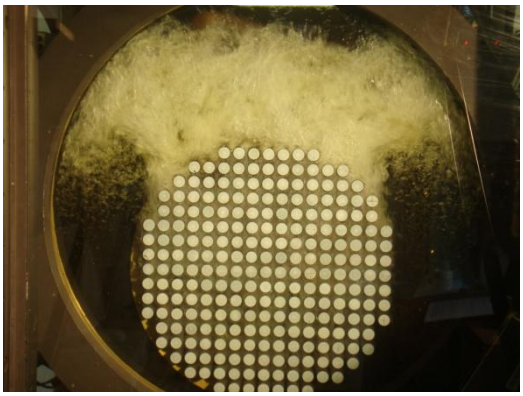

Figure 7.1: Flow pattern distribution at 10 kW/m^2

7.2.2 Void fraction distribution

The distribution of void fraction for different values of α_{out}: 0, 0.5, and 0.9, at a heat flux of 10 kW/m^2 is illustrated in Fig.7.2. The void fraction increases vertically with increasing row number and also increases horizontally towards the bundle centre line. Hence, the values of void fractions are approximately zero at the bottom of the tube bundle and maximum at the top. When α_{out} is zero, the surrounding fluid in the pool is liquid. This case should be similar to the static liquid cases mentioned for one-fluid models [5]. When the value of α_{out} is increased, the pressure surrounding the bundle is reduced because the density of the pool is reduced near the bundle top. The experimentally observed flow pattern is compared with the predicted void distribution for values of α_{out} of 0.0, 0.5 and 0.9.

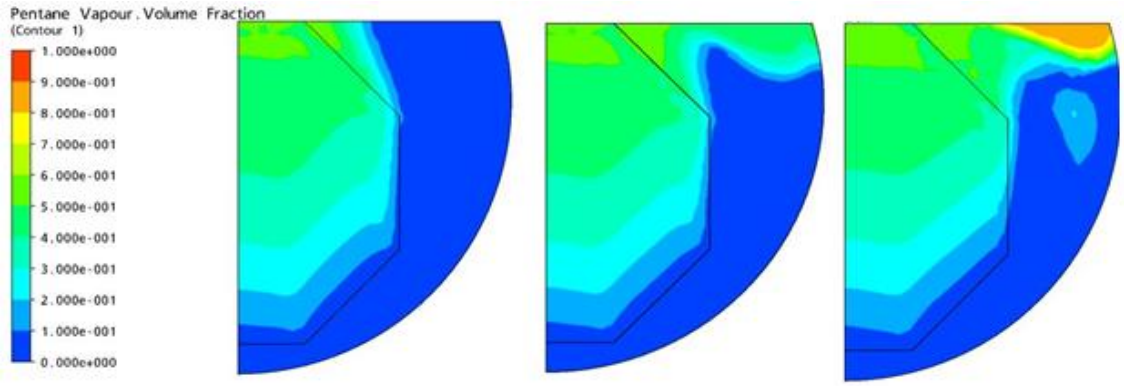

α_{out}= 0.0 α_{out}= 0.5 α_{out}= 0.9

Figure 7.2: Void fraction distribution on at 10 kW/m^2

The predicted void distributions show vapour exiting along the north and all of the north east surfaces. This flow distribution is not experimentally observed. The vapor zone observed close to the pool top is smaller than the predicted void distributions with the closest agreement occurring for α_{out} values of 0.0 and 0.5. However, the vapour pocket in the north east corner of the pool for α_{out}=0.9 is not experimentally observed, giving α_{out}=0.0 as the better prediction.

7.2.3 Liquid velocity distribution

Figure 7.3 shows the predicted liquid velocity vectors for the two fluid model at a heat flux of 10 kW/m^2 for different values of re-entry void fraction. The liquid velocity vectors mainly move vertically from the bottom to the upper rows of the bundle, but some of the liquid velocity vectors move horizontally towards the south east boundary of the bundle. It is observed that the exit liquid velocity decreases at the north boundary of the bundle when the value of α_{out} rises. The change in the bundle velocity vectors at the pool top is indicated clearly in Fig. 7.3. When the value of α_{out} is zero, large velocities at the pool top are observed. When the value of α_{out} increases, smaller magnitude velocities are observed. This is caused by the low pressure on the north east boundary caused by the reduced fluid density. The creation of a low pressure makes the flow move away from the tube bundle towards the pool and creates a vortex within the pool. The same phenomena were observed by McNeil et al. [7].

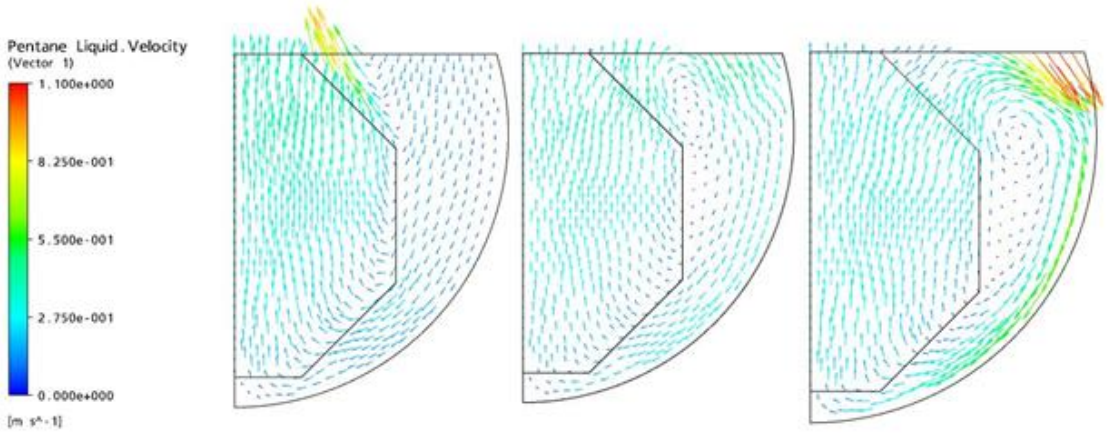

α_{out}= 0.0 α_{out}= 0.5 α_{out}= 0.9

Figure 7.3: Liquid velocity distributions at 10 kW/m^2

The experimentally observed flow, Fig. 7.1 is compared with predicted liquid velocities shown in Fig. 7.3. It is clear from the observed flow pattern that a strong flow enters into the bottom rows of the tube bundle, moves vertically upwards towards the bundle upper rows and moves away from the tube bundle into a region where a high void fraction exists. The predicted liquid velocities are comparable with the visually observed pattern with α_{out} = 0.0 and 0.5.

7.2.4 Vapor velocity distribution

Figure 7.4 show the predicted vapour velocity vectors. The behavior of the vapour velocity is similar to the liquid velocity. As the value of α_{out} increases, the vapour moves into the pool and also disperses along more of the north boundary of the pool. The magnitudes of the vapour velocity vectors are higher than the liquid velocity vectors for the same conditions. This is because of difference in the densities of the vapour and liquid phases.

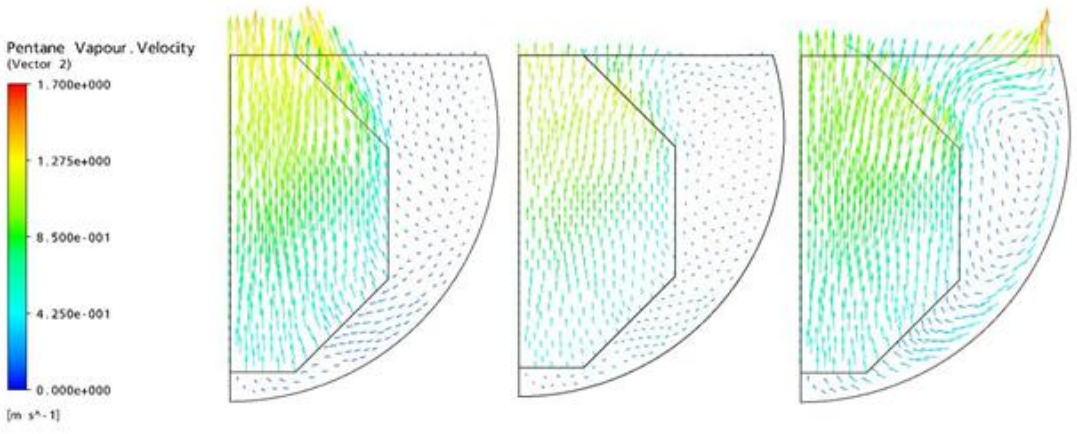

Figure 7.4: Vapour velocity distributions at 10 kW/m^2

The experimentally observed flow, Fig. 7.1, is compared with predicted vapour velocities shown in Fig. 7.4. The predicted vapour velocities at values of α_{out}=0.0 and 0.5 agree reasonably well with the experimental vapour behaviour at the north boundary. For the case of α_{out}=0.0, a small amount of vapour flow moves parallel to north east surface of the bundle. But when α_{out}=0.9, the predicted vapour velocities move towards the pool, which is not observed experimentally. The cause of this may be

that the incoming liquid prevents the vapour from moving towards the pool at the north –east boundary.

7.2.5 Pressure drop

Figure 7.5 shows the comparison between the predicted pressure drop from the two-fluid model and the measured data. The observed static liquid pressure drop for n-pentane is 304 Pa. A constant pressure drop is consistent with a constant vertical mass flux [58]. As the value of α_{out} rises, the predicted pressure drop reduces in column 9.5 and 12.5. This is due to fluid moving from the tube bundle towards the bundle-pool interface. The predicted pressure drop is almost constant and not affected by the variation of α_{out} in column 15.5, and there is consistency between the predicted pressure drop and static liquid head in the pool. The best agreement between the predicted and experimental pressure drops at a heat flux of 10 kW/m^2 occurs when the value of α_{out} is equal to zero.

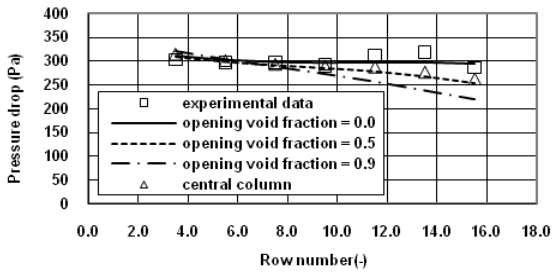

(a) Column 9.5

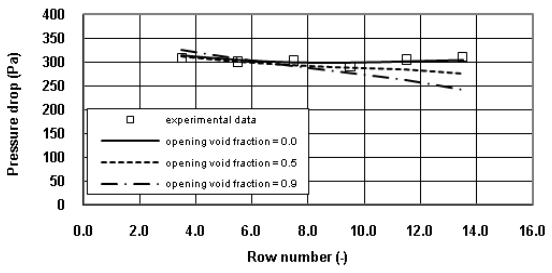

(b) Column 12.5

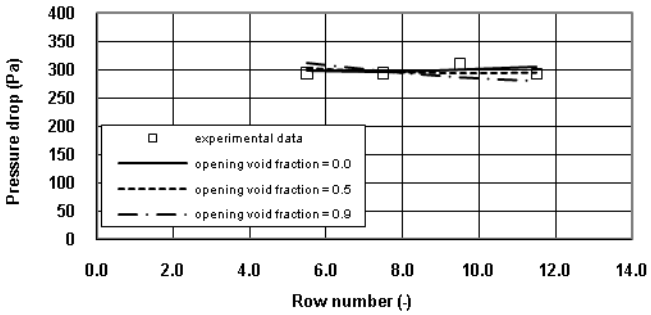

(c) Column 15.5

Figure 7.5: Experimental and predicted pressure drop at 10 kW/m^2

7.2.6 Vertical mass flux

The two-fluid model predictions of mass flux for α_{out} = 0.0, 0.5 and 0.9 at a heat flux of 10kW/m^2 are compared to the one-fluid model predictions in Fig. 7.6. The static liquid boundary was used with the one-fluid model. In column 9.5 and 12.5, the predicted vertical mass flux agrees reasonably well with the one-fluid model when α_{out} = 0.0. For column 15.5 the agreement is poor.

Figure 7.6 (c) shows a negative value of vertical mass near the bottom of the column 15.5 for the two-fluid model. This results from the movement of the liquid towards the pool bottom.

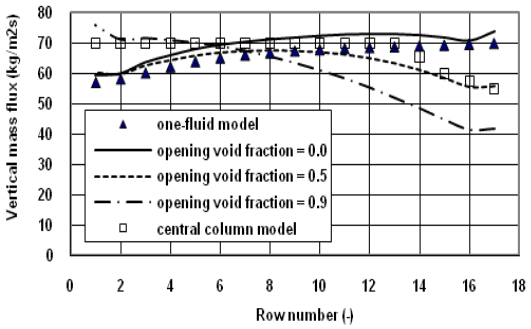

(a) Column 9.5

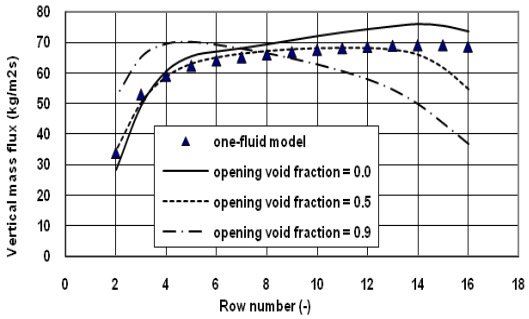

(b) Column 12.5

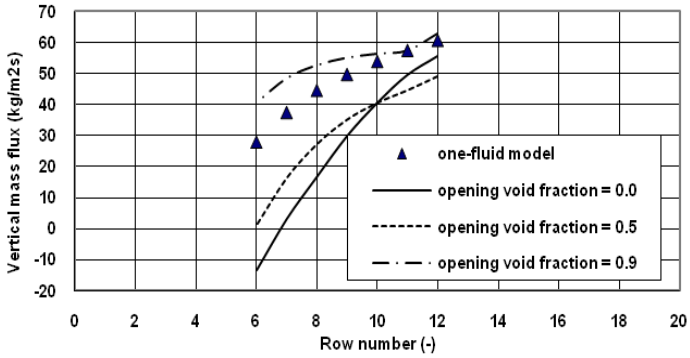

(c) Column 15.5

Figure 7.6: One- and two-fluid models vertical mass flux distribution at 10 kW/m^2

7.2.7 Void fraction distribution

In Fig. 7.7 void fraction predictions by the two-fluid model for values of α_{out} of 0.0, 0.5 and 0.9 and at a heat flux of 10 kW/m^2 are compared with the void fraction prediction from the one-fluid model. For columns 9.5 and 12.5, the predicted void fraction increases with increases in row number for both the models. In column 15.5 the void fraction increases less in comparison to columns 9.5 and 12.5, which was expected because column 15.5 is shorter. In column 9.5 and 12.5, the two-fluid model predictions of void fraction agree reasonably well with the one-fluid model independent of α_{out}. For column 15.5, the agreement is quite good when α_{out} = 0.0.

The two-fluid model with a value of α_{out} equal to zero shows the best agreement with the one-fluid model. The discrepancies observed near to the bundle periphery, as presented in Figs. 7.6 (c) and 7.7 (c), result from boundary condition of the one-fluid model. The exact location to apply the hydrostatic pressure is not clear, so the edge is assumed, which may not be accurate.

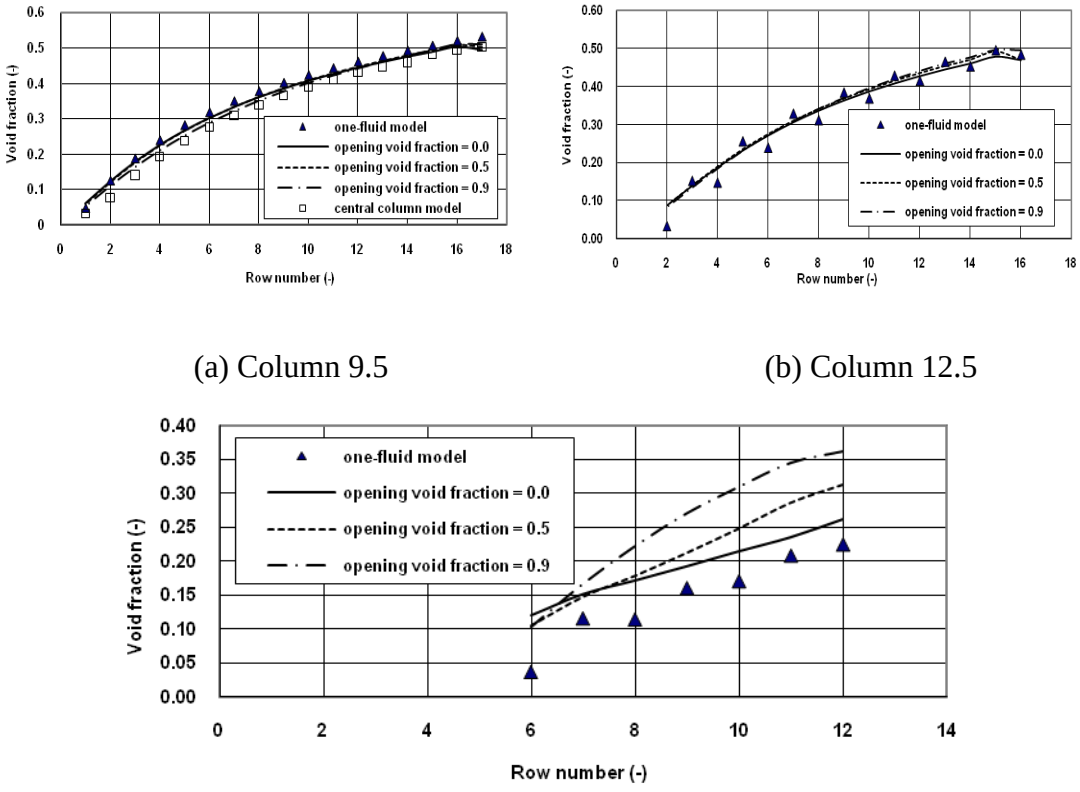

(a) Column 9.5 (b) Column 12.5

(c) Column 15.5

Figure 7.7: One and two-fluid models void fraction distribution at 10 kW/m^2

For a heat of flux 10 kW/m^2, the above comparisons show that there is a consistency between the predicted flow and the empirically evidence when α_{out} is equal to zero. This flow regime is reported as a bubbly flow regime by McNeil et al [58].

7.3 Heat flux of 20 kW/m^2

7.3.1 Flow pattern observation

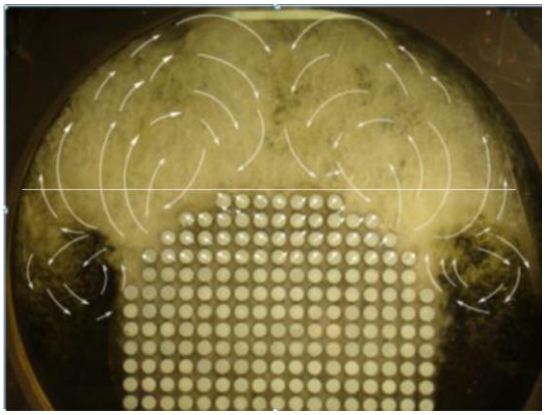

Figure 7.8: Flow distribution at 20 kW/m^2

For a heat flux of 20 kW/m^2, the flow pattern observed in the kettle reboiler is shown in Fig. 7.8. The two-phase flow moves upward between the tube columns within the bundle and discharges to a high void fraction separation area through the north, north west and north east faces of the bundle. The discharged two-phase flow moves towards the shell wall. Also from row 11 or 12, the vapour flow begins to exit from the bundle. In the separation flow region, the vapour that left through the north, north west and north east faces of the bundle impacts on the shell wall causing a recirculation zone at the top of the bundle. The recirculating zone causes liquid to enter into the pool. This re-entering flow was stronger than that which occurred at a heat flux of 10 kW/m^2. This flow is pushed downwards into the pool region to the lower rows and back into the bundle interior. A considerable amount of two-phase flow is observed in the pool region near the upper rows of bundle.

7.3.2 Void fraction distribution

The predicted void fraction distributions for different values of α_{out} , 0, 0.5 and 0.9 at a heat flux of 20 kW/m^2 are depicted in Fig. 7.9. The void fraction increases with the proximity to the bundle centreline and to the top of the bundle. The maximum value occurs at the top of the bundle. When the value of α_{out} is zero, the surrounding fluid in the pool is liquid. As the value of α_{out} is raised, the density at the pool top is decreased; this causes the reduction of the pressure surrounding the tube bundle. At the higher value of α_{out} (α_{out} = 0.5, 0.9), the 2-phase flow extends into the pool. This is consistent with the experimental observations, indicated in Fig. 7.8.

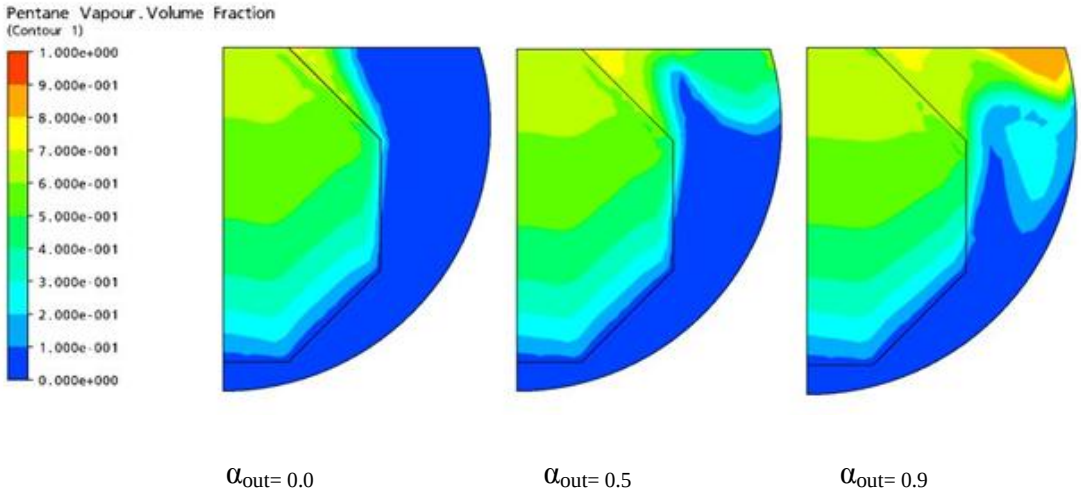

Figure 7.9: Void fraction distributions at 20 kW/m^2

7.3.3 Liquid velocity distribution

For different values of α_{out} , the predicted liquid velocity vectors for the two-fluid model at a heat flux of 20 kW/m^2 are presented in Fig. 7.10. Flow recirculation is observed as liquid flows down into the pool and the 2-phase mixture flows up through the bundle. The predicted liquid velocity vectors appear to have the same behaviour as those at 10kW/m^2 (Figure 7.3). However, liquid velocity vectors with a larger magnitude are observed at a heat flux of 20 kW/m^2. For an α_{out} of zero, large magnitude velocities are observed at the bundle top. When the value of α_{out} is increased, the magnitude of these velocities is decreased as the flow moves out of the bundle through the north–east boundary and creates additional circulation within the pool. In the pool region, stronger downward flow is shown for increasing α_{out} . This circulation is caused by the density difference between the fluid in the pool and bundle. The recirculation centre point is

defined as the point in the flow region where the vector of the velocity is zero, and this describes how the flow circulates within the reboiler [60].

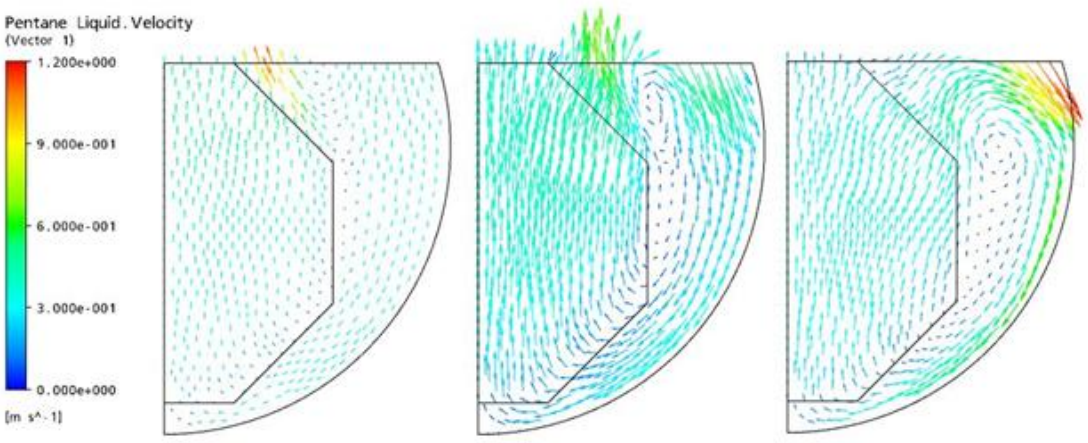

Figure 7.10: Liquid velocity distributions at 20 kW/m^2

The recirculation centres are observed in the pool near to the north-east boundary and at the top of the east boundary when values of α_{out} are 0.5 and 0.9 respectively, as indicated in Fig. 7.10. The experimentally observed flow, Fig.7.8, is compared with the predicted liquid velocities shown in Fig. 7.10. It is seen that within the bundle in the middle rows the flow moves vertically upwards, while in the lower and upper rows the flow has significant horizontal components. The values of re-entry void fractions of α_{out}=0.5 and 0.9 are shown to be consistent with the experimental observations shown in Fig. 7.8.

7.3.4 Vapour velocity distribution

Figure 7.11 indicates the predicted vapour velocity vectors. The vapour velocities are observed to be larger than the liquid velocities everywhere in the bundle. For the case of 20 kW/m^2, the lateral flow in the upper region of the re-boiler is increased as the amount of vapour in the pool increases. With an increasing value of α_{out} the vapour distributes through the pool and spreads across the northern boundary of the pool.

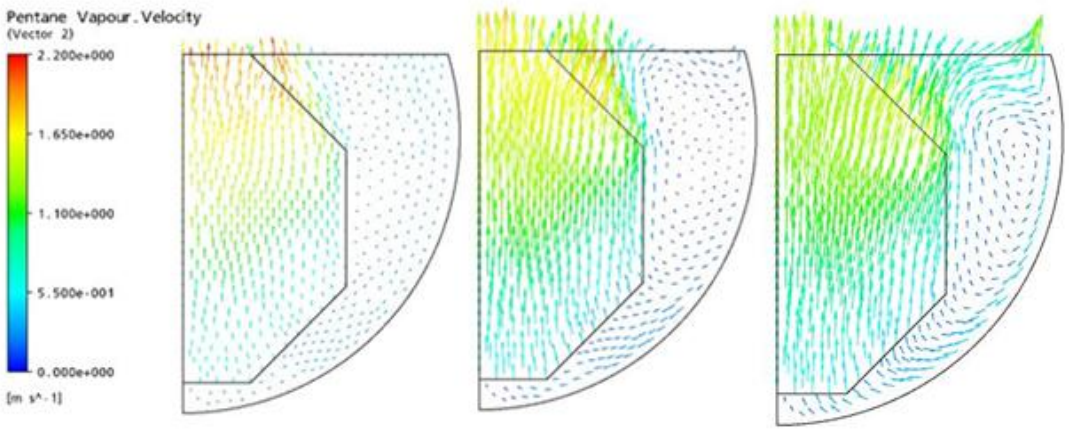

α_{out}= 0.0 α_{out}= 0.5 α_{out}= 0.9

Figure 7.11: Vapour velocity distributions at 20 kW/m^2

The experimentally observed flow, Fig. 7.8, is compared with predicted vapour velocities shown in Fig.7.11. The predicted vapour velocities at values of α_{out} = 0.5 and 0.9 are consistent with the experimental vapour behaviour at the north boundary. For the case of α_{out}= 0.9, a significant amount of vapour flow moves towards the pool, but when α_{out}=0.0, most of the vapour flow moves vertically upwards, which is not observed experimentally.

7.3.5 Pressure drop

The predicted pressure drop from the two fluid model and the measured pressure drop are compared in Fig. 7.12. When the value of α_{out} rises, the predicted pressure drop decreases. The reduction in pool pressure causes the lateral flow to develop as illustrated in Figs. 7.10 and 7.11.

When the value of α_{out} is 0.5 the predicted pressure drop in column 9.5 is similar to the static liquid value until row 8 when it decreases. This reduction in the pressure drop is due to a vertical mass flux reduction observed in the predicted vertical mass flux in Fig. 7.13 (a). Hence, at the high values of α_{out} (0.5 and 0.9) the predictions are consistent with the experimental data.

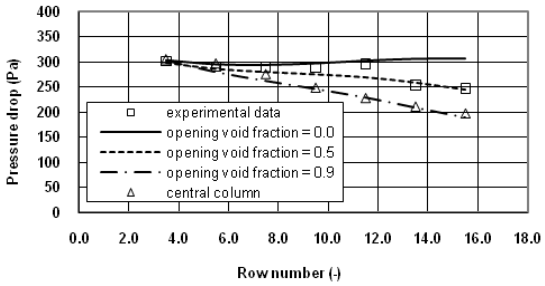

(a) Column 9.5

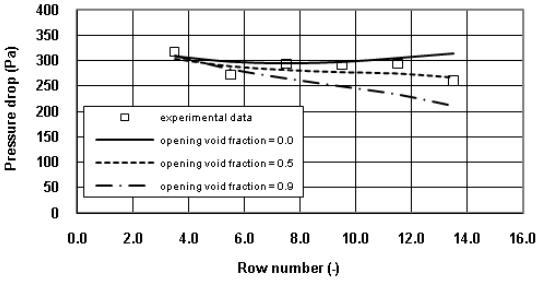

(b) Column 12.5

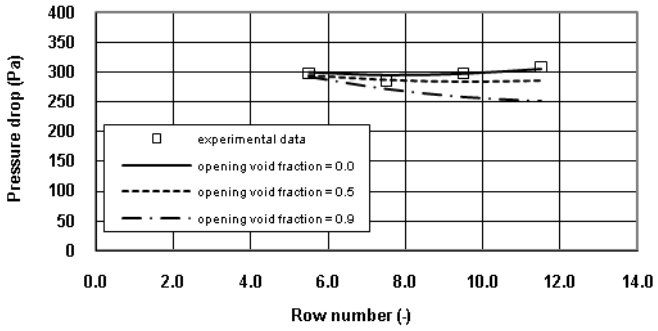

(c) Column 15.5

Figure 7.12: Measured and predicted pressure drop at 20 kW/m^2

7.3.6 Vertical mass flux distribution

The predicted vertical mass fluxes for α_{out}= 0.0, 0.5 and 0.9, at a heat flux of 20 kW/m^2, are compared to the one-fluid model predictions in Fig. 7.13. The one-fluid model results are based on the intermittent boundary condition. For columns 9.5 and 12.5, the vertical mass flux increases with increasing row number until row 4 and then decreases with increasing row number.

For columns 9.5 and 12.5, the predicted vertical mass flux agrees reasonably well with the one-fluid model for values of α_{out} of 0.5 and 0.9. For column 15.5, it deviates from the one-fluid model. This deviation may be due to the difficulty in exactly applying the pressure boundary condition to the one-fluid model [5].

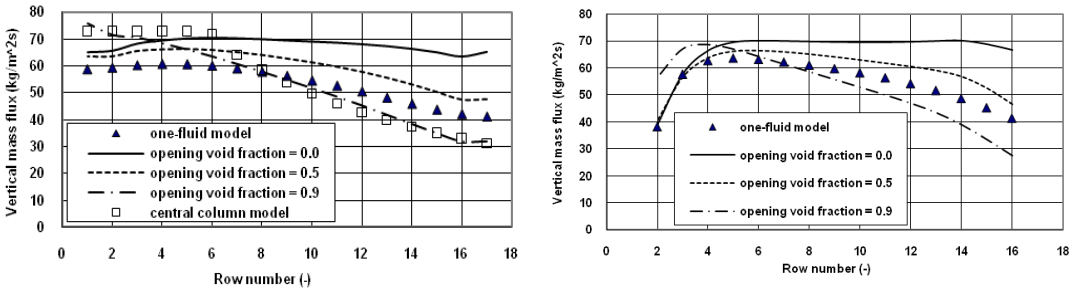

(a) Column9.5 (b) Column 12.5

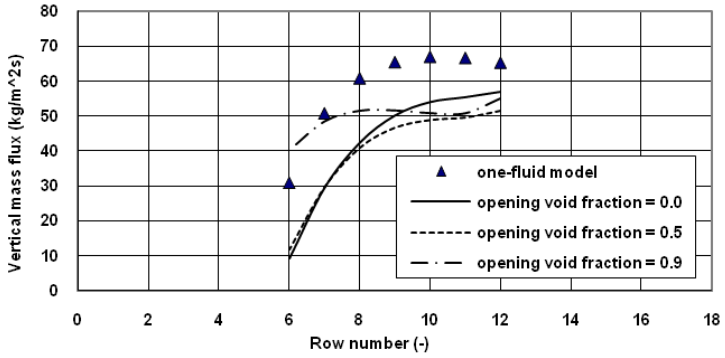

(c) Column 15.5

Figure 7.13: Comparisons of one and two-fluid model vertical mass flux distribution at 20 kW/m^2

From these models, considerable decreases in mass flux are observed as the row number increases, which agrees with the intermittent flow regime presented by McNeil et al [58]. This intermittent flow pattern is produced in the two-fluid model by high values of α_{out} (0.5 and 0.9).

7.3.7 Void fraction distribution

It is observed in Fig. 7.14 for column 9.5, 12.5 and 15.5 that the void fraction predictions agree reasonably well with the one fluid model.

The predicted void fractions increase towards the top of the bundle for both of the models. When the column number rises, the maximum value of the void fraction reduces, which is also represented in Fig. 7.14. The reduction may occur because of the

increase in horizontal liquid in the pool, the liquid penetrating from the bundle bottom and because lower tube counts have less heat. For a heat flux of 20 kW/m^2, the above comparison shows that there is a consistency between the predicted two-fluid model flow in the re-boiler and the one-fluid model at the high $\alpha_{out\ values}$ of 0.5 and 0.9.

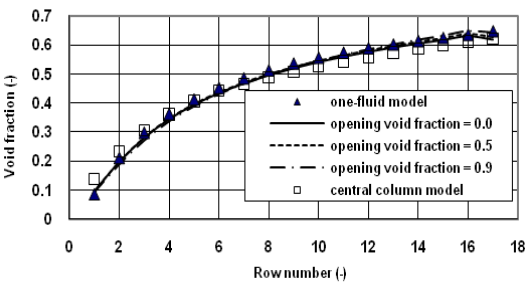

(a) Column 9.5

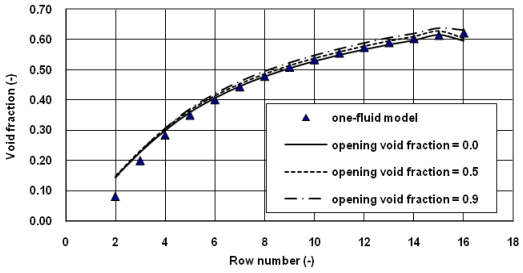

(b) Column 12.5

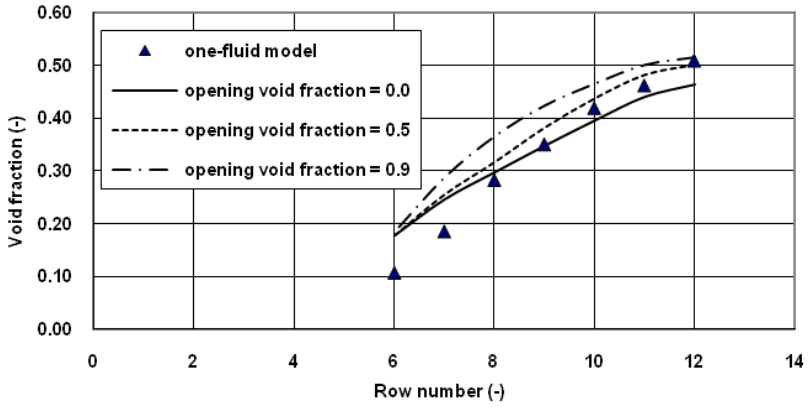

(c) Column 15.5

Figure 7.14: Comparisons of the one- and two-fluid model void fraction distribution at 20 kW/m^2

7.4 Heat flux of 30 kW/m^2

7.4.1 Flow pattern observation

The flow pattern observed with the kettle re-boiler at a heat flux of 30 kW/m^2 is illustrated in Fig. 7.15. At this higher heat flux, the flow regime is evidently in intermittent flow [58]. The two-phase mixture flow moves upwards between the tube columns, and lateral flow develops from the 9th or 10th row. The fluid is discharged across the north, north west and north east faces of the bundle to a high void fraction

area. In the upper tube rows, a considerable quantity of fluid discharges towards the pool. This separation region is larger than that produced at the low heat fluxes of 10 and 20 kW/m^2. At 30 kW/m^2 the circulating zone on top of the bundle extends further down into the pool relative to the previous cases. This provides the inflow near to the bundle bottom. A considerable amount of two-phase flow appears in the top of the pool zone.

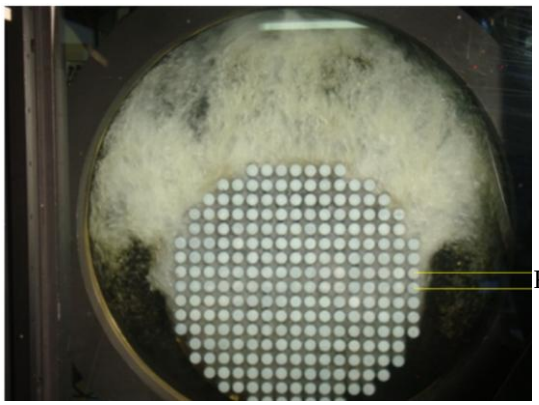

Figure 7.15: Flow distribution at 30 kW/m^2

7.4.2 Void fraction distribution

At a 30 kW/m^2 heat flux an intermittent flow regime is identified. Therefore, a high value of α_{out} (0.9) is considered for the north boundary condition in the two-fluid model [7]. Figure 7.16 represents the predicted void fraction distribution for a value of α_{out} = 0.9. The void fraction varies from zero at the bottom of the bundle, the saturated liquid region, to nearly 0.8 at the top of the bundle. The maximum value of void fraction observed is 0.9 at the pool top close to the shell wall. The two-phase flow expands further downwards into the pool with a greater extent than at a heat flux of 20 kW/m^2. The void fraction decreases horizontally across the bundle from the centreline to the bundle edge. The predicted void fraction for the value of α_{out} = 0.9 is consistent with the experimental flow pattern (Fig. 7.15).

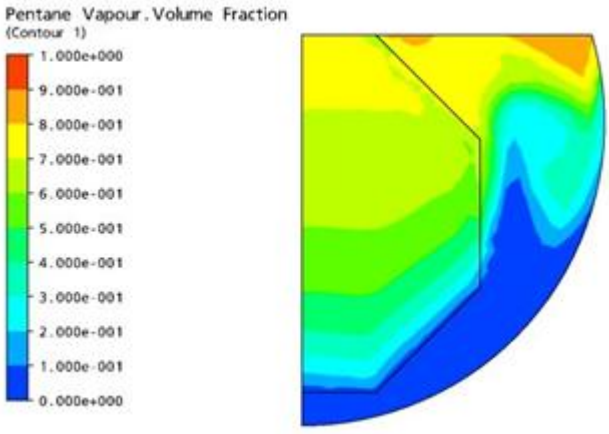

Figure 7.16: Void fraction distribution at 30 kW/m^2

7.4.3 Liquid velocity distribution

Figure 7.17 represents the predicted liquid velocity vectors for the re-entry void fraction, α_{out} =0.9. These are in good agreement with the experimental observations. The liquid velocity vectors are observed as low magnitude and upward moving at the top of the bundle close to the centre line, while at the shell wall, these are noted to be of high magnitude and in the downward direction. The high flow velocities are observed at the upper level of the pool because of the low pressure on the pool side. This makes the fluid move away from the bundle and produces more recirculation in the pool side.

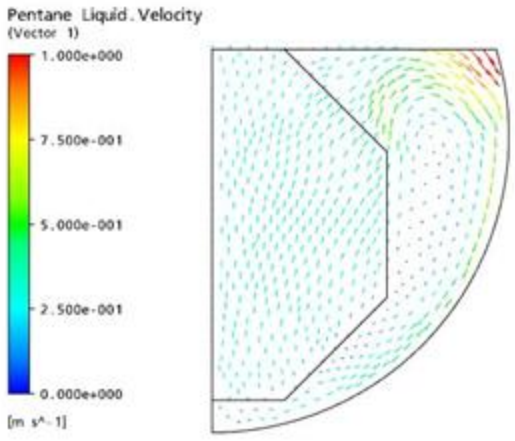

Figure 7.17: Liquid velocity distribution at 30 kW/m^2

The centre of recirculation appears further down in the pool. This movement of the flow recirculating centre is consistent with the experimental flow pattern. The liquid flow

from the pool side enters into the lower bundle section. The predicted data shows horizontal flow in the lower and upper bundle area, and the vertically upwards flow in the middle bundle area, which agrees reasonably well with the experimental flow field.

7.4.4 Vapour velocity distribution

The overall behaviour of the vapour velocity vectors obtained with a value of α_{out} =0.9 for the heat flux of 30 kW/m^2 is shown in Fig. 7.18. The horizontal flow is larger and more significant than the vertical flow at the north–east boundary in the bundle upper rows. More vapour discharges across the top of the pool. The magnitude of the vapour velocity increases with increasing row number, with the minimum at the bottom of the bundle and the maximum values at the north east boundary in the upper rows. A similar trend of predicted vapour velocity fields was observed for the heat flux of 20 kW/m^2 with the high value of α_{out} =0.9. The only difference for 30 kW/m^2 is that the magnitude of the predicted vapour velocities across the bundle is larger than that at the heat flux of 20 kW/m^2. The predicted vapour velocities at the value of α_{out} =0.9 is found to be consistent with the experimental observations, shown in Fig. 7.15.

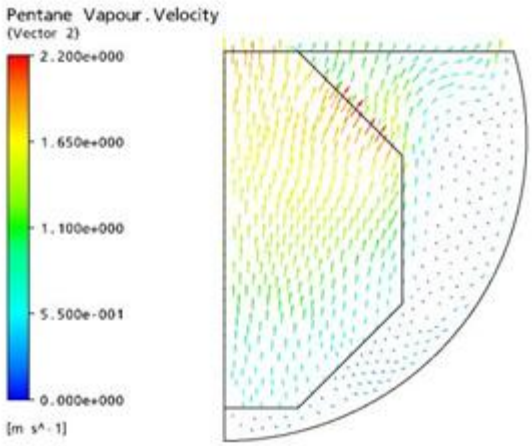

Figure 7.18: Vapour velocity distribution at 30 kW/m^2

7.4.5 Pressure drop

The comparison between the predicted and measured pressure drops are indicated in Fig. 7.19. The bubbly flow regime and intermittent flow regime predictions are shown, i.e. values of α_{out} of 0 and 0.9. The predictions at the high value of α_{out} (0.9) and the experimental observations are in better agreement in column 9.5 and 12.5. The agreement is reasonably acceptable for column 15.5 close to the bundle edge. With respect to the vertical position in the bundle, the predicted pressure drop data significantly decreases. This is consistent with a significant lateral flow predicted by the distribution of the velocities, and the corresponding simulation is represented in Fig. 7.17. The magnitude of the predicted pressure drop at a heat flux of 30 kW/m^2 is lower than that at 20 kW/ m^2.

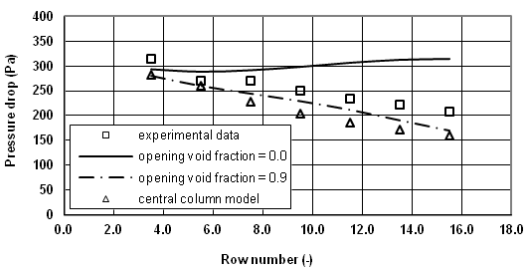

(a) Column 9.5

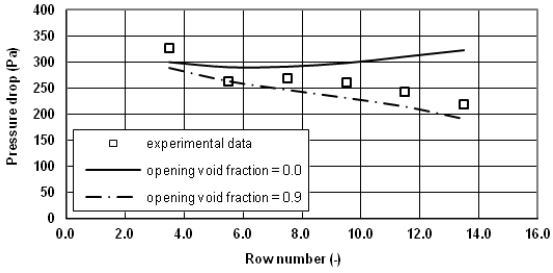

(b) Column 12.5

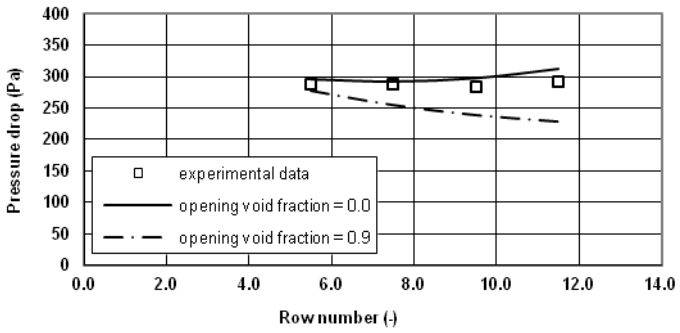

(c) Column 15.5

Figure 7.19: The measured and predicted pressure drop at 30 kW/m^2

7.4.6 Vertical mass flux distribution

The predicted vertical mass flux from the two-fluid model for α_{out} = 0.0 and 0.9 and the one fluid model at a heat flux of 30 kW/m^2 is shown for different columns in Fig.7.20.

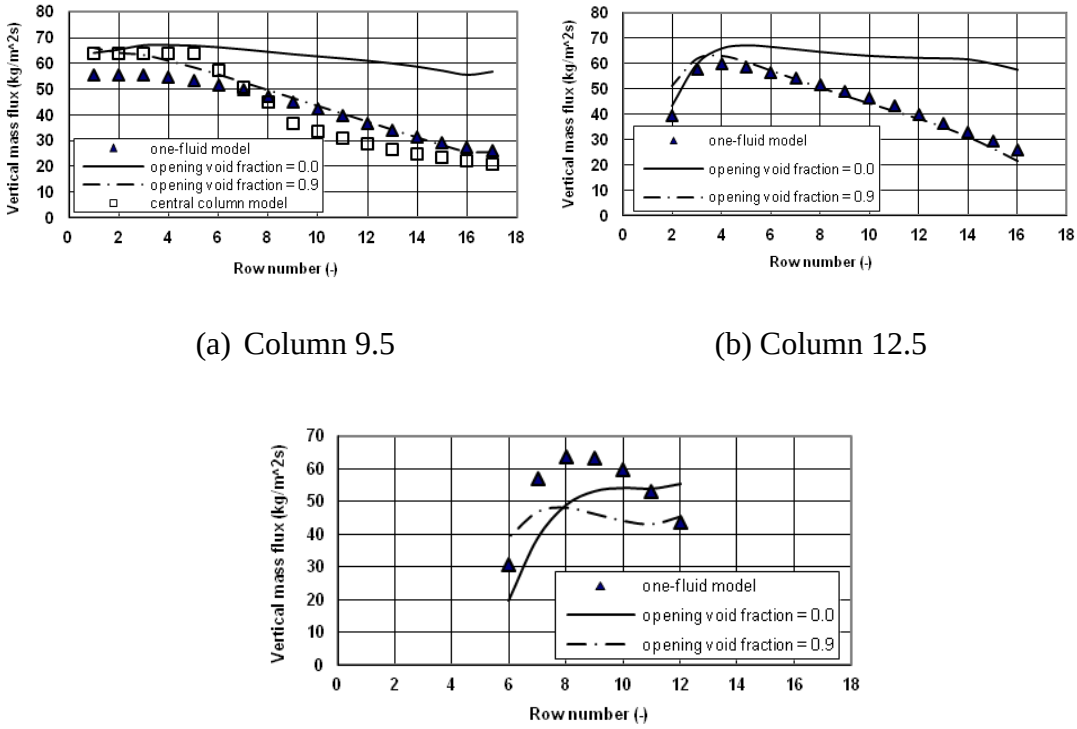

(a) Column 9.5 (b) Column 12.5

(c) Column 15.5

Figure 7.20: Comparisons of the one and two-fluid model for the vertical mass flux distribution at 30 kW/m^2

An intermittent flow boundary was used for the one-fluid model, whereas, for the two-fluid model, bubbly and intermittent flows are shown. For columns 9.5 and 12.5, both models show that the reduction in the vertical mass flux increases with the bundle row number, and that the vertical 2-fluid mass flux results agree very well for the high value of α_{out} of 0.9 with the one-fluid model. In general, the variation of predicted mass flux for the liquid re-entry void fraction (α_{out} = 0.0) and high re-entry void fractions (α_{out} = 0.9) indicates a drop in mass flux. The increased drop in the mass flux at α_{out} = 0.9 is mainly caused by fluid regime changes in the kettle boiler. A similar observation was obtained by McNeil at el. [7].

7.4.7 Void fraction distribution

The prediction of void fraction from the results of the one- [5] and two-fluid models at a heat flux of 30 kW/m^2 is shown in Fig.7.21. For columns 9.5, 12.5 and 15.5, a lower void fraction occurs in the lower rows of the bundle due to low vapour generation. Both models show a similar trend: the void fraction increases with the bundle height. The maximum void fraction is found to be 0.7 at the top of the bundle, for columns 9.5 and 12.5, and 0.6 for column 15.5. For columns 9.5, 12.5 and 15.5 the void fraction results agree very well with the one-fluid model for the high value of α_{out} =0.9.

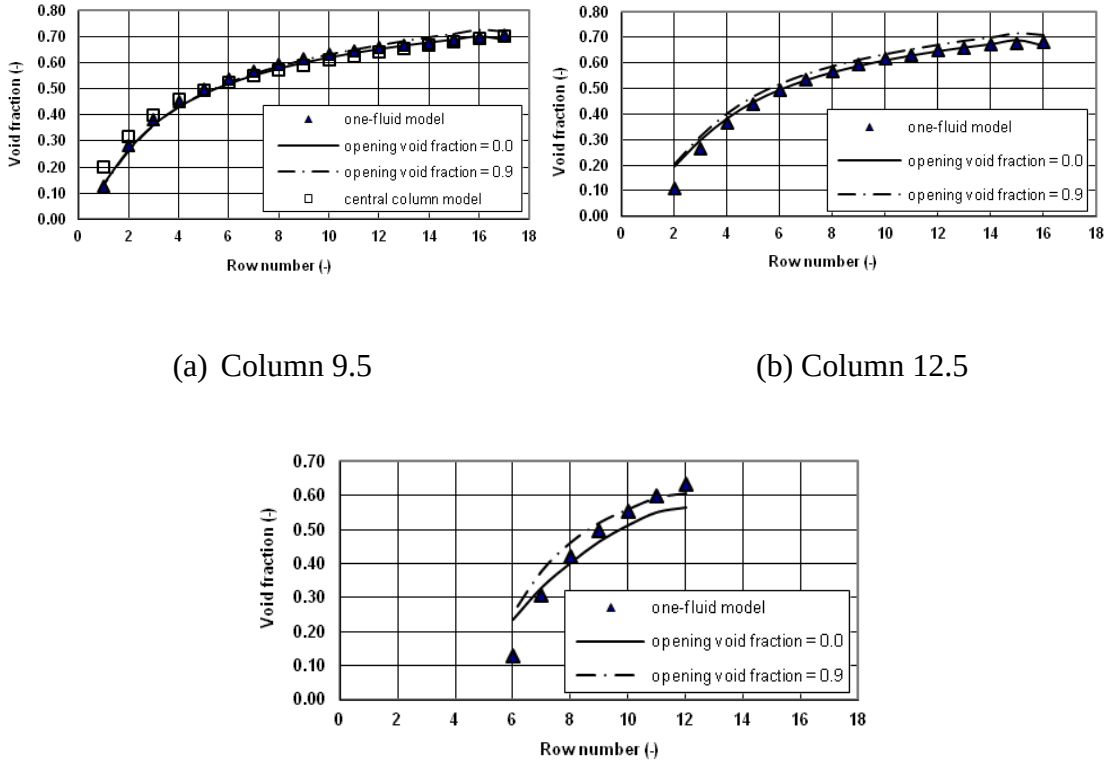

(a) Column 9.5 (b) Column 12.5

(c) Column 15.5

Figure 7.21: Comparisons of the one and two-fluid model void fraction distribution at 30 kW/m^2

7.5 Heat flux of 40 kW/m^2

7.5.1 Flow pattern observation

The experimental flow pattern at a heat flux of 40 kW/m^2 is represented in Fig. 7.22. There is similarity between the 30 and 40 kW/m^2 heat flux flow patterns. At the north, north west and north east faces of the tube bundle, intermittent flow with large vapour plumes was discharged. Two-phase fluid with a high void fraction fills the area above the bundle top and also circulates. The gas velocity across the pool top side is larger than that at a heat flux of 30 kW/m^2. This high velocity flow strength creates the intense re-circulation with a centre whose position has moved further down into the pool. Flow circulation at the lower level of the pool is observed and, along with the liquid, a significant quantity of vapour is present at lower levels of the bundle. Starting with row 7 or 8, out flow is observed and increases with increasing row number. In the upper rows, flow with a high velocity, high void fraction, and high turbulence level is observed.

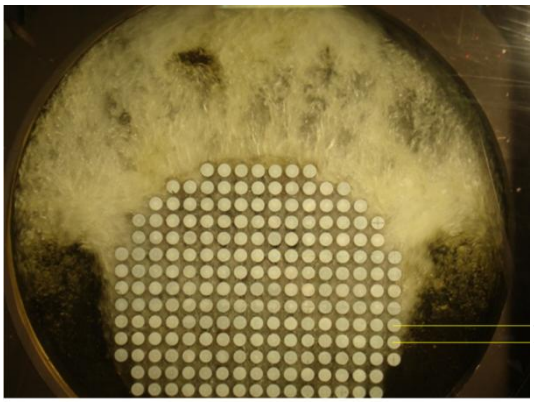

Figure 7.22: Flow distribution at 40 kW/m^2

7.5.2 Void fraction distribution

As with the simulation at the heat flux of 30 kW/m^2, the α_{out} value of 0.9 was taken for the north boundary condition at 40 kW/m^2. Figure 7.23, shows the predicted void fraction distribution. A strong re-circulating flow in the reboiler is observed. Increased heat flux causes an increase in void fraction in the upper regions of the bundle. The void fraction increases with vertical position from 0.0 at the bottom of the bundle to 0.9 at the top. Similar to a heat flux of 30 kW/m^2, the two-phase flow expanded more

downwards inside the pool than previously. At the north east face in the pool, an area with higher void fraction is noted. The high void fraction zone is probably created as a result of the increased void fraction of the discharging fluid. The void fraction increases from the edge to the centre line of the bundle. The experimental flow pattern shown in Fig.7.22 agrees reasonably well with the predicted void fraction at α_{out}=0.9 (Fig. 7.23).

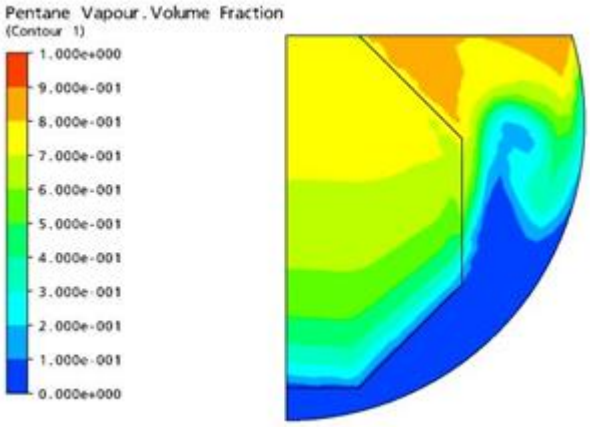

Figure 7.23: Void distribution at 40 kW/m^2

7.5.3 Liquid velocity distribution

The predicted liquid velocities vectors at a heat flux of 40 kW/m^2, with the value of α_{out} of 0.9 are shown in Fig. 7.24. The predicted liquid velocities vectors are consistent with experimental observation in the kettle reboiler. Within the bundle the flow moves upwards from the region of minimum to maximum void fraction. This is due to the latter region having a lower pressure value. Away from the north and north east top faces of the tube bundle, the flow moves up and creates a re-circulatory pattern within the pool. This recirculation and its centre has moved further down in the pool relative to previous cases with heat fluxes 10, 20 and 30 kW/m^2, which confirms that the circulation centre location is dependent on the heat flux value . The movement of the recirculation centre to the lower side of the pool is due to change in flow pattern occurring at lower levels of the bundle [58]. The reboiler performance is changed in two ways by the recirculation centre movement: the characteristics of the flow within the bundle are altered and there is a reduction in the recirculating flow rate in the pool. The

movement of the recirculation centre is also consistent with experimental flow observations shown in Fig. 7.22.

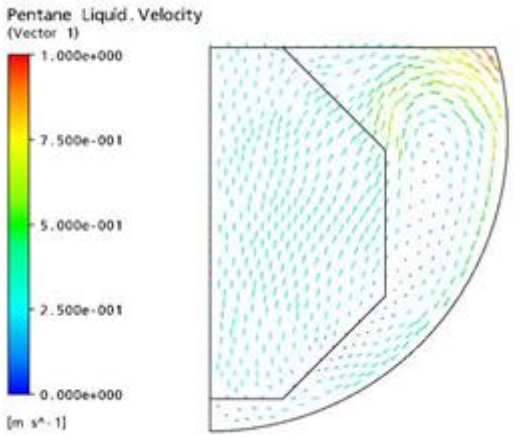

Figure 7.24: Liquid velocity distribution at 40 kW/m^2

Inside the pool, the horizontal flow enters the tube bundle from the lower side and flows approximately vertically upwards particularly near to the tube bundle centreline, the region of high void fraction. It is also noted that the flow vectors close to the centre of the bundle move upwards and the flow vectors near the shell wall flow downward.

7.5.4 Vapour velocity distribution

There is a significant similarity between the velocity vectors that occurred at 30 kW/m^2, with a value of α_{out} of 0.9, and that at 40 kW/m^2. The vapour velocity vectors are distributed across the top of the bundle and pool, as indicated in Fig. 7.25.

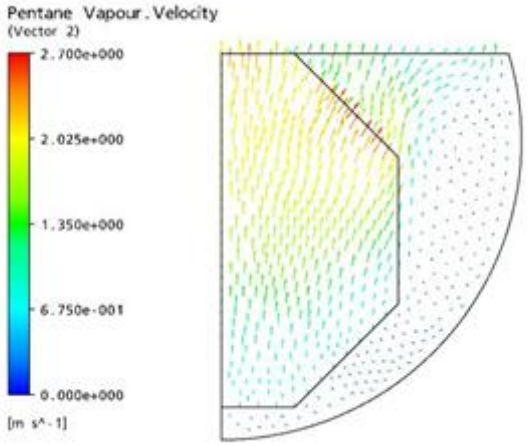

Figure 7.25: Vapour velocity distribution at 40 kW/m^2

Apart from this, large variations in the velocity vectors are noticed in the lower and upper regions of the tube bundle as the vapour rises and the velocity of the vapour increases. At a heat flux of 40 kW/m^2 a large quantity of vapour is generated by the bundle, and the vapour flow leaving the bundle is no longer restricted to the top and north east faces; vapour flow also exits at the east face. This is consistent with the experimental flow observations shown in Fig. 7.22.

7.5.5 Pressure drop

The predicted pressure drop and the experimental data at a heat flux of 40 kW/m^2 are compared in Fig. 7.26. The predictions for intermittent and bubbly flow are presented for values of α_{out} of 0 and 0.9. The value of α_{out} of 0.9 shows good agreement with the measured data. The reduction in the pressure drop with the height is due to a drop in flow-rate in the upper row level. This reduction of the flow rate is caused by flow moving horizontally, as a result of the flow pattern change, which is in turn a result of an accumulation of the two-phase flow at the pool [5].

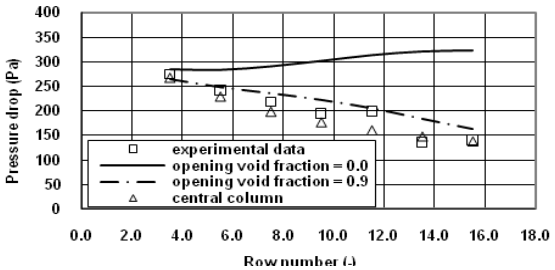

(a) Column 9.5

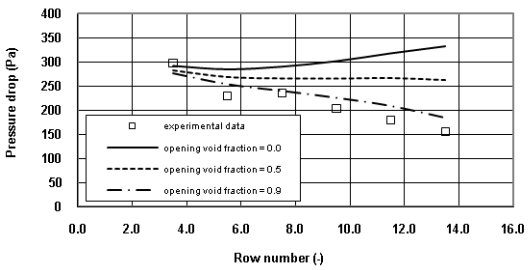

(b) Column 12.5

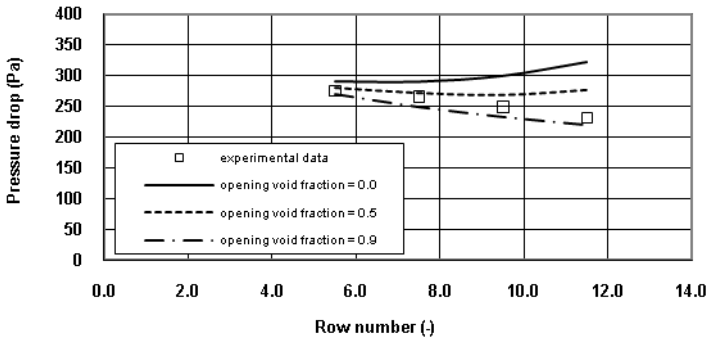

(c) Column 15.5

Figure 7.26: Comparison of the measured and predicted pressure drop at 40 kW/m^2

7.5.6 Vertical mass flux distribution

A comparison between the predictions from the one and two fluid models for vertical mass flux at α_{out}=0.0 and 0.9 at a heat flux of 40 kW/m^2 is shown in Fig. 7.27. Similar to 30 kW/m^2, an intermittent flow boundary was used for the one-fluid model data generation. Bubbly and intermittent flow boundaries were used for the two-fluid model data generation. For columns 9.5, 12.5 and 15.5, the variation of mass flux with respect to row numbers is decreased. Reasonable agreement is observed between the predicted vertical mass flux for the value of α_{out} of 0.9 and the one-fluid model.

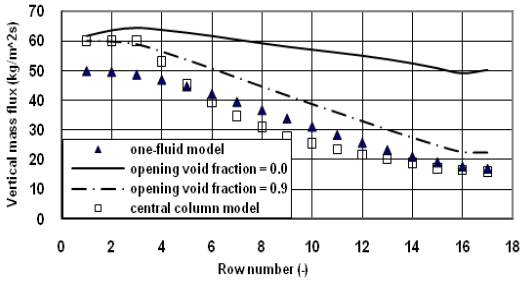

(a) Column 9.5

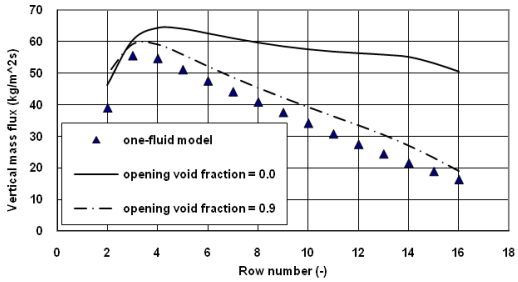

(b) Column 12.5

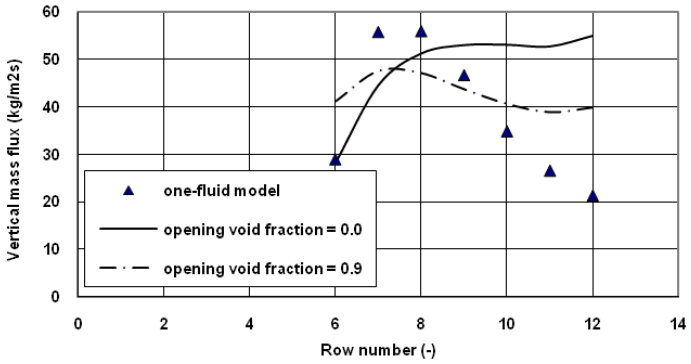

(c) Column 15.5

Figure 7.27: Comparisons of one and two-fluid model at 40 kW/m^2

7.5.7 Void fraction distribution

Void fraction predictions by the two-fluid model for α_{out} values of 0.0 and 0.9 and at a heat flux of 40 kW/m^2 are compared with the prediction from the one-fluid model in Fig. 7.28. For columns 9.5, 12.5 and 15.5, the variation of the void fraction with row number increases and a good agreement is observed between the predicted void fraction for both values of α_{out} and the one-fluid model.

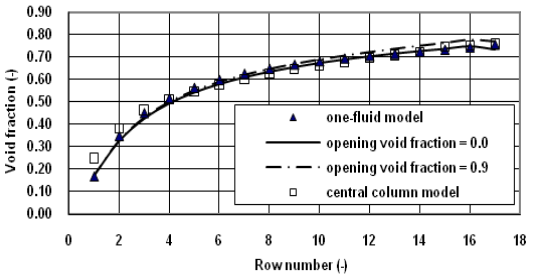

(a) Column 9.5

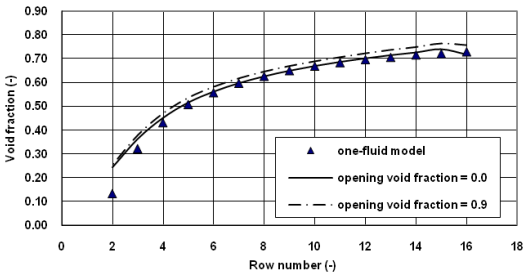

(b) Column 12.5

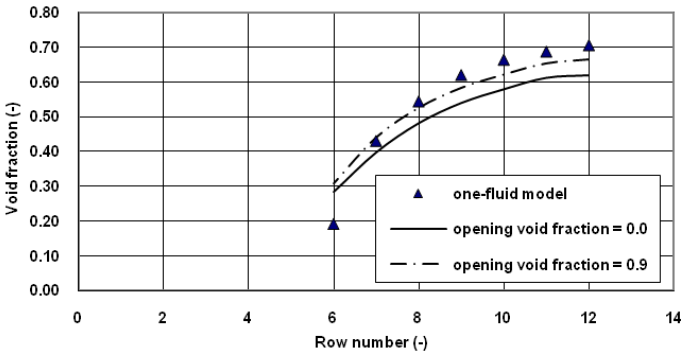

(c) Column 15.5

Figure 7.28: Comparisons of one and two-fluid model at 40 kW/m^2

In general, a good agreement is obtained between predicted and measured data, indicating that the developed interfacial drag coefficient for pentane used in the bundle, combined with that used in the pool, generates quantitative results. The convergence at 30 kW/m^{2}and 40 kW/m^2 reached RMS residuals of about 5.0 e-4, whereas at lower heat fluxes the convergence was better. This might be due to the more complicated flow pattern at higher heat fluxes.

7.6 The central column model

To obtain intermittent flow in the two fluid models, the value of 0.9 for the re-entry void fraction is used. Among the flows in different columns of the bundle, the fluid movement in the central column is most likely to be similar to 1-D flow. This is caused by the prevention of the movement of the horizontal mass flux by the symmetry boundary condition at the bundle centreline. The pressure gradient in the central column is described by:

$$\frac{\partial p}{\partial y} = -\rho_{tp} g + \frac{1}{\emptyset}\left(F_{sL}^{y} + F_{sg}^{y}\right) \tag{7.1}$$

Keeping the vertical mass flux constant, this gradient reduces to a critical value of the gas-mass fraction, after which it starts increasing. At the point where the critical gas-mass fraction is reached, the partial derivative of the pressure gradient with respect to gas mass fraction is zero, i.e.:

$$\frac{\partial}{\partial z}\left(\frac{\partial p}{\partial y}\right) = 0 \tag{7.2}$$

The two-fluid model inlet value of the vertical mass flux was used in the central column model for different values of heat flux. The energy equation in one-dimensional form is given as:

$$m_v h_{fg} \frac{dz}{dy} = \frac{\pi D q}{p^2} \tag{7.3}$$

Equations (7.1) and (7.3) were solved simultaneously, until Eq. (7.2) was satisfied. In order to satisfy Eq. (7.2), the vertical mass flux was reduced. The equations were solved using a specially written computer program, with the data input being the geometry of the tube bundle, the heat flux, the fluid properties and the inlet value of the vertical mass flux based on two-fluid model. This numerical prediction is named the central column model and is shown for all values of heat flux in the central column 9.5 in the figures for pressure drop, vertical mass flux distribution, and void fraction distribution i.e., Figs. 7.5a ,7.6a ,7.7a, 7.12a, 7.13a, 7.14a, 7.19a, 7.20a, 7.21a,7.26a, 7.27a and 7.28a. By comparing the numerical predictions of the one-fluid model [5], two-fluid model and central column model, the value of the re-entry void fraction (0.9), determines the closeness of the two-fluid model with the central column model.

7.7 Vertical superficial gas velocity

The predictions for the observations of bubbly and intermittent flow were obtained by altering the value of α_{out} at the north boundary. Bubbly flows were found at a value of α_{out} of zero, an all liquid condition, and intermittent flows were found at a value of α_{out} of 0.9, close to all vapour. The experimental data suggest that the vertical superficial gas velocity between the smallest distance in the tubes, corresponds to $Ku = 0.9$ at the alteration from a bubbly flow regime to intermittent regime.

The variation of the vertical superficial gas velocities for different heat flux values is represented in Fig. 7.29. The superficial gas velocity of 1.92 m/s corresponds to $Ku = 0.9$ for n-pentane at atmospheric pressure and is given as the upper limit for the contour plots, so that the region about this corresponds to the region in intermittent flow.

In Fig. 7.29 (a), there is no significant region in intermittent at 10 kW/m^2. The re-entry void fraction, α_{out}, is zero and this gives bubbly flow. At higher heat flux values, Figure 7.29 (b, c, and d), significant regions of intermittent flow area regime are observed. As the heat flux increases, the regions in intermittent flow increase and it moves downwards to occupy more area of the tube bundle. In the experimental results, it was observed that intermittent flow arises at different locations for different heat flux values. At 20 kW/m^2 the transition occurs between row 12 and 13 and is shown in Figure 7.29 (b).

Similarly, at 30 kW/m^2, the transition occurs between row 8 and 9 and at 40 kW/m^2 occurs between row 7 and 8. This location of the transition for 30 and 40 kW/m^2 is also indicated in Figure 7.29 (c and d, respectively). These experimental locations of the transition flow for different heat flux conditions are consistent with the numerical results.

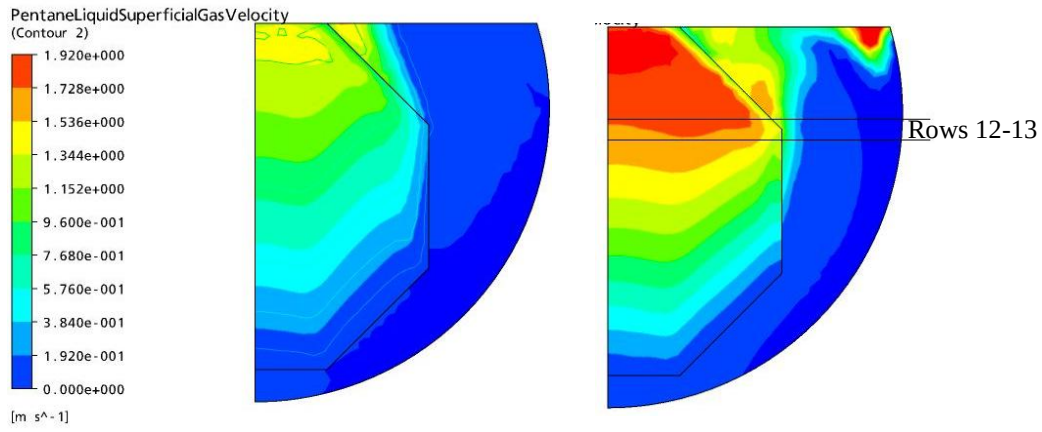

(a) at q= 10kW/m^2 (b) at q=20kW/m^2

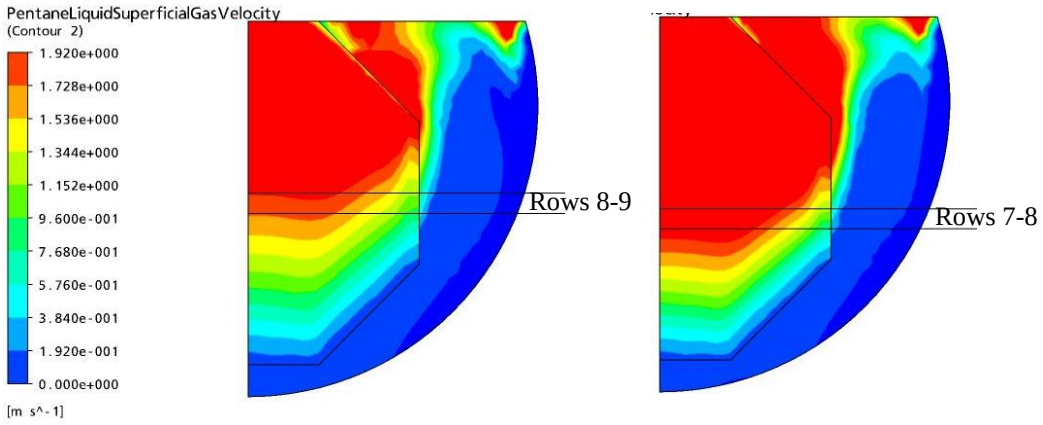

(c) at q=30kW/m^2 (d) at q=40kW/m^2

Figure 7.29: Variation of the vertical superficial gas velocities at different heat fluxes.

7.8 Summary

This chapter has introduced results that confirm the suitability of the use of the two-fluid model in the design of the kettle reboiler and in the understanding of how it works. The results give information within the kettle reboiler about the local flow conditions (void fraction, liquid and vapor velocities vectors, pressure drop, vertical mass flux and void fraction profiles). While the previously available model is able to predict some aspects of the results, the two-fluid model provides more detailed predictions that are in better agreement with the experimental results, but require more time to compute. The following paragraphs discuss the reasons for this.

The presented two-fluid model is based on a number of assumptions. For constructing the two-fluid model, the tube resistance and drag coefficient were developed from the 1-D model. For the two-fluid model Equ. (6.25) was used for obtaining C_D and this correlation can only be used for this particular bundle geometry with boiling pentane at atmospheric pressure. For other bundle configurations, fluid or pressure values, another correlation would be needed. Despite the turbulent activity in the pool, the Grace et al drag coefficient [85], has produced good agreement with the measured data, as presented in the Figs. 7.19 and 7.26. In order to confirm the flow predictions in the pool, an investigation of the velocity distribution in the pool should be carried out. This is done in Chapter 8.

It is worth noting that from this study for pentane, and that of McNeil et al [7], for R113, that various results can be found through the assumed values of α_{out} at the north boundary [7, 69]. Based on the experimental results, only two solutions occur in practice. These correspond to liquid re-entry and vapour re-entry [7], and result from the tube bundle operating in the bubbly and intermittent flow regimes, respectively, using the appropriate α_{out} to give the correct flow pattern and pressure drop distribution. In the bubbly flow regime, the vapour follows the profile of the bundle geometry and exits the domain without deviating into the pool, as indicated in Figs. 7.2 and 7.9. In the intermittent flow regime, vapour passes out of the north, north west and north east faces of the tube bundle and flows into the pool.

The present model shows good agreement with experimental results of the pressure drop distribution (Figs. 7.5, 7.12, 7.19 and 7.26), and flow distributions (Figs. 7.2, 7.3 and 7.4 with Figs. 7.1; Figs. 7.9 , 7.10 and 7.11 with Figs. 7.8; Fig. 7.16, 7.17 and 7.18 with Fig. 7.15; and Figs. 7.23, 7.24 and 7.25 with Fig. 7.22). In the columns close to the bundle-pool interface (Figs. 7.6c, 7.13c, 7.20c and 7.27c), some disagreement has been observed between the predictions of the one-fluid model and the two-fluid model data. This is thought to be due to the difficulty in assigning the pressure variation at the pool with satisfactory precision to the one-fluid model [5]. This drawback has been removed by including the shell arrangement in the present two-fluid model, which leads to a better agreement with the measured results, as illustrated in Figs. 7.5, 7.12, 7.19 and 7.26.

It is necessary to analyze why the variation of flow patterns in the tube bundle occurs for different values of re-entry void fraction α_{out} at the north boundary. It is well known

that bubbly flows are buoyancy driven and, before transition, the flow in the bubbly regime always moves up vertically and never enters into the pool side. After transition, within the intermittent flow pattern, the gas flow is small and not able to drag the liquid upwards. Therefore, a portion of the liquid, carrying vapour with it, enters into the pool side [7]. The two-fluid model reproduces the bubbly regime at the value of $\alpha_{out} = 0$ (only liquid re-enters from the north boundary). This prevents vapour flowing into the pool side. In the intermittent flow regime, the liquid exiting across the north face is in equilibrium with the liquid flow re-entering through the north boundary [7]. Thus, the value of α_{out} of 0.9 greatly reduces the liquid flow that comes through the north boundary. An all-gas value of α_{out} would completely prevent liquid from leaving through the north boundary, but this case does not occur in reality. Thus, a near-vapour, $\alpha_{out}=0.9$, allows a small quantity of liquid to exit from the north boundary, forcing the remainder through the north east and northwest boundaries. Therefore, changing the void fraction (α_{out}) from 0 to 0.9 at the north boundary changes the flow to resemble the bubbly and intermittent flow patterns. A similar conclusion for R113 was obtained by McNeil at el. [7].

CHAPTER 8

Velocity Distribution and Mass Flow Rate in the Pool

8.1 Introduction

The most critical aspect of design of the kettle reboiler involves the estimation of the flow field within the bundle. This information is essential for determining the heat transfer rate. Miller used particle image velocimetry (PIV) to measure velocity profiles within the pool in the kettle reboiler. Miller [15] measured velocity distributions at the bottom and sides of the pool and this is the only study to have experimental data for the recirculating flow velocities in the shell. These data were used for comparison to, and validation of, the present model. In this chapter, CFD simulations are obtained to compare with the measured velocity distributions at heat fluxes of 10, 20, 30 and 40 kW/m^2. An example of the predicted velocity distributions obtained is shown in Fig. 8.1 for a heat flux of 20 kW/m^2.

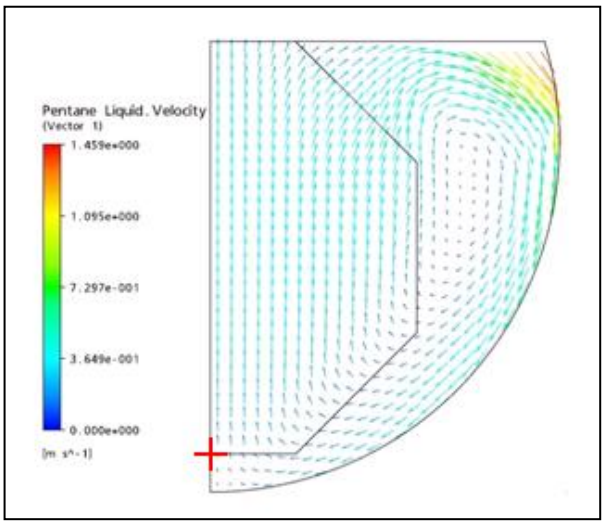

Figure 8.1: Velocities vectors distribution within reboiler at 20 kW/m^2

It is clear from this figure that the flow movement in the kettle rebolier is two-dimensional. The fluid follows a path around the bundle that follows the geometry profile of the pool wall and predominantly enters the tube bundle at the bottom. Inside the tube bundle, the gas-mass fraction of the flow increases towards the top rows, as the flow partially evaporates and moves vertically upwards [4]. Near the centre line at the top of the bundle, the fluid exits vertically, with the remaining fluid moving more and more towards the pool side as the distance from the centre line increases. This causes a

large flow circulation to exist in the pool and this has a constantly changing centre of circulation as its position depends on the bundle heat flux [13]. Hence the liquid velocity varies between the edge of the bundle and the pool wall.

Across some vertical and horizontal planes in the pool, the velocities were used to obtain mass flow rates at different heat fluxes of 10, 20, 30 and 40 kW/m^2.The selected horizontal planes corresponded to row numbers and the vertical planes to column numbers. These planes were extended horizontally and vertically from the sides of the bundle to the pool wall and are shown in Fig. 8.4. The origin is given as a cross on this figure. These planes are the same as those used by Miller when he obtained the experimental data [2,15]. Hence, using the two-fluid model, the velocity component u and v and the mass flow rates m_x and m_y were numerically predicted for different heat fluxes. Velocity components u, v were in the x and y direction, respectively, in the horizontal planes and the vertical planes. m_y indicates the mass flow rate in the y-direction over the entire horizontal plane, and m_x indicates the mass flow rate in the x-direction over the entire vertical plane.

8.2 Procedure for mass flow rate evaluation

To compare the present numerical results with Miller's experimental data [2,15], the mass flow rate across any particular plane below or beside the bundle is required. The equations for calculating the horizontal and vertical mass flow rates, m_x and m_y, through vertical and horizontal planes can be written as:

$$m_x = \rho L \int_{y_1}^{y_2} u \; dy \tag{8.1}$$

$$m_y = \rho L \int_{x_1}^{x_2} v \; dx \tag{8.2}$$

where, ρ is the liquid pentane density and L is the plane depth.

The variation in the flow velocities at different planes near columns and rows is evaluated from the numerical data. The velocity profiles were approximated by third order polynomials for vertical and horizontal velocities using a least square curve fit. Integrating these velocity profile equations between given limits of the vertical and horizontal planes using Eqs. 8.1 and 8.2 gives the mass flow rates through the planes.

For example, at column 11.5 (x=63.5 mm), Fig. 8.4, the vertical plane horizontal velocities and the third order polynomial fit at 20 kW/m^2 are shown in the Figure 8.2.

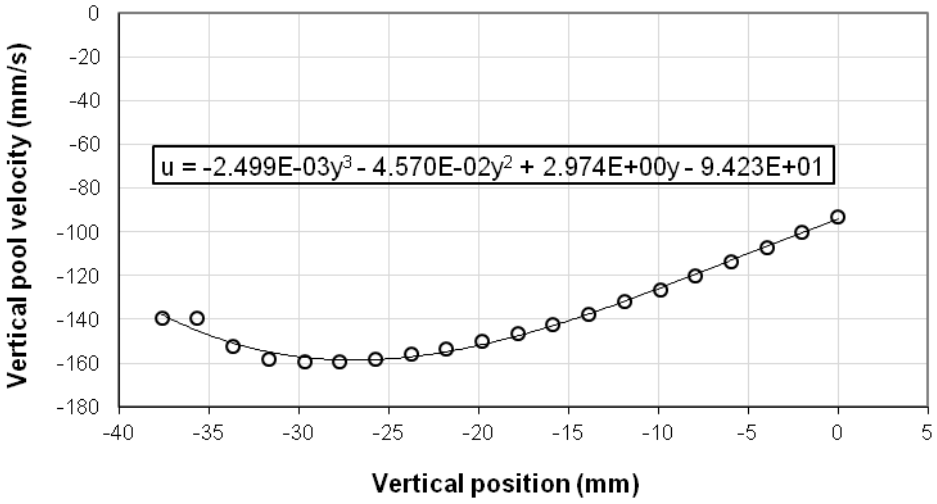

Figure 8.2: Velocity profile equation at the level of column 11.5 (x = 63.5 mm) for 20 kW/m^2

Similarly, at row 6.5 (y = 152.4 mm), Fig.8.4, the vertical velocities and the third order polynomial fit at 20 kW/m^2 is shown in Fig. 8.3. By integrating these profiles, the mass flow m_x rates and m_y through the vertical and horizontal planes are found to be 0.5 and 0.6 kg/s respectively.

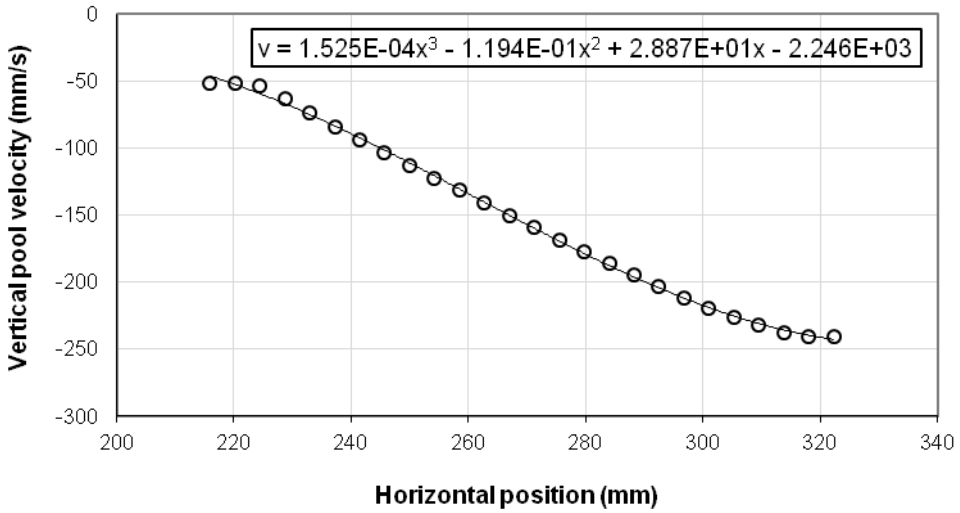

Figure 8.3: Velocity profile equation at the level of row 6.5 (y = 152.4 mm) for 20 kW/m^2

8.3 Heat flux of 10 kW/m^2

The velocities in the x and y directions and the mass flow rates for the selected horizontal and vertical planes were obtained at a heat flux of $10\,\mathrm{kW/m^2}$ for the horizontal and vertical planes shown in Fig. 8.4 (a) and (b).

To test for mesh dependency, different mesh sizes of 2, 4, 8 and 10 mm were considered. For each mesh size, to satisfy the continuity equation, the mass liquid flow rate through plane a-b should be the same as that through plane a-c, Fig. 8.4 (a). The integrated mass flow rate through a-b and a-c for each mesh size is given in Table 8.1. By subtracting the mass flow rate through planes a-b and a-c, the differences were calculated. These gave errors of 10% for the mesh size of 10 mm, 2% for 8mm, and less than 1% for 4 and 2mm. This error was found by Eq. (8.3).

$$Error\ \% = \left|\frac{\dot{m}_{ac}-\dot{m}_{ab}}{\dot{m}_{ac}}\right| \text{x}100 \qquad (8.3)$$

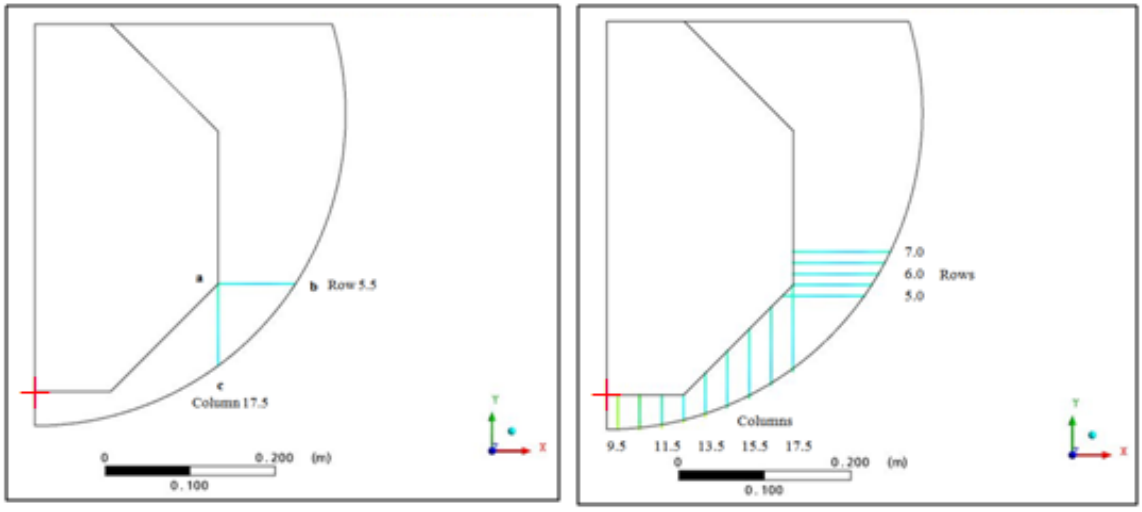

(a) (b)

Figure 8.4 Schematic of different horizontal and vertical planes at 10 kW/m^2

Table 8.1 Mass flow rate balance for different mesh sizes

$\dot{m}$ (kg/s) On Planes	q=10 kW/m^2			
	Δx=10 mm	Δx=8 mm	Δx= 4mm	Δx=2 mm
a-c	0.54953	0.56322	0.59245	0.59364
a-b	0.60618	0.56311	0.58920	0.58834

Thus, balance agreement is obtained for mesh sizes of 2 and 4 mm. Below the bundle, the mass flow rates, m_x, through the vertical planes shown in Fig. 8.4b were obtained for each horizontal position. Based on the velocity distribution, u, over the entire vertical plane, the corresponding mass flow rates, m_x, were obtained by integration and are shown in Fig. 8.5. The mass flow rates decreased from the edge of the bundle towards the centre line. Starting from column 17, the mass flow rate passed from the vertical plane below column 17 towards the vertical plane below column 16. The drop in flow rate between the vertical plane at column 17 and 16 resulted from the flow entering the bundle between column 17 and 16. The same phenomenon was observed between other columns until the flow reached the centreline of the bundle. The present numerical results show the same trend in mass flow rate as the Miller's experimental results [15, 2].

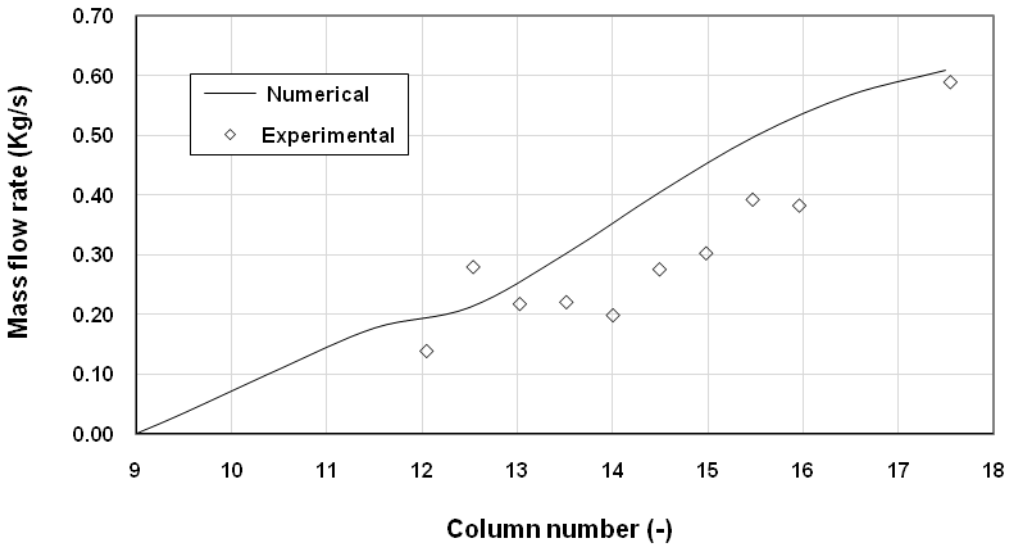

Figure 8.5 Variation of the mass flow rates below the tube bundle at 10 kW/m^2

The vertical pool mass flow rates, m_y, were obtained by integrating the velocities v ,through each horizontal plane. The variation of the vertical mass flow rates, m_y, for each vertical position shown in Fig. 8.4 (b), is given in Fig. 8.6. The mass flow rate decreases slightly from row 7 to row 5.5 .The reduction of the flow rate in this zone is due to a small horizontal movement of flow into the bundle. The predicted results are in close agreement with Miller's [15, 2] measurements from row 7 to row 6. Further down, small deviations are observed. These are mainly due to differences in the length of the horizontal planes, used because of difficulties in measuring the velocities near the tube bundle and shell wall. Higher values of mass flow rate would be expected if the data for the velocities near to the bundle and shell wall were available [2].

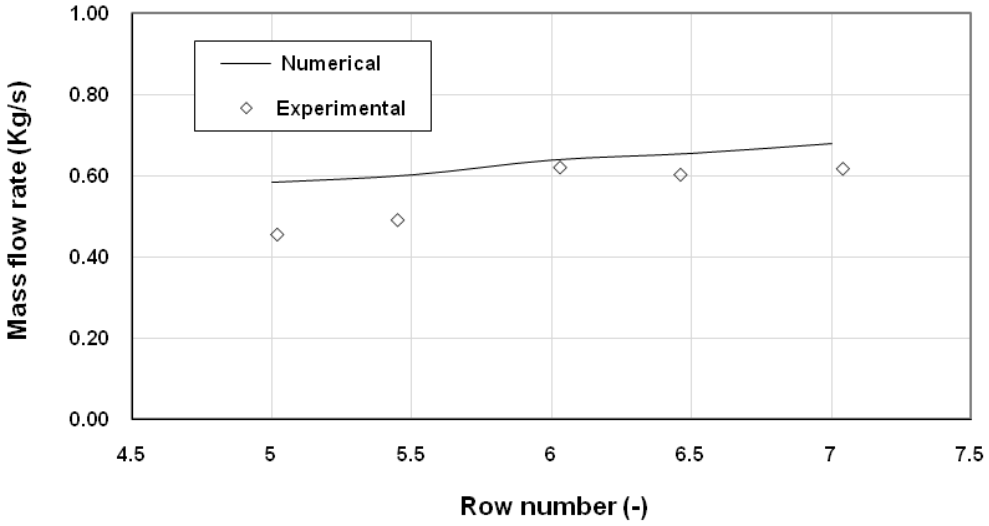

Figure 8.6: Variation of the mass flow rates beside the tube bundle at 10 kW/m^2

The vertical and horizontal velocity predictions at row 5, Fig. 8.4b, (y = 114.3 mm) are shown for different mesh sizes of 2, 4 and 10 mm in Fig. 8.7. Figure 8.7 (a) shows the variation of the vertical velocity, v, and Fig 8.7 (b) the horizontal velocity, u. Both the vertical and horizontal velocities are at their lowest value near to the tube bundle for all mesh sizes. This trend in velocity profile results from boiling fluid moving upwards within the tube bundle. Similar trends are observed between the present numerical study and Miller's experiments [15, 2].

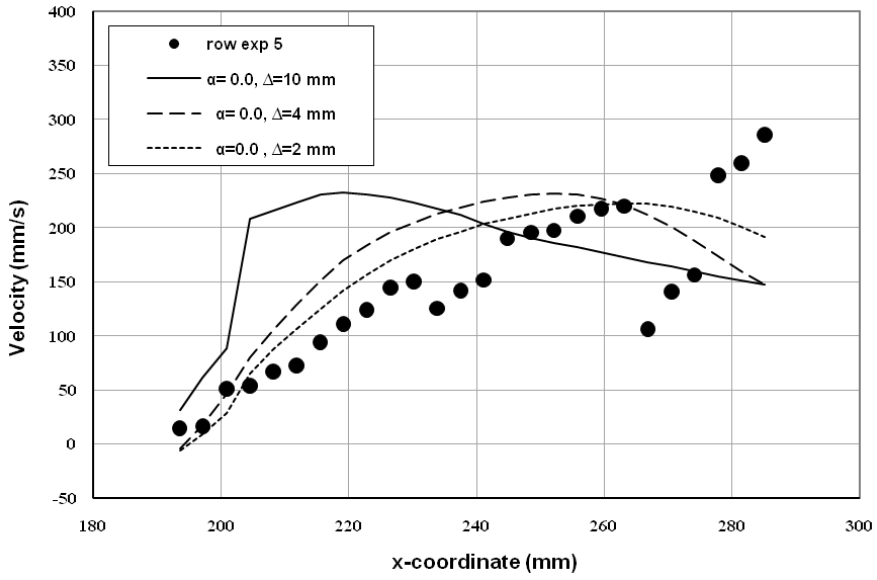

(a) Vertical velocity

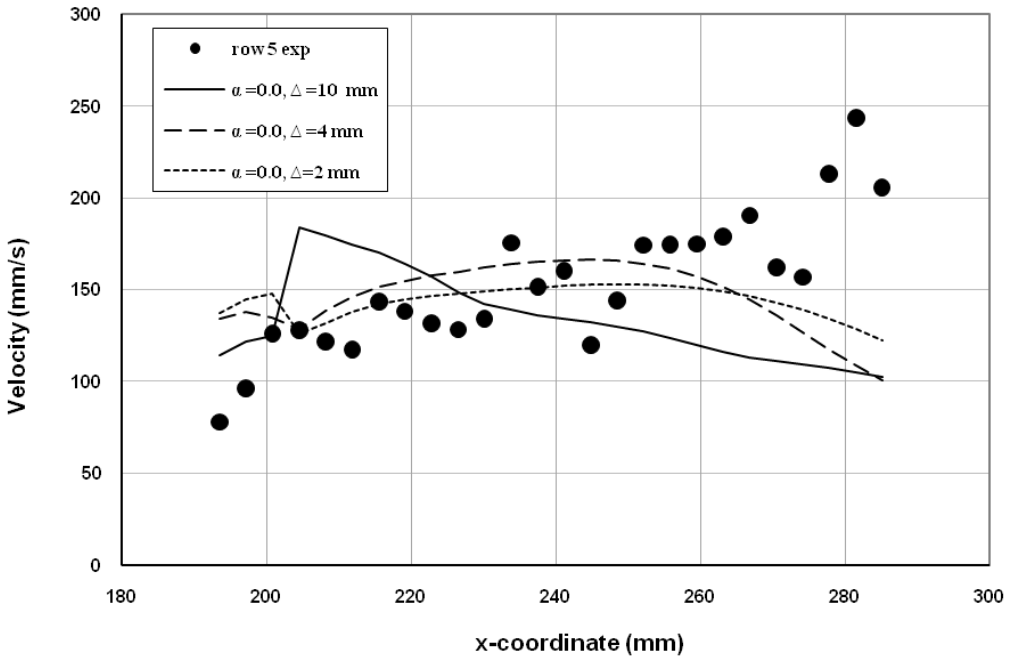

(b) Horizontal velocity

Figure 8.7: Variation of vertical and horizontal velocities along the horizontal plane at row 5 for 10 kW/m^2

8.4 Heat flux of 20 kW/m^2

The locations of the vertical and horizontal planes used at a heat flux of 20 kW/m^2 are shown in Fig. 8.8.

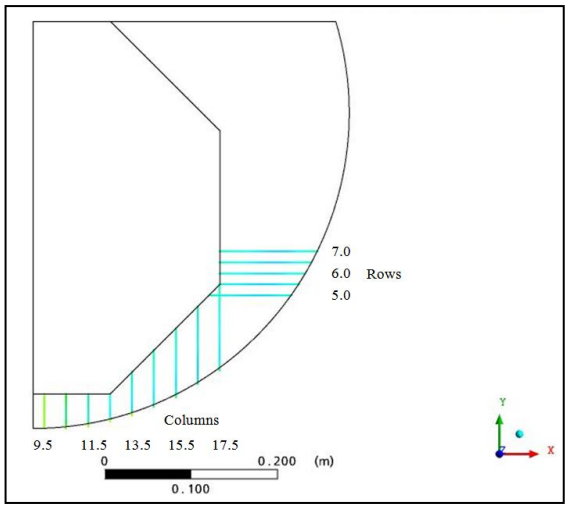

Figure 8.8: Schematic of horizontal and vertical planes at 20 kW/m^2

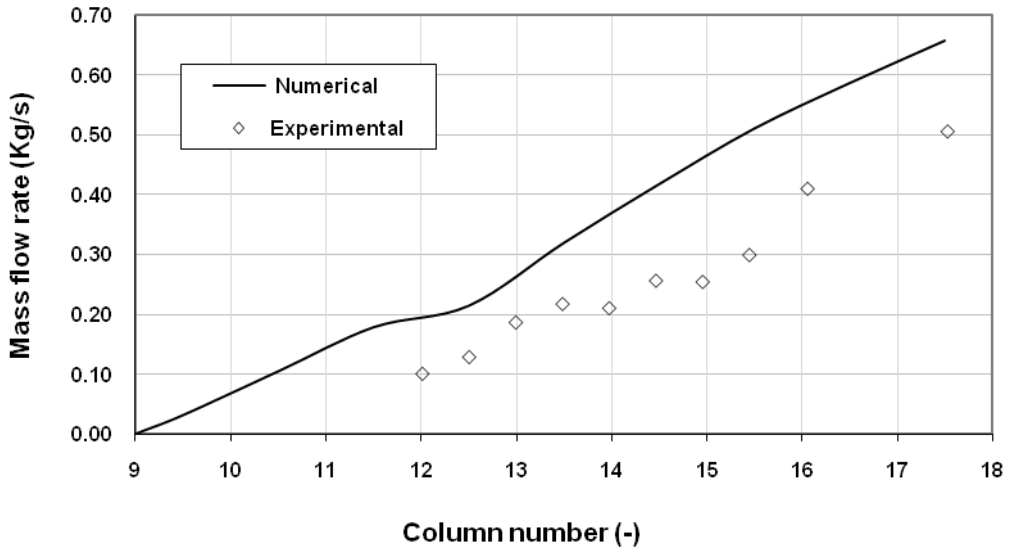

Figure 8.9: Variation of the mass flow rates below the tube bundle at 20 kW/m^2

The mass flow rates, m_x and m_y were obtained as before. Below the bundle, the flow rate, m_x, decreases as the fluid moves towards the centreline. A large flow rate drop, m_x is observed between columns 17 and 12. This reduction is due to a quantity of the flow moving upwards into the bundle. The horizontal incoming flows between the tubes below row 5 were partially guided towards the bundle. A slight decrease in the horizontal mass flow rate was observed between column 12.5 and column 11.5. This occurred because of the balance of the upward fluid with the change in the cross sectional area below the tube bundle. Beyond column 11, due to variation in the fluid density within the tube bundle and shell, the flow was moving vertically upwards. In general, a similar trend is observed between the present numerical mass flow rates and Miller's experiments [2, 15]. Deviations were observed between the two results. This may be due to underestimated values of the experimental velocities in the vertical planes near the tube bundle and shell wall.

The variation of the mass flow rate in the y-direction, m_y, through the different horizontal planes shown in Fig. 8.8 is given in Fig. 8.10. As the flow moves down from row 7 to row 5, the mass flow rate decreases slightly until row 6.5. This is due to horizontal movement of the flow towards the tube bundle. This flow is also guided to move upwards by two-phase flow inside the tube bundle. Further down, there is an insignificant change in the mass flow rate till row 5. This insignificant change is

consistent with a vertical flow movement towards the bottom of the shell. The predicted mass flow rates are in good agreement with Miller's experiments [15, 2].

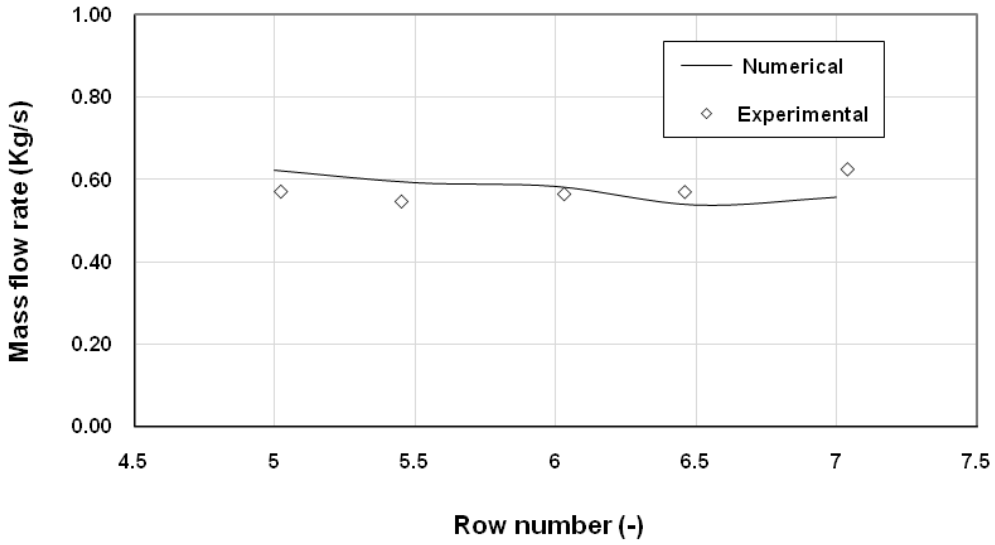

Figure 8.10: Variation of mass flow beside the tube bundle at 20 kW/m^2

Figure 8.11 (a) and (b) show the variation in vertical and horizontal flow velocity, v and u, at row 5 Fig. 8.8 for different mesh sizes. The largest flow velocities of v and u are found near to the shell wall and the smallest flow values are observed near the bundle edge. The upward two-phase flow inside the bundle causes the reduction in the velocities. The vertical velocity is reduced from 326 mm/s (near the shell wall) to 23 mm/s close to the edge of the bundle. Similarly, the horizontal velocity is reduced from 250 mm/s to 100 mm/s. The same trend in velocity profiles is obtained in Miller's experiments [2, 15].

For the vertical plane below column 17, Fig. 8.8, The variation in vertical and horizontal velocity profiles v and u are given in Fig. 8.12 (a) and (b) (x=203.2 mm). The minimum velocities (horizontal and vertical) occur near the shell wall and the maximum near the bundle edge. Diminishing horizontal velocity, u, results from upward two-phase flow in the bundle. The magnitude of the horizontal velocity varies from 250 mm/s close to the shell wall to 100 mm/s near to the bundle edge. Similarly, the vertical velocity varies from 150 mm/s to 5 mm/s. The numerical results are again in approximately agreement with Miller's experimental values [15, 2].

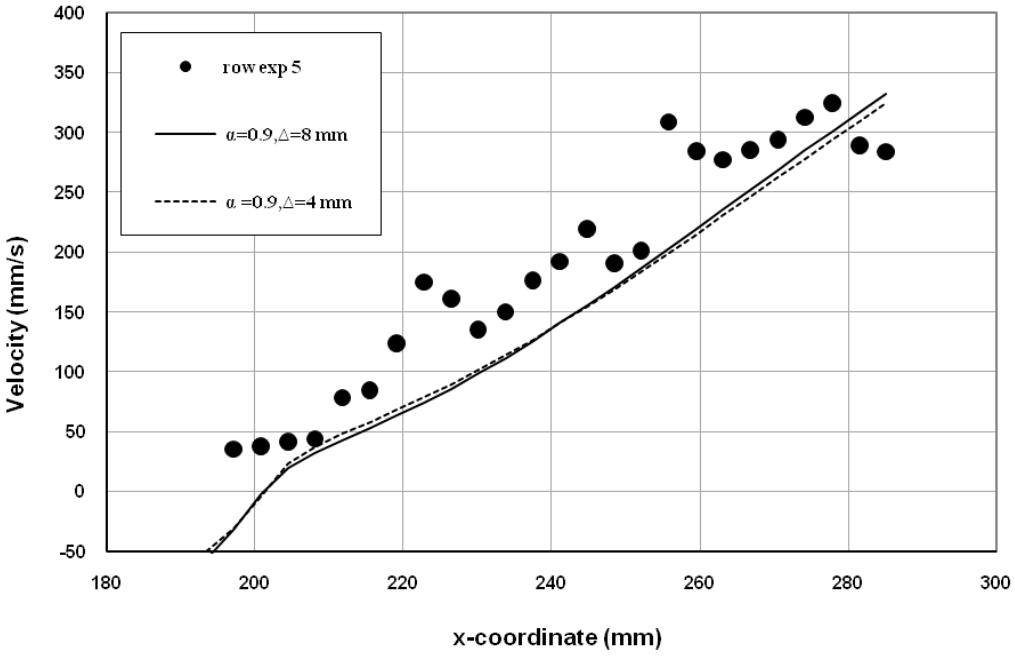

(a) Vertical velocity

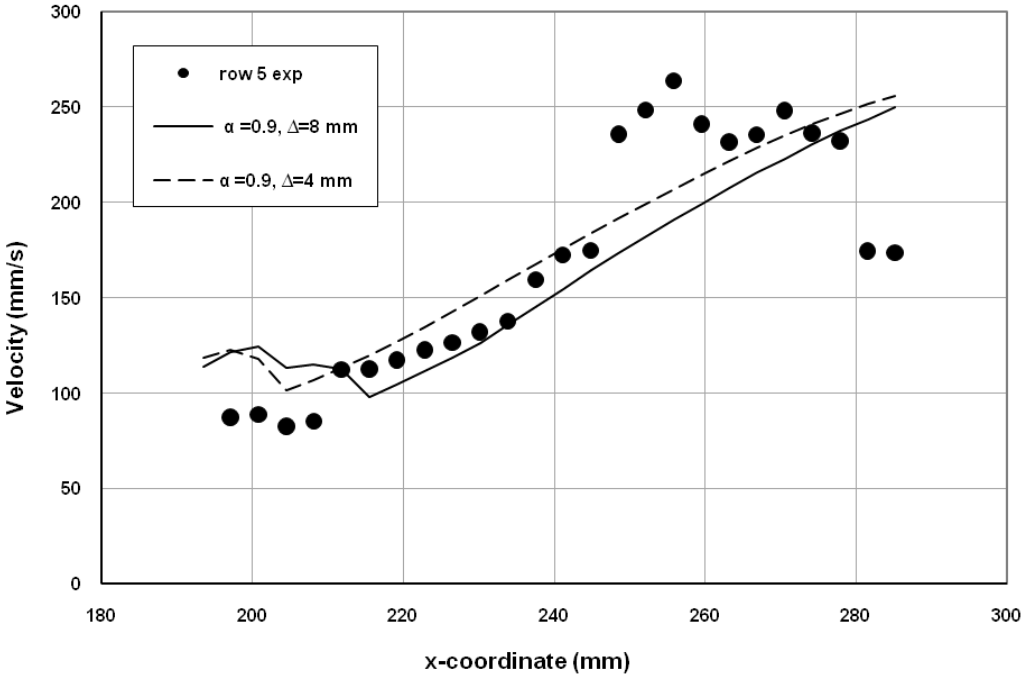

(b) Horizontal velocity

Figure 8.11: Variation of vertical and horizontal velocities across the horizontal plane at row 5 for 20 kW/m^2

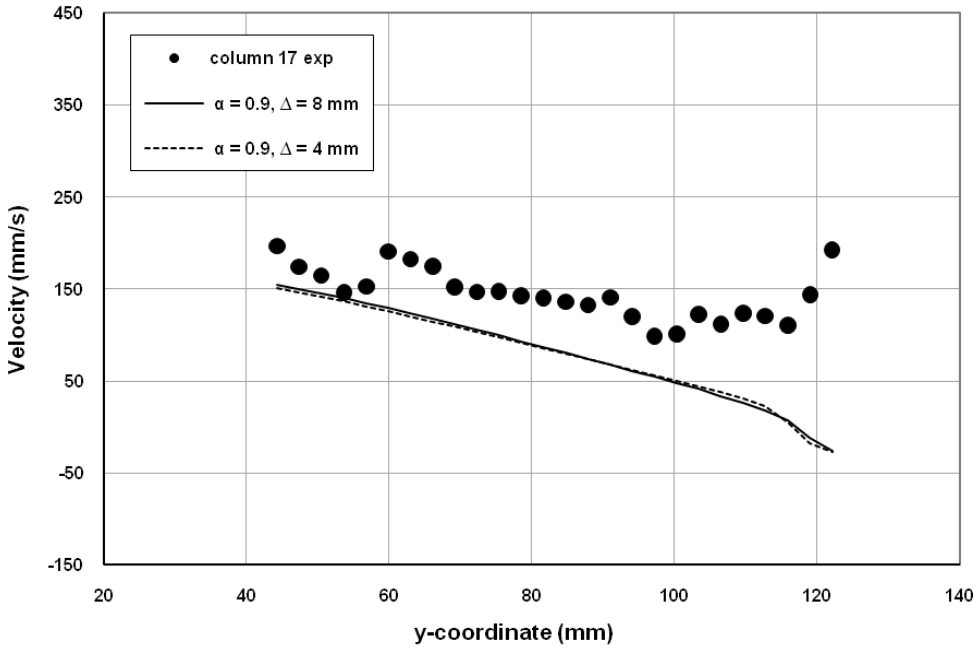

(a) Vertical velocity

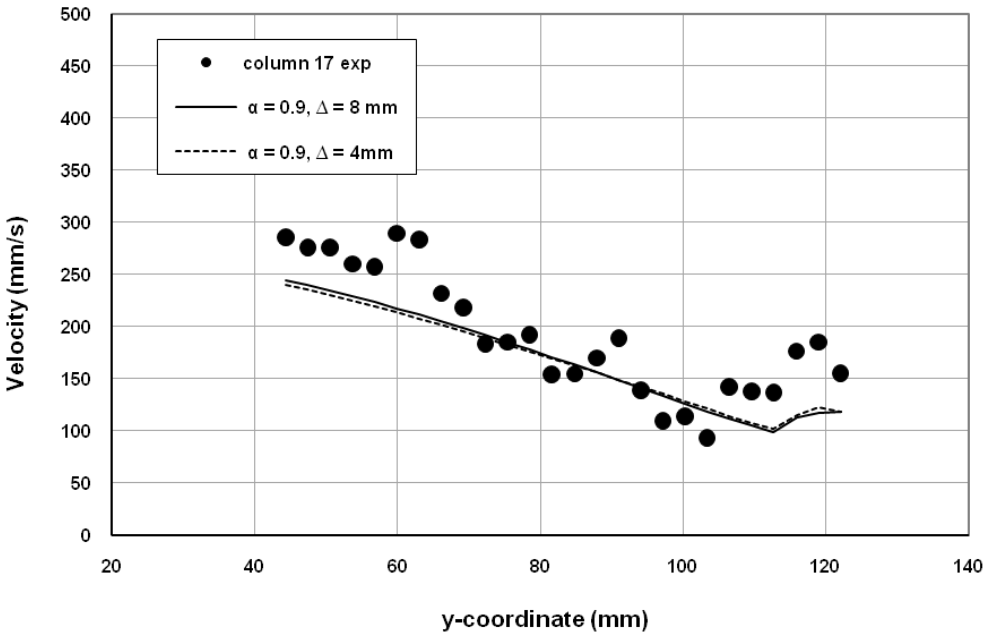

(b) Horizontal velocity

Figure 8.12: Variation of vertical and horizontal normal velocities across the vertical plane at column 17 for 20 kW/m^2

8.5 Heat flux of 30 kW/m^2

The positions of the vertical and horizontal planes for predicting velocities and normal mass flow rates in the reboiler at a heat flux of 30 kW/m^2 are shown in Fig. 8.13

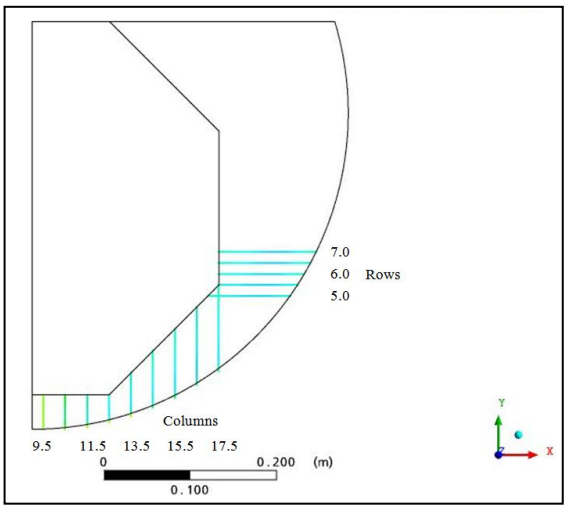

Figure 8.13: Schematic of horizontal and vertical planes at 30 kW/m^2

The variation of the horizontal mass flow rate for these vertical planes at different positions is depicted in Fig 8.14. Again the flow rate reduces from column 17 to the centre line of the bundle. From column 17 to 13, the flow rate is changed from 0.60 kg/s to 0.25 kg/s. The change in mass flow rate (0.35 kg/s) moves up into the bundle through the gaps between the columns. The mass flow rate is reduced slightly from column 12.5 to column 11.5. For columns 11.5 to 9 the flow rate drops to zero as the bundle centre line is approached. This clearly shows that all of the flow moves up into the bundle. Figure 8.14 also compares Miller's measured results [15, 2] with the numerical results. The measured results follow a similar trend. There is a fair agreement between them over a wide range of horizontal positions. Towards the bundle edge significant discrepancies are shown.

The variation in vertical mass flow rate for the horizontal planes shown in Fig. 8.13 is given in Figure 8.15. In the gap enclosed between the shell wall and the bundle, the mass flow rate decreased slightly from row 7 to row 6.5. This drop in flow rate is due to a horizontal movement of flow towards the bundle. This horizontal movement causes the flow to move laterally within the tube bundle, which is consistent with intermittent flow at this heat flux (McNeil at el [58]). From row 6.5 to row 5 minor rises in mass flow rate are shown, which is expected due to the flow into the inter-row gaps balancing

out the decreased flow area. The predicted results follow the shape of Miller's experimental data [15, 2]. Due to the periodic variations of the flow between the shell wall and the bundle, some deviations were observed, with errors in the measurement of circulation velocities occurring at high heat fluxes (Miller [15, 2]). However, the data confirm that the model predicts the correct re-circulation flow rate.

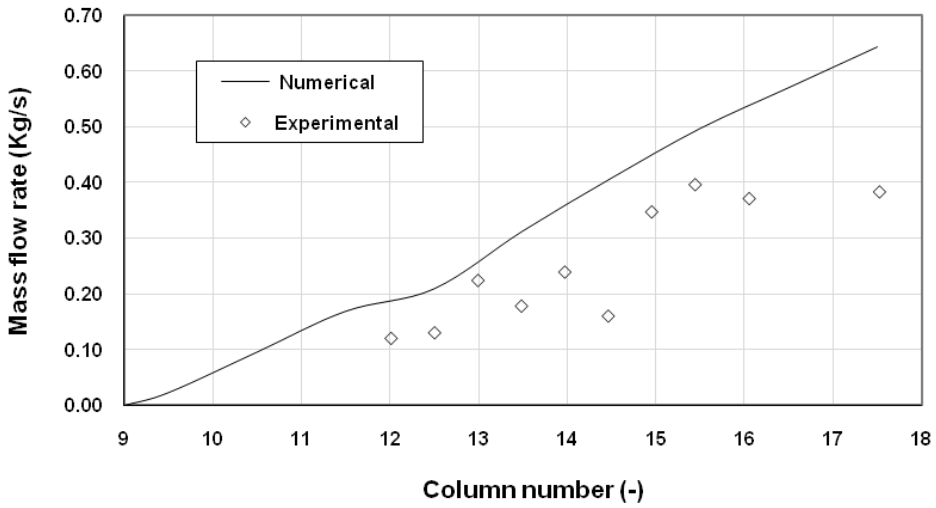

Figure 8.14: Variation of the mass flow rates below the tube bundle at 30 kW/m^2

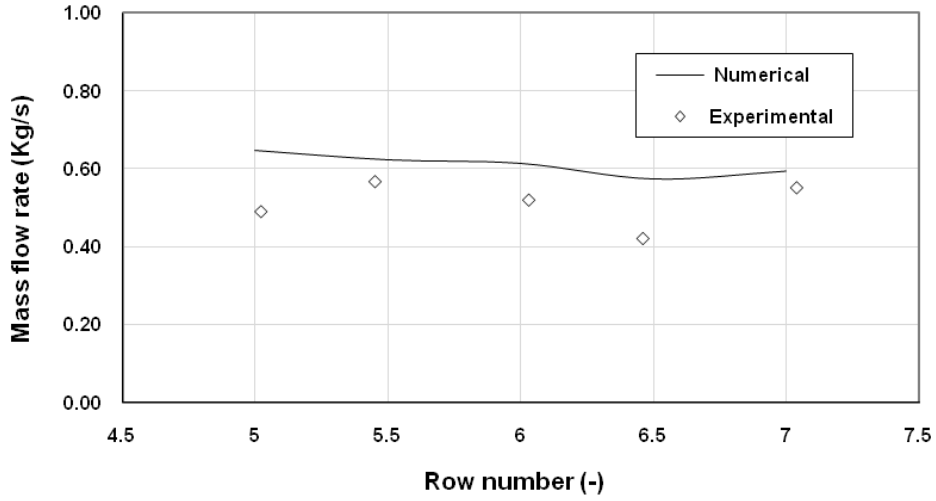

Figure 8.15: Variation of the mass flow beside the tube bundle at 30 kW/m^2

The variation of vertical and horizontal velocities for different positions in the space enclosed between the shell wall and tube bundle at row 5, Fig. 8.13, is shown in Fig. 8.16. For both the vertical and horizontal velocity curves, the maximum velocities (350 mm/s and 280 mm/s, respectively) occur close to the shell wall and the minimum velocities (0 mm/s, 80 mm/s) at the bundle edge. In both curves, the drop in the velocity is caused by upward flow in the bundle. The existence of flow fluctuations in

the pool at 30 kW/m^2 is the probable cause of the deviations between numerical and experimental results.

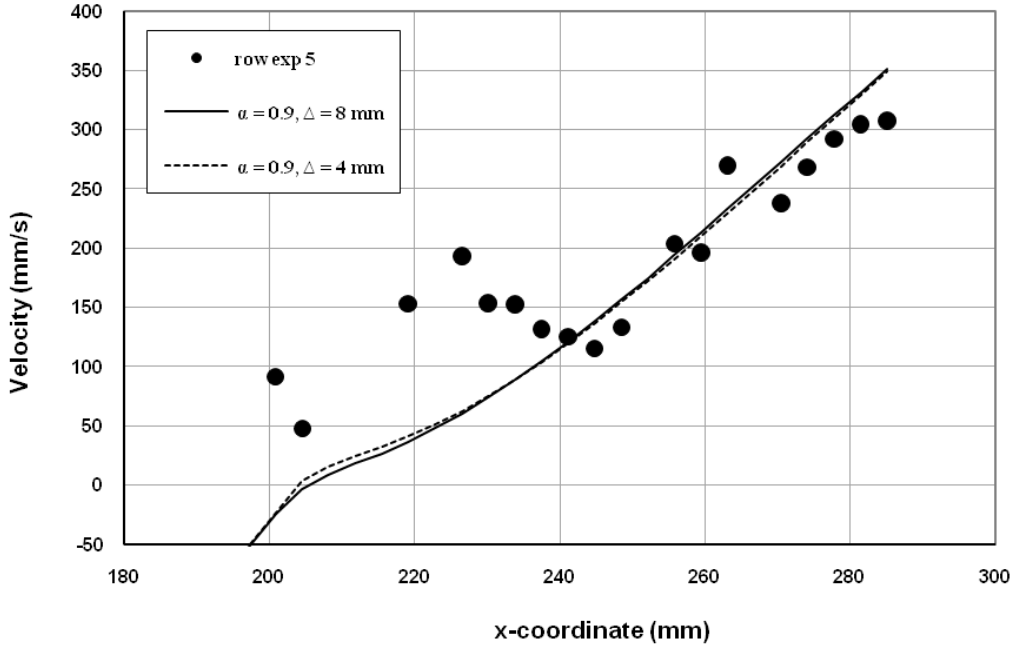

(a) Vertical velocity

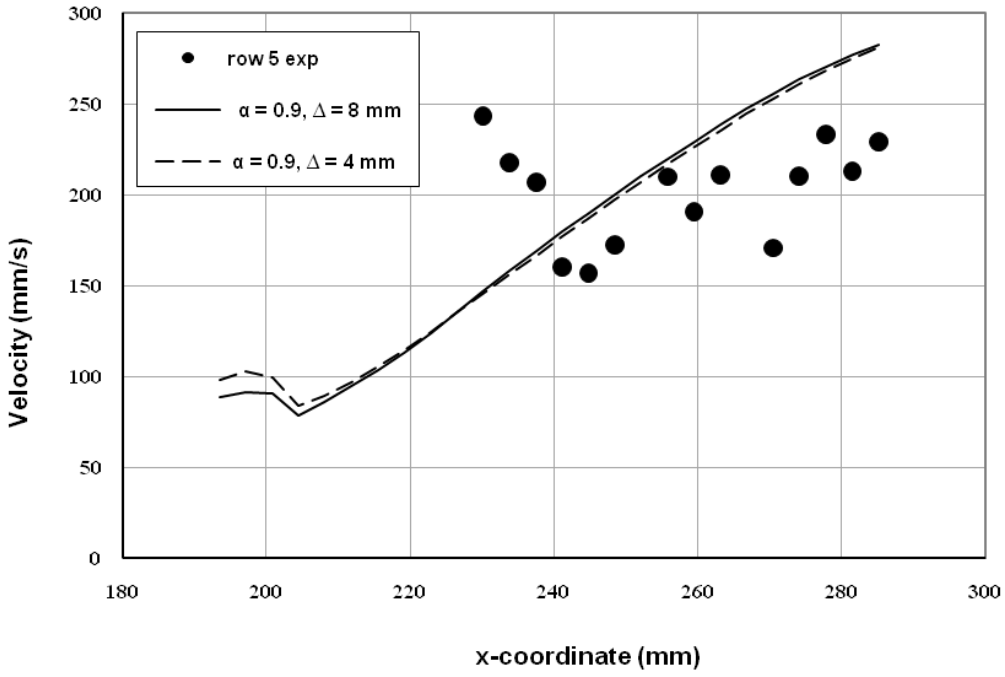

(b) Horizontal velocity

Figure 8.16: velocities at row 5 for different mesh sizes at 30 kW/m^2

8.6 Heat flux of 40 kW/m^2

The location of selected planes, where the velocity and mass flow rates were computed at 40 kW/m^2 is shown in Fig. 8.17.

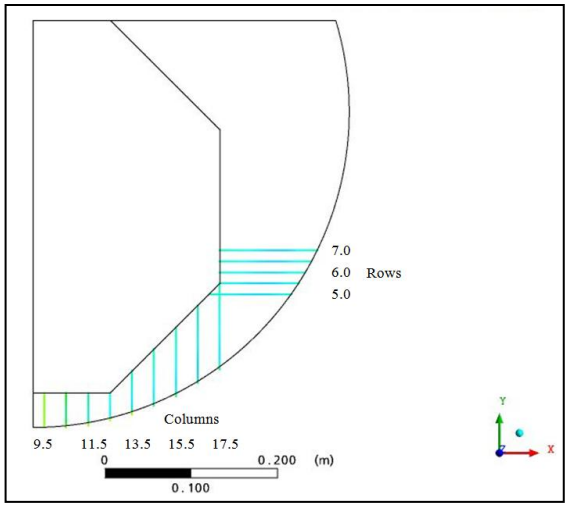

Figure 8.17: Schematic of vertical and horizontal planes at 40 kW/m^2

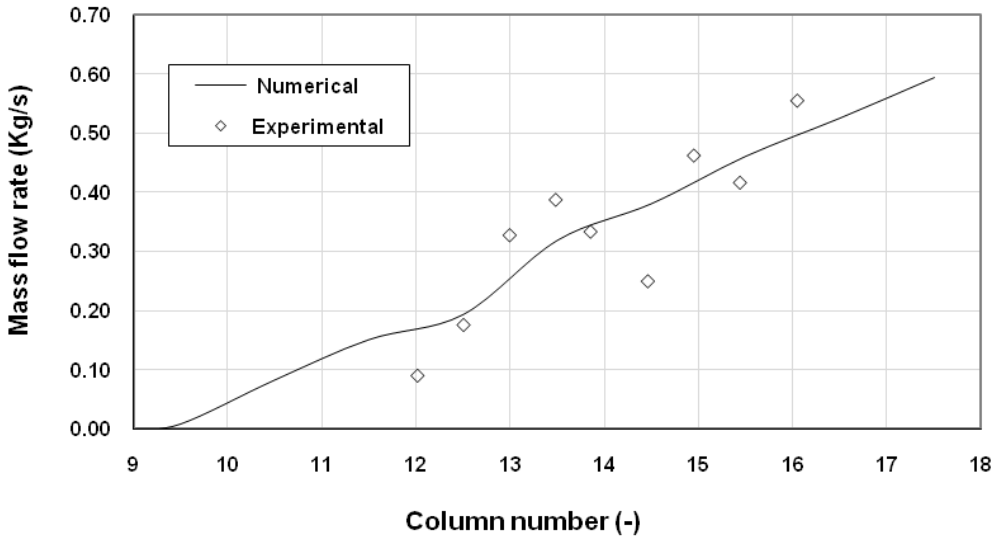

Figure 8.18: Variation of the mass flow below the tube bundle at 40 kW/m^2

The predicted horizontal mass flow rate for these horizontal positions is plotted in Fig. 8.18. As the flow approached the centreline of the bundle, three distinct regions are predicted. In the first region, the mass flow rates decreased gradually from column 17 to column 13.5. In the second region, a more rapid decrease in the mass flow rate is observed between column 13.5 and column 12.5. In the third region, from column 12.5 to the bundle centreline, the mass flow rate decreases gradually again. In the first and third regions, the reduction in the mass flow rate is due to reasonably uniform up flow

into the bundle. An increase in up flow in the second region leads to the sudden fall in the flow rate. The predicted results agree well with Miller's measurements [15, 2].

The predicted mass flow rates for the horizontal planes, Fig. 8.17, are shown in the Fig. 8.19. An almost constant mass flow rate is maintained between row 7 and row 6.5. After that, there was a small increase in the mass flow rate till row 6 due to flow out of the bundle. Down from row 6, an insignificant change in mass flow rate was found until row 5. Due to the large quantity of vapour at the pool above row 4 at a high heat flux, Miller did not produce experimental velocity data for this zone [15].

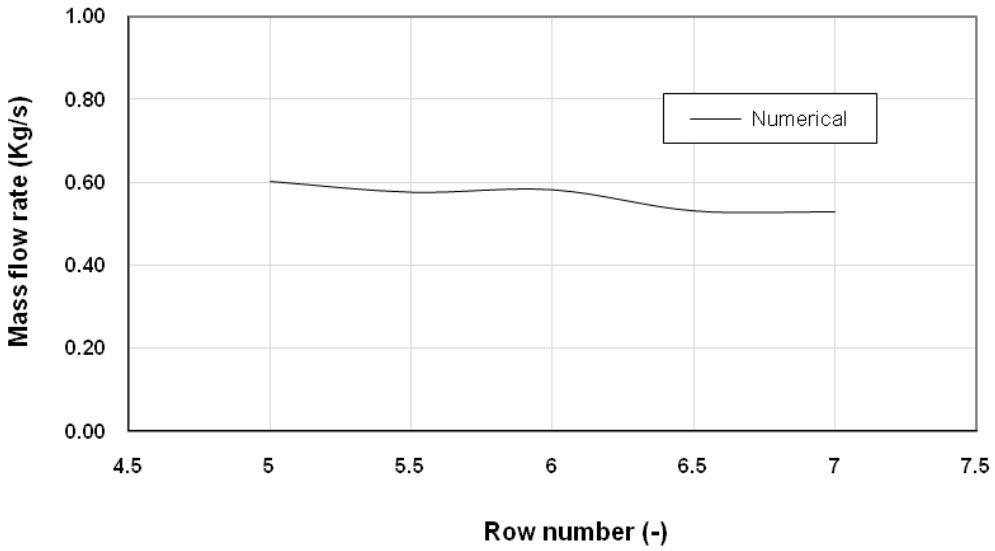

Figure 8.19: Variation of mass flow rate beside the tube at 40 kW/m^2

The row 5 (y = 114.3 mm), Fig. 8.17, vertical and horizontal velocity curves are shown in the Fig. 8.20. Similar to previous heat flux cases, the vertical and horizontal velocities have largest values of 340 mm/s and 275 mm/s and lowest values of 0 mm/s and 62 mm/s close to shell wall and bundle edge respectively. At the shell wall the flow moves vertically downwards and near the bundle edge, the flow changed to horizontal. This flow behaviour is caused by the shell shape. Experimental data were not available for comparison.

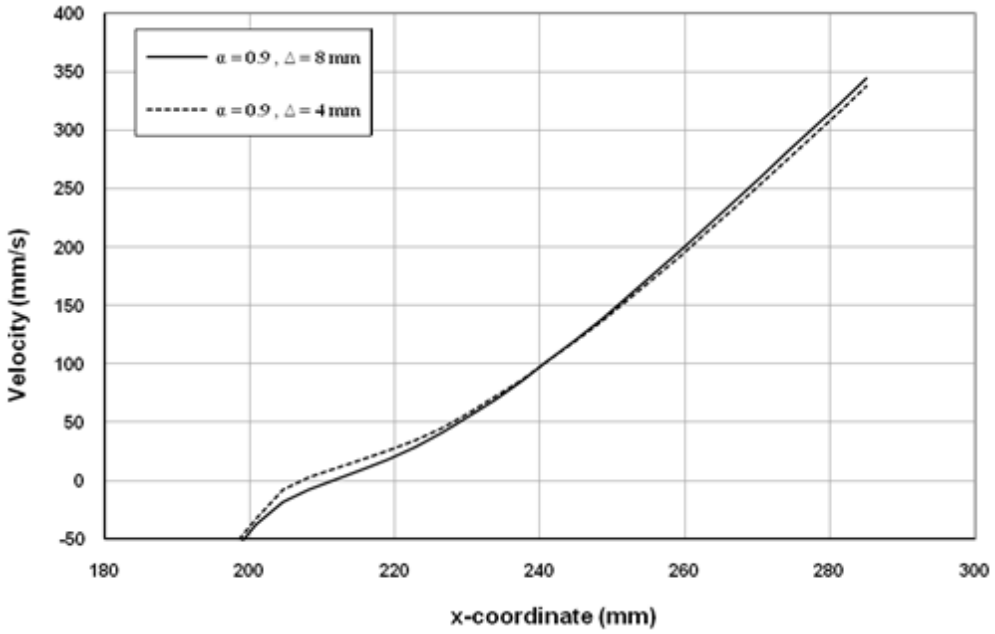

(a) Vertical velocity

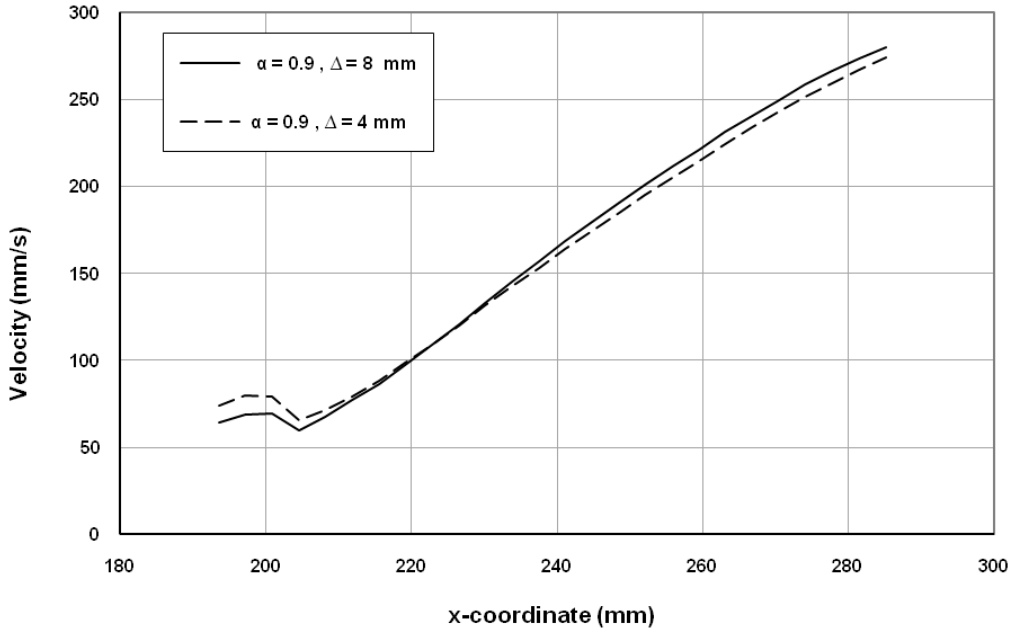

(b) Horizontal velocity

Figure 8.20: Normal velocities at row 5 for 40 kW/m^2

8.7 Effect of heat flux on velocities and mass flow rates

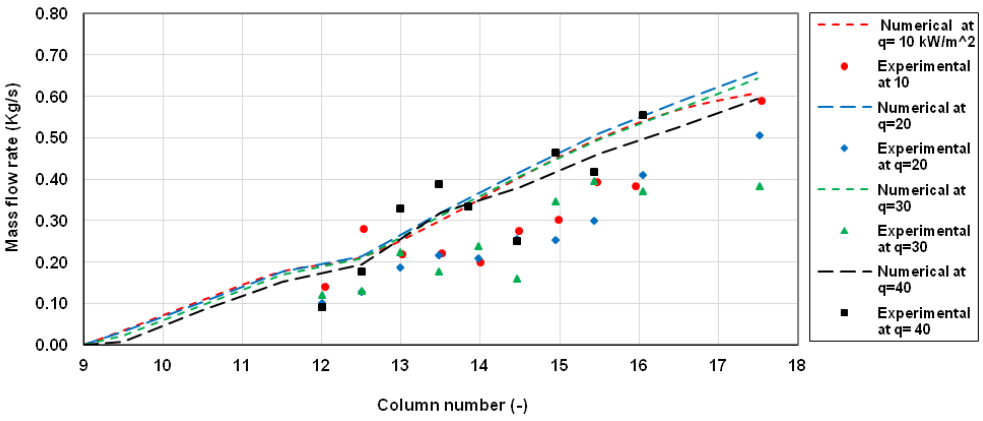

Figure 8.21: Comparisons of horizontal mass flow rate below the bundle with horizontal positions for different heat flux values.

The horizontal mass flow rate for different vertical planes across different horizontal positions below the tube bundle is shown for heat fluxes of 10, 20, 30, 40 kW/m^2 in Fig. 8.21. For all heat fluxes, the mass flow rates decreased from a maximum value at the bundle edge to minimum value close to bundle centreline. The drop in the mass flow from bundle edge to the centreline is due to up flow into the tube bundle through the spaces between the columns. The vapour generated in the tube bundle accelerates the rising up flow. From Fig. 8.21, the heat fluxes affect the flow rates. At column 16.5, the mass flow rate was noted at various heat fluxes for the purpose of comparison. The values of the mass flow rate at 10, 20, 30, and 40 kW/m^2 were observed as 0.57, 0.59, 0.57, 0.54 kg/s respectively. The changes of the flow rate for various heat flux conditions were seen in Miller's experimental results [15, 2]. The comparison of the vertical flow rate across the shell with vertical positions (across various horizontal planes) at 10, 20, 30, 40 kW/m^2 is shown in the Fig. 8.22. Small mass flow rate changes occur from row 7 to row 5. This drop is because of flow movement towards or from the bundle. At a high heat flux value, a slight flow rate decrease was observed. This is probably due to high turbulence in the pool. For row 7, the mass flow rates of 0.68, 0.55, 0.58 and 0.52 kg/s were noted at heat fluxes 10, 20, 30 and 40 kW/m^2 . These mass flow rate variations are consistent with Miller's experiments [15, 2].

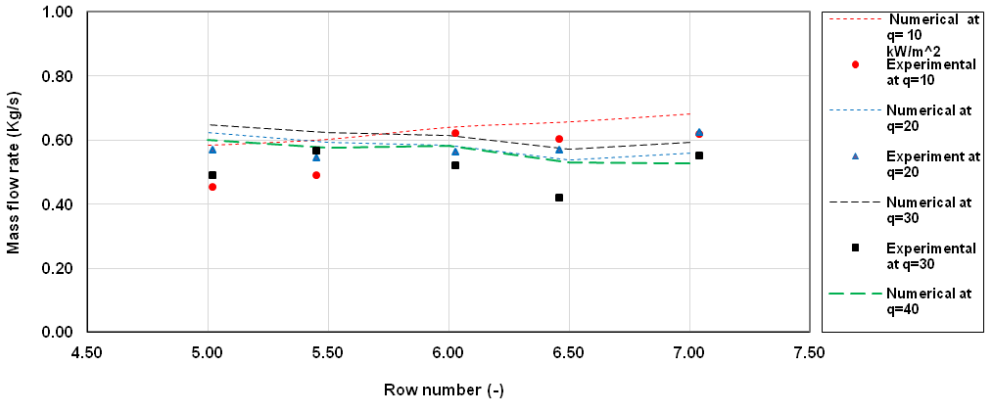

Figure 8.22: Comparison of normal flow rate beside the bundle for different heat flux values

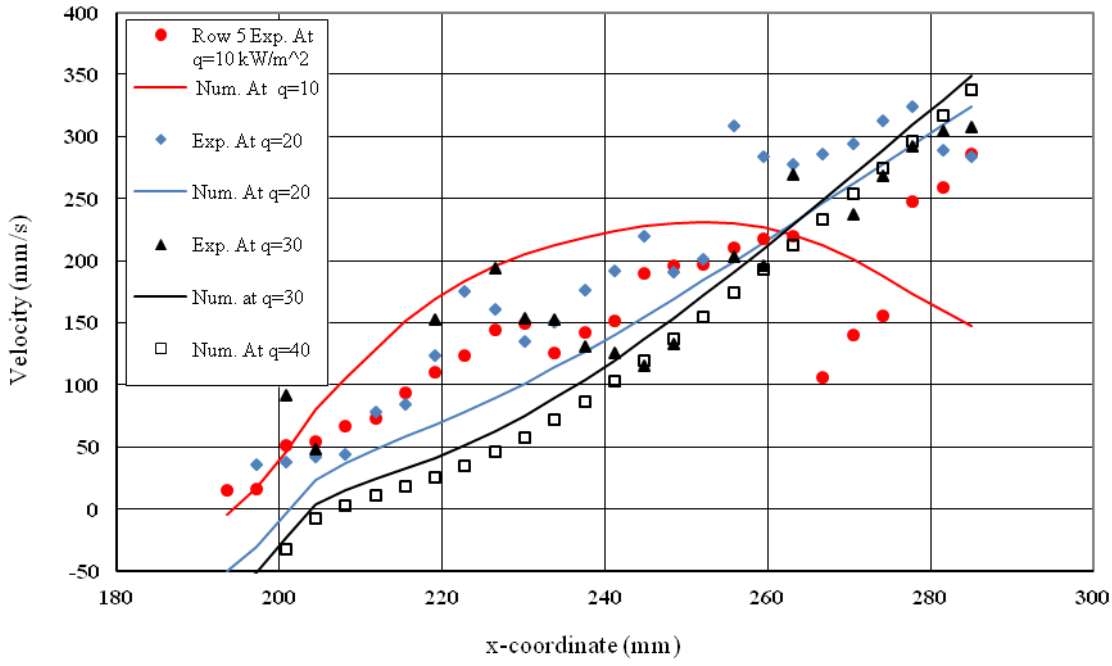

Figure 8.23: Comparisons of the vertical velocities at row 5 beside the tube bundle for different heat flux values**.**

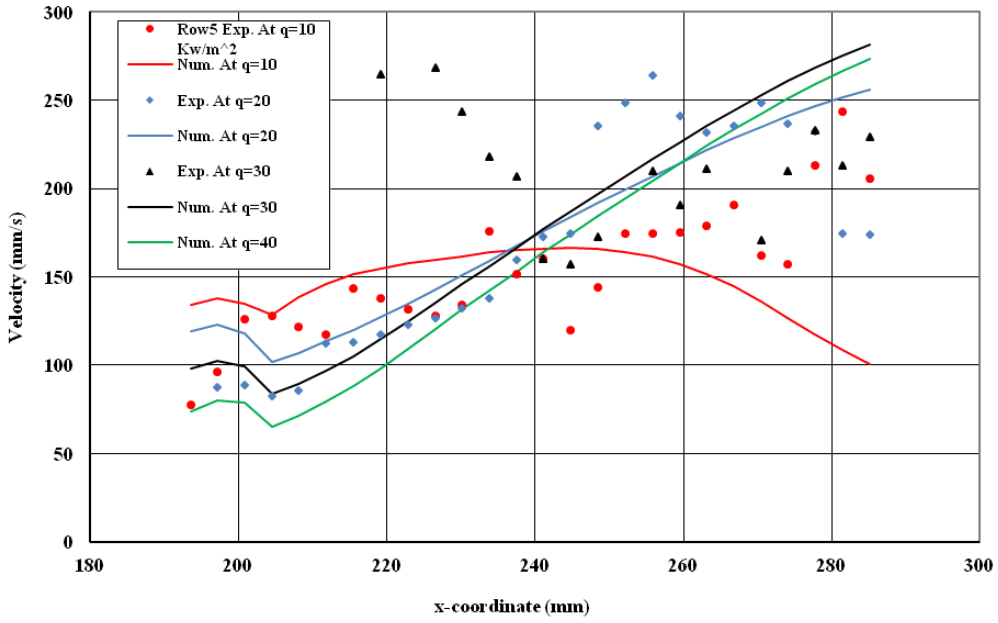

Figure 8.24: Comparison of horizontal velocities at row 5 beside the tube bundle positions for different heat flux values

For 10, 20, 30, 40 kW/m^2, the comparisons of the vertical and horizontal velocity profiles at row 5 are shown in Figs. 8.23 and 8.24, respectively. As the heat flux is changed, the velocity profiles change. At 10, 20, 30 and 40 kW/m^2, the corresponding maximum vertical velocities of 231, 324, 349 and 337 mm/s were observed. Similarly, the maximum horizontal velocities were 167, 256, 281 and 273 mm/s. For both vertical and horizontal, the maximum velocities occur near to the shell wall and minimum velocities at the bundle edge. For different heat flux values, the change in the velocity profiles was observed by Miller [15, 2]. The predicted data is in reasonable agreement with the measured results despite there being scatter at some of the heat fluxes.

8.8 Summary

It was recommended by McNeil et al. [7] that further validation of their model was needed. Comparing the prediction results with a different working fluid was therefore done. Pentane was selected because a test programme could be undertaken to measure pressure distributions that could be applied to the existing velocity data of Burnside et al. [2]. As the fluid properties of pentane differ from R113, different correlations for drag coefficient and tube resistance force were developed and implement in the model. The model was validated by showing reasonable agreement between the predicted results of pressure drop and flow pattern and the measurements of pressure drop and the observation of the flow pattern from the actual kettle reboiler. Further verification was observed by showing reasonable agreement between the predicted void fraction and mass flux with the results from the one-fluid model of McNeil et al. [5], described in Chapter 7. In addition to this, novel to the present investigation and described in this chapter, the predicted vertical and horizontal velocities in the pool were compared favourably with experimental horizontal and vertical velocities measured by particle image velocimetry by Burnside et al. [2]. The predicted vertical and horizontal mass flow rates in the pool were also compared favourably with the experimental vertical and horizontal mass flow rates.

The results of this investigation using pentane as the working fluid and the results of McNeil at al.[7], where R113 was used, has demonstrated that this two-dimensional, two-fluid model is more general and can therefore be used with more confidence as a tool to assist in the design of kettle reboilers.

CHAPTER 9

Simplified Two-Fluid Model for Kettle Reboiler: the Bundle-Only Model

9.1 Description of the model

As discussed in chapters 6, 7 and 8, a numerical two-dimensional model has been developed to investigate flow in a kettle reboiler. The results of the two dimensional model are validated and compared with the experimental results and the one-fluid model data, and the results from Chapter 8 show that the bundle flow does not depend significantly on the pool flow. Therefore in this chapter, the two-dimensional model has been modified to reduce the complexity and computational time compared to the previous model. The modified model is a bundle-only, two-fluid model which will be named as the bundle-only model, and will be used to predict the flow behaviour in the kettle reboiler by restricting the flow domain to the tube bundle. An octagonal shape was chosen to represent an actual bundle as indicated in Fig. 9.1. The effect of the pool was imposed by setting the pressure variation along the boundaries at the bundles.

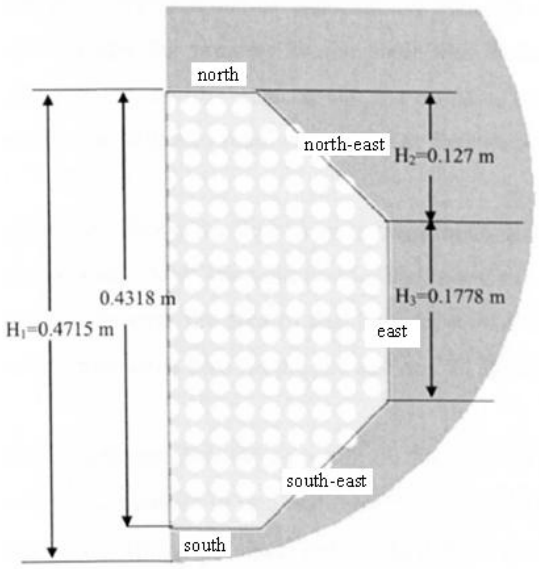

Figure 9.1: Layout of a tube bundle

Figure 9.1 shows the geometry and physical dimensions of the tube bundle. The geometry of tube bundle in the modified model is identical to the experimental test section. As mentioned in the earlier chapters, the bundle contained 241 tubes with an outside diameter of 19.0 mm. The tubes were arranged in an in-line square configuration with a pitch-to-diameter ratio of 1.34. Because of the symmetry in the

test section of the kettle reboiler only half of the tube bundle is considered here. In this model, pentane was used as a working fluid and different heat fluxes (10, 20, 30 and 40 kW/m^2) were applied.

9.2 Boundary conditions

As depicted in Fig. 9.2, the side faces of the octagonal shape tube bundle were named as south, south-east, east, north-east and north. Symmetrical boundary conditions were applied at the front, back and west faces. In this model, two pressure boundary conditions were used on the side faces. The first boundary condition assumed that the bundle was surrounded by liquid so that the static local liquid pressure was applied along each face. Each of the side faces of the bundle was considered as an opening boundary with static pressure, i.e. zero relative pressure, so that the flow is able to move in and out of the domain. For an opening boundary condition, the void fraction needs to be set to specify the flow condition for any incoming flow at the south, south-east, east, north-east and north faces of the model. The value of this void fraction was set for zero for liquid only entry. As reported by McNeil et al.[5], in some circumstances, the bundle was surrounded by liquid in one region and two-phase flow in another. The second boundary condition accommodated this, which resulted from bubbly flow and intermittent flow in the tube bundle. If bubbly flow occurs in the bundle, the faces were surrounded by liquid, whereas an intermittent flow in the bundle was surrounded by two-phase flow. Here, as in previous works [5], the value of the Kutateladze number (Ku) was used to define these two regions. When $Ku \leq 1.09$, the bundle flow was surrounded by liquid, and if $Ku > 1.09$, the bundle flow was surrounded by a two-phase mixture. The transition from bubbly to intermittent flow in the bundle, based on the Kutateladze number, was applied as a step function using the CFX Expression Language (CEL). To complete the second boundary condition, iterations were required to update the CFX expressions (see Figure 9.2). The first iteration used the all liquid boundary result to calculate the value of H_L, the height where the faces were surrounded by liquid, which is the region on the boundaries where $Ku \leq 1.09$. The average void fraction above the transition ($\bar{\alpha}$) for the boundary faces that were surrounded by two-phase flow, i.e. the height region H_{tp} was also found. The second iteration used this height and average void fraction to re-calculated H_L and $\bar{\alpha}$ this was repeated until $H_{Lnew}=H_{Lold}$.

9.3 Discretization and numerical procedure

The flow domain was discretized as shown in Fig. 9.2. The data from this study were required to accurately predict the local flow conditions of the bundle. Based on a previous grid independence study for the bundle and pool model, a mesh size of 10 mm was chosen for the tube bundle. This reduced computational time. It was also checked that the mesh size was small enough to give accurate average local flow conditions. With a mesh size of 10 mm the results were not significantly different from mesh sizes of 8, 4 and 2 mm.

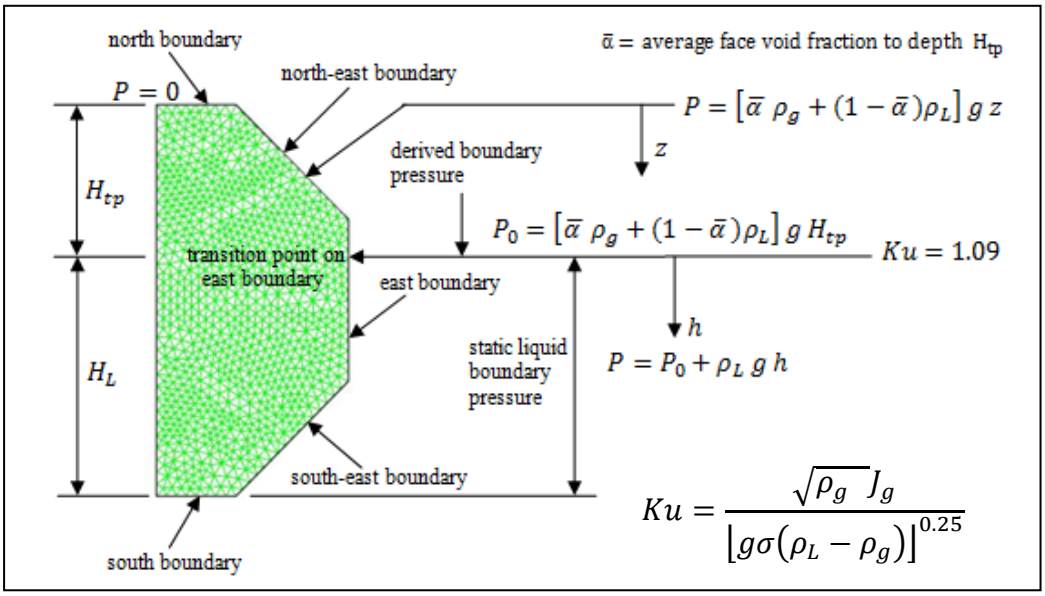

Figure 9.2: Mesh used for the tube bundle model with boundary conditions

The flow in the tube bundle was assumed to be turbulent. The governing equations of the modified model (the bundle-only model) were solved by using the k-ε turbulence model (k represents the turbulent kinetic energy and ε -the rate of dissipation). The solutions were computed until the momentum equations were solved to a root mean square (RMS) residual value of less than 10^{-5}, and the volume and turbulence equations solved to less than 10^{-4}.

9.4 Results and discussion

Simulation data were obtained for the bundle-only two-fluid model using pentane, for boundary conditions 1 and 2. Liquid flow velocity, pressure drop, vertical mass flux distribution and void fraction distribution at heat fluxes of 10, 20, 30 and 40 kW/m^2 are discussed here. The simulated pressure drop data and flow pattern data are compared with the experimental data described in chapter 5. The predicted vertical mass flux and void fraction are compared with the one-fluid model of McNeil et al. [5] and the pool and bundle two-fluid model.

9.5 Heat flux of 10 kW/m^2

9.5.1 Pressure drop

The predicted and measured pressure drop results are compared for a heat flux of 10 kW/m^2 in Fig. 9.3. The trend lines of both boundary conditions 1 and 2 are the same because only bubbly flow was observed in the bundle and the transition state was not reached. The experimental and predicted data in columns 9.5, 12.5 and 15.5 are located on the static head value of 300 Pa. Hence, good agreement is obtained with little variation occurring between the predicted pressure drop and experimental data.

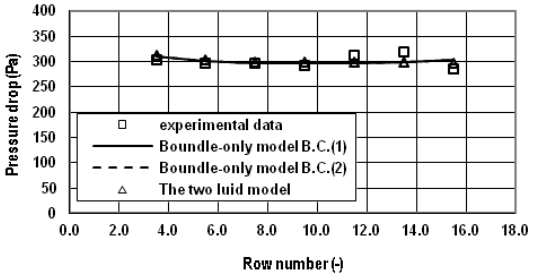

(a) Column 9.5

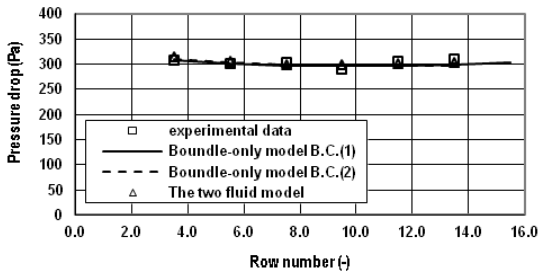

(b) Column 12.5

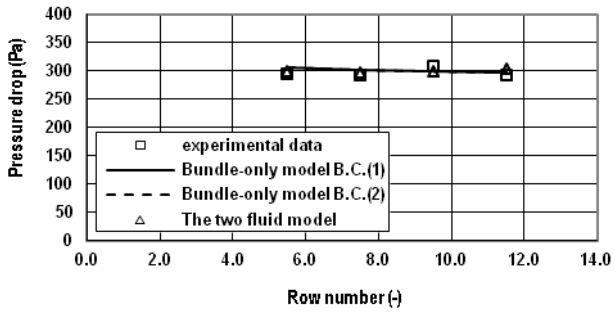

(c) Column 15.5

Figure 9.3: Comparison of experimental and predicted pressure drop at 10 kW/m^2

9.5.2 Flow pattern distribution

Figure 9.4 shows the comparison of the predicted liquid velocity field using boundary condition 1 and the observed experimental flow pattern in the tube bundle. It is clear from the predicted liquid velocity data that, in the main, flow moves vertically within the bundle. Consistency is shown between the predicted fluid flow and the observed flow. Within the tube bundle, the liquid flow moves upwards near the top of the bundle, mainly due to the buoyancy force [5]. By contrast, in the lower rows the predicted liquid velocity data show that flow enters strongly into the bundle from the sides, which was also observed in experimental bubbly flow data. This phenomenon decreases with increasing row height.

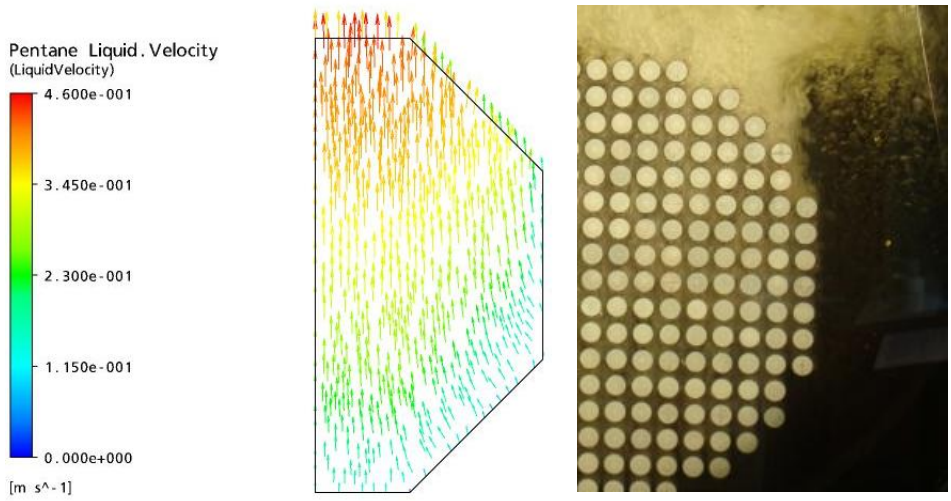

Figure 9.4: Flow pattern distribution at 10 kW/m^2

9.5.3 Vertical mass flux distribution

Figure 9.5 compares the predicted vertical mass flux data obtained for pentane at atmospheric pressure generated by the one-fluid model of McNeil et al. [5], the two-fluid model and the bundle-only two-fluid model. The one-fluid model predictions were obtained using the static liquid boundary condition, consistent with bubbly flow. The two-fluid model predictions were obtained for the bubbly flow boundary condition. At 10 kW/m^2, boundary conditions (1) and (2) are the same in the bundle-only two fluid model because the flow in the bundle is bubbly throughout. The vertical mass flux predictions agree reasonably well in columns 9.5 and 12.5. The agreement between the bundle-only two-fluid model and the one–fluid model is good in column 15.5, close to

the bundle edge, but the vertical mass flux prediction from the two-fluid model is shown to start at a considerably lower value than the bundle-only two-fluid model value and to increase towards it.

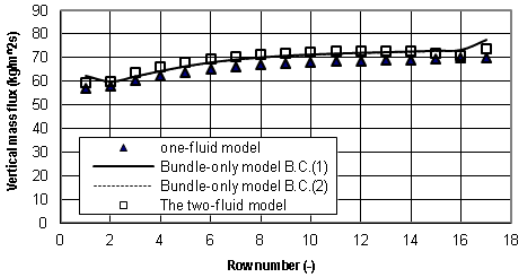

(a) Column 9.5

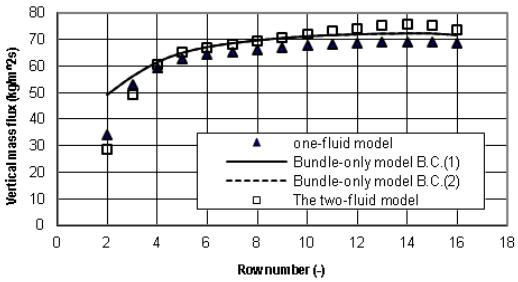

(b) Column 12.5

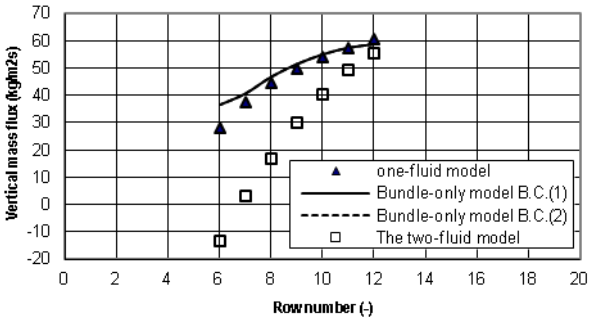

(c) Column 15.5

Figure 9.5: Comparison of vertical mass flux for three models at a heat flux of 10 kW/m^2

9.5.4 Void fraction distribution

Figure 9.6 shows a comparison between the predicted void fraction from the one-fluid model of McNeil et al. [5], the two-fluid model, and the bundle-only two fluid model. The void fraction predictions agree reasonably well in columns 9.5 and 12.5. The agreement is less good in column 15.5.

For a heat flux of 10 kW/m^2, the evidence suggests that the flow in the tube bundle is consistent with it being surrounded by static liquid. This is consistent with the bubbly

flow pattern identified by McNeil et al. [58], and is predicted reasonably well by the bundle-only two-fluid model.

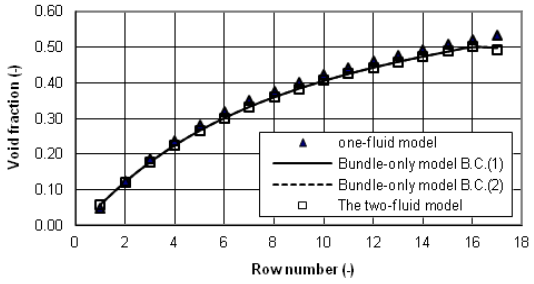

(a) Column 9.5

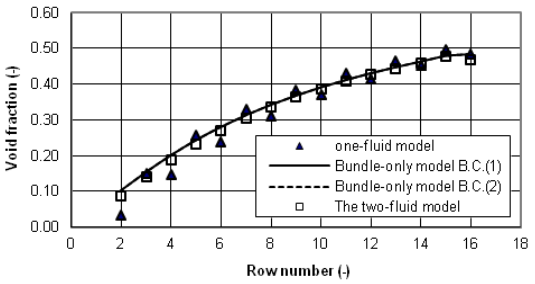

(b) Column 12.5

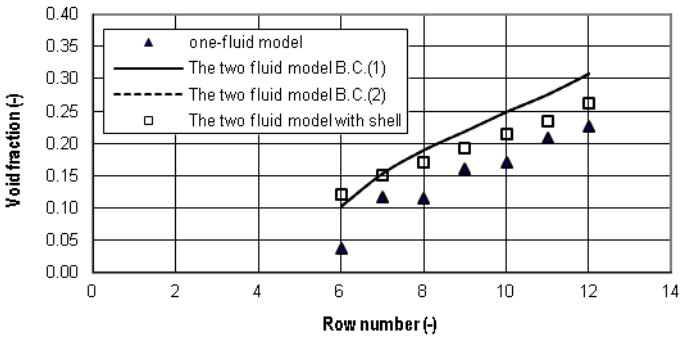

(c) Column 15.5

Figure 9.6: Comparison of void fraction distribution for three models at a heat flux of 10 kW/m^2

9.6 Heat flux of 20 kW/m^2

9.6.1 Pressure drop

To observe the effect of heat flux on the tube bundle, the input power was increased by an increment of 10 kW/m^2 and the pressure drop in the tube bundle was observed. For 20 kW/m^2 the pressure drop results obtained from the present model were compared with the measured pressure drop in Fig. 9.7. It can be observed that in the central column 9.5, the trend lines are not the same as for 10 kW/m^2. The difference in the predicted pressure drop data between boundary conditions 1 and 2 increases with row

number, particularly in the upper rows. This occurs due to the change of flow pattern from bubbly to intermittent flow, starting from row 12-13. The simulated liquid velocity at 20 kW/m^2 illustrated that there was a significant lateral flow beyond row 12-13, Fig. 9.8. Therefore, the predicted pressure drop results using boundary condition 2 are in good agreement with the measured data, whereas the predicted pressure drop results using boundary condition 1 are not because of the outflow from the tube bundle caused by the change in flow pattern.

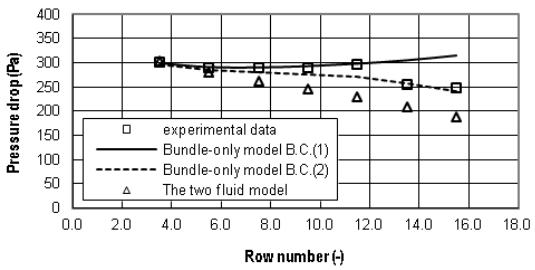

(a) Column 9.5

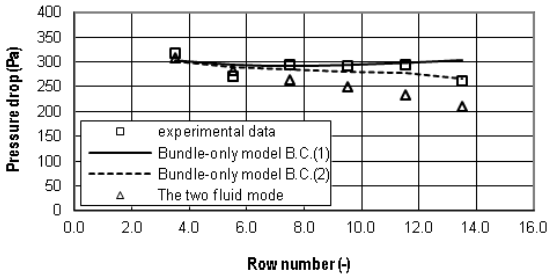

(b) Column 12.5

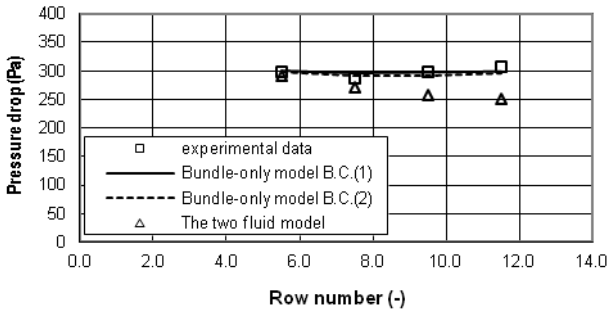

(c) Column 15.5

Figure 9.7: Comparison of measured and predicted pressure drop at 20 kW/m^2

For column 12.5, which is in middle column between the bundle centre line and edge, the predicted pressure results with boundary condition 2 closely match the measured data. This is due to the transition Kutateladze number occurring leading to a reduction in pool pressure and the formation of lateral flow, as indicated in Fig. 9.8.

In column 15.5, which is close to the bundle edge, the results show that boundary condition 2 results in a good match between the predicted and experimental data, even where complicated interactions occur between liquid in the pool and two-phase flow in the bundle.

9.6.2 Flow pattern distribution

Figure 9.8 compares the predicted bundle liquid velocity distribution using boundary conditions 1and 2 with the experimental flow pattern at 20kW/m^2. Using boundary condition 2, the liquid velocity data shows that the flow was no longer moving vertically towards the top of the bundle, as occurred at a heat flux of 10 kW/m^2.

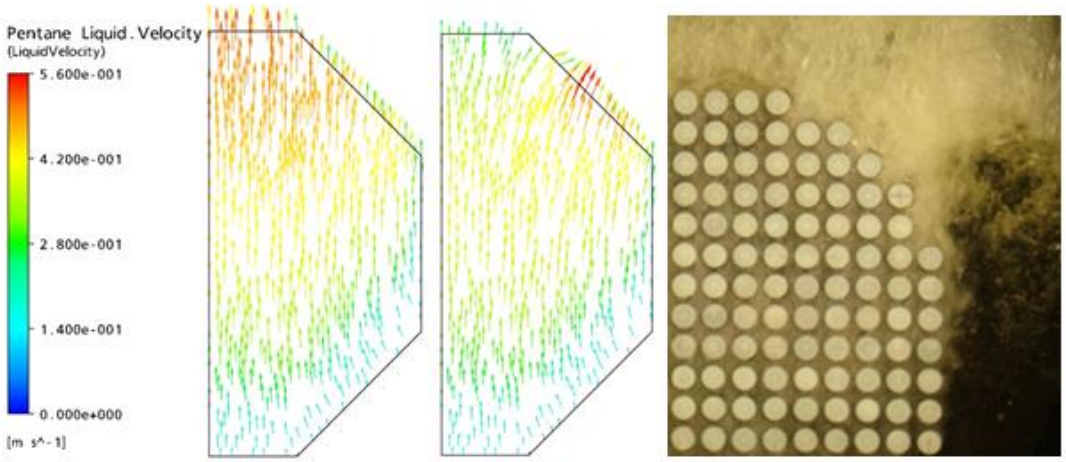

B.C. (1) B.C. (2)

Figure 9.8: Flow pattern distribution at 20 kW/m^2

At the north-east face of the present model with boundary condition 2, the flow direction has been changed to be more lateral towards the pool side. In addition to this, the flow enters strongly at the south and south-east faces and starts to exit the bundle close to the top of the east face. In row 12-13, at the top of the east face, the flow pattern changes from bubbly to intermittent. These phenomena can be observed experimentally in Fig. 9.8. Hence the predicted data using boundary condition 2 agree well with the experimental evidence.

9.6.3 Vertical mass flux distribution

Figure 9.9 shows a comparison between the vertical mass flux predictions from the one-fluid model of McNeil et al.[5], the two-fluid model, and the bundle-only model for a heat flux of 20 kW/m^2. The three models show a significant reduction in mass flux as the flow moves upward through the columns. The one and two fluid model predictions were obtained for the intermittent flow boundary condition. Using boundary condition 2 in the bundle-only model allows the transition from bubbly to intermittent flow to occur at Ku >1.09.This results in a significant reduction in the vertical mass flux. The vertical mass flux predictions using boundary condition 2 agree reasonably well with the one-fluid and two-fluid model in columns 9.5 and 12.5. In column 15.5, the agreement is good between the bundle-only model and the one fluid model.

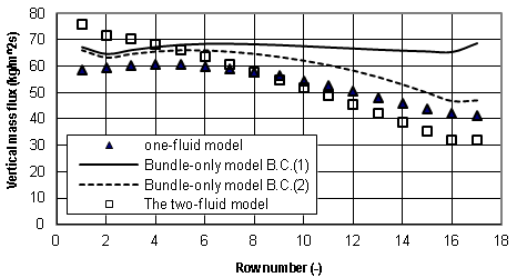

(a) Column 9.5

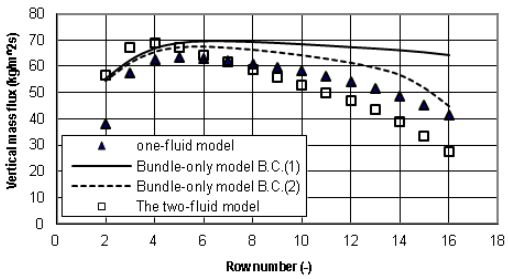

(b) Column 12.5

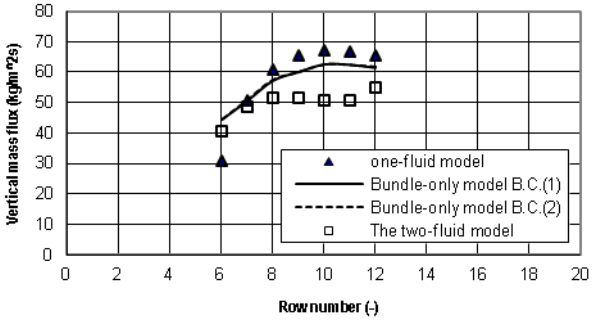

(c) Column 15.5

Figure 9.9: Comparison of vertical mass flux for three models at a heat flux of 20 kW/m^2

9.6.4 Void fraction distribution

Figure 9.10 compares the void fraction predicted by the bundle-only two-fluid model with the one-fluid model of McNeil et al. [5] and the two-fluid model.

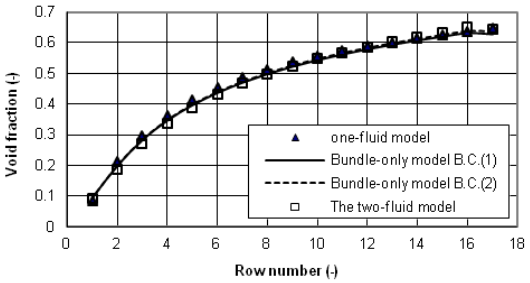

(a) Column 9.5

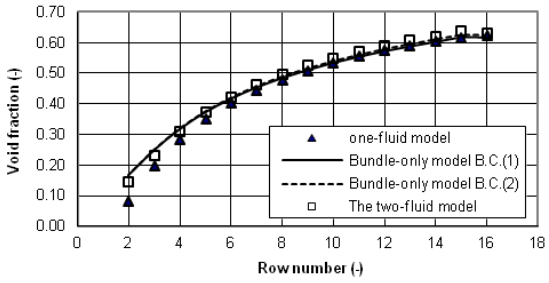

(b) Column 12.5

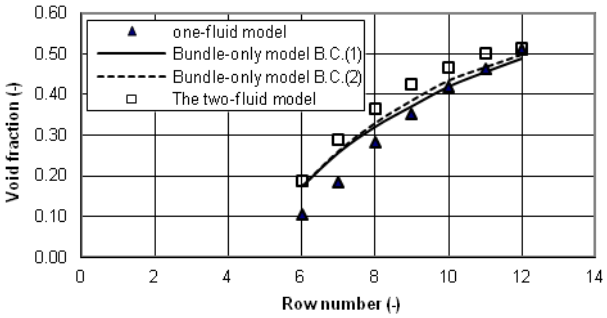

(c) Column 15.5

Figure 9.10: Comparison of void fraction distribution for three models at a heat flux of 20 kW/m^2

All three models follow the same trends and the void fraction predictions agree reasonably well with the one and two-fluid model in columns 9.5 and 12.5. The agreement is reasonable in column 15.5.

For a heat flux of 20 kW/m^2, the evidence suggests that the flow in the bottom tube bundle is bubbly and that the transition to intermittent flow occurs at a Kutateladze number, Ku > 1.09. This is produced in the present model by using boundary condition 2.

9.7 Heat flux 30 kW/m^2

9.7.1 Pressure drop

For a heat flux of 30 kW/m^2, a comparison between the experimental pressure drop data in the tube bundle and the bundle-only model using boundary condition 1 and 2 is shown in Fig. 9.11. The two-fluid model is also included.

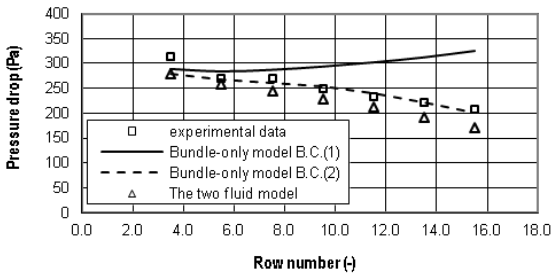

(a) Column 9.5

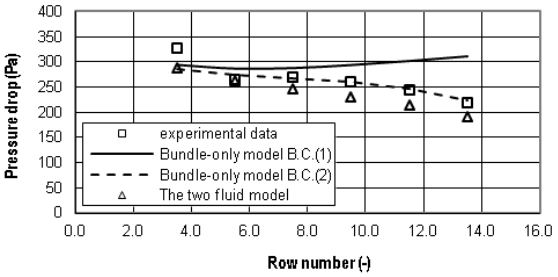

(b) Column 12.5

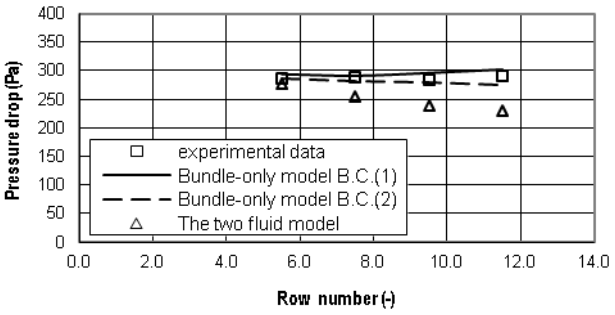

(c) Column 15.5

Figure 9.11: Comparison of measured and predicted pressure drop at 30 kW/m^2

In Fig. 9.11, for all three columns 9.5, 12.5 and 15.5, the bundle-only predicted pressure drop results using boundary condition 2 show a similar trend and agree reasonably well with the experimental data. These predicted data also confirm the effect of the Kutateladze number on the present model as the boundary condition 1 predictions deviate significantly from the experimental pressure drop results. The deviation observed between the predicted two-fluid model data and the experimental data is larger. Boundary condition 1 is not appropriate for higher heat fluxes, as is shown by an inconsistency with the experimental pressure drop distributions. The significant reduction in the experimental pressure drops from the bottom to the top of the tube bundle are consistent with using boundary condition 2 in the bundle-only model making

it more appropriate than boundary condition 1. This is due to the effect of significant lateral flow in tube bundle as illustrated in Fig. 9.12.

9.7.2 Flow pattern distribution

Vapour generation increases in the tube bundle with increasing heat flux. At a heat flux of 30 kW/m^2 significant vapour content covers most of the bundle. The effect of boundary condition 2 on the liquid velocity distribution in the bundle data has been compared with the experimental observations in Fig. 9.12. This shows that the flow enters strongly at the lower rows of the south and south-east faces and exits at the east and north east faces. The liquid velocities are higher near the top of the bundle. The experimental data confirm this phenomenon, Fig. 9.12, where circulation at the upper of the bundle is observed. Boundary condition 2 confirms that the Kutateladze number capture the flow pattern transition condition in this model.

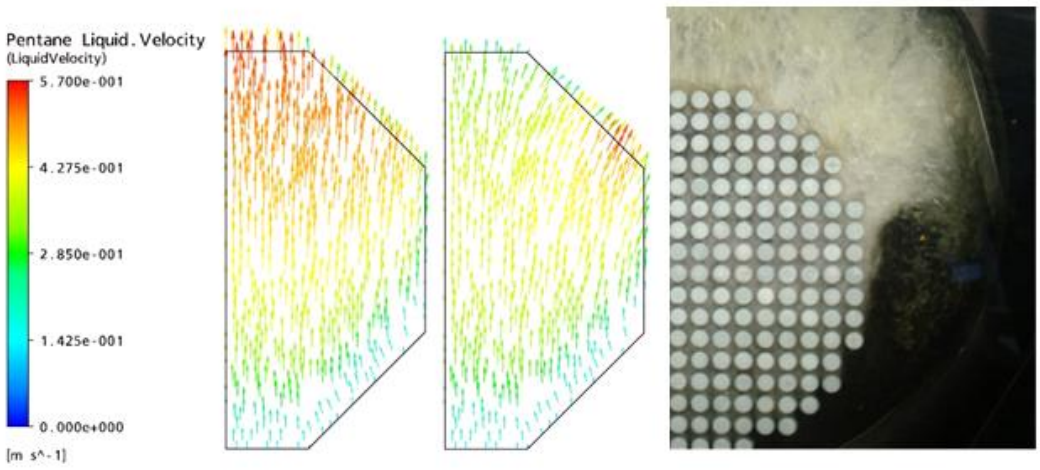

B.C. (1) B.C. (2)

Figure 9.12: Flow pattern distribution at 30 kW/m^2

9.7.3 Vertical mass flux distribution

A comparison between the vertical mass flux prediction from the two-fluid model, the one-fluid model of McNeil et al. [5] and the bundle-only model is shown in Fig. 9.13 for a heat flux of 30 kW/m^2. The one and two-fluid model predictions were obtained for the intermittent flow boundary condition. The bundle-only model predictions were

obtained for boundary conditions 1 and 2. In columns 9.5 and 12.5 , the vertical mass flux reduces substantially towards the upper rows as the flow moves upward through the tube bundle and past the transition point based on Kutateladze number: Ku=1.09.

The vertical mass flux from the one-fluid model agrees reasonably well with predictions from the bundle-only model when boundary condition 2 is used. The differences between the vertical mass flux predictions of the bundle-only model for boundary conditions 1 and 2 , shows the reduction in mass flux that occurs as a result of flow pattern changing from bubbly to intermittent flow.

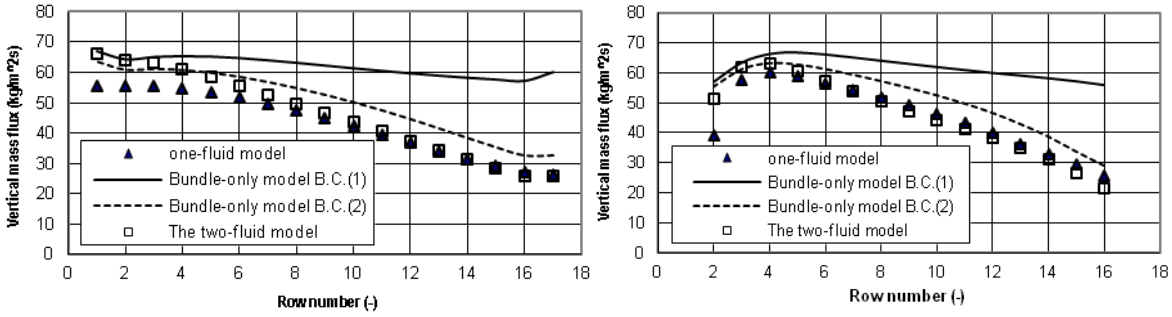

(a) Column 9.5 (b) Column 12.5

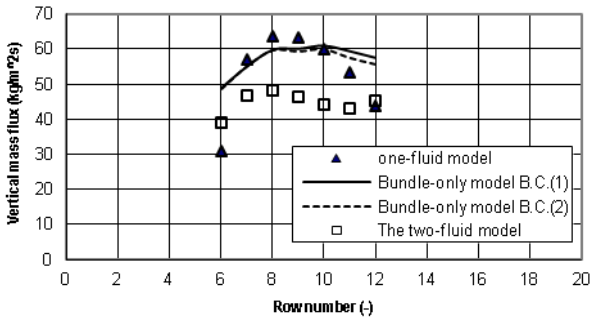

(c) Column 15.5

Figure 9.13: Comparison of vertical mass flux for three models at a heat flux of 30 kW/m^2

9.7.4 Void fraction distribution

Figure 9.14 shows the comparison of the predicted void fraction from the bundle-only model, the one-fluid model of McNeil et al. [5] and the two-fluid model for a heat flux of 30 kW/m^2. It is clear that the data from the bundle-only model follows the trends of

the void fraction prediction of the other models and that the agreement between them is good in columns 9.5, 12.5 and 15.5.

As the heat flux increases, the number of rows subjected to the static liquid pressure decreases and transition occurs at lower row numbers. This is consistent with decreasing liquid levels present in the pool next to the tube bundle, Fig. 9.12. This phenomenon is captured very well by using boundary condition 2 in the bundle-only model and again confirms using the Kutateladze number to determine the flow pattern transition point.

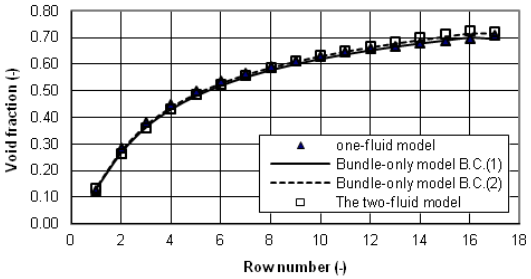

(a) Column 9.5

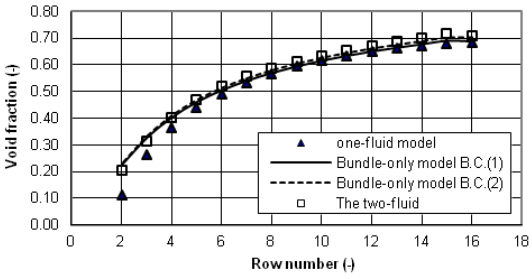

(b) Column 12.5

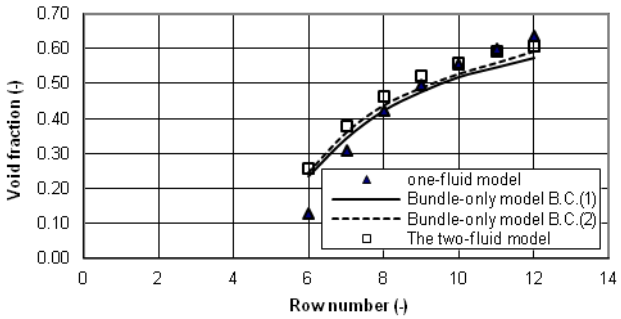

(c) Column 15.5

Figure 9.14: Comparison of void fraction distribution for three models at a heat flux of 30 kW/m^2

9.8 Heat flux of 40 kW/m^2

9.8.1 Pressure drop

To further examine the effect of increasing heat flux on the present model, the heat input was increased to 40kW/m^2 and simulations carried out with boundary conditions 1 and 2. The predicted results are compared to the experimental data of boiling pentane. The predicted results with boundary condition 2 and experimental pressure drops show reasonable agreement and are presented in Fig. 9.15.

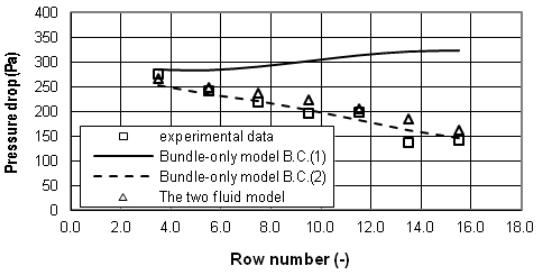

(a) Column 9.5

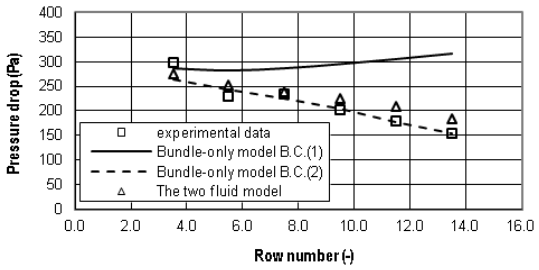

(b) Column 12.5

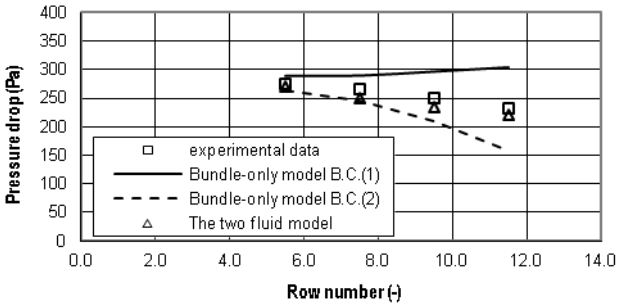

(c) Column 15.5

Figure 9.15: Measured and predicted pressure drop at 40 kW/m^2

A transition from bubbly to intermittent flow occurs at row 7-8, as compared to heat fluxes of 10, 20 and 30 kW/m^2. The boundary condition 1 predictions from the bundle-only model deviate significantly from the pressure drop data. This is due to the higher heat flux generating higher gas void fraction on the lower rows. Hence, the pressure is reduced in the tube bundle at lower row numbers. A reduction of the liquid level in the pool was observed, as shown in Fig. 9.16. For columns 9.5 and 12.5, close to the centre of the bundle, good agreement is obtained between measured and predicted pressure drop data using boundary condition 2. However, in column 15.5, close to edge of the

bundle, the measured pressure drop data were found to be reasonably similar to the predicted pressure drop results in the lower rows, but were higher in the upper rows. One reason for this deviation might be due to the complexity of the two-phase fluid flow at the bundle-pool interface.

9.8.2 Flow pattern distribution

Figure 9.16 shows the predicted bundle liquid velocity distribution and the experimental flow patterns at 40 kW/m^2. The experimental flow observations indicate that the flow moves upward within the bundle from the bottom. At 40kW/m^2, more chaotic two-phase flows were observed, particularly at the top region of the bundle. The vapour flow exits the bundle at the east face at row 7-8 and re-enters the bundle from the south and south-east faces. The predicted liquid velocity distribution using boundary condition 2 also illustrates that the flow enters into the bundle bottom from the south and south-east faces, and exits more intensively with increasing row number. It is detected that the flow pattern has changed from bubbly to intermittent at row 7-8. At the north face, a higher quantity of flow exits compared with the lower heat flux values. Hence, the predicted phenomena are consistent with experimental observation. According to the present results, the values of the pool pressures are higher for boundary condition 1 than boundary condition 2. This leads to a reduction in lateral flow in the bundle for boundary condition 1 flows. Hence, the flow shows one-dimensional behaviour, as seen in Fig. 9.16 B.C.(1).

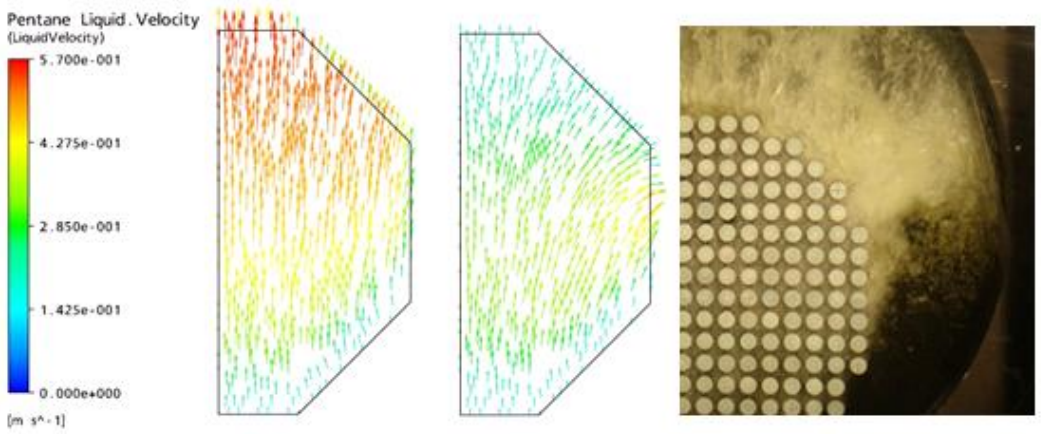

B.C. (1) B.C. (2)

Figure 9.16: Flow pattern distribution at 40 kW/m^2

By contrast, using boundary condition 2, the pool pressure will change due to the flow pattern change allowing lateral flow from the bundle. Therefore, use of boundary

condition 2 in the bundle-only model will predict the flow more accurately than boundary condition 1.

9.8.3 Vertical mass flux distribution

A comparison between the vertical mass flux from the one fluid model of McNeil et al. [5], the two-fluid model and the bundle-only model is shown in Fig. 9.17 for a heat flux of 40 kW/m^2. The one and two-fluid model predictions were obtained for the intermittent flow boundary condition. The bundle-only model predictions were obtained using boundary conditions 1 and 2.

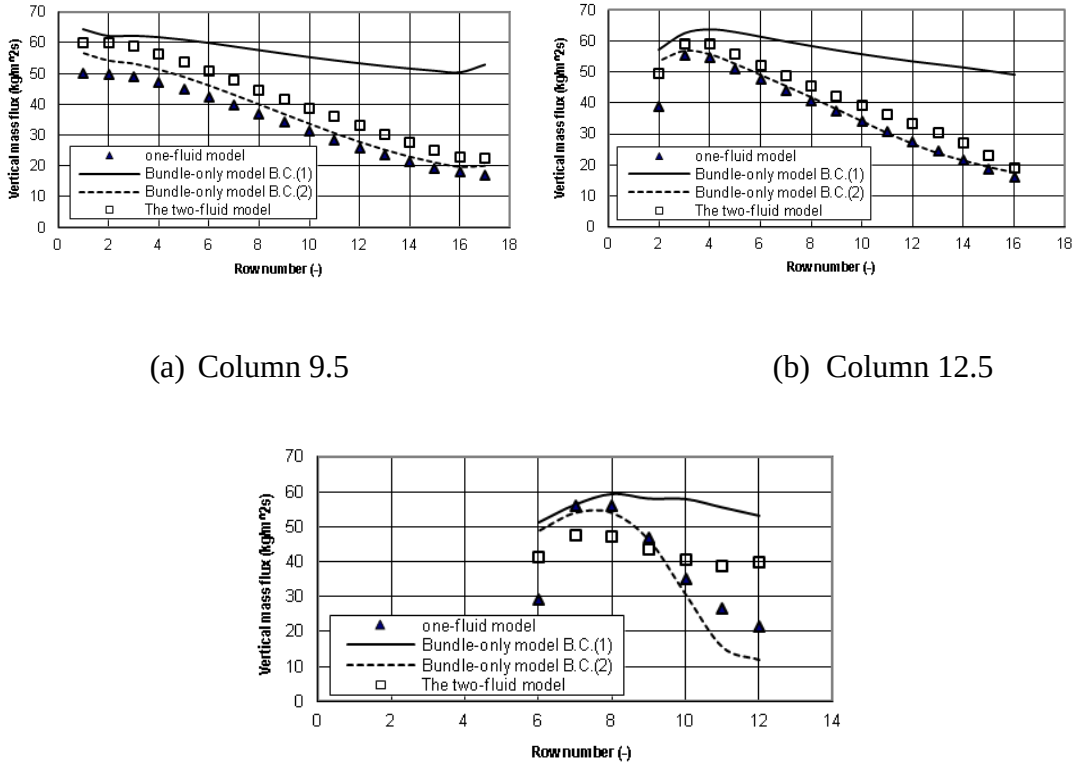

(a) Column 9.5 (b) Column 12.5

(c) Column 15.5

Figure 9.17: Comparison of vertical mass flux for three models at a heat flux of 40 kW/m^2

In columns 9.5 and 12.5 the vertical mass flux reduces significantly towards the upper tube rows as the flow move upwards across the tube bundle and past the transition point. In column 15.5, the trends are different, the mass flux starts low because of the constant pressure drop low gas-mass fraction [5] (Fig. 9.17(c)), and the vertical mass flux increases until the transition point before falling significantly.

The vertical mass flux predictions from the one-fluid model agree reasonably well with the predictions from the bundle-only model when boundary condition 2 is used.

The difference between the vertical mass flux predictions of the bundle-only model for boundary conditions 1 and 2, shows the reduction in vertical mass flux that occurs as result of the change in flow pattern from bubbly flow to intermittent flow. It is clear that the Kutateladze number used in boundary condition 2 to specify the transition point is changing the physical effect.

9.8.4 Void fraction distribution

Figure 9.18 shows a comparison between the void fraction predictions from the one–fluid model of McNeil et al. [5], the two-fluid model and the bundle-only model for columns 9.5, 12.5 and 15.5.

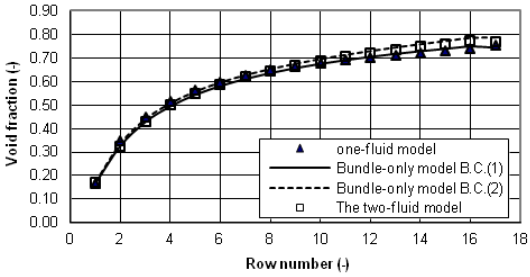

(a) Column 9.5

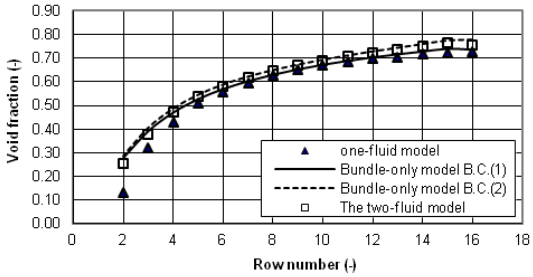

(b) Column 12.5

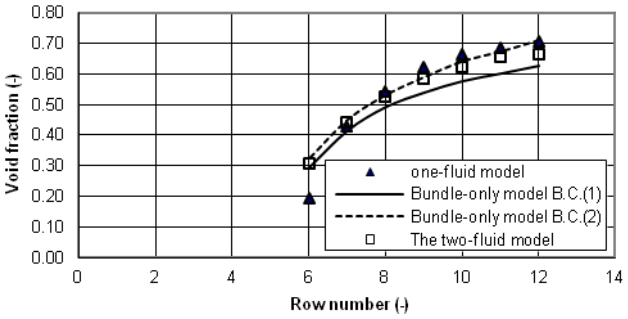

(c) Column 15.5

Figure 9.18: Comparison of void fraction distribution for three models at a heat flux of 40 kW/m^2

The void fraction increased as the flow moves up towards the top of the bundle, which indicates the increase in vapour fraction. The void fraction predictions from the bundle-only model agree reasonably well with the prediction from the one-fluid model in columns 9.5 and 12.5. The present model with boundary condition 2 gives a reasonable agreement with the one and two-fluid model in column 15.5.

9.9 Effect of heat flux on the tube bundle parameters

The effect of changing the heat flux on different tube bundle variables such as pressure drop, vertical mass flux and void fraction at different tube row numbers are discussed here. The predicted data was produced using the bundle-only model with boundary condition 2 for boiling pentane in columns 9.5, 12.5 and 15.5 at heat fluxes of 10, 20, 30 and 40 kW/m^2.

9.9.1 Effect of heat flux on pressure drop

Figure 9.19 shows the variation of predicted pressure drop with tube row number across the bundle along columns 9.5, 12.5 and 15.5 at heat fluxes of 10, 20, 30 and 40 kW/m^2. The predicted pressure drop data is calculated as the difference between two successive row points, e.g. 2.5 and 4.5 in column 9.5. At 10 kW/m^2, for columns 9.5 and 12.5, the predicted pressure drop data are almost constant and very close to the liquid head of pentane: 300 Pa. This is consistent with the bubbly flow pattern through the tube bundle where the flow moves vertically upwards through the bundle. At higher heat fluxes of 20, 30 and 40 kW/m^2, the predicted pressure drop continuously decreases from the bottom to the top of the bundle, which is consistent with the intermittent flow pattern occurring in the tube bundle, since the flow is 2-D and the mass flux falls towards the bundle top. For column 15.5, close to the bundle edge, for heat fluxes of 10, 20 and 30 kW/m^2, the predicted pressure drop remains approximately constant across the tube bundle. In general at a given tube row number, an increase in the heat flux decreases the pressure drop.

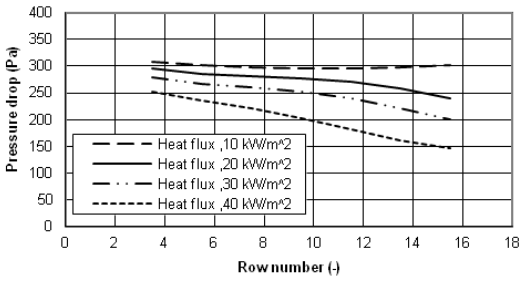

(a) Column 9.5

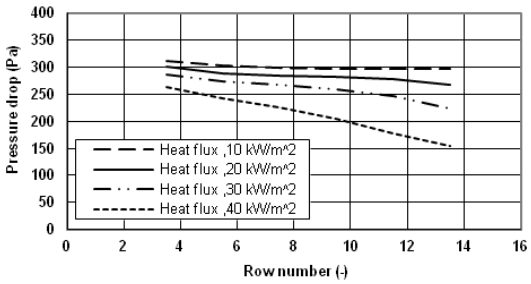

(b) Column 12.5

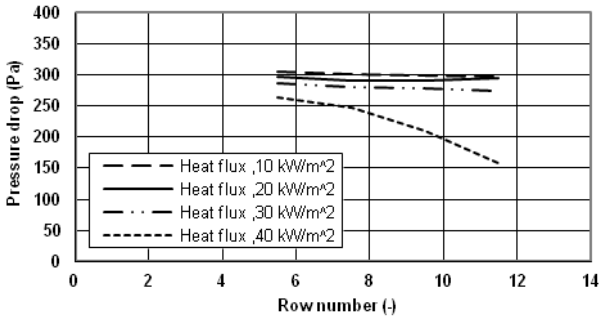

(c) Column 15.5

Figure 9.19: Variation of pressure drop with tube row number at different heat fluxes

9.9.2 Effect of heat flux on vertical mass flux distribution

Figure 9.20 shows the variation of predicted vertical mass flux with tube row number in the tube bundle for columns 9.5, 12.5 and 15.5. For columns 9.5, 12.5 and 15.5 at a heat flux of 10 kW/m^2 the vertical mass flux increases with row number until row 12 and then stays approximately constant until the top row. This is consistent with the bubbly flow pattern in the tube bundle as the flow move vertically towards the bundle top. In columns 9.5 and 12.5, for heat fluxes of 20, 30 and 40 kW/m^2, the vertical mass flux continuously decreases from the bottom to the top tube rows of the bundle. Also, in the same columns, an increases in heat flux above 10 kW/m^2 shifts the curves in a downward direction, indicating a decreases in mass flux. At higher heat fluxes the flow pattern is intermittent and the liquid flow rate undergoing vaporisation decreases with tube row from bottom to top. In addition, the lateral flow out of the bundle increases as the flow move from bottom to the top of the bundle. Hence, the vertical mass flux prediction is found to decrease from bottom to top of the tube bundle. For column 15.5 the behaviour is different, which may be due to its location close the bundle edge. The vertical mass flux increases with row number at heat fluxes of 10, 20 and 30 kW/m^2.

However, at 40 kW/m^2, the vertical mass flux increases until it reaches a maximum value at a particular row number and then decreases with row number.

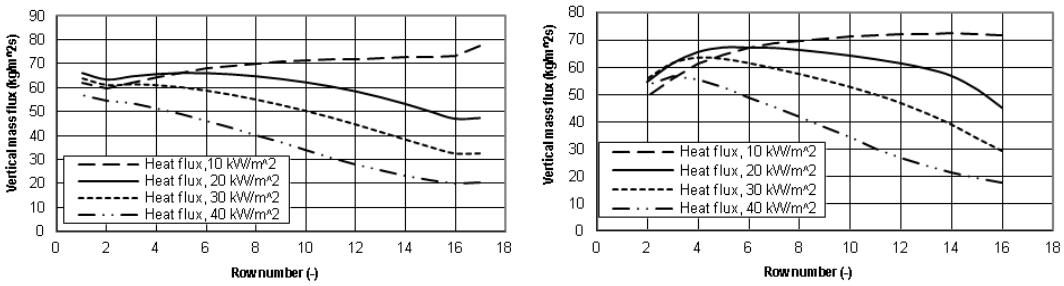

(a) Column 9.5 (b) Column 12.5

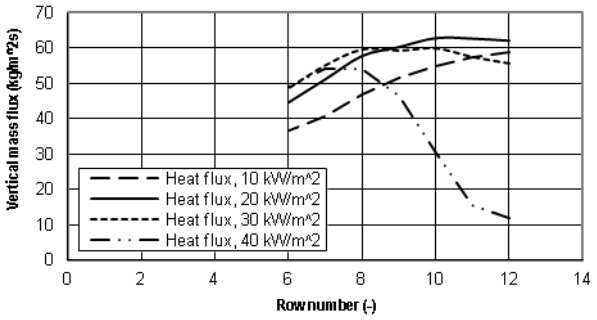

(c) Column 15.5

Figure 9.20: Variation of vertical mass flux with tube row number at different heat fluxes

9.9.3 Effect of heat flux on void fraction distribution

Figure 9.21 shows the variation of predicted void fraction with tube row number in the tube bundle (columns 9.5, 12.5, and 15.5) for pentane boiling at atmospheric pressure. It can be observed that the void fraction for a given heat flux value increases gradually as the flow proceeds from bottom to the top of the tube bundle. This is expected as saturated liquid enters the bundle bottom and vapour content increases as the vapour constantly moves towards the bundle top. In addition, at a given tube row number an increase in heat flux increases the void fraction. This results from the increasing heat flux generating a large quantity of vapour in the tube bundle. For all heat fluxes, the rate of void fraction increase is higher in the bottom rows than the upper rows.

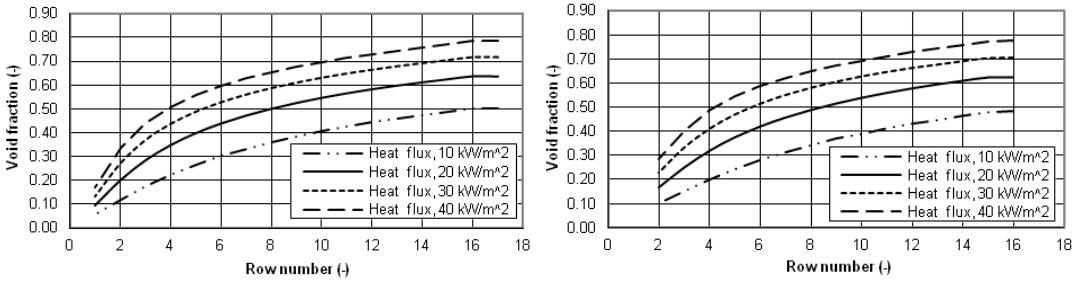

(a) Column 9.5 (b) Column 12.5

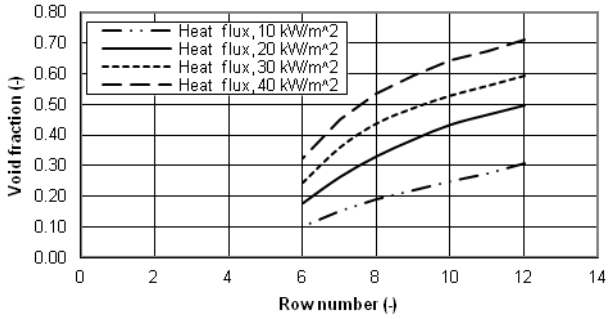

(c) Column 15.5

Figure 9.21: Variation of void fraction distrbution with tube row number at different heat fluxes

From the above discussion, it can be concluded that heat flux is an important operating parameter, which has a considerable effect on the pressure drop, vertical mass flux and void fraction within a tube bundle.

9.10 Summary

From the descriptions of the 2D two-fluid model in previous chapters it can be observed that the flow through the tube bundle was relatively unaffected by the flow conditions at the sides of the pool. Hence, a bundle-only model has been developed to accurately predict the two-phase fluid flow behaviour in the kettle boiler using the tube bundle only. Information available from earlier studies has been used to develop this model because of the difficulties involved in measuring the void fraction and velocities within the tube bundle. Two different boundary conditions of (1) static pressure in the pool and

(2) variation of pressure in the pool based on the flow pattern transition have been applied to the model. The predicted results have been compared with experimental data and with the one and two-fluid models at different heat fluxes. The boundary condition comparisons were found to be in good agreement with the experimental data and the one and two-fluid models at the lower heat flux of 10 kW/m^2 because the transition flow pattern was not achieved and the bundle was surrounded by static pool pressure. Boundary condition 2 is based on the Kutateladze number, which sets the transition point from bubbly to intermittent flow at a specific height in the bundle. When $Ku \leq 1.09$, the bundle flow would be surrounded by liquid, and if $Ku > 1.09$, the bundle flow would be surrounded by two-phase flow. This transition criterion was introduced by McNeil at el. [5] for their one-fluid model. At higher heat fluxes (20, 30 and 40 kW/m^2) boundary condition 2 has been found to be in good agreement with the experimental data and the prediction from the one- and two-fluid models for liquid velocities, vertical mass flux and void fraction (Figs. 9.7-9.18). The present model accurately predicts the trend line of constant and decaying pressure drop measured at low and high heat fluxes, respectively, and the observed flow phenomena in the kettle reboiler. A large reduction in the computational time was achieved with the present model. For example, to solve the same problem using a desktop PC with an Intel (R) Pentium (R) 4CPU 3.00 GHz processor and with 0.99 GB of RAM, the computational time for the 2D, two–fluid model was 13 hours , 13 minutes and 20 seconds and the file size was 255 KB. However when the bundle-only model was used the computational time 32 minutes and the file size was 130 KB. Hence, the key feature of the present model is that simulations of two-phase flow in the kettle reboiler can be done by modelling the tube bundle alone, and this simplifies the model and reduces computational time.

CHAPTER 10

Conclusions and Recommendations

10.1 Conclusions

In the present research, a numerical and experimental investigation of two-phase flow in a kettle reboiler has been carried out using pentane as the working fluid. The flow patterns were observed and the pressure drops were measured across different regions of the kettle reboiler. In the numerical analysis a two-fluid model and bundle-only model were utilised to predict the pressure drop, flow patterns, void fraction, velocities and vertical mass flux distribution within the kettle reboiler.

The following paragraphs summarise the conclusions drawn from the study:

- Using photographic techniques (high speed camera), the flow patterns inside the kettle reboiler were observed. It was noted that within the tube bundle the flow behaviour was 2-D for heat fluxes above 10 kW/m^2. Hence it is worth noting that the vertical mass flux decreases as the flow rises up the tube bundle. For heat fluxes of 10 kW/m^2 and below the pressure drop changes with bundle height were not significant and were equal to the static liquid head of 304Pa.
- Depending on the imposed heat flux, the foam quantity and recirculation phenomenon on the top of the kettle reboiler changed. It was observed that the size of the recirculation zone changed and its position moved down into the pool as the heat flux increased. It was also noted that the downward liquid flows onto the upper tube rows disturbed fluid movement in the centre columns of the bundle. The liquid entered the pool across the top and sides of the bundle and again re-circulated through the bottom and sides of the bundle.
- Variations in the pressure drop for different rows of the tube bundle were observed. Two different types of flow patterns were observed in the kettle reboiler: bubbly flow and intermittent flow. It was noted that the pressure drop was almost constant for bubbly flow and tended to decrease from the bottom to the upper rows of the bundle in intermittent flow. At low heat fluxes, vapour rises upwards, because of the buoyancy force, and small-sized

bubbles were observed between the tubes in the bundle. This corresponds to bubbly flow. At high heat fluxes, the gas bubbles combined together to cover a large part of the tube bundle and two observations were noted for the movement of the flow: firstly that within the bundle, the liquid is forced to move up by the vapour, and, secondly, that there is an insufficient drag force to raise the liquid [58]. A similar trend has been observed by McNeil et al. [58] for boiling R113 in the kettle reboiler.

- As for previous studies and in the the present experiments, it is well detailed that the experimental pressure drop values are not in good agreement with the one-dimensional model. At low heat flux values, when insignificant changes in the pressure drop take place, the 1-D model is valid. However, this model deviates at high heat flux values when a greater difference in pressure drop exists.
- For the present two-fluid model, the drag coefficient and tubes' resistance were deduced from the one-dimensional model. These values were applicable to the specific geometry of the kettle reboiler, working fluid (pentane) and pressure. For different parameters it would be necessary to develop new coefficients. Despite the presence of turbulence in the pool, the Grace at al. [85] drag coefficient was used and agrees well with the experimental results.
- From the current study with pentane and that of McNeil et al. [7] with R113, various solutions where obtained for various imposed values of re-entry void fraction at the north boundary in the two-fluid model. According to the experimental results, only liquid re-entry and vapour re-entry take place in practice [7]. The liquid re-entry fraction corresponds to the bubbly flow regime and vapour re-entry corresponds to the intermittent flow regime. In the bubbly flow regime the vapour slides along the contour of the tube bundle and exits without entering the pool, whereas in the intermittent flow regime the vapour flows out of the top and corner of the tube bundle in transverse and lateral directions, and re-enters into the pool side.
- In spite of the inherent difficulties described above, the two-fluid model predictions of the pressure drop and flow distribution developed in this study are in agreement with the experimental results for the kettle reboiler. This developed model replicates the flow patterns when re-entry void fraction is

approximately set. However, some discrepancies are observed near the bundle-pool interface.

- At different locations in the pool, a comparison was made between the velocities and mass flow rates predicted from the two-fluid model with those calculated from the liquid velocity measurements made using the PIV technique by Burnside et al. [2]. It was possible to make a comparison at heat fluxes of 10, 20 and 30 kW/m^2, which were common to both the two-fluid model and the Burnside et al. [2] studies. The compared results showed good agreement.
- For the two-fluid model, grid sizes of 10, 8 and 4 mm for the tube bundle and the pool were considered. It was found that the predicted bundle results were not affected by changing the grid size. However, in the pool region a small grid size was required. A grid size of 10 mm was used in the bundle while 4 mm was used in the pool. The present results show that the bundle flow does not depend significantly on the pool flow.
- Based on the results of the developed two-fluid model for the kettle reboiler, it was concluded that the two-phase fluid behaviour in the bundle is relatively unaffected by the pool flow. Thus, a new bundle-only model for two-phase flow in a kettle reboiler was developed using ANSYS-CFX. This new model predicts the flow behaviour, pressure drop, void fraction and mass flux. The results of this bundle-only model have been compared with experimental and two fluid model values with a good agreement obtained.
- The central column model has been developed based on the one dimensional model, the momentum equation for a fully developed vertical flow and the energy equation. The model used the minimum pressure gradient to predict vertical mass flux and void fraction distribution in the central column of the tube bundle. The results obtained from the model were compared with the experimental data and the two-dimensional two-fluid model and the bundle-only model predictions. Reasonable agreements were obtained, indicating that the flow distribution may be linked to the minimum pressure gradient.

10.2 Recommendation for Future Work

Additional experimental and numerical studies are required for producing more informative results and developing a more accurate model for kettle reboiler design.

- As numerical models cannot be more accurate than the experimental observations, additional experimental work is required to obtain flow circulation, pressure drop, void fraction, liquid velocities and heat transfer in the tube bundle.
- Measurements of the void fraction through the kettle for the tube bundle and pool are vital so that the numerical results from the models can be compared with the experimental data. In this way an efficient design more for the kettle reboiler can be deduced.
- The drag coefficient correlation used in the two-fluid model is only applicable to this particular tube bundle geometry while boiling pentane at atmospheric pressure. For different fluids, pressures and bundle configurations, other correlations would be needed. To validate these correlations, additional measurements such as void fraction are required. A more general method is needed.
- The development of the present two-fluid model is based on the assumption that the flow of saturated vapour/liquid occurs over all of the reboiler. In reality there are some areas that contain subcooled liquid and superheated vapour. Also, since the saturation temperature varies with pressure, the fluid properties are not constant. Adding the energy equation to the model would allow subcooled and superheated fluid to be simulated. Allowing the fluid properties to change with temperature would produce a more accurate simulation for actual reboilers. A further improvement to the two-fluid model can also be made by assuming multi-component fluids. These liquids are used in most industrial kettle reboilers.
- Distributions of the heat transfer coefficient in the tube bundle of the kettle reboiler can be obtained from the current model by adding the appropriate heat transfer correlations.
- Since the flow movements in actual kettle reboilers are three dimensional, developing a three dimensional model would give a more accurate simulation.

References

1. Fujita, Y., Bai, Q. and Hidaka, S., *Heat Transfer and flow pattern in Horizontal tube bundles under Pool and flow boiling conditions*. *Convective flow and pool boiling II Engineering Foundation Conferences*, Irsee Germany, 1997. Paper XII-7.

2. Burnside, B.M., Miller, K.M., McNeil , D.A., and Bruce, T., *Flow Velocities in an Experimental Kettle Reboiler Determined by Particle Image Velocimetry*. International Journal of Heat and Mass Transfer, 2005. **48**(5): p.1000-1016.

3. Bamardouf, K, and McNeil, D.A., *Experimental and numerical investigation of two-phase pressured drop in vertical cross-flow over a horizontal tube bundle.* Journal of Applied Thermal Engineering, 2009. **29**: p. 1356-1365.

4. Kumar, S., Jain, A., Mohanty, B., and Gupta, S.C., *Recirculation Model of Kettle Reboiler*. International Journal of Heat and Mass Transfer, 2003. **46**(15): p.2899-2909.

5. McNeil, D.A., Bamardouf, K. and Burnside, B.M., *A one- fluid, Two-dimensional flow simulation model for a kettle reboiler*. International Journal of Heat and Mass Transfer, 2010. **53**: p 825-835.

6. Shire, N.F., *Heat Transfer and Hydrodynamics of Boiling over Tube Bundles*. Ph.D. Thesis, Heriot- Watt University, 1995.

7. McNeil, D.A., Bamardouf, K. and Burnside, B.M., *Two-dimensional flow modelling a thin slice kettle reboiler*. International Journal of Heat and Mass Transfer, 2011. **53**: p. 836-848.

8. Burnside, B.M., *2-D Kettle Reboiler Circulation Model*. International Journal of Heat and Fluid Flow, 1999. **20**(4): p. 437-445.

9. Cornwell, K. and Houston, S.D., *Nucleate Pool Boiling on Horizontal Tubes: A Convection-Based Correlation*. International Journal Heat and Mass Transfer, 1994. **37**(1): p.303-309.

10. Bamardouf, K.H., *An Experimental and Numerical Study of Two-Phase Flow in a Kettle Reboiler*. PhD Thesis, Heriot-Watt University, 2008.

11. Cornwell, K., Duffin, N.W., and Schueller, R.B., *Experimental Study of the Effects of Fluid Flow on Boiling within a Kettle Reboiler Tube Bundle*. American Society of Mechanical Engineers, 1980. (80-HT-45): p.7.

12. Andrews, P.R. and Cornwell, K.J., *Cross-Sectional and Longitudinal Heat Transfer Variations in a Reboiler Tube Bundle Section*. Chemical Engineering Research and Design, 1987. **65**(a): p. 127-130.

13. King, M.P. and Jensen, M.K., *Local Heat Transfer and Flow Pattern Distributions in a Kettle Reboiler*. Two-phase flow modelling and experimentation, 1995: p. 1289-1296.

14. Cornwell, K. and Schuller, R., *A study of boiling outside a tube bundle using high speed photography*. International Journal Heat and Mass Transfer, 1982. **25**(5): p. 683-690.

15. Miller, K.M., *Heat Transfer and Velocity Measurements in a Kettle Reboiler*. Ph.D. Thesis, Heriot-Watt University, 2000.

16. Burnside, B.M., Miller, K.M., McNeil, D.A., and Bruce, T., *Heat Transfer Coefficient Distributions in an Experimental Kettle Reboiler Thin Slice*. Chemical Engineering Research and Design, 2001a. **79**(4): p. 445-452.

17. Noghrehkar, G.R., Kawaji, M., and Chan, A.M.C., *Investigation of Two-Phase Flow Regimes in Tube Bundles under Cross-Flow Conditions*. International Journal of Multiphase Flow, 1999. **25**(5): p. 857-874.

18. Taitel, Y. and Dukler, A.E., *A Theoretical to Lockhart- Martinelli Correlation for Stratified Flow*. International Journal of Multiphase Flow, 1976. **2**(5-6): p. 591-595.

19. Grant, I.D.R. and Chisholm, D., *Two-Phase Flow on the Shell-Side of a Segmentally Baffled Shell-and-Tube Heat Exchanger*. Journal of Heat Transfer, Transactions ASME, 1979. **101**(1): p. 38-42.

20. Pettigrew, M.J., Taylor, C.E., and Kim, B.S., *Vibration of Tube Bundles in Two-Phase Cross- Flow-Part 1: Hydrodynamic Mass and Damping Proc. of ASME Int. Symp. On flow- Induced Vibration and Noise,* ASME WA Meeting, Chicago, December 1988.

21. Ulbrich, R. and Mewes, D., *Vertical Upward Gas-Liquid Two-Phase Flow across a Tube Bundle*. International Journal of Multiphase Flow, 1994. **20**(2): p. 249-272.

22. Hanhe, E., Spindker, K., Chen, Q. and Windisch, R., *Local Void Fraction Measurements in Finned Tube Bundles, Proc. of the 9th International Conference on Heat Transfer*, Jersalem, Israel, 1990. **6**: p. 41-45.

23. Xu, G.P., Tso, C.P., and Tou, K.W., *Hydrodynamics of Two-Phase Flow in Vertical up and Down-Flow across a Horizontal Tube Bundle*. International Journal of Multiphase Flow, 1998b. **24**(8): p. 1317-1342.

24. Kondo, M. and Nakajima, K.I., *Experimental Investigation of Air-Water Two Phase Upflow across Horizontal Tube Bundles Em Dash 1. Flow Pattern and Void Fraction*. Bulletin of the JSME, 1980. **23**(177): p. 385-393.

25. Burnside, B.M. and Shire, N.F., *Heat Transfer in Flow Boiling over a Bundle of Horizontal Tubes*. Chemical Engineering Research and Design, 2005. **83**(5A): p.527-538.

26. Aprin, L., Mercier, P., and Tadrist, L., *Experimental Analysis of Local Void Fractions Measurements for Boiling Hydrocarbons in Complex Geometry*. International Journal of Multiphase Flow, 2007. **33**(4): p. 371-393.

27. Hong, W.P. and Liu, Y., *Investigation of Gas-Liquid Two-phase Flow Patterns Based on High- speed Imaging Methods, Proc. of the 3rd International Congress on Image and Signal Processing* (ISP 2010), 2010. p.154-156.

28. Jensen, M.K., *Model for the Recirculating Flow in a Kettle Reboiler. In Proc. AIChE*., New York, 1988. 114-119.

29. Shire, N.F., Burnside, B.M. and Disbury, R., *Circulation velocity measurements a model multi tube kettle reboiler using Laser Doppler anemometry, Proc. 10th International Conference of Heat transfer*, 1994. p. 539-542.

30. Chan, A.M.C. and Shoukri, M., Boiling *Characteristics of Small Multitube Bundles*. Journal of Heat Transfer, Transactions ASME, 1987.**109**(3): p. 753-760.

31. Schrage, D.S., Hsu, J.T., and Jensen, M.K., *Two-Phase Pressure Drop in Vertical Crossflow across a Horizontal Tube Bundle.* AIChE Journal, 1988. **34**(1): p. 107-115

32. Dowalti, R., Kawaji, M., Chisholm, D., and Chan, A.M.C., *Void Fraction Prediction in Two-Phase Flow across a Tube Bundle*. AIChE Journal, 1992a. **38**(4): p. 619-622.

33. Dowalti, R., Cgan, A.M.C. and Kawahi, M., *Measurement of Void Fraction and Pressure Drop in Flow Boiling of R113 Across Horizontal Tube Bundles*. ASME Paper, 1993. 93-HT-17.

34. Gebbie, J.G. and Jensen, M.K., *Void Fraction Distributions in a Kettle Reboiler*. Experimental Thermal and Fluid Science, 1997. **14**(3): p. 297-311.

35. Hinata, S., Sakurai, M., Kuga, O. and Nakazawa, M., *Void Fraction and Temperature Measurements for Pool Boiling around a Horizontal Cylinder Surface*, Heat Transfer Japanese Research, 1991. 21(4): p. 404-411

36. Hahne, E., Spindler, K., Chen, Q., and Windisch, R., *Local Void Fraction Measurements in Finned Tube Bundles*, Heat Transfer, 1990. **6**(18)-TPF-7: p. 41-46.

37. Suzuta, T., Ueno, T., Hirao, Y., Tomomatsu, K., Kawanishi, K. and Tsuge, A., *Measurement of interfacial velocities in gas- liquid upward two-phase flow across tube bundle, 7th International Conference on Nuclear Engineering*, Tokyo, Japan, April 19-23, 1999, ICONE-7483.

38. Zuber, N. and Findlay, J.A., *Average Volumetric Concentration in Two-Phase Flow Systems*. Journal of Heat Transfer, Trans. of ASME, 1965. **87**: p. 453-468.

39. Dowlati, R., Chan, A.M.C., and Kawaji, M., *Hydrodynamics of Two-Phase Flow across Horizontal in-Line and Staggered Road Bundles*. Journal of Fluids Engineering, Transactions of the ASME, 1992B. **114**(3): p. 450-456.

40. Xu, G.P., Tou, K.W., and Tso, C.P., *Two-Phase Void Fraction and Pressure Drop in Horizontal Crossflow across a Tube Bundle*. Journal of Fluids Engineering, Transactions of the ASME, 1998A. **120**(1): p. 140-145.

41. Feenstra, P.A., Weaver, D.S., and Judd, R.L., *Improved Void Fraction Model for Two-Phase Cross –Flow in Horizontal Tube Bundles*. International Journal of Multiphase Flow, 2000. **26**(11):p. 1851.

42. Axisa, F., Boheas, M.A., and Villard, B., *Vibration of Tube Bundles Subjected to Steam Water CrossFlow: A Comparative Study of Square and Triangular Arrays. In Proc. 8th Int. Conf. on S.M.R.T.*, Brussels, 1985. p. 122-131.

43. Ribatski, G., and Thome, J.R., *Dynamics of two-phase flow across horizontal tube bundles- a review*. Thermal Engineering, 2005. **4**(2): p.122-131.

44. Consolini, L., Robinson, D., and Thome, J.R., *Void Fraction and Two-phase Pressure Drops for Evapourating Flow over Horizontal Tube Bundles*. Heat Transfer Engineering, 2006. **27**(3): p. 5-21.

45. Taylor, C.E., and Pettigrew, M.J., *Effect of Flow Regime and Void Fraction on Tube Bundle Vibration*. Journal of Pressure Vessel Technology, 2001, **123**: p. 407-413.

46. Ishihara, K., Palen, J.W., and Taborek, J., *Critical Review of Correlations for Predicting Two-Phase Flow Pressure Drop across Tube Banks*. Heat Transfer Engineering, 1980. **1**(3):p.23-32.

47. Chisholm, D., and Laird, A. D.K., *Two-Phase Flow in Rough Tubes*. ASME Trans, 1958. **80**: p. 276-286.

48. Dowlati, R., Kawaji, M., and Chan, A.M.C., *Pitch-to-Diameter Effect on Two-Phase Flow across an in-Line Tube Bundle*. AIChE Journal, 1990. **36**(5): p. 765-772.

49. Dowalti, R., Kawaji, M., and Chan, A.M.C., *Two-Phase Crossflow and Boiling Heat Transfer in Horizontal Tube Bundles*. Journal of Heat Transfer, Transaction ASME, 1996. **118**(1): p. 124-131.

50. Diehl, J.E., *Calculate Condenser Pressure Drop*, Petroleum Refiner, 1957, **36**: p.147-153.

51. Hsu, J.T. and Jensen, M.K., *The Effect of Pitch to Diameter Ratio on Crossflow boiling Heat Transfer in an In-Line Tube Bundle, ASME HTD*, 1989. **104**: p. 239-246.

52. Hsu, J.T., *A Parametric Study of Boiling Heat Transfer in Horizontal Tube Bundles*, Ph.D. Thesis, University of Wisconsin, Milwaukee, 1987

53. Reinke, M.J., *A Comparison of the Boiling Heat Transfer and Two-Phase Pressure Drop Characteristics of an In-line and a Staggered Tube Bundle*, M.Sc. thesis, University of Wisconsin, Milwaukee, 1987

54. Zukauskas, A., *Heat Transfer from Tubes in Crossflow (Heat Transfer and Hydraulic Resistance of Single Banks and Systems of Tubes in Cross Flow of Gases and Viscous Liquids).* Advances in heat transfer, 1972. **8**: p. 93-160.

55. Shire, N.F. and Burnside, B.M., 2-*Phase Pressure Drop Measurements in Vertical Crossflow over a Horizontal Tube Bundle. In Proc. 6th UK Heat Transfer Conference*, 1999.

56. Burnside, B.M., Miller, K.M., McNeil, D.A., and Bruce, T., *Pressure Drop Measurements in a Section of a Kettle Reboiler*. *In Proc. 34th National Heat Transfer Conf*, Pittsburgh, PA, 2000. ASME Paper No. NHTC2000-12306.

57. Brisbane, T.W.C., Grant, I.D.R., and Whalley, P.B., *Prediction Method for Kettle Reboiler Performance*. American Society of Mechanical Engineers, 1980(80-HT-42): p. 10.

58. McNeil, D.A., Bamardouf, K., Burnside, B.M. and Almeshaal, M., *Investigation of flow phenomena in a kettle reboiler*. International Journal of Heat and Mass Transfer, 2010, **53**: p. 836- 848.

59. Carlucci, L.N., Galpin, P.F., and Brown, J.D., *Numerical Predictions of Shellside Heat Exchanger Flows*. HTD(Publ.), Am. Soc. Mech. Eng., 1986. **36**.

60. Edwards, D.P. and Jensen, M.K., *Two-Dimensional Numerical Model of Two-Phase Heat Transfer and Fluid Flow in a Kettle Reboiler.* ASME, HTD, Minneapolis, MN, USA, 1991. **159**: 9-16.

61. Butterworth, D., *The correlation of Cross-Flow Data by Means of the Permability Concept*, United Kingdom Automatic Energy Authority Report, AERE-R-9435, April 1979.

62. Patankar, S.V. and Spalding, D.B., *A Calculations Procedure for the Transient and Steady- State Behaviour of Shell and Tube Heat Exchangers*, Chapter in Heat Exchangers: Design and Theory Source book, edited by Afgan, N.H. and Schlunder, E.U., Hemisphere, Washington D.C., 1974.

63. Lahey, R.T., Sim, S., and Drew, D.A., *Evaluation of Interfacial Drag Models for Bubbly Two-Phase Flows*. *In Proc. 18th National Heat Transfer Conference San Diego*, California, 1979.

64. Lahey, R.T. and Drew, D.A., *The Three-Dimensional Time and Volume Averaged Conservation Equations of Two-Phase Flow*, Advances in Nuclear Science and Technology, Plenum Press, 1988: p.1-69.

65. Rahman, F.H., Gebbie, J.G., and Jensen, M.K., *Interfacial Friction Correlation for Shell-Side Vertical Two-Phase Cross- Flow Past Horizontal in-Line and Staggered Tube Bundles*. International Journal of Multiphase Flow, 1996. **22**(4): p. 753-766.

66. Stevanovic, V.D., Stosic, Z.V., Kiera, M., and Stoll, U., *Horizontal Steam Generator Thermal-Hydraulics at Various Steady-State Power Levels*. *In Proc. the tenth International Conference on Nuclear Engineering*, Arlington, VA, United States, 2002a. 767-779.

67. Stosic, Z.V. and Stevanovic, V.D, *Advanced Three-Dimensional Two-Fluid Porous Media Method for Transient Two-Phase Flow Thermal-Hydraulics in Complex Geometries*. Numerical Heat Transfer, Part B: Fundamentals, 2002. **41**(3-4): p. 263-289.

68. Stevanovic, V.D., Stosic, Z.V., Kiera, M., and Stoll, U., *Numerical Simulation and Analysis of the Loss of Feedwater Transient at the Unit 4 of Kola Npp. In Proc. the tenth International Conference on Nuclear Engineering*, Arlington, VA, United States, 2002b. 781-792.

69. Pezo, M., Stevanovic, V.D., and Stevanovic, Z., *A Two-Dimensional Model of the Kettle Reboiler Shell Side Thermal-Hydraulics*. International Journal of Heat and Mass Transfer, 2006.**49**(7-8): p. 1214-1224.

70. Ishii, M. and Zuber, N., *Drag Coefficient and Relative Velocity in Bubbly, Droplet or Particular Flows*. AIChE Journal, 1979. **25**(5): p. 843-855.

71. Simovic, Z.R., Ocokljic, S., Stevanovic, V.D., *Interfacial friction correlations for the two-phase flow across tube bundle*. International Journal of Multiphase Flow, 2007, **33**: p. 217-226.

72. Morris, D., Teyssedou, A., Lapierre, J., and Tapucu, A., *Optical fibre probe to measure local void fraction profiles*, Applied Optics, 1987. **26**(21): p. 4660-4664

73. Hamad, F.A., Imberton, F. and Bruun, H., *An optical probe for measurement in liquid-liquid two-phase flow*, Meas. Sci. Technol.,1997, **8 :**p.1122-1132

74. Miller, N., Mitchie, R.E., *Measurement of local voidage in liquid/gas two phase flow systems using a universal probe*, J. Br. Nucl. Energy. Soc. 1970. **9**(2): p. 94-100.

75. Danel, F. and Delhaye, J.M., *Sonde optique pour measure du taux de presence local en ecoulement diphasique*, Mesures Regulatio Automatisme, 1971. **36**: p. 99-101

76. Abuaf, N., Jones, O.C., and Zimmer, G.A., *Optical probe for local void fraction and interface velocity measurements*, Rev. Sci. Instrum, 1978. **49**(8): p. 1090-1094.

77. Sekoguchi, K. and Sato, Y., *Liquid Velocity Distribution in Two-Phase Bubble Flow*, International Journal of Multiphase Flow, 1975, **2**: p. 79-95.

78. Moujaes, S. and Dougall, R.S., *Experimental Investigation of Cocurrent Two-Phase Flow in a Vertical Rectangular Channel*, Canadian Journal of Chemical Engineering, 1987, **65**, p: 70-715.

79. Gartelliller, A., *Optical Probes for Local Void Fraction Measurements: Characterisation of performance*, Rev. Sci. Instrum. American Institute of Physics, 1989. **61**(2): p. 279-303.

80. McNeil, D.A., Azmahani, S. and Bamardouf, K., *A Mechanistic Analysis of Shell –Side Two-Phase Flow in an Idealised In –Line Tube Bundle*, International Journal of Multiphase Flow, 2012, **45**: p: 53-69.

81. Chan, A.M.C. and Banerjee, S., *Design Aspects of gamma densitometers for void fraction measurements in small scale two-phase flows*, Nuclear Instruments and Methods, 1989. **190**, 135.

82. Spindler, K., Bierer, M., Lorenz, G., Erhard, A. and Hahne, E., *Measurements in vertical gas liquid two-phase flow using an optical fiber probe, in Proc. 1st World Conference on Experimental Heat Transfer, Fluid Mechanics and Thermodynamics*, Dubrovnik, 1988: p. 348-357.

83. ESDU, *Crossflow Pressure Loss over Banks of Plain Tubes in Square and Triangular Arrays Including Effects of Flow Direction*, Engineering Sciences Data Unit, 1979(79034): p. 17.

84. Sato, Y. and Sekoguchi, K., *Liquid velocity distribution in two-phase bubble flow*, Int. J. Multiphase Flow, 1975. **2**: p. 79-95.

85. Clift, R., Grace, J.R., and Weber, M.E., *Bubbles, Drops, and Particles*. Academic Press, New York, 1978.

86. Niels, G., Some Boiling Aspects in kettle Evaporators, Ch.29, Boiling Phenomena: Physicochemical and Engineering Fundamentals and Applications, Hemisphere Publishing Co., 1079, **2**: p. 937-945.

APPENDIX A

Experimental Results for Kettle Reboiler –Pentane

Heat flux of 10 kW/m^2

Table A.1: Pressure drop at heat flux of 10 kW/m^2

Column 9.5	
Row number	Pressure Drop (Pa)
3.5	303.3756
5.5	297.2567
7.5	297.5311
9.5	293.2168
11.5	311.6540
13.5	319.0090
15.5	286.2265
Column 12.5	
3.5	308.3919
5.5	290.5311
7.5	302.9255
9.5	290.4560
11.5	305.2015
13.5	310.5344
Column 15.5	
5.5	294.0699
7.5	293.6613
9.5	309.4813
11.5	292.5959

Heat flux of 20 kW/m^2

Table A.2: Pressure drop at heat flux of 20 kW/m^2

Column 9.5		
Row number	Pressure Drop (Pa) Test 1	Pressure Drop (Pa) Test2
3.5	301.5991	301.3553
5.5	288.6608	289.7139
7.5	290.5582	289.0944
9.5	287.9829	288.9241
11.5	292.3738	296.2366
13.5	242.6243	253.966
15.5	254.7899	246.7337
Column 12.5		
3.5	330.37	316.9578
5.5	260.3268	272.2077
7.5	291.1787	294.1079
9.5	290.111	291.7215
11.5	291.3928	293.9371
13.5	271.1544	261.0326
Column 15.5		
5.5	294.3447	296.6268
7.5	284.551	286.1429
9.5	289.8521	288.6162
11.5	310.5714	308.1468

Heat flux of 30 kW/m^2

Table A.3: Pressure drop at heat flux of 30 kW/m^2

Column 9.5		
Row number	Pressure Drop (Pa) Test 1	Pressure Drop (Pa) Test2
3.5	304.3824	313.8089
5.5	278.7245	271.3623
7.5	271.1180	270.1212
9.5	250.2478	249.5187
11.5	241.3735	233.9776
13.5	216.5467	222.0154
15.5	222.7038	207.7322
Column 12.5		
3.5	326.3305	326.7047
5.5	265.4831	264.3596
7.5	268.5249	269.6916
9.5	257.3810	261.2382
11.5	247.4974	243.885
13.5	227.9974	219.2003
Column 15.5		
5.5	286.9293	286.6959
7.5	284.4403	287.4856
9.5	281.3714	282.5303
11.5	295.4736	290.9541

Heat flux of 40 kW/m^2

Table A.4: Pressure drop at heat flux of 40 kW/m^2

Column 9.5		
Row number	Pressure Drop (Pa) Test 1	Pressure Drop (Pa) Test 2
3.5	281.9071	274.7779
5.5	228.4697	242.2156
7.5	220.6255	218.4962
9.5	193.3679	195.3094
11.5	181.6604	198.719
13.5	142.7711	136.334
15.5	145.279	141.1955
Column 12.5		
3.5	305.9916	298.2723
5.5	214.6842	229.4244
7.5	231.6093	234.4883
9.5	205.3059	202.4528
11.5	174.3307	180.0726
13.5	157.136	155.5223
Column 15.5		
5.5	270.9581	275.3516
7.5	268.8296	265.7896
9.5	250.5506	248.5808
11.5	207.447	231.2117

APPENDIX B

Two –Fluid Model Results

Heat flux of 10 kW/m^2

Table B.1: Pressure drop at heat flux of 10 kW/m^2 (Column 9.5)

Column 9.5				
Row number	Pressure Drop			
	α_{out} =0.0	α_{out} =0.5	α_{out} =0.9	central column model
3.5	311.8	309.3	322.3	315.5
5.5	303.6	299.0	304.9	302.1
7.5	299.3	291.8	289.1	294.3
9.5	298.0	285.8	273.5	290.3
11.5	298.6	279.1	257.2	288.4
13.5	298.5	268.6	238.3	277.9
15.5	295.8	254.6	219.5	263.5

Table B.2: Pressure drop at heat flux of 10 kW/m^2 (Column 12.5)

Column 12.5			
Row number	Pressure Drop		
	α_{out} =0.0	α_{out} =0.5	α_{out} =0.9
3.5	315.3	311.8	326.4
5.5	305.0	301.2	307.7
7.5	299.1	293.9	291.8
9.5	298.7	288.9	277.0
11.5	301.5	285.2	261.9
13.5	304.4	276.8	241.0

Table B.3: Pressure drop at heat flux of 10 kW/m^2 (Column 15.5)

Column 15.5			
Row number	Pressure Drop		
	α_{out} =0.0	α_{out} =0.5	α_{out} =0.9
5.5	299.2	302.5	312.7
7.5	297.3	296.5	297.8
9.5	300.5	294.3	286.0
11.5	304.5	295.2	279.3

Heat flux of 20 kW/m^2

Table B.4: Pressure drop at heat flux of 20 kW/m^2 (Column 9.5)

Column 9.5				
Row number	Pressure Drop			
	α_{out} =0.0	α_{out} =0.5	α_{out} =0.9	central column model
3.5	303.9	297.2	302.7	304.6
5.5	295.9	285.5	279.7	296.4
7.5	294.9	279.4	262.1	275.0
9.5	297.7	274.8	246.0	248.3
11.5	302.8	269.1	228.9	227.6
13.5	306.4	258.7	208.7	210.8
15.5	306.9	244.9	188.8	197.0

Table B.5: Pressure drop at heat flux of 20 kW/m^2 (Column 12.5)

Column 12.5			
Row number	Pressure Drop		
	α_{out} =0.0	α_{out} =0.5	α_{out} =0.9
3.5	309.4	303.0	309.1
5.5	298.3	289.0	282.8
7.5	295.1	282.1	264.7
9.5	297.9	278.0	249.0
11.5	305.8	275.5	233.2
13.5	314.9	267.8	210.9

Table B.6: Pressure drop at heat flux of 20 kW/m^2 (Column 15.5)

Column 15.5			
Row number	Pressure Drop		
	α_{out} =0.0	α_{out} =0.5	α_{out} =0.9
5.5	299.8	295.2	292.3
7.5	294.5	287.6	271.4
9.5	297.0	284.4	257.7
11.5	305.4	286.4	250.6

Heat flux of 30 kW/m^2

Table B.7: Pressure drop at heat flux of 30 kW/m^2 (Column 9.5)

Column 9.5			
Row number	Pressure Drop		
	α_{out} =0.0	α_{out} =0.9	central column model
3.5	293.6	279.3	282.0
5.5	288.6	259.0	260.4
7.5	291.6	243.8	227.0
9.5	298.7	228.7	203.2
11.5	307.3	211.4	185.0
13.5	313.3	190.4	170.8
15.5	315.2	169.8	159.1

Table B.8: Pressure drop at heat flux of 30 kW/m^2 (Column 12.5)

Column 12.5		
Row number	Pressure Drop	
	α_{out} =0.0	α_{out} =0.9
3.5	300.5	288.4
5.5	290.8	263.2
7.5	291.8	246.8
9.5	298.8	231.4
11.5	311.0	214.9
13.5	323.3	191.3

Table B.9: Pressure drop at heat flux of 30 kW/m^2 (Column 15.5)

Column 15.5		
Row number	Pressure Drop	
	α_{out} =0.0	α_{out} =0.9
5.5	295.1	277.8
7.5	291.4	255.3
9.5	296.8	239.6
11.5	311.5	229.3

Heat flux of 40 kW/m^2

Table B.10: Pressure drop at heat flux of 40 kW/m^2 (Column 9.5)

Column 9.5			
Row number	Pressure Drop		
	α_{out} =0.0	α_{out} =0.9	central column model
3.5	285.2	265.5	266.9
5.5	284.0	248.9	228.5
7.5	291.2	236.3	197.5
9.5	302.2	222.5	175.9
11.5	313.7	205.3	159.7
13.5	321.2	183.5	147.0
15.5	323.2	162.3	136.8

Table B.11: Pressure drop at heat flux of 40 kW/m^2 (Column 12.5)

Column 12.5		
Row number	Pressure Drop	
	α_{out} =0.0	α_{out} =0.9
3.5	292.8	275.9
5.5	285.7	253.3
7.5	291.2	239.5
9.5	302.4	225.1
11.5	318.5	208.2
13.5	332.9	183.7

Table B.12: Pressure drop at heat flux of 40 kW/m^2 (Column 15.5)

Column 15.5		
Row number	Pressure Drop	
	α_{out} =0.0	α_{out} =0.9
5.5	291.1	269.6
7.5	290.6	249.3
9.5	299.9	233.6
11.5	322.0	221.0

Heat flux of 10 kW/m^2

Table B.13: Vertical mass flux at heat flux of 10 kW/m^2 (Column 9.5)

Column 9.5				
Row number	Vertical Mass Flux (kg/m^2 s)			
	α_{out} =0.0	α_{out} =0.5	α_{out} =0.9	central column model
1	59.49	60.56	76.18	56.98
2	60.07	59.94	71.46	58.15
3	63.71	62.80	71.88	60.17
4	66.01	64.52	71.18	62.22
5	68.03	66.06	70.41	63.91
6	69.45	67.06	69.23	65.21
7	70.44	67.60	67.68	66.19
8	71.21	67.80	65.83	66.94
9	71.80	67.62	63.68	67.53
10	72.38	67.22	61.28	67.99
11	72.80	66.44	58.58	68.36
12	73.00	65.22	55.54	68.66
13	72.97	63.54	52.14	68.92
14	72.60	61.35	48.69	69.18
15	71.82	58.66	44.92	69.47
16	70.79	55.76	41.61	69.79
17	73.83	56.02	41.97	70.05

Table B.14: Vertical mass flux at heat flux of 10 kW/m^2 (Column 12.5)

Column 12.5			
Row number	Vertical Mass Flux		
	α_{out} =0.0	α_{out} =0.5	α_{out} =0.9
2	28.41	34.81	52.23
3	49.28	50.43	65.35
4	60.52	58.76	69.69
5	65.37	62.97	20.27
6	66.90	64.99	69.35
7	67.97	66.23	68.08
8	69.23	67.08	66.56
9	70.59	67.65	64.84
10	71.92	67.99	62.90
11	73.11	68.12	60.66
12	74.14	68.03	58.00
13	75.09	67.53	54.57
14	75.82	65.85	49.84
15	75.25	61.61	43.51
16	73.41	54.69	36.74

Table B.15: Vertical mass flux at heat flux of 10 kW/m^2 (Column 15.5)

Column 15.5			
Row number	Vertical Mass Flux		
	α_{out} =0.0	α_{out} =0.5	α_{out} =0.9
6	-13.50	1.36	40.47
7	3.04	16.47	48.47
8	16.64	27.25	52.68
9	29.77	35.12	55.15
10	40.47	40.51	56.43
11	49.47	44.52	57.45
12	55.53	48.99	62.99

Heat flux of 20 kW/m^2

Table B.16: Vertical mass flux at heat flux of 20 kW/m^2 (Column 9.5)

Column 9.5					
Row number	Vertical Mass Flux (kg/m^2 s)				
	α_{out} =0.0	α_{out} =0.5	α_{out} =0.9	one fluid model	central column model
1	65.11	63.76	75.71	58.67	73.0
2	65.66	63.63	71.45	59.30	73.0
3	68.27	65.82	70.51	60.18	73.0
4	69.39	66.36	68.36	60.66	73.0
5	70.14	66.53	66.07	60.57	73.0
6	70.36	66.16	63.51	59.99	72.03
7	70.19	65.35	60.72	59.03	64.18
8	69.84	64.28	57.83	57.77	58.63
9	69.39	62.95	54.83	56.26	53.77
10	69.00	61.53	51.79	54.52	49.67
11	68.58	59.90	48.66	52.57	45.92
12	68.03	58.00	45.39	50.42	42.74
13	67.33	55.81	41.95	48.13	39.88
14	66.34	53.29	38.58	45.83	37.29
15	65.07	50.49	35.15	43.69	35.09
16	63.53	47.63	32.13	42.00	33.09
17	65.24	47.78	32.15	41.05	31.31

Table B.17: Vertical mass flux at heat flux of 20 kW/m^2 (Column 12.5)

Column 12.5			
Row number	Vertical Mass Flux		
	α_{out} =0.0	α_{out} =0.5	α_{out} =0.9
2	39.02	40.41	56.56
3	57.77	56.56	67.19
4	66.37	63.72	68.80
5	69.47	66.18	67.10
6	70.02	66.43	64.34
7	69.93	65.95	61.50
8	69.73	65.12	58.62
9	69.55	64.10	55.75
10	69.46	62.95	52.91
11	69.47	61.75	50.00
12	69.63	60.52	46.94
13	69.91	59.07	43.42
14	70.07	56.78	38.96
15	68.75	52.50	33.41
16	66.62	46.52	27.43

Table B.18: Vertical mass flux at heat flux of 20 kW/m^2 (Column 15.5)

Column 15.5			
Row number	Vertical Mass Flux		
	α_{out} =0.0	α_{out} =0.5	α_{out} =0.9
6	9.19	11.66	40.41
7	29.49	29.59	48.54
8	42.38	40.84	51.54
9	50.18	46.61	51.63
10	54.06	48.80	50.87
11	55.46	49.53	50.81
12	56.99	51.45	54.99

Heat flux of 30 kW/m^2

Table B.19: Vertical mass flux at heat flux of 30 kW/m^2 (Column 9.5)

Column 9.5				
Row number	Vertical Mass Flux (kg/m^2 s)			
	α_{out} =0.0	α_{out} =0.9	one fluid model	central column model
1	63.96	66.05	55.46	64.0
2	65.24	64.16	55.61	64.0
3	66.92	63.31	55.52	64.0
4	67.02	61.07	54.79	64.0
5	66.77	58.55	53.47	63.86
6	66.18	55.74	51.72	57.17
7	65.32	52.73	49.66	50.49
8	64.41	49.68	47.38	45.03
9	63.47	46.60	44.91	36.70
10	62.65	43.56	42.29	33.53
11	61.85	40.52	39.56	30.84
12	60.95	37.43	36.77	28.54
13	59.94	34.30	34.01	26.55
14	58.67	31.31	31.38	24.84
15	57.13	28.34	29.05	23.34
16	55.55	25.80	27.25	22.00
17	56.78	25.69	26.24	20.84

Table B.20: Vertical mass flux at heat flux of 30 kW/m^2 (Column 12.5)

Column 12.5		
Row number	Vertical Mass Flux	
	α_{out} =0.0	α_{out} =0.9
2	43.34	51.19
3	59.91	61.76
4	66.16	62.95
5	67.44	60.56
6	66.85	57.17
7	65.85	53.79
8	64.85	50.47
9	63.96	47.29
10	63.25	44.22
11	62.74	41.21
12	62.43	38.19
13	62.25	34.93
14	61.86	31.05
15	60.10	26.50
16	57.72	21.58

Table B.21: Vertical mass flux at heat flux of 30 kW/m^2 (Column 15.5)

Column 15.5		
Row number	Vertical Mass Flux	
	α_{out} =0.0	α_{out} =0.9
6	19.77	38.87
7	38.75	46.78
8	49.01	48.11
9	53.30	46.20
10	54.28	44.06
11	54.08	43.03
12	55.54	45.38

Heat flux of 40 kW/m^2

Table B.22: Vertical mass flux at heat flux of 40 kW/m^2 (Column 9.5)

Column 9.5				
Row number	Vertical Mass Flux (kg/m^2 s)			
	α_{out} =0.0	α_{out} =0.9	one fluid model	central column model
1	61.70	59.93	50.03	60.00
2	63.58	59.80	49.75	60.00
3	64.40	58.82	48.78	60.00
4	63.70	56.38	47.09	53.10
5	62.77	53.63	44.86	45.40
6	61.66	50.70	42.33	39.40
7	60.42	47.66	39.64	34.70
8	59.23	44.67	36.87	31.00
9	58.08	41.70	34.06	28.00
10	57.08	38.80	31.26	25.50
11	56.10	35.96	28.52	23.40
12	55.05	33.11	25.89	21.70
13	53.87	30.27	23.43	20.20
14	52.49	27.59	21.20	18.90
15	50.87	24.97	19.30	17.00
16	49.16	22.74	17.88	16.50
17	50.28	22.56	17.10	16.00

Table B.23: Vertical mass flux at heat flux of 40 kW/m^2 (Column 12.5)

Column 12.5		
Row number	Vertical Mass Flux	
	α_{out} =0.0	α_{out} =0.9
2	46.24	49.54
3	60.32	59.06
4	64.31	59.05
5	64.05	55.85
6	62.61	52.13
7	61.08	48.63
8	59.69	45.33
9	58.51	42.20
10	57.56	39.22
11	56.85	36.31
12	56.33	33.45
13	55.88	30.46
14	55.16	27.05
15	53.19	23.20
16	50.54	19.00

Table B.24: Vertical mass flux at heat flux of 40 kW/m^2 (Column 15.5)

Column 15.5		
Row number	Vertical Mass Flux	
	α_{out} =0.0	α_{out} =0.9
6	28.29	41.14
7	44.66	47.53
8	51.35	47.07
9	53.11	43.68
10	53.19	40.62
11	52.83	38.85
12	55.07	39.83

Heat flux of 10 kW/m^2

Table B.25: Void fraction at heat flux of 10 kW/m^2 (Column 9.5)

Column 9.5					
Row number	Void Fraction				
	α_{out} =0.0	α_{out} =0.5	α_{out} =0.9	one fluid model	central column model
1	0.05844	0.05783	0.05212	0.04660	0.03253
2	0.12080	0.12000	0.11020	0.12469	0.07712
3	0.17620	0.17580	0.16330	0.18737	0.14032
4	0.22390	0.22410	0.21040	0.23885	0.19274
5	0.26520	0.26590	0.25200	0.28181	0.23744
6	0.30050	0.30170	0.28860	0.31832	0.27593
7	0.33170	0.33340	0.32140	0.34981	0.30962
8	0.35970	0.36170	0.35090	0.37741	0.33938
9	0.38390	0.38640	0.37720	0.40185	0.36590
10	0.40630	0.40890	0.40100	0.42374	0.38975
11	0.42560	0.42860	0.42230	0.42374	0.41131
12	0.44330	0.44690	0.44220	0.46144	0.43098
13	0.45950	0.46350	0.46080	0.47788	0.44760
14	0.47440	0.47920	0.47820	0.49306	0.45964
15	0.48810	0.49330	0.49420	0.50716	0.48260
16	0.50230	0.50860	0.51020	0.52031	0.49344
17	0.49370	0.50230	0.50980	0.53249	0.50369

Table B.26: Void fraction at heat flux of 10 kW/m^2 (Column 12.5)

Column 12.5			
Row number	Void Fraction		
	α_{out} =0.0	α_{out} =0.5	α_{out} =0.9
2	0.08728	0.08801	0.08203
3	0.13880	0.14100	0.13380
4	0.18660	0.19030	0.18380
5	0.23140	0.23580	0.23090
6	0.27070	0.27530	0.27220
7	0.30560	0.31030	0.30900
8	0.33610	0.34120	0.34160
9	0.36280	0.36850	0.37040
10	0.38650	0.39290	0.39620
11	0.40760	0.41490	0.41960
12	0.42680	0.43530	0.44120
13	0.44430	0.45390	0.46090
14	0.45990	0.47040	0.47710
15	0.47780	0.49170	0.49680
16	0.46890	0.46960	0.49540

Table B.27: Void fraction at heat flux of 10 kW/m^2 (Column 12.5)

Column 15.5			
Row number	Void Fraction		
	α_{out} =0.0	α_{out} =0.5	α_{out} =0.9
6	0.11990	0.10580	0.10270
7	0.15120	0.14800	0.16630
8	0.17120	0.17880	0.22200
9	0.19210	0.21260	0.27050
10	0.21420	0.24810	0.30950
11	0.23490	0.28610	0.34500
12	0.26120	0.31240	0.36180

Heat flux of 20 kW/m^2

Table B.28: Void fraction at heat flux of 20 kW/m^2 (Column 9.5)

Column 9.5					
Row number	Void Fraction				
	α_{out} =0.0	α_{out} =0.5	α_{out} =0.9	one fluid model	central column model
1	0.09789	0.09888	0.09184	0.0862	0.14353
2	0.19810	0.19980	0.18810	0.2111	0.24293
3	0.28070	0.28330	0.27070	0.2979	0.31556
4	0.34480	0.34820	0.33690	0.3624	0.37221
5	0.39450	0.39850	0.38890	0.4122	0.41759
6	0.43420	0.43860	0.43110	0.4522	0.45483
7	0.46740	0.47230	0.46690	0.4849	0.47943
8	0.49580	0.50090	0.49730	0.5124	0.50049
9	0.51990	0.52550	0.52380	0.5357	0.51972
10	0.54140	0.54710	0.54690	0.5558	0.53713
11	0.55980	0.56590	0.56720	0.5731	0.55334
12	0.57640	0.58290	0.58610	0.5881	0.56817
13	0.59130	0.59830	0.60320	0.60130	0.58196
14	0.60490	0.61270	0.61950	0.6130	0.59486
15	0.61700	0.62520	0.63380	0.6239	0.60689
16	0.63050	0.63940	0.64960	0.6348	0.61811
17	0.61850	0.62910	0.64460	0.6465	0.62876

Table B.29: Void fraction at heat flux of 20 kW/m^2 (Column 12.5)

Column 12.5			
Row number	Void Fraction		
	α_{out} =0.0	α_{out} =0.5	α_{out} =0.9
2	0.14570	0.14840	0.14410
3	0.22830	0.23300	0.23080
4	0.29960	0.30600	0.30780
5	0.35970	0.36700	0.37220
6	0.40680	0.41460	0.42170
7	0.44560	0.45380	0.46220
8	0.47790	0.48660	0.49570
9	0.50510	0.51440	0.52390
10	0.52860	0.53840	0.54830
11	0.54910	0.55960	0.56970
12	0.56740	0.57880	0.58910
13	0.58360	0.59590	0.60650
14	0.59760	0.61060	0.62030
15	0.61560	0.62870	0.63800
16	0.59610	0.60520	0.63170

Table B.30: Void fraction at heat flux of 20 kW/m^2 (Column 15.5)

Column 15.5			
Row number	Void Fraction		
	α_{out} =0.0	α_{out} =0.5	α_{out} =0.9
6	0.17720	0.17710	0.18600
7	0.24570	0.25510	0.28870
8	0.29710	0.31670	0.36580
9	0.34740	0.38220	0.42380
10	0.39530	0.43770	0.46500
11	0.44010	0.48240	0.50030
12	0.46340	0.50160	0.51460

Heat flux of 30 kW/m^2

Table B.31: Void fraction at heat flux of 30 kW/m^2 (Column 9.5)

Column 9.5				
Row number	Void Fraction			
	α_{out} =0.0	α_{out} =0.9	one fluid model	central column model
1	0.13460	0.13300	0.1255	0.19896
2	0.26540	0.26350	0.2838	0.31885
3	0.36100	0.36140	0.3815	0.39906
4	0.42950	0.43240	0.4490	0.45806
5	0.47970	0.48450	0.4987	0.49404
6	0.51870	0.52520	0.5370	0.52303
7	0.55060	0.55910	0.5675	0.54849
8	0.57730	0.58730	0.5924	0.57085
9	0.59990	0.61180	0.6129	0.59091
10	0.61950	0.63270	0.6302	0.60903
11	0.63650	0.65120	0.6447	0.62557
12	0.65160	0.66830	0.6571	0.64069
13	0.66510	0.68400	0.6677	0.65467
14	0.67730	0.69890	0.6773	0.66775
15	0.68840	0.71190	0.6864	0.67994
16	0.70050	0.72680	0.6962	0.69142
17	0.68740	0.72030	0.7077	0.70230

Table B.32: Void fraction at heat flux of 30 kW/m^2 (Column 12.5)

Column 12.5		
Row number	Void Fraction	
	α_{out} =0.0	α_{out} =0.9
2	0.19810	0.20320
3	0.30250	0.31380
4	0.38540	0.40190
5	0.44950	0.46890
6	0.49680	0.51750
7	0.53440	0.55600
8	0.56500	0.58700
9	0.59040	0.61260
10	0.61200	0.63450
11	0.63070	0.65370
12	0.64720	0.67120
13	0.66190	0.68690
14	0.67440	0.69950
15	0.69010	0.71590
16	0.66860	0.70900

Table B.33: Void fraction at heat flux of 30 kW/m^2 (Column 15.5)

Column 15.5		
Row number	Void Fraction	
	α_{out} =0.0	α_{out} =0.9
6	0.2338	0.2555
7	0.3294	0.3792
8	0.4016	0.4623
9	0.4652	0.5201
10	0.5133	0.5595
11	0.5516	0.5932
12	0.5654	0.6060

Heat flux of 40 kW/m^2

Table B.34: Void fraction at heat flux of 40 kW/m^2 (Column 9.5)

Column 9.5				
Row number	Void Fraction			
	α_{out} =0.0	α_{out} =0.9	one fluid model	central column model
1	0.1688	0.1706	0.1661	0.24989
2	0.3224	0.3260	0.3471	0.38212
3	0.4229	0.4287	0.4491	0.46459
4	0.4916	0.4992	0.5149	0.51191
5	0.5405	0.5493	0.5619	0.54677
6	0.5778	0.5878	0.5970	0.5764
7	0.6081	0.6195	0.6245	0.60193
8	0.6330	0.6457	0.6466	0.6245
9	0.6540	0.6683	0.6647	0.64454
10	0.6722	0.6875	0.6797	0.66259
11	0.6878	0.7046	0.6924	0.67908
12	0.7017	0.7204	0.7033	0.69433
13	0.7141	0.7349	0.7131	0.70852
14	0.7253	0.7487	0.7222	0.72179
15	0.7352	0.7608	0.7313	0.74464
16	0.7464	0.7749	0.7417	0.75108
17	0.7325	0.7675	0.7541	0.75751

Table B.35: Void fraction at heat flux of 40 kW/m^2 (Column 12.5)

Column 12.5		
Row number	Void Fraction	
	α_{out} =0.0	α_{out} =0.9
2	0.2453	0.2531
3	0.3641	0.3783
4	0.4518	0.4702
5	0.5158	0.5359
6	0.5612	0.5819
7	0.5966	0.6177
8	0.6250	0.6461
9	0.6484	0.6694
10	0.6682	0.6893
11	0.6852	0.7067
12	0.7002	0.7228
13	0.7134	0.7373
14	0.7248	0.7492
15	0.7384	0.7643
16	0.7167	0.7575

Table B.36: Void fraction at heat flux of 40 kW/m^2 (Column 15.5)

Column 15.5		
Row number	Void Fraction	
	α_{out} =0.0	α_{out} =0.9
6	0.6200	0.3086
7	0.6127	0.4414
8	0.5796	0.5265
9	0.5401	0.5839
10	0.4819	0.6223
11	0.3979	0.6545
12	0.2840	0.6660

APPENDIX C

Two-Fluid Model and Experimental Mass Flow Rates and Velocity Results in the Pool

Heat flux of 10 kW/m^2

Table C.1: Mass flow rates below the tube bundle at heat flux of 10 kW/m^2

Below the tube bundle			
Vertical Plane Position Column number (-)	Numerical Mass Flow Rate (kg/s)	Vertical Plane Position Column number (-)	Experimental Mass Flow Rate [2,15] (kg/s)
9.0	0.00000	12.04	0.139
9.5	0.03458	12.53	0.280
10.5	0.10805	13.02	0.218
11.5	0.17704	13.51	0.221
12.5	0.21164	14.00	0.199
13.5	0.30075	14.49	0.276
14.5	0.40504	14.98	0.303
15.5	0.49902	15.47	0.393
16.5	0.56822	15.96	0.383
17.5	0.60951	17.55	0.590

Table C.2: Mass flow rates beside the tube bundle at heat flux of 10 kW/m^2

Beside the tube bundle			
Horizontal Plane Position Column number (-)	Numerical Mass Flow Rate (kg/s)	Horizontal Plane Position Column number (-)	Experimental Mass Flow Rate [2,15] (kg/s)
5.0	0.58460	5.02	0.454
5.5	0.60299	5.45	0.490
6.0	0.63975	6.03	0.621
6.5	0.65639	6.46	0. 603
7.0	0.68040	7.04	0.618

Heat flux of 20 kW/m^2

Table C.3: Mass flow rates below the tube bundle at heat flux of 20 kW/m^2

Below the tube bundle			
Vertical Plane Position Column number (-)	Numerical Mass Flow Rate (kg/s)	Vertical Plane Position Column number (-)	Experimental Mass Flow Rate [2,15] (kg/s)
9.0	0.0000	12.01	0.100
9.5	0.03148	12.5	0.128
10.5	0.10451	12.99	0.186
11.5	0.17800	13.48	0.217
12.5	0.21407	13.97	0.210
13.5	0.31920	14.46	0.256
14.5	0.41720	14.95	0.254
15.5	0.50999	15.44	0.299
16.5	0.58594	16.05	0.410
17.5	0.65673	17.52	0.506

Table C.4: Mass flow rates beside the tube bundle at heat flux of 20 kW/m^2

Beside the tube bundle			
Horizontal Plane Position Column number (-)	Numerical Mass Flow Rate (kg/s)	Horizontal Plane Position Column number (-)	Experimental Mass Flow Rate [2,15] (kg/s)
5.0	0.62380	5.02	0.570
5.5	0.59347	5.45	0.546
6.0	0.58444	6.03	0.564
6.5	0.53897	6.46	0.569
7.0	0.55803	7.04	0.624

Heat flux of 30 kW/m^2

Table C.5: Mass flow rates below the tube bundle at heat flux of 30 kW/m^2

Below the tube bundle			
Vertical Plane Position Column number (-)	Numerical Mass Flow Rate (kg/s)	Vertical Plane Position Column number (-)	Experimental Mass Flow Rate [2,15] (kg/s)
9.0	0.00000	12.01	0.120
9.5	0.02301	12.5	0.130
10.5	0.09572	12.99	0.224
11.5	0.16907	13.48	0.178
12.5	0.20938	13.97	0.239
13.5	0.31302	14.46	0.160
14.5	0.40795	14.95	0.347
15.5	0.49694	15.44	0.396
16.5	0.57015	16.05	0.371
17.5	0.64317	17.52	0.383

Table C.6: Mass flow rates beside the tube bundle at heat flux of 30 kW/m^2

Beside the tube bundle			
Horizontal Plane Position Column number (-)	Numerical Mass Flow Rate (kg/s)	Horizontal Plane Position Column number (-)	Experimental Mass Flow Rate [2,15] (kg/s)
5.0	0.64760	5.02	0.490
5.5	0.62301	5.45	0.568
6.0	0.61368	6.03	0.520
6.5	0.57289	6.46	0.420
7.0	0.59340	7.04	0.552

Heat flux of 40 kW/m^2

Table C.7: Mass flow rates below the tube bundle at heat flux of 30 kW/m^2

Below the tube bundle			
Vertical Plane Position Column number (-)	Numerical Mass Flow Rate (kg/s)	Vertical Plane Position Column number (-)	Experimental Mass Flow Rate [2,15] (kg/s)
9.0	0.0000	12.01	0.09
9.5	0.00844	12.5	0.176
10.5	0.08285	12.99	0.328
11.5	0.15123	13.48	0.388
12.5	0.19363	13.85	0.334
13.5	0.31920	14.46	0.250
14.5	0.38135	14.95	0.463
15.5	0.46145	15.44	0.417
16.5	0.52604	16.05	0.556
17.5	0.59445		

Table C.8: Mass flow rates beside the tube bundle at heat flux of 30 kW/m^2

Beside the tube bundle	
Horizontal Plane Position Column number (-)	Numerical Mass Flow Rate (kg/s)
5.0	0.60180
5.5	0.57574
6.0	0.58171
6.5	0.53049
7.0	0.52820

Heat flux of 10 kW/m^2

Table C.9: Vertical velocity beside the tube bundle (row 5) at heat flux of 10 kW/m^2

Beside the tube bundle (Row 5)				
Position X (mm)	Vertical Velocity (mm/s)			
	Numerical			Experimental, [2,15]
	Δx=10 mm	Δx= 4 mm	Δx= 2mm	
193.5	31.4	-4.16	-6.2	14.7
197.1	61.3	17.63	8.4	16.3
200.8	88.2	46.61	28.7	51.0
204.5	207.6	80.17	65.4	54.0
208.1	215.2	104.76	87.1	66.8
211.8	222.8	129.01	106.0	72.6
215.5	230.4	151.15	125.0	93.8
219.1	232.5	169.43	142.0	110.7
222.8	230.7	183.99	157.0	123.7
226.5	227.2	195.55	170.0	144.3
230.1	222.8	204.75	180.0	149.9
233.8	217.4	212.33	189.0	125.2
237.5	211.4	218.57	196.0	141.9
241.1	203.4	223.69	203.0	151.6
244.8	195.5	227.91	208.0	189.7
248.5	190.6	230.57	213.0	195.5
252.1	185.9	231.26	217.0	197.1
255.8	181.5	230.06	220.0	210.5
259.5	177.0	227.05	221.0	217.6
263.1	172.6	221.07	222.0	219.6
266.8	168.1	212.11	222.0	106.2
270.5	163.8	200.67	219.0	140.6
274.1	159.4	187.27	215.0	156.1
277.8	155.1	173.36	209.0	248.0
281.5	151.0	159.83	201.0	259.3
285.1	146.9	147.22	1910	285.4

Table C.10: Horizontal velocity beside the tube bundle (row 5) at a heat flux of 10 kW/m^2

Beside the tube bundle (Row 5)				
Position X (mm)	Horizontal Velocity (mm/s)			
	Numerical			Experimental, [2,15]
	Δx=10 mm	Δx= 4 mm	Δx= 2mm	
193.5	114.0	134.0	137.4	77.8
197.1	121.8	137.8	144.7	96.2
200.8	124.5	135.0	147.7	126.1
204.5	184.1	128.7	126.3	128.0
208.1	179.4	138.2	131.3	121.8
211.8	174.7	146.2	137.6	117.3
215.5	170.0	151.3	142.2	143.4
219.1	164.2	154.8	144.9	138.1
222.8	157.0	157.5	146.4	131.8
226.5	148.7	159.8	147.6	128.2
230.1	142.5	161.8	148.8	134.2
233.8	139.0	163.8	150.0	175.5
237.5	135.9	165.1	151.1	151.5
241.1	134.1	166.1	152.0	160.3
244.8	132.4	166.5	152.7	119.8
248.5	130.0	165.9	152.9	144.0
252.1	127.2	164.2	152.8	174.3
255.8	123.5	161.2	152.1	174.5
259.5	119.7	157.3	150.8	174.9
263.1	116.0	151.6	148.9	178.8
266.8	113.2	144.5	146.4	190.5
270.5	111.3	136.1	143.0	162.1
274.1	109.5	126.8	138.9	156.9
277.8	107.2	117.5	133.9	213.0
281.5	104.6	108.6	128.3	243.5
285.1	102.2	100.5	122.2	205.5

Heat flux of 20 kW/m^2

Table C.11: Vertical velocity beside the tube bundle (row 5) at heat flux of 20 kW/m^2

Beside the tube bundle (Row 5)			
Position X (mm)	Vertical Velocity (mm/s)		
	Numerical		Experimental, [2.15]
	Δx=8 mm	Δx= 4 mm	
193.5	-56.8	-50.44	
197.1	-31.8	-30.70	35.4
200.8	-2.7	-4.00	37.9
204.5	19.5	-23.61	41.8
208.1	32.4	37.03	44.1
211.8	42.9	48.16	78.4
215.5	53.1	58.32	84.5
219.1	63.5	68.15	123.6
222.8	74.4	78.57	175.1
226.5	85.8	89.68	161.2
230.1	98.6	101.38	135.4
233.8	111.8	113.97	150.2
237.5	126.2	127.06	176.4
241.1	140.6	140.64	192.3
244.8	155.5	154.71	219.4
248.5	171.0	169.17	190.6
252.1	186.8	184.11	201.4
255.8	203.0	199.29	308.6
259.5	219.1	214.77	284.2
263.1	235.8	230.42	277.3
266.8	252.3	246.24	285.4
270.5	268.5	262.14	293.7
274.1	285.2	278.03	312.6
277.8	301.0	293.64	324.5
281.5	316.8	309.16	289.3
285.1	332.4	324.25	283.9

Table C.12: Horizontal velocity beside the tube bundle (row 5) at a heat flux of 20 kW/m^2

Beside the tube bundle (Row 5)			
Position X (mm)	Horizontal Velocity (mm/s)		
	Numerical		Experimental, [2,15]
	Δx=8 mm	Δx= 4 mm	
193.5	114.0	118.9	
197.1	121.8	122.7	87.5
200.8	124.5	117.8	88.9
204.5	113.3	101.9	82.8
208.1	115.3	106.8	85.4
211.8	113.0	113.3	112.4
215.5	98.0	119.9	112.7
219.1	104.5	127.2	117.4
222.8	111.8	134.8	122.9
226.5	118.7	142.8	126.6
230.1	126.5	151.1	132.1
233.8	135.6	159.3	137.7
237.5	145.1	167.5	159.5
241.1	154.7	175.7	172.5
244.8	164.5	183.7	174.8
248.5	173.5	191.7	235.8
252.1	182.5	199.4	248.4
255.8	191.1	207.0	263.9
259.5	199.5	214.5	241.0
263.1	207.6	221.7	231.7
266.8	215.6	228.5	235.6
270.5	223.1	235.0	248.3
274.1	230.4	241.1	236.5
277.8	237.4	246.5	232.2
281.5	243.6	251.6	174.5
285.1	249.9	256.0	173.7

Table C.13: Vertical velocity below the tube bundle (column 17) at a heat flux of 20 kW/m^2

Below the tube bundle (Column 17)			
Position Y (mm)	Vertical Velocity (mm/s)		
	Numerical		Experimental, [2,15]
	Δx=8 mm	Δx= 4 mm	
44.3	154.6	150.8	196.7
47.4	149.9	146.1	174.3
50.5	145.1	141.4	164.5
53.7	140.1	136.4	146.3
56.8	134.7	131.2	153.0
59.9	129.3	125.8	190.7
63.0	123.5	120.3	182.8
66.1	117.7	114.7	174.9
69.2	111.8	109.0	152.1
72.3	105.7	103.2	147.0
75.4	99.6	97.3	147.5
78.5	93.4	91.4	142.5
81.6	87.0	85.5	140.5
84.8	80.6	79.5	136.2
87.9	74.2	73.5	132.6
91.0	67.7	67.5	141.2
94.1	61.1	61.5	120.1
97.2	54.6	55.5	98.9
100.3	47.9	49.5	101.3
103.4	41.3	43.6	122.9
106.5	33.7	37.7	112.0
109.6	25.9	31.0	124.1
112.7	18.6	23.1	121.0
115.9	7.3	4.8	110.8
119.0	-11.2	-17.8	143.9
122.1	-26.4	-27.5	192.4

Table C.14: Horizontal velocity below the tube bundle (column 17) at a heat flux of 20 kW/m^2

Below the tube bundle (Column 17)			
Position Y (mm)	Horizontal Velocity (mm/s)		
	Numerical		Experimental, [2 ,15]
	Δx=8 mm	Δx= 4 mm	
44.3	244.8	240.1	286.0
47.4	239.9	235.3	276.1
50.5	234.8	230.3	275.8
53.7	229.4	225.0	260.4
56.8	223.6	219.4	257.2
59.9	217.7	213.7	289.5
63.0	211.4	207.7	283.5
66.1	205.1	201.5	231.9
69.2	198.6	195.3	218.6
72.3	191.8	188.9	183.3
75.4	184.9	182.4	185.2
78.5	178.1	175.9	192.2
81.6	170.9	169.3	154.2
84.8	163.7	162.6	154.8
87.9	156.4	155.8	169.9
91.0	148.9	149.1	188.7
94.1	141.3	142.2	138.8
97.2	133.7	135.2	109.8
100.3	126.2	128.2	113.9
103.4	118.6	121.0	93.6
106.5	112.0	113.8	142.4
109.6	105.6	107.4	137.6
112.7	99.0	102.3	136.7
115.9	113.3	114.5	176.3
119.0	117.4	122.7	184.9
122.1	118.3	118.5	155.2

Heat flux of 30 kW/m^2

Table C.15: Vertical velocity beside the tube bundle (row 5) at heat flux of 30 kW/m^2

Beside the tube bundle (Row 5)			
Position X (mm)	Vertical Velocity (mm/s)		
	Numerical		Experimental, [2,15]
	Δx=8 mm	Δx= 4 mm	
193.5	-77.5	-72.48	-
197.1	-52.3	-50.71	-
200.8	-23.9	-22.97	91.4
204.5	-3.3	3.39	47.7
208.1	8.2	15.30	-
211.8	17.9	24.50	-
215.5	26.8	32.71	-
219.1	36.7	41.20	152.9
222.8	47.9	51.05	-
226.5	60.0	62.41	193.4
230.1	74.0	75.00	153.5
233.8	88.4	89.11	152.2
237.5	104.7	104.13	131.3
241.1	121.0	119.98	125.3
244.8	138.2	136.63	115.2
248.5	156.2	153.95	132.9
252.1	174.6	172.07	-
255.8	193.7	190.63	203.4
259.5	212.8	209.70	196.4
263.1	232.7	229.14	269.4
266.8	252.5	248.96	-
270.5	272.2	269.05	237.6
274.1	292.6	289.29	268.2
277.8	312.1	309.41	292.1
281.5	331.7	329.56	304.6
285.1	351.2	349.39	307.6

Table C.16: Horizontal velocity beside the tube bundle (row 5) at a heat flux of 30 kW/m^2

Beside the tube bundle (Row 5)			
Position X (mm)	Horizontal Velocity (mm/s)		
	Numerical		Experimental, [2,15]
	Δx=8 mm	Δx= 4 mm	
193.5	88.5	8.0	-
197.1	91.4	102.6	-
200.8	90.6	99.3	223.0
204.5	78.2	84.0	256.3
208.1	85.8	89.5	-
211.8	94.6	97.0	-
215.5	103.2	105.2	-
219.1	112.8	114.6	264.7
222.8	123.7	124.7	-
226.5	135.0	135.1	268.2
230.1	146.4	145.7	243.5
233.8	158.0	16.2	217.9
237.5	168.9	166.6	206.9
241.1	179.7	176.9	160.2
244.8	190.2	187.1	156.99
248.5	200.4	197.2	172.6
252.1	210.3	207.1	-
255.8	220.1	216.8	209.9
259.5	229.4	226.3	190.7
263.1	238.6	235.6	211.1
266.8	247.3	244.5	-
270.5	255.4	253.1	170.8
274.1	263.6	261.1	210.2
277.8	270.5	268.4	233.3
281.5	277.1	275.3	212.9
285.1	282.9	281.3	229.2

Heat flux of 40 kW/m^2

Table C.17: Vertical velocity beside the tube bundle (row 5) at heat flux of 40 kW/m^2

Beside the tube bundle (Row 5)		
Position X (mm)	Vertical Velocity (mm/s)	
	Numerical	
	Δx=8 mm	Δx= 4 mm
193.5	-90.6	-82.94
197.1	-65.4	-59.99
200.8	-37.3	-32.12
204.5	-17.9	-7.93
208.1	-7.4	2.98
211.8	1.4	11.05
215.5	9.3	18.14
219.1	18.4	25.68
222.8	29.1	34.78
226.5	41.0	45.60
230.1	54.9	57.83
233.8	69.3	71.76
237.5	85.9	86.68
241.1	102.5	102.53
244.8	120.1	119.23
248.5	138.7	136.68
252.1	157.7	154.99
255.8	177.6	173.81
259.5	197.4	193.18
263.1	218.3	213.01
266.8	239.1	233.29
270.5	260.0	253.93
274.1	281.6	274.83
277.8	302.4	295.79
281.5	323.5	316.87
285.1	344.7	337.80

Table C.18: Horizontal velocity beside the tube bundle (row 5) at a heat flux of 40 kW/m^2

Beside the tube bundle (Row 5)		
Position X (mm)	Horizontal Velocity (mm/s)	
	Numerical	
	Δx=8 mm	Δx= 4 mm
193.5	64.4	74.0
197.1	68.6	80.0
200.8	69.4	78.9
204.5	59.5	65.3
208.1	67.7	71.3
211.8	77.1	79.3
215.5	86.6	88.2
219.1	97.1	98.3
222.8	108.8	109.1
226.5	120.9	120.2
230.1	133.1	131.4
233.8	145.4	142.3
237.5	156.9	153.1
241.1	168.3	163.8
244.8	179.4	174.2
248.5	190.3	184.6
252.1	200.8	194.7
255.8	211.2	204.7
259.5	221.2	214.6
263.1	221.1	224.2
266.8	240.4	233.6
270.5	249.3	242.6
274.1	258.3	251.3
277.8	266.0	259.2
281.5	273.4	266.9
285.1	280.1	273.7

APPENDIX D

The bundle Only Model Results

Heat flux of 10 kW/m^2

Table D.1: Pressure drop at heat flux of 10 kW/m^2 (Column 9.5)

Column 9.5		
Row number	Pressure Drop (Pa)	
	B.C.(1)	B.C.(2)
3.5	309.10	309.10
5.5	301.10	301.10
7.5	297.20	297.20
9.5	295.80	295.80
11.5	296.30	296.30
13.5	298.50	298.50
15.5	302.90	302.90

Table D.2: Pressure drop at heat flux of 10 kW/m^2 (Column 12.5)

Column 12.5		
Row number	Pressure Drop (Pa)	
	B.C.(1)	B.C.(2)
3.5	310.9	310.9
5.5	303.3	303.3
7.5	298.3	298.3
9.5	296.6	296.6
11.5	296.4	296.4
13.5	297.7	297.7

Table D.3: Pressure drop at heat flux of 10 kW/m^2 (Column 15.5)

Column 15.5		
Row number	Pressure Drop (Pa)	
	B.C.(1)	B.C.(2)
5.5	305.9	305.9
7.5	300.5	300.5
9.5	299.2	299.2
11.5	297.5	297.5

Heat flux of 20 kW/m^2

Table D.4: Pressure drop at heat flux of 20 kW/m^2 (Column 9.5)

Column 9.5		
Row number	Pressure Drop (Pa)	
	B.C.(1)	B.C.(2)
3.5	299.40	295.42
5.5	291.60	285.15
7.5	290.90	280.41
9.5	293.60	276.45
11.5	298.4	269.98
13.5	305.0	257.65
15.5	314.3	240.70

Table D.5: Pressure drop at heat flux of 20 kW/m^2 (Column 12.5)

Column 12.5		
Row number	Pressure Drop (Pa)	
	B.C.(1)	B.C.(2)
3.5	303.7	300.567
5.5	294.9	289.635
7.5	292.3	284.041
9.5	294.3	281.351
11.5	298.4	277.653
13.5	303.9	267.288

Table D.6: Pressure drop at heat flux of 20 kW/m^2 (Column 15.5)

Column 15.5		
Row number	Pressure Drop (Pa)	
	B.C.(1)	B.C.(2)
5.5	300.3	297.665
7.5	295.6	291.86
9.5	296.9	291.794
11.5	298.9	295.362

Heat flux of 30 kW/m^2

Table D.7: Pressure drop at heat flux of 30 kW/m^2 (Column 9.5)

Column 9.5		
Row number	Pressure Drop (Pa)	
	B.C.(1)	B.C.(2)
3.5	289.0	278.7
5.5	284.2	267.6
7.5	287.3	261.2
9.5	293.6	253.1
11.5	301.9	240.2
13.5	311.7	221.1
15.5	324.2	200.6

Table D.8: Pressure drop at heat flux of 30 kW/m^2 (Column 12.5)

Column 12.5		
Row number	Pressure Drop (Pa)	
	B.C.(1)	B.C.(2)
3.5	294.5	286.1
5.5	287.5	273.5
7.5	288.6	266.6
9.5	294.2	259.7
11.5	301.7	246.8
13.5	310.4	223.4

Table D.9: Pressure drop at heat flux of 30 kW/m^2 (Column 15.5)

Column 15.5		
Row number	Pressure Drop (Pa)	
	B.C.(1)	B.C.(2)
5.5	294.458	287.195
7.5	291.987	280.811
9.5	296.415	278.904
11.5	301.704	274.592

Heat flux of 40 kW/m^2

Table D.10: Pressure drop at heat flux of 40 kW/m^2 (Column 9.5)

Column 9.5		
Row number	Pressure Drop (Pa)	
	B.C.(1)	B.C.(2)
3.5	285.2	252.3
5.5	284.0	235.4
7.5	291.2	220.5
9.5	302.2	202.4
11.5	313.7	181.7
13.5	321.2	161.2
15.5	323.2	145.7

Table D.11: Pressure drop at heat flux of 40 kW/m^2 (Column 12.5)

Column 12.5		
Row number	Pressure Drop (Pa)	
	B.C.(1)	B.C.(2)
3.5	286.0	262.6
5.5	281.7	242.6
7.5	286.3	225.4
9.5	295.0	204.2
11.5	305.2	177.9
13.5	316.2	154.4

Table D.12: Pressure drop at heat flux of 30 kW/m^2 (Column 15.5)

Column 15.5		
Row number	Pressure Drop (Pa)	
	B.C.(1)	B.C.(2)
5.5	288.9	264.5
7.5	289.6	246.6
9.5	296.9	209.9
11.5	304.4	158.3

Heat flux of 10 kW/m^2

Table D.13: Vertical mass flux at heat flux of 10 kW/m^2 (Column 9.5)

Column 9.5		
Row number	Vertical Mass Flux (kg/m^{2}s)	
	B.C.(1)	B.C.(2)
1	62.22	62.22
2	59.78	59.78
3	62.02	62.02
4	64.31	64.31
5	66.35	66.35
6	67.97	67.97
7	69.19	69.19
8	70.12	70.12
9	70.80	70.80
10	71.30	71.30
11	71.71	71.71
12	72.02	72.02
13	72.29	72.29
14	72.58	72.58
15	72.89	72.89
16	73.28	73.28
17	77.55	77.55

Table D.14: Vertical mass flux at heat flux of 10 kW/m^2 (Column 12.5)

Column 12.5		
	Vertical Mass Flux (kg/m^{2}s)	
Row number	B.C.(1)	B.C.(2)
2	49.04	49.04
3	55.91	55.91
4	61.38	61.38
5	64.94	64.94
6	67.15	67.15
7	68.59	68.59
8	69.69	69.69
9	70.58	70.58
10	71.22	71.22
11	71.69	71.69
12	71.98	71.98
13	72.23	72.23
14	72.31	72.31
15	72.28	72.28
16	71.71	71.71

Table D.15: Vertical mass flux at heat flux of 10 kW/m^2 (Column 15.5)

Column 12.5		
	Vertical Mass Flux (kg/m^{2}s)	
Row number	B.C.(1)	B.C.(2)
6	36.55	36.55
7	40.70	40.70
8	46.80	46.80
9	51.42	51.42
10	54.95	54.95
11	57.40	57.40
12	58.65	58.65

Heat flux of 20 kW/m^2

Table D16: Vertical mass flux at heat flux of 20 kW/m^2 (Column 9.5)

Column 9.5		
Row number	Vertical Mass Flux (kg/m^{2}s)	
	B.C.(1)	B.C.(2)
1	67.21	65.94
2	64.50	63.20
3	66.06	64.56
4	67.28	65.49
5	68.12	65.96
6	68.50	65.91
7	68.53	65.40
8	68.35	64.58
9	68.00	63.44
10	67.56	62.03
11	67.11	60.34
12	66.65	58.30
13	66.20	55.86
14	65.81	53.04
15	65.50	49.93
16	65.31	46.87
17	68.71	47.14

Table D.17: Vertical mass flux at heat flux of 20 kW/m^2 (Column 12.5)

Column 12.5		
	Vertical Mass Flux (kg/m^{2}s)	
Row number	B.C.(1)	B.C.(2)
2	55.21	54.58
3	62.22	61.36
4	66.73	65.56
5	68.80	67.27
6	69.46	67.54
7	69.44	67.10
8	69.17	66.35
9	68.79	65.40
10	68.29	64.26
11	67.75	62.94
12	67.17	61.41
13	66.64	59.50
14	66.02	56.78
15	65.23	51.85
16	64.18	44.98

Table D.18: Vertical mass flux at heat flux of 20 kW/m^2 (Column 15.5)

Column 15.5		
	Vertical Mass Flux (kg/m^{2}s)	
Row number	B.C.(1)	B.C.(2)
6	44.54	44.52
7	50.66	51.05
8	57.18	57.63
9	59.99	60.10
10	62.45	62.62
11	62.34	62.48
12	61.35	61.90

Heat flux of 30 kW/m^2

Table D.19: Vertical mass flux at heat flux of 30 kW/m^2 (Column 9.5)

Column 9.5		
Row number	Vertical Mass Flux (kg/m^{2}s)	
	B.C.(1)	B.C.(2)
1	66.82	63.81
2	64.17	61.07
3	64.94	61.39
4	65.20	61.06
5	65.07	60.13
6	64.59	58.76
7	63.87	57.03
8	63.05	55.04
9	62.16	52.79
10	61.27	50.33
11	60.42	47.64
12	59.60	44.73
13	58.85	41.65
14	58.16	38.48
15	57.58	35.40
16	57.13	32.70
17	60.03	32.73

Table D.20: Vertical mass flux at heat flux of 30 kW/m^2 (Column 12.5)

Column 12.5		
	Vertical Mass Flux (kg/m^{2}s)	
Row number	B.C.(1)	B.C.(2)
2	57.10	55.60
3	63.44	61.31
4	66.32	63.33
5	66.77	62.87
6	66.12	61.34
7	65.12	59.42
8	64.06	57.33
9	63.01	55.07
10	61.96	52.62
11	60.95	49.86
12	59.99	46.74
13	59.13	43.02
14	58.23	38.85
15	57.20	33.84
16	55.96	29.17

Table D.21: Vertical mass flux at heat flux of 30 kW/m^2 (Column 15.5)

Column 15.5		
	Vertical Mass Flux (kg/m^{2}s)	
Row number	B.C.(1)	B.C.(2)
6	48.92	48.51
7	55.07	55.12
8	59.84	59.68
9	60.17	59.35
10	61.03	60.01
11	59.46	57.52
12	57.59	55.66

Heat flux of 40 kW/m^2

Table D.22: Vertical mass flux at heat flux of 40 kW/m^2 (Column 9.5)

Column 9.5		
Row number	Vertical Mass Flux (kg/m^{2}s)	
	B.C.(1)	B.C.(2)
1	64.38	56.81
2	62.22	54.38
3	62.29	53.39
4	61.82	51.50
5	61.01	49.10
6	59.97	46.32
7	58.80	43.31
8	67.64	40.20
9	56.48	37.03
10	55.36	33.91
11	54.33	30.86
12	53.36	28.01
13	52.46	25.43
14	51.65	23.18
15	50.95	21.30
16	50.41	19.89
17	52.92	20.23

Table D.23: Vertical mass flux at heat flux of 40 kW/m^2 (Column 12.5)

Column 12.5		
	Vertical Mass Flux (kg/m^{2}s)	
Row number	B.C.(1)	B.C.(2)
2	57.32	53.38
3	62.60	56.72
4	63.87	55.62
5	63.02	52.53
6	61.52	48.99
7	59.96	45.41
8	58.50	41.75
9	57.14	37.91
10	55.85	34.04
11	54.65	30.18
12	53.54	26.70
13	52.56	23.69
14	51.58	21.34
15	50.46	19.25
16	49.25	17.47

Table D.24: Vertical mass flux at heat flux of 40 kW/m^2 (Column 15.5)

Column 15.5		
	Vertical Mass Flux (kg/m^{2}s)	
Row number	B.C.(1)	B.C.(2)
6	51.15	48.80
7	56.33	54.02
8	59.38	53.99
9	58.03	46.25
10	57.92	30.70
11	55.48	15.67
12	53.10	11.98

Heat flux of 10 kW/m^2

Table D.25: Void fraction at heat flux of 10 kW/m^2 (Column 9.5)

Column 9.5		
Row number	Void Fraction	
	B.C.(1)	B.C.(2)
1	0.05603	0.05603
2	0.12050	0.12050
3	0.17600	0.17600
4	0.22380	0.22380
5	0.26520	0.26520
6	0.30100	0.30100
7	0.33230	0.33230
8	0.35980	0.35980
9	0.38420	0.38420
10	0.40600	0.40600
11	0.42570	0.42570
12	0.44350	0.44350
13	0.45980	0.45980
14	0.47470	0.47470
15	0.48860	0.48860
16	0.50110	0.50110
17	0.49930	0.49930

Table D.26: Void fraction at heat flux of 10 kW/m^2 (Column 12.5)

Column 12.5		
	Void Fraction	
Row number	B.C.(1)	B.C.(2)
2	0.10110	0.10110
3	0.15260	0.15260
4	0.20030	0.20030
5	0.24260	0.24260
6	0.27990	0.27990
7	0.31290	0.31290
8	0.34200	0.34200
9	0.36790	0.36790
10	0.39120	0.39120
11	0.41200	0.41200
12	0.43100	0.43100
13	0.44810	0.44810
14	0.46390	0.46390
15	0.47950	0.47950
16	0.48460	0.48460

Table D.27: Void fraction at heat flux of 10 kW/m^2 (Column 12.5)

Column 15.5		
	Void Fraction	
Row number	B.C.(1)	B.C.(2)
6	0.10310	0.10310
7	0.15350	0.15350
8	0.18970	0.18970
9	0.21850	0.21850
10	0.24850	0.24850
11	0.27530	0.27530
12	0.30730	0.30730

Heat flux of 20 kW/m^2

Table D.28: Void fraction at heat flux of 20 kW/m^2 (Column 9.5)

Column 9.5		
Row number	Void Fraction	
	B.C.(1)	B.C.(2)
1	0.09535	0.09608
2	0.19940	0.20080
3	0.28280	0.28470
4	0.34640	0.34860
5	0.39620	0.39870
6	0.43610	0.43880
7	0.46930	0.47230
8	0.49740	0.50060
9	0.52150	0.52500
10	0.54270	0.54640
11	0.56130	0.56530
12	0.57800	0.58230
13	0.59300	0.59750
14	0.60660	0.61130
15	0.61900	0.62410
16	0.63040	0.63640
17	0.62650	0.63540

Table D.29: Void fraction at heat flux of 20 kW/m^2 (Column 12.5)

Column 12.5		
	Void Fraction	
Row number	B.C.(1)	B.C.(2)
2	0.16810	0.16910
3	0.24920	0.25110
4	0.31760	0.32020
5	0.37240	0.37560
6	0.41650	0.42020
7	0.45300	0.45720
8	0.48380	0.48850
9	0.51010	0.51530
10	0.53300	0.53880
11	0.55300	0.55930
12	0.57080	0.57780
13	0.58670	0.59410
14	0.60100	0.60910
15	0.61530	0.62260
16	0.61530	0.62260

Table D.30: Void fraction at heat flux of 20 kW/m^2 (Column 15.5)

Column 15.5		
	Void Fraction	
Row number	B.C.(1)	B.C.(2)
6	0.17350	0.17610
7	0.25700	0.26220
8	0.32070	0.33060
9	0.37130	0.38560
10	0.41970	0.43410
11	0.45590	0.46660
12	0.48920	0.49740

Heat flux of 30 kW/m^2

Table D.31: Void fraction at heat flux of 30 kW/m^2 (Column 9.5)

Column 9.5		
Row number	Void Fraction	
	B.C.(1)	B.C.(2)
1	0.13080	0.13310
2	0.26660	0.27080
3	0.36340	0.36860
4	0.43080	0.43640
5	0.48100	0.48710
6	0.52020	0.52660
7	0.55210	0.55900
8	0.57860	0.58590
9	0.60120	0.60900
10	0.62080	0.62920
11	0.63790	0.64690
12	0.65310	0.66280
13	0.66670	0.67710
14	0.67900	0.69040
15	0.69020	0.70280
16	0.70060	0.71510
17	0.69590	0.71500

Table D.32: Void fraction at heat flux of 30 kW/m^2 (Column 12.5)

Column 12.5		
	Void Fraction	
Row number	B.C.(1)	B.C.(2)
2	0.22580	0.70270
3	0.32690	0.70150
4	0.40320	0.68860
5	0.46060	0.67500
6	0.50470	0.66100
7	0.54010	0.64450
8	0.56390	0.62600
9	0.59390	0.60420
10	0.61500	0.57920
11	0.63330	0.54940
12	0.64940	0.51330
13	0.66360	0.46850
14	0.67640	0.41000
15	0.68920	0.33220
16	0.68690	0.22900

Table D.33: Void fraction at heat flux of 30 kW/m^2 (Column 15.5)

Column 15.5		
	Void Fraction	
Row number	B.C.(1)	B.C.(2)
6	0.23700	0.24630
7	0.34380	0.36030
8	0.42280	0.43860
9	0.47600	0.48860
10	0.51830	0.52910
11	0.54550	0.56020
12	0.57230	0.59310

Heat flux of 40 kW/m^2

Table D.34: Void fraction at heat flux of 40 kW/m^2 (Column 9.5)

Column 9.5		
Row number	Void Fraction	
	B.C.(1)	B.C.(2)
1	0.16440	0.17190
2	0.32420	0.33650
3	0.42600	0.44010
4	0.49320	0.50810
5	0.54200	0.55780
6	0.57950	0.59610
7	0.60970	0.62730
8	0.63460	0.65340
9	0.65560	0.67580
10	0.67380	0.69570
11	0.68960	0.71340
12	0.70360	0.72970
13	0.71610	0.74460
14	0.72740	0.75870
15	0.73770	0.77200
16	0.74720	0.78500
17	0.74220	0.78670

Table D.35: Void fraction at heat flux of 40 kW/m^2 (Column 12.5)

Column 12.5		
	Void Fraction	
Row number	B.C.(1)	B.C.(2)
2	0.32420	0.28680
3	0.42600	0.40530
4	0.49320	0.48630
5	0.54200	0.54470
6	0.57950	0.58780
7	0.60970	0.62150
8	0.63460	0.64900
9	0.65560	0.67220
10	0.67380	0.69290
11	0.68960	0.71090
12	0.70360	0.72790
13	0.71610	0.74330
14	0.72740	0.75890
15	0.73770	0.77420
16	0.74720	0.77800

Table D.36: Void fraction at heat flux of 40 kW/m^2 (Column 15.5)

Column 15.5		
	Void Fraction	
Row number	B.C.(1)	B.C.(2)
6	0.29360	0.32620
7	0.41440	0.45240
8	0.49140	0.53340
9	0.53870	0.59160
10	0.57620	0.64300
11	0.60090	0.67520
12	0.62640	0.71240

APPENDIX E

Lab View Program for Optical probe

LabView is graphical source software that was used to build a program to capture and store the analogue signal from the optical probe. The programme consists of two main screens: a block diagram screen and a frontal panel screen (the Virtual Instrument: VI). The block diagram screen contained the graphical code, including indicators, control objects, control loops, functions and other objects connected to each other to make the program. The front panel is the user interface, containing control objects connected to the block diagram to simplify chaining the setting values required to run the program. This includes the required number of readings to be obtained by setting the frequency of the data.

The program, named OPSL, was developed for logging the signals from the phase discrimination optical sensor. The logged signals were captured from the optical probe at 10-30 kHz and for approximately 10-30 seconds. The collected measurement results were graphed on the front panel, Fig. E1. Furthermore, the results were time sampled and written on an Excel file (.xls) for storage and further data processing. Since LabView is a graphically oriented software package, the program is probably best to understand by looking at the block diagram, i.e. the back panel shown in Fig. E2. The programme is able to capture the data under different testing conditions.

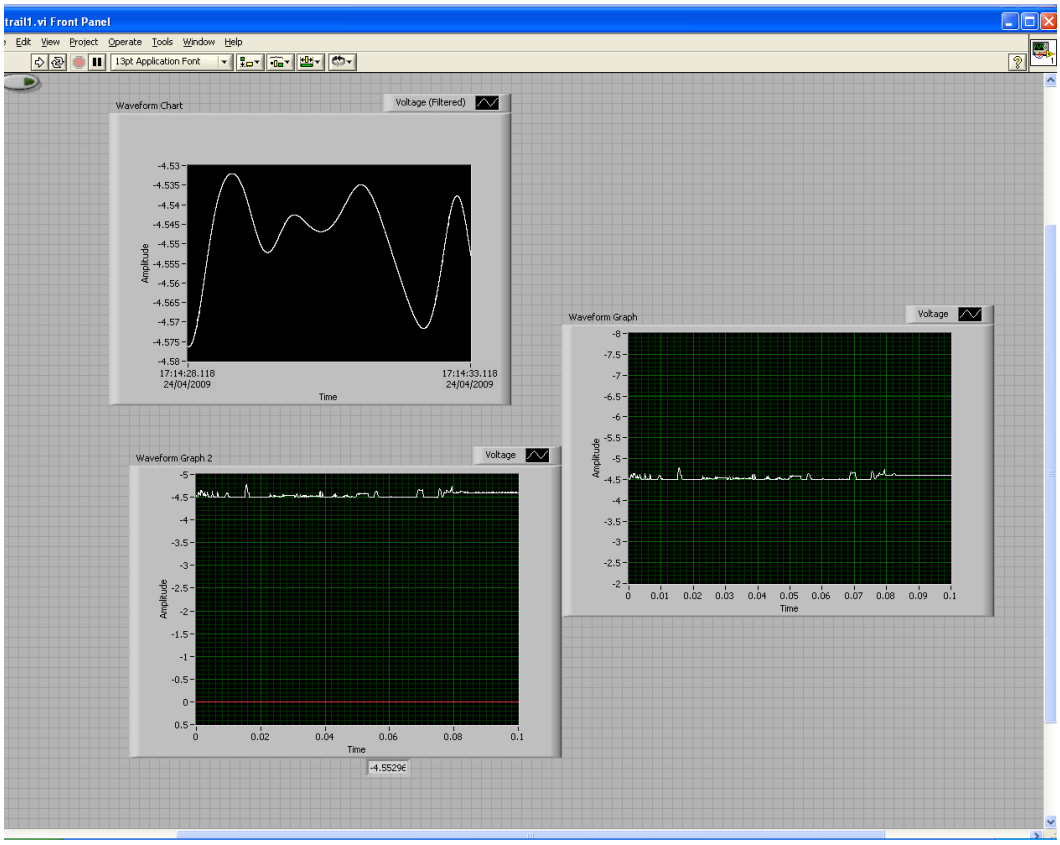

Figure E1: The front panel of the program developed in LabView for data acquisition from the phase discrimination optical probe.

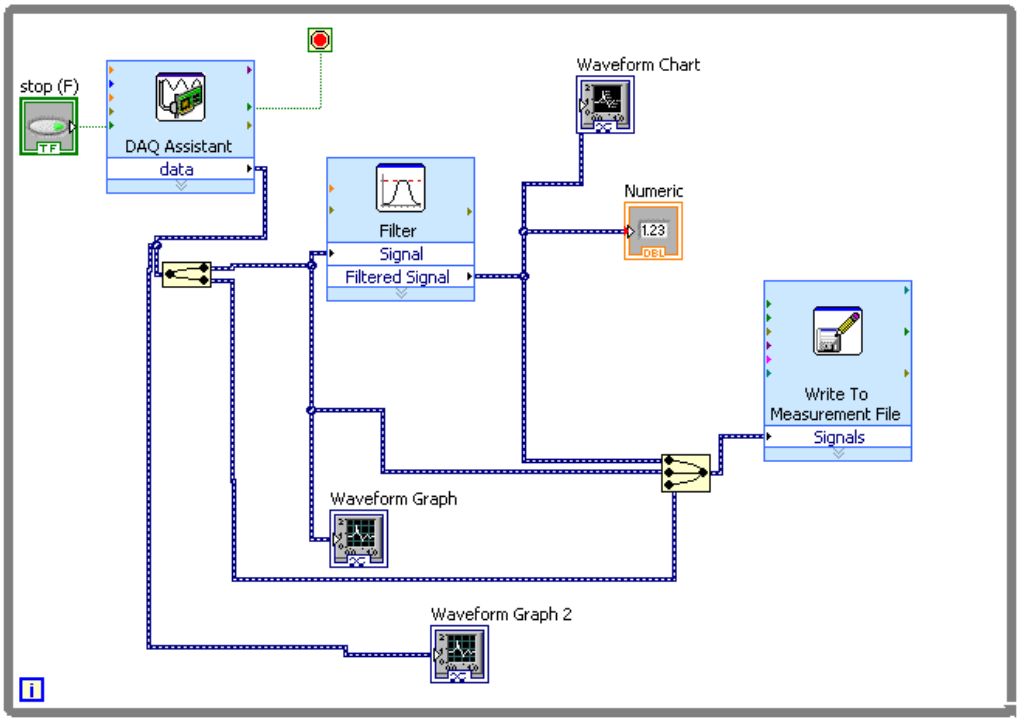

Figure E2: The back panel of the program developed in LabView for data acquisition from the phase discrimination optical probe.